AD-773 021

# ADVANCED TORQUE MEASUREMENT SYSTEM

Jee-Da Chang, et al

AiResearch Manufacturing Company

Prepared for:

Army Air Mobility Research and Development Laboratory

August 1973

DISTRIBUTED BY:

NTIS
National Technical Information Service
U. S. DEPARTMENT OF COMMERCE
5285 Port Royal Road, Springfield Va. 22151

## DISCLAIMERS

## DISPOSITION INSTRUCTIONS

Unclassified
Security Classification

## DOCUMENT CONTROL DATA - R & D

*(Security classification of title, body of abstract and indexing annotation must be entered when the overall report is classified)*

| | |
|---|---|
| 1. ORIGINATING ACTIVITY *(Corporate author)*<br>AiResearch Manufacturing Company, a division of<br>The Garrett Corporation,<br>Los Angeles, California | 2a. REPORT SECURITY CLASSIFICATION<br>Unclassified<br>2b. GROUP |

3. REPORT TITLE

ADVANCED TORQUE MEASUREMENT SYSTEM

4. DESCRIPTIVE NOTES *(Type of report and inclusive dates)*

Final Technical Report

5. AUTHOR(S) *(First name, middle initial, last name)*

Dr. Jee-Da Chang
Dr. Joseph Kukel

| | | |
|---|---|---|
| 6. REPORT DATE<br>August 1973 | 7a. TOTAL NO. OF PAGES<br>202 | 7b. NO. OF REFS<br>2 |

| | |
|---|---|
| 8a. CONTRACT OR GRANT NO.<br>DAAJ02-72-C-0044<br>b. PROJECT NO.<br>Task 1F162205A11908 | 9a. ORIGINATOR'S REPORT NUMBER(S)<br>USAAMRDL Technical Report 73-54 |
| c.<br>d. | 9b. OTHER REPORT NO(S) *(Any other numbers that may be assigned this report)*<br>AiResearch Report No. 73-9343 |

10. DISTRIBUTION STATEMENT

Approved for public release; distribution unlimited.

| | |
|---|---|
| 11. SUPPLEMENTARY NOTES | 12. SPONSORING MILITARY ACTIVITY<br>Eustis Directorate U.S. Army Air Mobility<br>Research and Development Laboratory,<br>Fort Eustis, Virginia |

13. ABSTRACT

This report documents the work performed by AiResearch Manufacturing Company during the Advanced Torque Measurement System program under contract from the Eustis Directorate, U.S. Army Air Mobility Research and Development Laboratory, Fort Eustis, Virginia.

Work covered in this program encompassed the preliminary research of application requirements, error sources, and special considerations; design of the advanced torque measurement system; fabrication of the advanced torque measurement system; and laboratory testing of the advanced torque measurement system under various conditions. Program results indicated that such a high-accuracy and high-environmental-tolerance torque measurement system for helicopter power-plant diagnostic purpose was both hardware implementable and economically feasible.

224

DD FORM 1 NOV 65 1473 REPLACES DD FORM 1473, 1 JAN 64, WHICH IS OBSOLETE FOR ARMY USE.

Unclassified
Security Classification

| 14 KEY WORDS | LINK A | | LINK B | | LINK C | |
|---|---|---|---|---|---|---|
| | ROLE | WT | ROLE | WT | ROLE | WT |
| Advanced Torque Measurement System | | | | | | |
| Helicopter Torque Sensor System | | | | | | |
| Rotating Shaft Torque Sensor | | | | | | |
| Diagnostic Torque Sensor | | | | | | |
| Engine Shaft Torque Measurement | | | | | | |
| Jet Engine Torque Sensor | | | | | | |
| Digital Torque Measurement System | | | | | | |
| Phase-Angle Torque Measurement System | | | | | | |
| Noncontacting Temperature Measurement Technique | | | | | | |

**DEPARTMENT OF THE ARMY**
**U. S. ARMY AIR MOBILITY RESEARCH & DEVELOPMENT LABORATORY**
**EUSTIS DIRECTORATE**
**FORT EUSTIS, VIRGINIA 23604**

This report was prepared by Garrett AiResearch Manufacturing Company under the terms of Contract DAAJ02-72-C-0044. It presents the findings of a 12-month study that was undertaken to evaluate an aircraft turboshaft engine torque-measuring system using the shaft angle of twist as the measurement transducer. This twisting motion is measured by a pair of proximity probes, external to the shaft. An eddy-current probe is also used to measure the shaft metal temperature, which is used for temperature compensation.

The objective of this contractual effort was to design, fabricate, and test an advanced-concept torque measurement system to measure actual torque on Army aircraft gas turbine engines. The program resulted in an increase in accuracy to 1% of point or better, over a power range of 30% to 100%. The torque-sensing technique investigated should also be capable of satisfactory operation on shafts having metal temperatures of up to 500°F, and should be adaptable to a wide range of rotational speeds and torques.

The conclusions and recommendations contained herein are concurred in by this Directorate. The study is considered to have adequately fulfilled the major objective.

Technical direction for this contractual effort was provided by Mr. Roger J. Hunthausen, Military Operations Technology Division.

Task 1F162205A11908
Contract DAAJ02-72-C-0044
USAAMRDL Technical Report 73-54
August 1973

# ADVANCED TORQUE MEASUREMENT SYSTEM

## Final Report

AiResearch Manufacturing Company Report 73-9343

By

Dr. J. D. Chang
Dr. Joseph Kukel

Prepared by

AiResearch Manufacturing Company
A Division of The Garrett Corporation
Los Angeles, California

for

EUSTIS DIRECTORATE
U.S. ARMY AIR MOBILITY RESEARCH AND DEVELOPMENT LABORATORY
FORT EUSTIS, VIRGINIA

# FOREWORD

This report presents the results of a program conducted by AiResearch Manufacturing Company, a Division of The Garrett Corporation, for the Eustis Directorate, U. S. Army Air Mobility Research and Development Laboratory, under Contract DAAJ02-72-C-0044, Task 1F162205A11908. The USAAMRDL technical monitor was Mr. Roger J. Hunthausen.

The principal investigator for the applied systems research group at AiResearch was Dr. J. D. Chang. Dr. J. Kukel was the project manager.

Contributors included Dr. J. Kukel, Dr. A. Saur, W. J. Harris, W. Reynolds, P. Wong, and C. R. Dolland.

Pages iii and iv are Blank

# TABLE OF CONTENTS

Page

## LIST OF ILLUSTRATIONS

# LIST OF TABLES

# INTRODUCTION

A means of directly measuring the torque from a rotating shaft has been needed and has presented an instrumentation problem for many years. The problem has been compounded further by the environmental and application constraints of Army helicopter gas turbines. Nevertheless, techniques and devices have been developed and are presently being utilized. Their application, however, is limited to control or limit functions. Accuracy is generally greater than 2 percent.

There is a need for a diagnostic torque sensor because of continued Army development of diagnostic systems to improve its maintenance and logistics posture. An accurate and repeatable torque measurement (1 percent or better) will enable an assessment of engine operating condition when combined with the gas turbine thermodynamic and gas generator characteristics. In addition, torque input/output measurements of the transmission can provide transmission diagnostic information.

A shaft that is transmitting torque must react in some physical way. The torque reaction produces torsion shear stress and a resulting angular twist. Also produced is an associated strain. Three materials phenomena--torsional stress, torsional strain, and angular twist--can serve as the basis for a suitable detection technique. The digital coincidence interpolation technique investigated during this program utilizes the angular twist as the basic torque-carrying parameter. The extraneous effects are deterministically compensated or statistically integrated by the use of a low-cost digital processor. Some of these additional accuracies are therefore obtained at the expense of the system response time, but for diagnostic purposes, the time delay is inconsequential as long as it lies below a reasonable limit.

This technique was implemented with hardware during the program. Its performance was thoroughly tested under a simulated condition. Test results indicated that such a technique should work equally well under the actual torqued-shaft condition.

# DIGITAL TORQUE MEASUREMENT APPROACH

## REVIEW OF TORQUE MEASUREMENT TECHNIQUES

All conceivable methods of measuring torque can be placed in the following three categories:

1. Techniques based on balancing an applied torque/force
2. Techniques based on measurement of changes of material characteristics with stress/strain
3. Techniques based on measurement of strain due to torque

Techniques in the first category have been used widely to measure torque in turboprop and turboshaft engines. In these techniques, an adjunct member of the drive train tends to rotate or move otherwise with applied torque. This movement is typically sensed by a hydraulic servo that acts to position the member to its null position. The hydraulic pressure required to restore the member to the null position is proportional to torque and is transduced to provide an indication of torque. This type of torque sensor is subject to wear and frictional effects in addition to pressure sensor and calibration errors. It is limited to accuracies on the order of ±5 percent. Response is typically slow.

Torque measurement based on the magnetostrictive effects is the most pertinent example of a technique based on measurement of changes of material characteristics with stress/strain. The technique is based on measuring the change in magnetization of a ferromagnetic material when it is subjected to a dimensional change. In one application, for example, magnetostrictive material is used as the core of the transformer.* The core is shaped in the form of a sleeve and is mounted on a torque-transmitting shaft. Shaft stress is transferred to the sleeve, and the resulting strain, through the magnetostrictive effect, causes the reluctance of the core to change. This change is used to modulate the transformer action and thereby measure torque. Although the magnetostrictive effect is highly nonlinear with stress, several methods of improving the linearity have been employed and accuracies as good as ±2 percent have been reported. The technique also appears to be suitable for temperatures as high as 250°F.

The last category, techniques based on measurement of strain, offers the largest number of possibilities. There are two principal subcategories of interest: (1) measurement of torque by means of strain gages, and (2) measurement of shaft angular twist. By far, the largest number of commercially available torquemeters are strain gage devices. For aircraft application, however, strain gage devices are considered unsuitable due to their

---

*Scoppe, F., MAGNETOSTRICTIVE MEASUREMENT OF TORQUE FROM HIGH SPEED ROTATING SHAFTS, Paper 69275, <u>ISA Symposium</u>, May 1969.

low life expectancy, environmental considerations, and the problem of signal acquisition.

A number of techniques are available for measuring shaft angular twist, including differential transformers and optical, inductive, and capacitive measuring techniques. In the differential transformer technique, the primary and secondary of a transformer are mounted to a torque-transmitting shaft such that as the shaft twists, the coupling between primary and secondary changes, thereby modulating the voltage generated in the secondary, yielding a variable voltage that is proportional to twist. In addition to reliability and signal acquisition problems, the accuracy of this technique is limited.

A common denominator of the last three techniques is that two signal pickoffs are required for each technique. For visualization, consider a shaft with identical gears at each end, the gears being exactly aligned under no-load conditions. A pickoff probe is located above each gear such that as the shaft rotates under no-load conditions, each probe generates a pulse train of identical frequency and phase. As the shaft begins to transmit torque, its ends will twist with respect to each other and the two pulse trains will be displaced in phase. This phase displacement is proportional to torque. In the case of the optical technique, the gear teeth are replaced by reflective strips and each probe consists of a light source and photo cell pair. In the inductive and capacitive cases, gear teeth or their equivalent are used together with variable-capacitance, variable-reluctance, monopole, or eddy-current probes. The optical technique is not considered suitable for this application due to its contamination susceptibility. Both the inductive and capacitive techniques appear well-suited, however, and the development of a digital torque measurement system based on the use of one of those techniques was the purpose of the subject program.

## DIGITAL PHASE ANGLE SENSING METHOD FOR TORQUE MEASUREMENT

As torque is applied to a rotating shaft, the shaft twists in proportion to the magnitude of the torque applied, and the direction of the twist is an indication of the polarity of the torque. In terms of the electrical pulses generated by sensing probes, the twist of the shaft changes the relative phase relationship of the pulse signals from the two sensing probes. Referring to Figure 1, the change in relative phase means a deviation of phase difference between the two probe signals from an initial no-torque value $\phi_0$. If the leading edges of the phasing pulses from the probes are used to control the start and stop of a sequence of gating pulses, and these gating pulses are then used to control the passage of fixed-frequency clock signals, the number of clock pulses (N) that pass through the gate will be proportional to the phase difference. The deviation $\delta N = N - N_0$ from the initial no-torque count ($N_0$) becomes a measure of the phase deviation and consequently the torque. The sign of $\delta N$ indicates torque polarity. Positive polarity indicates that the torque is being delivered to the load, while negative polarity indicates the acceptance of torque from the external load. Measuring the clock pulse count deviation not only allows measurement of torque magnitude, but also allows determination of whether the

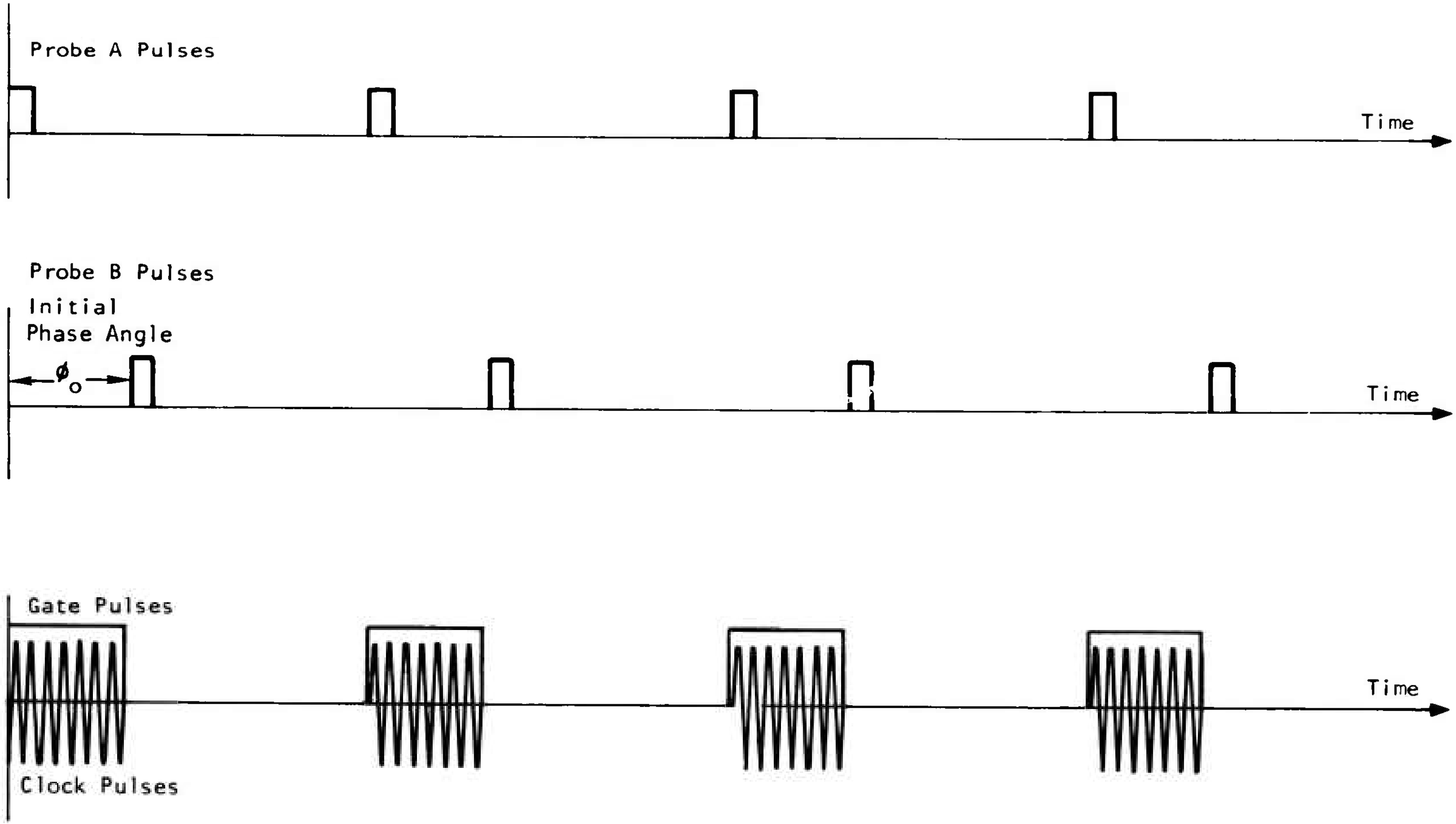

$\phi_o \longleftrightarrow N_o$ $\delta\phi = \phi - \phi_0$ $\delta\phi \longleftrightarrow \delta N$

$\phi \longleftrightarrow N$ $\delta N = N - N_0$ and $\delta N \longleftrightarrow \propto$ Torque

Figure 1. Principle of Digital Phase Measuring Technique.

torque is applied to the load by the engine or is applied to the engine temporarily by the external load. This information may also be of importance from a diagnostic point of view.

The accuracy of the torque measurement will depend on such factors as the rise time and shape of the phasing pulses from the sensing probes, the frequency and stability of the oscillator used to generate the clock pulses, and the accuracy of the pulse count. For accuracy and repeatibility of the gate opening and closing, the phasing pulses must be well shaped with a fast rise time. Accuracy increases with the number of clock pulses that can be obtained during the time the gate is open--thus, a high-frequency oscillator is desirable. Stability of the oscillator also is an important consideration for obtaining accuracy and repeatability, as is speed and stability of the device used to count the clock pulses.

The ability to count the number of clock pulses during the gate opening period demands the use of digital counting and computing. Due to electronic circuit stability, there is a limitation on the maximum frequency the clock pulses can reach. To circumvent this limitation, an improved computational algorithm can be devised based on a coincidence interpolation technique.

Coincidence interpolation allows accurate measurement of a quantity that is smaller than the units of a reference frame by utilizing the coincidence information between the known and unknown quantities. Figure 2 illustrates the application of this technique. Given a known length of 0.5 in. per division, the problem is to measure the unknown per-division length of the lower trace in Figure 2 using the upper line as a ruler. Since the per-division length of the lower trace is smaller than that of the given ruler, direct measurement becomes impossible. However, as shown in the plot, four units of the known quantity coincide with 7 units of the unknown quantity. Therefore, the unknown quantity can be interpolated to be 4/7 of the known quantity (0.5 in.), or 0.285714 in.

In the phase-angle measurement case, coincidence occurs in the time domain. The known quantity is the period (or frequency) of the clock pulses, and the unknown quantity is the differential time corresponding to the phase difference between the phasing pulses from the two sensing probes.

The basic functions implemented in this digital torque measurement approach are shown in block diagram form in Figure 3. The measurement system consists of four major units: sensing unit, temperature unit, digital signal processing and computing unit, and display unit.

The sensing unit provides relative shaft twist angle sensing through probes A and B and their respective shaft-mounted phasing poles. Shaft temperature is sensed by probes C and D to provide for compensation of the effects of temperature on the modulus of rigidity of the torque shaft.

The temperature unit accepts the electrical signals from probes C and D, performs linearization, provides analog voltage proportional to shaft temperature, converts the analog signal to digital form by an A/D converter, and outputs the resulting digital value.

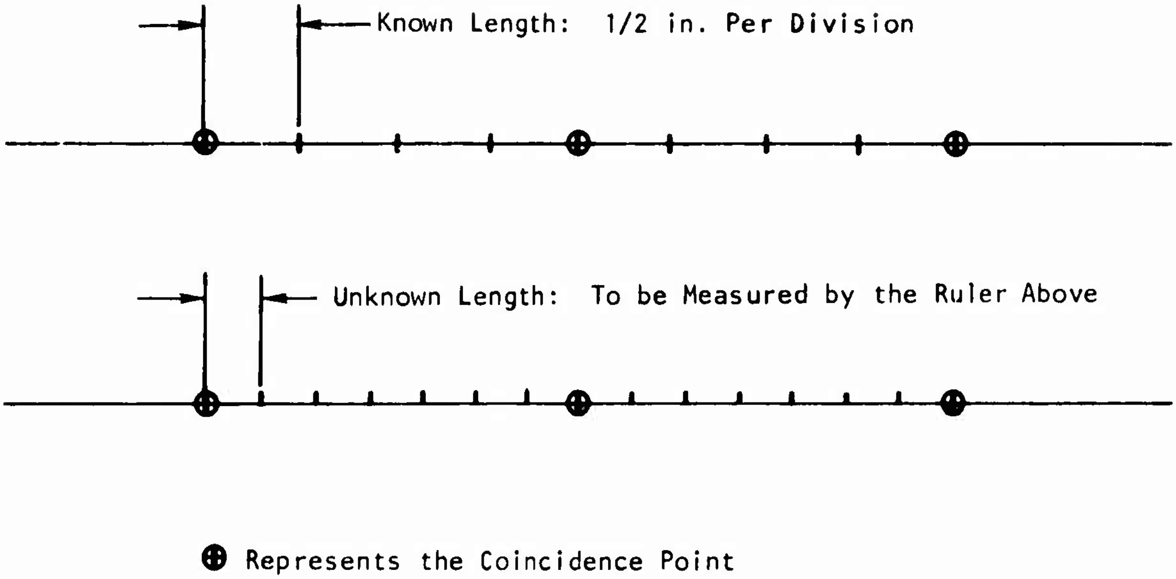

Figure 2. An Example of Coincidence Interpolation Technique.

The digital signal processing and computing unit consists of three modules: conditioner module, discrimination module, and computation module. The conditioner module accepts probe A and B electrical outputs and shapes them to suitable voltage triggers for the discriminator module. The discriminator module accepts the conditioned signals of probes A and B and an internal fixed rate pulse generator signal into a coincidence checking logic circuit. An accurate determination is made of the shaft speed and the time difference between the signals of probes A and B. The torque computation module accepts the digital signals from the discrimination module and temperature unit and digitally computes torque from the relationships:

$$\theta = 360 \left[ \left( \frac{N_2}{N_4} \right) N_3 - N_1 \right] \tag{1}$$

$$G = G_o \, (1 - K_2 \, T) \tag{2}$$

$$T = \frac{J \times G \times \theta}{57.3 \times L} \tag{3}$$

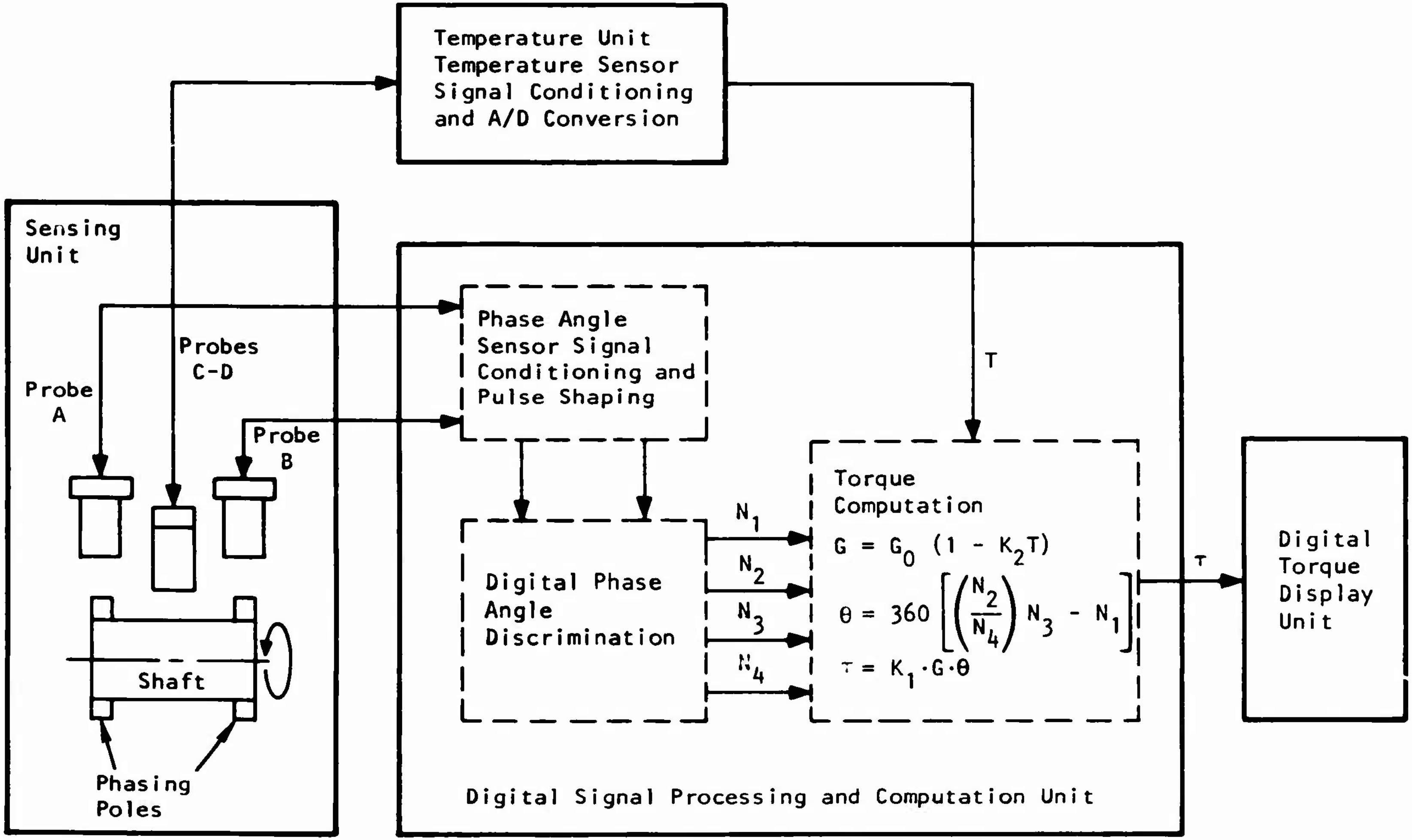

Figure 3. Digital Torque Measurement System.

where $\tau$ = the torque transmitted through the shaft, in.-lb

$J$ = the polar moment of inertia of the shaft, $\text{in.}^4$

$G$ = the modulus of rigidity of the shaft, $\text{lb/in.}^2$

$L$ = the length of the shaft, in.

$\theta$ = the shaft twist angle, deg

$N_1$ = the number of counts of probe B pulses counted between the coincidence of the probe A signals and the clock and the first coincidence of the probe B signal and the same clock signal

$N_2$ = the number of counts of the clock signal during the same time period as for $N_1$

$K_1$ = $J/57.3L$

$N_3$ = the number of counts of probe B signal counted between the first and the second coincidence of the probe B signal and the clock

$N_4$ = the number of counts of the clock signal during the same time period as for $N_3$

$G_o$ = the value of the modulus of rigidity at a reference temperature of $T_o$

$K_2$ = a proportional constant

$T$ = the differential temperature measured with respect to a reference temperature $T_o$

The display accepts the digital signal from the computation module and converts it to a visual numeric display.

## APPLICATION REQUIREMENTS

Development of the digital torque measurement sensor is aimed at fulfilling a need for an accurate (within 1 percent) torque measurement to support helicopter engine monitoring and diagnostics. Since the approach is a passive measurement technique (as opposed to a hydraulic force balance technique), it can be considered for both external (to the engine) drive shaft torque measurement and internal torsion shaft torque measurement.

Figures 4 and 5 illustrate the installation of the sensors and phasing gears necessary to sense shaft angular twist and temperature for both the external and internal applications. These two applications impose different requirements on the measurement system, even for the same engine, because of differences in environment (primarily temperature), torque level, shaft dimensions, and rotational speeds.

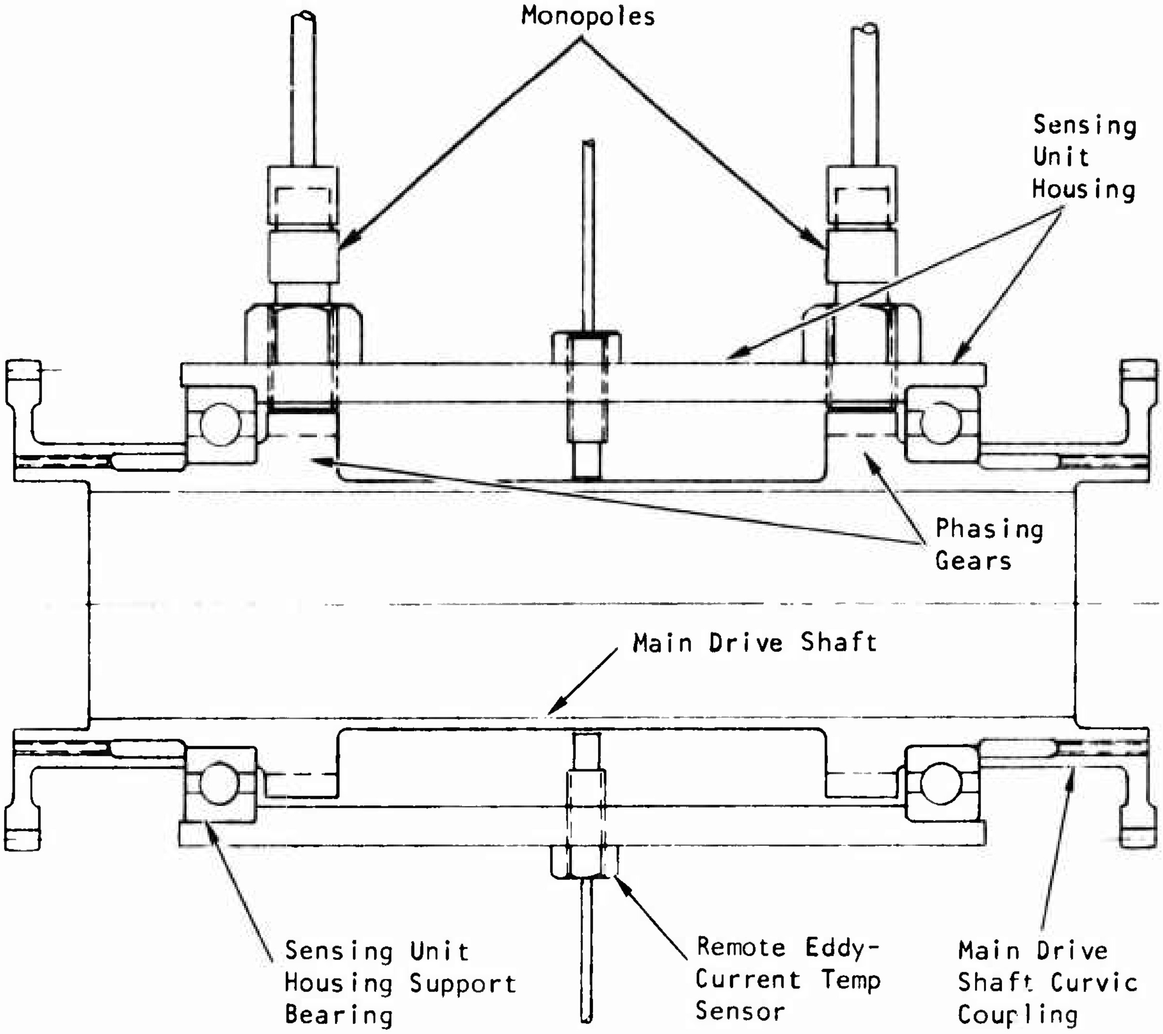

Air Gap for Monopoles: 20 to 50 mils
Air Gap for Eddy-Current Temperature Sensors: 100 to 200 mils

Figure 4. Typical External Torque Measurement Application.

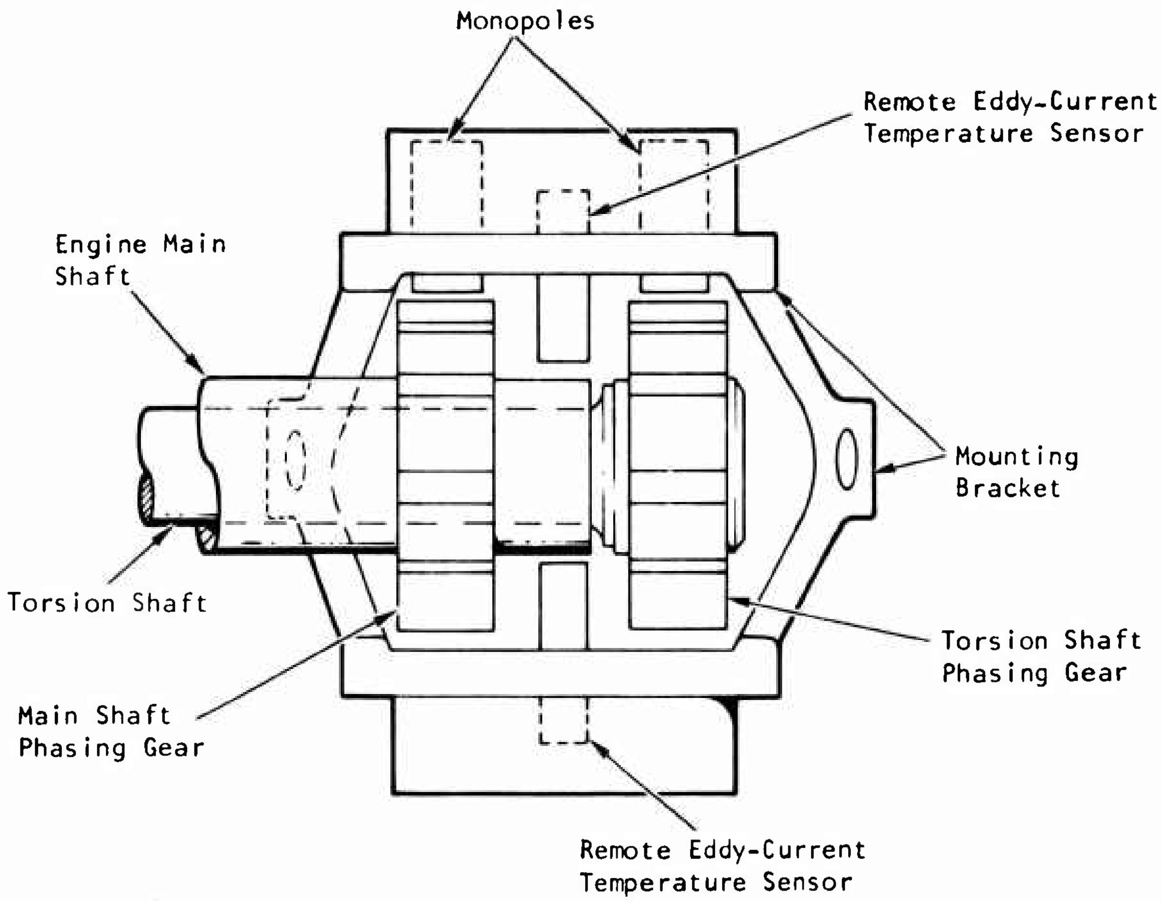

Air Gap for Monopoles: 20 to 50 mils
Air Gap for Eddy-Current Probes: 100 to 200 mils

Figure 5. Typical Engine Internal Torsion Shaft Torque Measurement Application.

To further illustrate the installation of the phase-angle sensors and associated parts for the internal installation, Figure 6 shows the parts which comprise the installation of a phase-angle torque sensing unit for the AiResearch T76 engine. The phase-angle sensor, shown at the right in the photograph, is a dual monopole pickup. The electronics for this system (not shown) implements an analog approach to torque computation.

Because of these differences, the application requirements for the two cases are listed separately below. The angular deflections and corresponding time increments listed are based on drive shaft sizing calculations included in the appendix. The requirements listed below are compatible with application to the UH-1 helicopter.

## External Installation

Shaft type--Hollow splined shaft connected to engine and transmission through curvic couplings

Shaft material--High-strength stainless steel such as AM355

Shaft length--1 ft

Outer diameter--Approximately 2 in.

Inner diameter--Approximately 1.9 in.

Torque-speed range--75 to 250 ft-lb at 6000 rpm
250 to 725 ft-lb at 6600 rpm

Full-scale twist angle--5 deg

Full-scale phase-angle time-delay--139 and 126 μsec, respectively

Maximum shaft temperature--165°F

Vibration environment--1 g to 10 g, 10 Hz to 10,000 Hz

## Internal Installation

Shaft type--Hollow, splined, internal torsion shaft

Shaft material--High-strength stainless steel such as AM355

Shaft length--2.5 ft

Outer diameter--Approximately 1 in.

Inner diameter--Approximately 0.8 in.

Torque speed range--100 to 300 ft-lb at 26,000 rpm

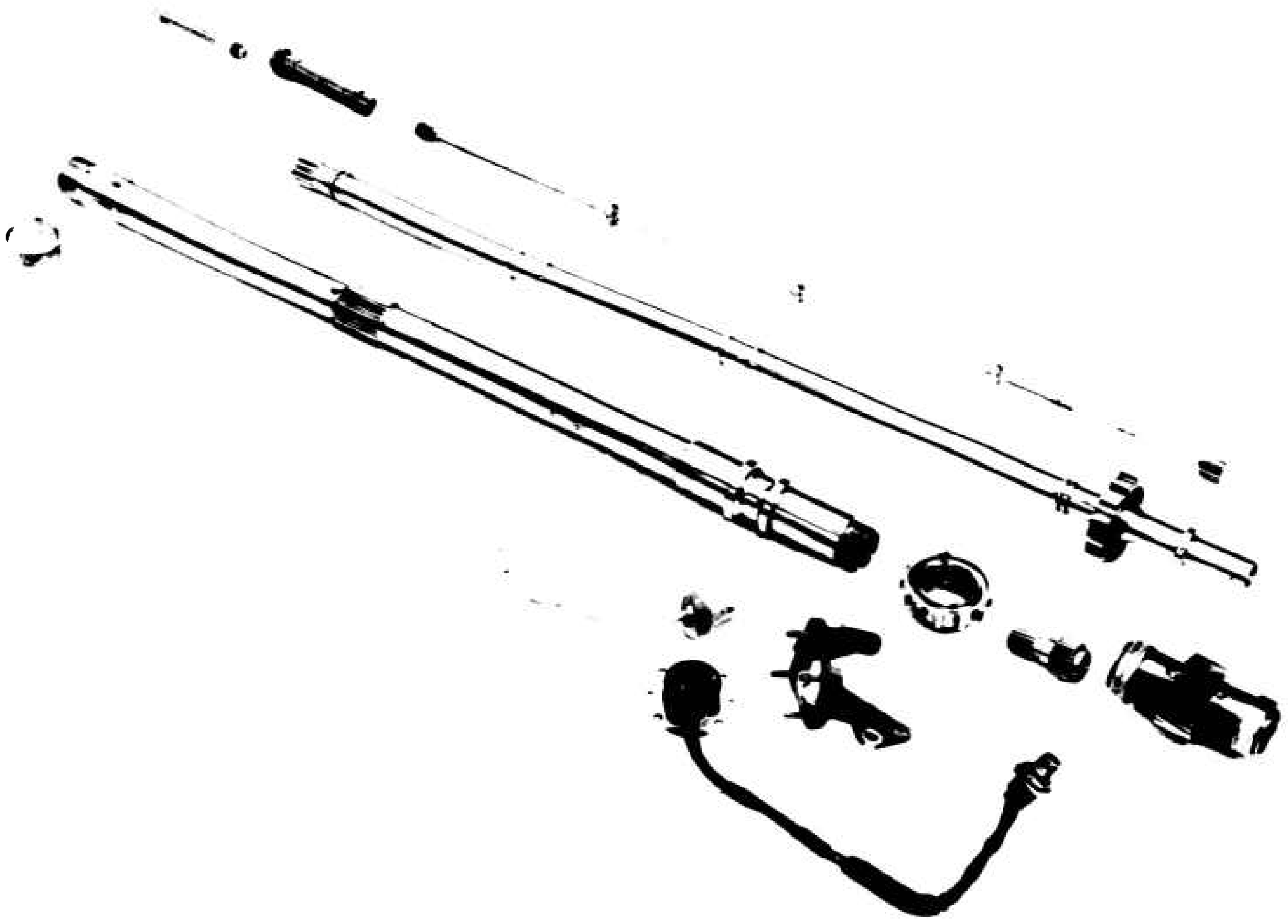

Figure 6. Phase-Shift System Internal Shafting, Gears, High-Speed Pinion, Monopole and Mount, and Oil Jet.

Full-scale twist angle--10 deg

Full-scale phase-angle time-delay--64 μsec

Maximum shaft temperature--500°F

Vibration environment--1 g to 10 g, 10 Hz to 10,000 Hz

## INSTALLATION AND ADAPTABILITY CONSIDERATIONS

### External Sensor Installation

Figure 4 illustrates a typical design of the sensing unit for external shaft application. The gears could be pressed onto the main drive shaft, then furnace-brazed to the shaft, or they could be pressed and welded on a pair of split collars which would be welded on the shaft to provide a larger diameter to allow the gears to clear the height of the two seal lands on the main drive shaft. The gears could also be machined as part of the main drive shaft. Among these choices, the third one appears best, because it provides better structural integrity, allows a new shaft design meeting the torsional angle requirement and the shaft dynamics requirements, and simplifies installation and maintenance.

The phase information pickup and the shaft temperature sensor can be mounted in a housing supported by two grease-pack type bearings or can be mounted on the nearby fixed structure through brackets. The bearing-supported approach requires the use of reliable bearings. The bracket-mounting approaches are more susceptible to shaft vibration and wobble; however, the shaft vibration and wobble effects can be compensated by using additional pickups located at different locations around the shaft to minimize the effects of gap variation. Due to the advancement in bearing seal material research, a grease-pack bearing designed to operate under the speed and temperature environment of a main drive shaft located at the inlet of the turboshaft engine (6600 rpm and a maximum temperature of 165°F) and subjected to a light load of the housing and the pickup probes (less than 10 lb) should provide highly reliable operation for a long period of time without difficulty. The bearings can be held in place by the original curvic couplings as shown in Figure 4. The bearing arrangement for pickup housing support also reduces the major part of the effect of shaft wobble (which is typical of the main drive shaft) on the pickup signals because the two-phase information pickups will move with the shaft in almost exactly the same manner. The housing can be kept from rotating with the shaft by a mechanism as shown in Figure 7. This mechanism allows the housing to move as needed to compensate for the shaft wobble, but prevents housing rotation.

### Internal Sensor Installation

Figure 5 shows an installation sketch for the engine internal torsion shaft application. Two phasing gears are placed at the same end of the engine

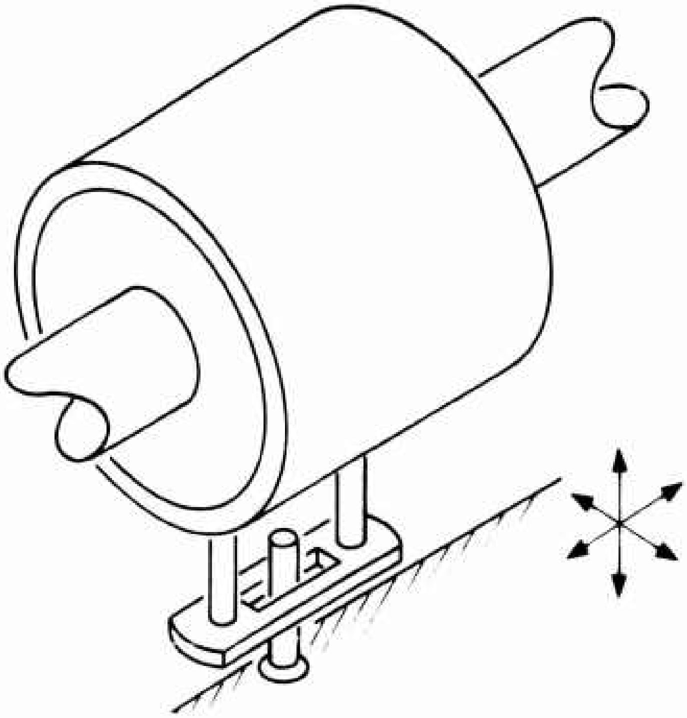

Figure 7. Mechanism To Prevent Torque Sensor Housing Rotation.

main shaft and the torsion shaft. The other end of the torsion shaft is attached to the engine main shaft through splines so that the phase difference between the two gears represents the angular twist of the torsion shaft. The phase angle and temperature sensors can be mounted on the stationary engine structure near the gears through a mounting bracket; with the shaft supported by sturdy engine bearings, they will exhibit very little wobble. The engine bearings are lubricated by the engine oil system and, consequently, are free from the temperature and speed problems of the grease-pack type bearings.

Figures 8 and 9 illustrate the type of adaptation modifications that are needed to change over from a hydromechanical torque sensing system to an electromagnetic torque sensing system. The illustrations are based on the modifications that were performed on the AiResearch T76 engine (a turboprop engine) to install an analog phase angle torquemeter. The modifications involve mainly replacing the hydromechanical torque sensor assembly by the phasing gears and phase angle and temperature sensors, re-routing the negative torque sensor regulator oil flow directly to the adaptor, removing the positive torque regulator valve and the orifice assembly, plugging the positive torque regulator chamber, replacing the orifice assembly with an adaptor, and replacing of the compensator assembly by a solenoid valve to provide the negative torque sensing information for control. Because of the inherent speed information existing in the phase angle signals, overspeed monitoring capability is an added benefit of the electromagnetic phase measurement approach.

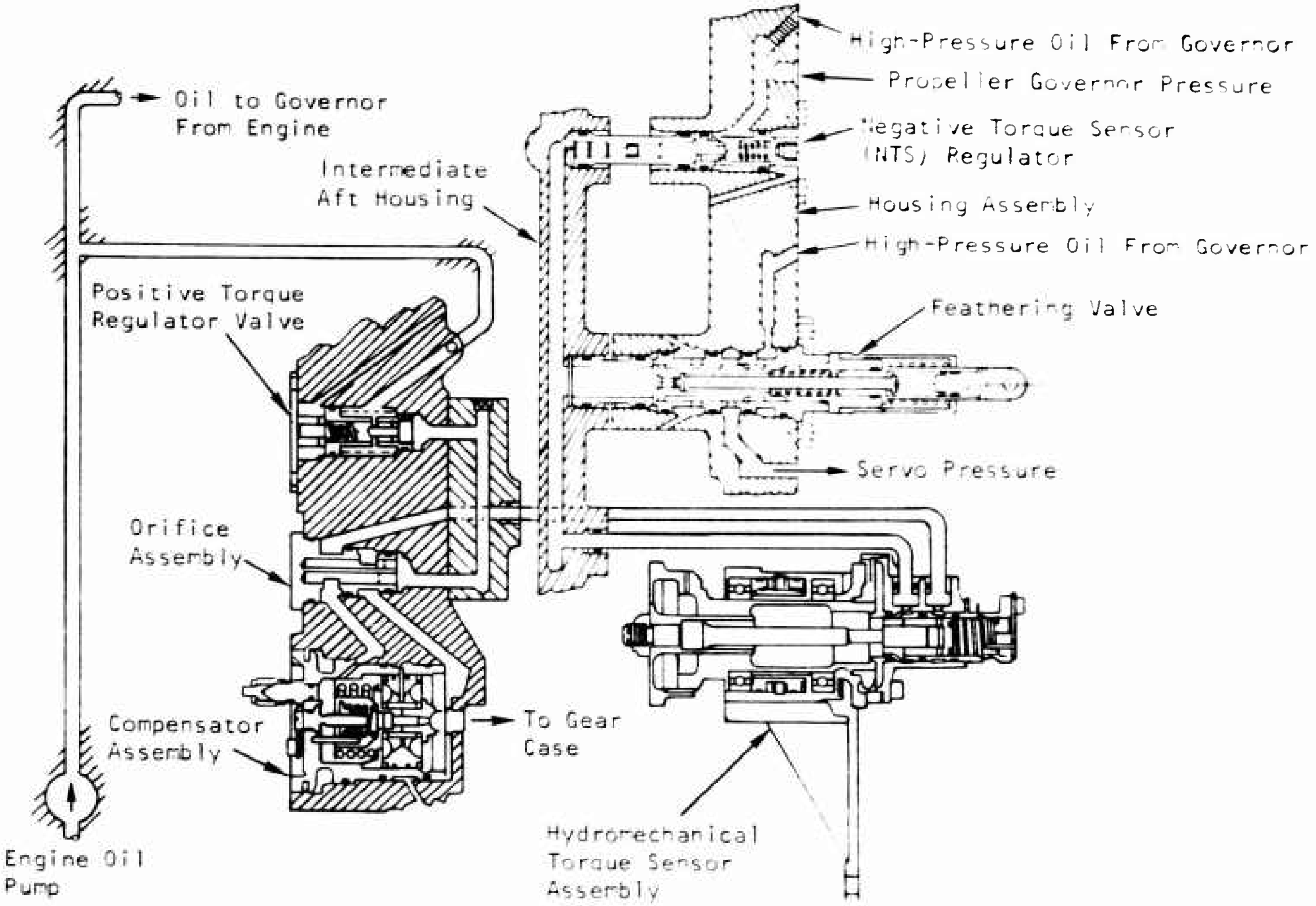

Figure 8. Hydromechanical Torque Sensing System.

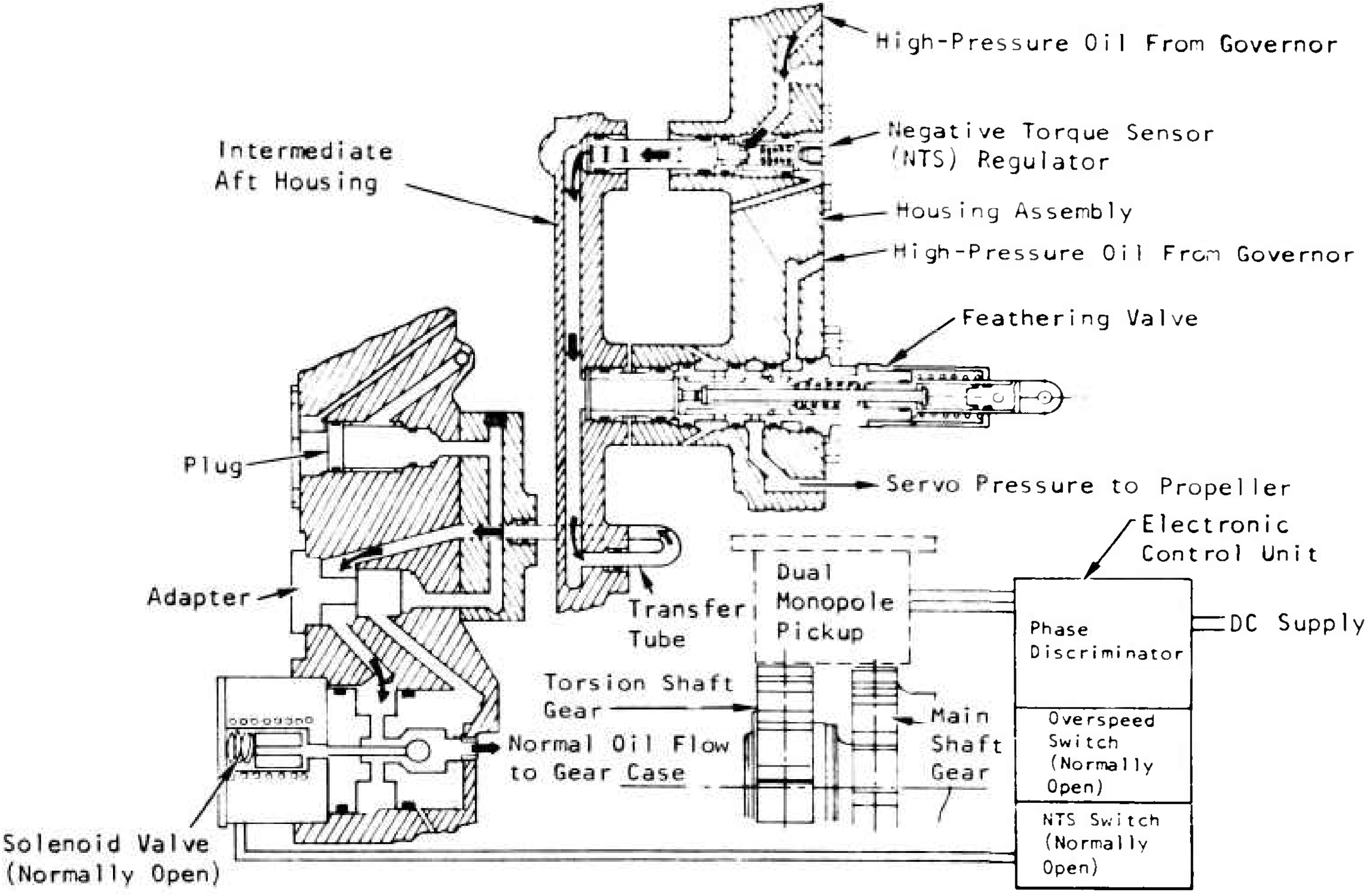

Figure 9. Electromechanical Phase-Shift Torque Sensing System.

### Onboard Location for Electronics

The system electronics is primarily affected through the influence of the environmental conditions of the onboard location.

Generally speaking, it is desirable to locate at least the signal conditioning modules of the system as close to the sensing units as possible in order to minimize noise interference. This problem becomes more critical if the sensor output is of the millivolt level. The criticality of the problem reduces when the output voltage of the sensor increases. Because of the adverse environment near the sensing unit, however, there is always a limit on how close the electronics can be located to the respective sensors and also on how much sophistication can be designed into these electronics so that they still will survive the hostile temperature and vibration environments, and operate reliably as anticipated.

The Army UH-I helicopter was considered for the assessment of this problem. Because of the relatively large output signal that can be obtained from the phase angle sensors, a cable length of at least 10 ft appears to be allowable. With such a cable length, the onboard location for the installation of the related signal conditioning electronic modules of the system seems to be little or no problem, at least for the UH-I model helicopter investigated. The relatively smaller size signal conditioning electronics required (especially for the magnetic pickups and the eddy-current probes) can be placed in some unused space near the battery or the engine oil cooler underneath the transmission cowling. The rest of the system electronics can be mounted inside the equipment compartment if there is any unused space, or installed inside either the aft passenger cabin or the cockpit. The temperature environment at those locations should be safe enough for almost any electronics. The vibration environment at those locations still could be quite severe for the electronic components; however, in the worst case, vibration-buffering shock mounts can be used on these modules to reduce the vibration to an acceptable level.

## MAINTAINABILITY CONSIDERATIONS

The maintainability of a system can be represented by the following figures of merit: mean time to repair (MTTR) a failure of the system, and the average maintenance cost per flight hour of operation. there are many factors that affect these figures of merit. The major contributors are considered to be the following:

1. Ease of fault detection
2. Ability to isolate the faults rapidly
3. Need for special skills and technical data in order to perform maintenance functions

4. Need for special tools, equipment, and facilities in order to perform maintenance functions

5. The frequency and duration of the scheduled on-aircraft maintenance

6. The frequency and duration of scheduled shop maintenance

7. Probability of unscheduled maintenance

8. The quantity and type of spare parts required

In order to achieve ease of fault detection, a system should be designed so that there is a positive indication when the system is functioning. To speed up the fault isolation, test points are provided, the system is partitioned into functional modules, and self-test on built-in automatic test capabilities is designed into the system. To minimize the need for special skills, technical data, special equipment, and special facilities to perform the maintenance operation, plug-in or even throwaway modules are being utilized. The frequency of scheduled maintenance and the probability of the need for unscheduled maintenance can be reduced by utilizing more reliable components and by employing reliability-enhancing hardware mechanizations. The number of hours needed to complete the maintenance action can be reduced by providing more accurate failure diagnosis, better accessibility to the parts, larger work space, higher work clearance, more mobility and transportability of the components or the system, and easier handling of the device. The use of a maximum number of interchangeable or common modules in the design can reduce the requirements on the quantity and the type of spare parts to be kept in inventory.

With respect to the sensing unit, ease of access, work space, and temperature environment appear to favor an externally located sensing unit (i.e., located between the engine and transmission). On the other hand, this is a more uncertain location with regard to environment, considering that the sensing unit would be exposed to abuse whenever the engine or transmission undergoes maintenance. Thus, in spite of the harsher temperature environment and relative inaccessibility of the internal location, it might well prove to be the preferred location. Retrofit ease and cost may be the deciding factors in the case of existing aircraft.

The high reliability of the sensors and of the digital electronic components should allow minimization of the frequency of both scheduled and unscheduled maintenance. The adoption of the digital approach also makes it easier to incorporate the many developed self-test, built-in test, and automatic checkout techniques into the system. The phase comparison scheme for the measurement of the shaft twist angle uses many common modules and interchangeable components. The system itself allows partitioning in such a way that it will help to speed up fault diagnosis and repair. On the basis of these factors, it can be concluded that the digital torque measurement system should prove highly maintainable as well as highly accurate.

## SYSTEM WEIGHT AND VOLUME ESTIMATE

The system consists of the sensing unit, electronic processing unit, and display unit.

The display unit will be a simple replacement of an existing torque indicator. Using solid-state LED type devices, the display needed for the digital approach investigated herein will be smaller and lighter than the existing indicator. A sketch of a possible LED display configuration is shown in Figure 10. This display should weigh no more than 0.5 lb.

In the case of the sensing unit it should be noted that more weight and volume may be eliminated than added, since the hydraulic torque measuring provisions (hydraulic supply lines, servo, and pressure transducer) could be eliminated with use of the digital torque measuring system.

The size and weight of the electronic processing unit will be the same regardless of application; however, the characteristics of the sensing unit depend on its manner of installation which is dependent upon the particular application.

Two installation possibilities were shown (Figures 4 and 5) that are compatible with both external and internal installation for the UH-1. Sensing unit weight breakdowns for these two illustrative cases are shown in Table I.

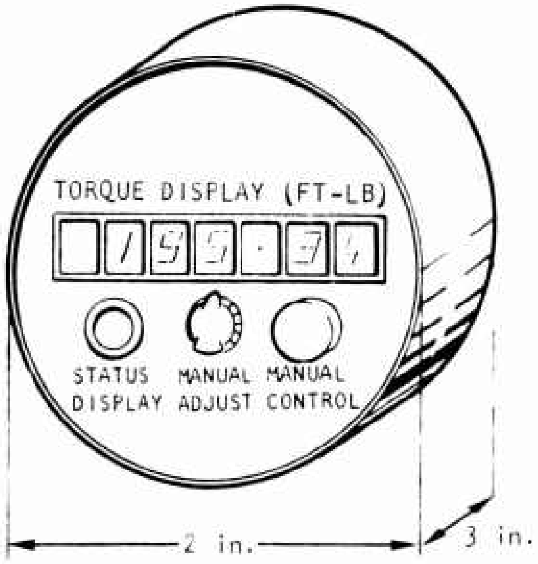

Figure 10. An Airborne Torque Display Unit.

TABLE I. INTERNAL AND EXTERNAL TORQUE MEASUREMENTS

| External Drive Shaft Application | | Internal Torsion Shaft Application | |
|---|---|---|---|
| Component | Weight Contribution (lb) | Component | Weight Contribution (lb) |
| Gears | 2.5 | Gears | 2.5 |
| Bearings | 2.5 | Mounting bracket | 2.5 |
| Housing | 5.0 | Pickups | 0.5 |
| Pickups | 0.5 | | |
| Total | 10.5 | Total | 5.5 |

The volume needed for the installation of the sensing unit is in general a function of the dimension of the shaft for which the unit is intended. In the external application case with a 2-in.-diameter drive shaft, the sensing unit would occupy a cylindrical volume of 6 in. in diameter and 7 in. in length. In the internal application case with a 1-1/2-in.-diameter torsion shaft, the volume needed for the installation of the sensing unit will be approximately the same as for the external application case.

A parts breakdown for the electronic processing unit is provided in Table II. This unit will be composed of a power supply and 35 to 40 integrated circuit packages mounted on 3 printed circuit boards. Based on current packaging techniques, this unit will occupy a space of approximately 130 cu in. (e.g., 5 x 7.5 x 3.5 in.) and will weigh 4 to 5 lb. A sketch of the electronic processing unit is shown in Figure 11.

Since the main purpose of this torque measurement system is for diagnostic application, there is a possibility of utilizing the central processor and display of the diagnostic system which could be available in the future. Therefore, the weight and size of the electronic unit can be reduced by approximately 1/3 of the present estimate. The display unit can be completely eliminated because of the availability of the central diagnostic display.

## SYSTEM RELIABILITY ESTIMATE

This estimate is based on the assumption that a failure of a component within a module or subassembly causes failure of the total system. This assumption may be more restrictive than necessary and, therefore, provides a conservative estimate of the system reliability. Further, the estimate is made for a nonredundant system.

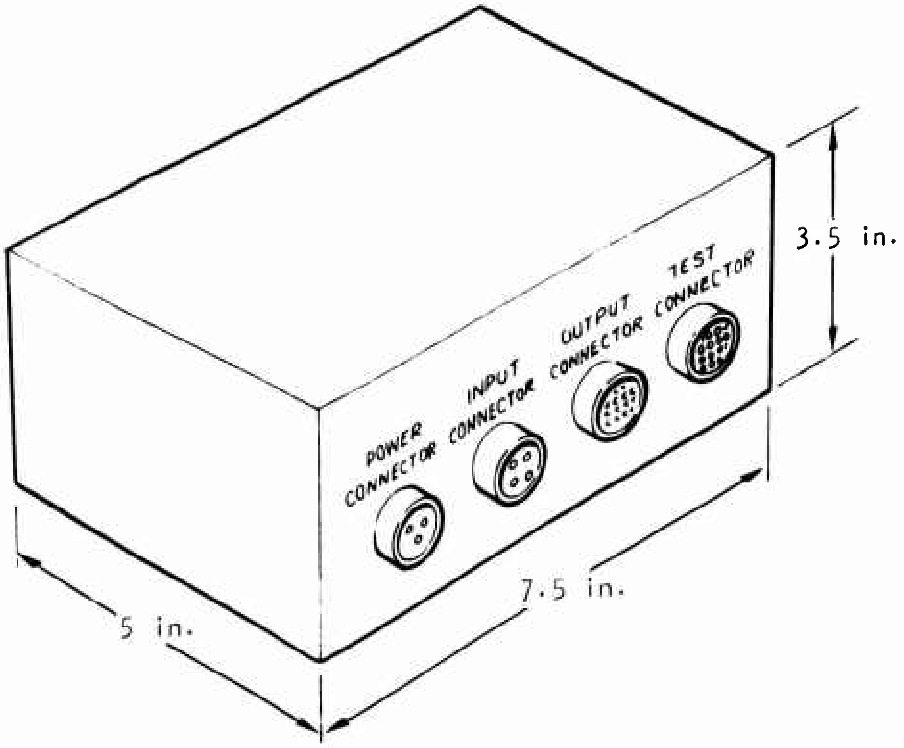

Figure 11. Electronic Processing Unit.

Assuming the failure rate of an $i^{th}$ component to be $\lambda_i$, the mean time between failures of a subassembly or of the system is calculated by the following relationship:

$$\text{MTBF} = \left( \sum_{i=1}^{N} \lambda_i \right)^{-1} \qquad (4)$$

Table II shows the parts count of the system in terms of electronic modules and the failure rate of the individual modules.

Therefore, the total system failure rate is the sum of all the component failure rates, and the overall system MTBF becomes

$$\text{MTBF}_{\text{system}} = \frac{1}{45.32 \times 10^{-6}} \text{ hr} \approx 22,000 \text{ hr} \qquad (5)$$

The electronic component failure rates have been conservatively assessed. Considering this and the further expected progress in microelectronics technology, the actual calculated MTBF of the system could reach an upper limit of about 50,000 hours (limited primarily by the sensing unit) by the time of its production implementation.

TABLE II. SYSTEM PARTS COUNT AND FAILURE RATE

| Subassembly and Modules in the Subassembly | Quantity | Typical Failure Rate, $\times 10^{-6}$/hr |
|---|---|---|
| Sensing Unit | | |
| Magnetic pickup | 2 | 5 |
| Eddy-current probe | 1 | 5 |
| Sensing unit housing support bearing | 2 | 3.97 |
| Processing and Computing Unit | | |
| Magnetic pickup signal conditioner | 2 | 0.2 |
| Pulse shaping circuit | 2 | 0.2 |
| Coincidence checking logic | 1 | 0.2 |
| Pulse counter | 2 | 1.2 |
| Counter control | 2 | 0.6 |
| Clock generator | 1 | 0.4 |
| Torque computation module | 1 | 3.4 |
| Temperature Compensation Unit | | |
| Eddy-current probe signal conditioner | 1 | 0.4 |
| A/D converter | 1 | 8.13 |
| Power Supply | | |
| Voltage conditioning circuit | 1 | 2.15 |
| Voltage regulator | 1 | 3.3 |

## EVALUATION OF ERROR SOURCES

### TEMPERATURE EFFECTS ON TWIST ANGLE

The twist angle of a shaft under the application of a torque is determined by the following relationship:

$$\theta = 57.3 \frac{\tau L}{JG} \tag{6}$$

where $\theta$ = twist angle in mechanical degrees

$\tau$ = applied torque in in.-lb

L = length of the shaft in inches

G = modulus of rigidity in $\mathrm{lb/in.}^2$

J = moment of inertia of the shaft in $\mathrm{in.}^4$

When the shaft is hollow and concentric with inner radius $r_0$ and outer radius $r_1$, the moment of inertia of this type of shaft can be calculated in terms of these two radii; i.e.,

$$J = \frac{1}{2} \pi \left(r_1{}^4 - r_0{}^4\right) \tag{7}$$

with $r_0$ and $r_1$ in inches. From these relationships, it can be seen that the temperature variation of the shaft could have three possible paths to influence the twist angle, i.e., through the influence on L, on J, and on G.

### Effect of Thermal Expansion Influence on Shaft Length

Thermal expansion or contraction of the shaft results in a twist angle error $d\theta$ caused by the shaft length variation due to a temperature change dT. This becomes

$$d\theta = \frac{\partial\theta}{\partial L} \cdot \frac{dL}{dT} \cdot dT \tag{8}$$

$$= 57.3 \left(\frac{\tau}{JG}\right) \cdot \frac{dL}{dT} \cdot dT \tag{9}$$

The relative twist angle error with respect to the operating point due to the thermal expansion or contraction can then be obtained by dividing the above result by the magnitude of the operating twist angle.

$$\frac{d\theta}{\theta} \quad \frac{1}{L}\,\frac{dL}{dT} \cdot dT \tag{10}$$

By substituting the average thermal expansion coefficient for $\frac{1}{L}\frac{dL}{dT}$ obtained from Table III over a 500°F temperature range for the assumed typical shaft, it can be shown that

$$\frac{d\theta}{\theta} \quad 7.35 \times 10^{-6}\, dT \tag{11}$$

Therefore, for a 100°F temperature variation, a twist angle error of 0.0735 percent will be contributed by the shaft thermal expansion or contraction. If the temperature uncertainty can be limited to 10°F, this error will be reduced to 0.00735 percent.

TABLE III. THERMAL EXPANSION COEFFICIENT OF AM355 STAINLESS STEEL

| Temperature (°F) | Thermal Expansion Coefficient (in./in./°F) | |
|---|---|---|
| | Annealed 1875°F/°F | Subzero Cooled Tempered 850°F/°F |
| 68 to 212 | $8.3 \times 10^{-6}$ | $6.4 \times 10^{-6}$ |
| 68 to 572 | $7.9 \times 10^{-6}$ | $6.8 \times 10^{-6}$ |
| 68 to 752 | $8.3 \times 10^{-6}$ | $7.0 \times 10^{-6}$ |
| 68 to 932 | $9.4 \times 10^{-6}$ | $7.2 \times 10^{-6}$ |
| 68 to 1150 | $9.2 \times 10^{-6}$ | $7.2 \times 10^{-6}$ |

## Effect of Temperature Influence on Moment of Inertia

The thermal error of twist angle due to the temperature effect on the moment of inertia of the shaft can be analyzed in a way similar to the previous case,

$$d\theta = \frac{\partial \theta}{\partial J} \cdot \frac{dJ}{dT} \cdot dT \qquad (12)$$

$$= 57.3 \left(\frac{\tau L}{G}\right)\left(\frac{-1}{J^2}\right) \cdot \left(\frac{dJ}{dT}\right) \cdot dT \qquad (13)$$

The relative error becomes

$$\frac{d\theta}{\theta} = -\left(\frac{1}{J} \cdot \frac{dJ}{dT}\right) \cdot dT \qquad (14)$$

Since J is a function of two linear dimensions $r_1$ and $r_0$, $\frac{dJ}{dT}$ will be evaluated in terms of $\frac{dr_1}{dT}$ and $\frac{dr_0}{dT}$. Using the formula of J discussed in this section, the relationship between $\frac{dJ}{dT}$ and $\frac{dr_1}{dT}$ and $\frac{dr_0}{dT}$ can be found to be

$$\frac{dJ}{dT} = \frac{\partial J}{\partial r_1} \cdot \frac{dr_1}{dT} + \frac{\partial J}{\partial r_0} \cdot \frac{dr_0}{dT} \qquad (15)$$

and

$$\frac{1}{J}\frac{dJ}{dT} = \frac{1}{J}\frac{\partial J}{\partial r_1} \cdot \frac{dr_1}{dT} + \frac{1}{J}\frac{\partial J}{\partial r_0} \cdot \frac{dr_0}{dT} \qquad (16)$$

$$= \frac{4r_1^3}{\left(r_1^4 - r_0^4\right)}\frac{dr_1}{dT} - \frac{4r_0^3}{\left(r_1^4 - r_0^4\right)}\frac{dr_0}{dT} \qquad (17)$$

$$= \frac{4r_1^4}{\left(r_1^4 - r_0^4\right)} \cdot \frac{1}{r_1}\frac{dr_1}{dT} - \frac{4r_0^4}{\left(r_1^4 - r_0^4\right)} \cdot \frac{1}{r_0}\frac{dr_0}{dT} \qquad (18)$$

Since the per-unit thermal expansion coefficients $\frac{1}{r_1}\frac{dr_1}{dT}$ and $\frac{1}{r_0}\frac{dr_0}{dT}$ are the same, let this common quantity be $\alpha = 7.35 \times 10^{-6}$ in./in./°F and factor them outside the equation; then

$$\frac{1}{J}\frac{dJ}{dT} = \frac{4\left(r_1^4 - r_0^4\right)}{\left(r_1^4 - r_0^4\right)} \cdot \alpha = 4\alpha = 29.4 \times 10^{-6} \text{ in./in./}^{\circ}\text{F} \tag{19}$$

and the corresponding relative effect on $\theta$ becomes

$$\frac{d\theta}{\theta} = -\left(\frac{1}{J} \cdot \frac{dJ}{dT}\right) \cdot dT \tag{20}$$

$$= -29.4 \times 10^{-6} \cdot dT \tag{21}$$

For a 100°F temperature variation, this error becomes -0.294 percent. For a 10°F measurement accuracy, this relative error on twist angle due to changes in J is only -0.0294 percent.

Effect of Temperature Influence on Modulus of Rigidity

The error in twist angle due to the thermal effect on the modulus of rigidity is given by

$$d\theta = \frac{\partial\theta}{\partial G} \cdot \frac{dG}{dT} \cdot dT \tag{22}$$

The relative error is given by

$$\frac{d\theta}{\theta} = \frac{1}{\theta}\,\frac{\partial\theta}{\partial G} \cdot \frac{dG}{dT} \cdot dT \tag{23}$$

$$= -\left(\frac{1}{G} \cdot \frac{dG}{dT}\right) \cdot dT \tag{24}$$

Based on the thermal data of the modulus of rigidity of the AM355 stainless steel material as listed in Table IV, the value of $\frac{dG}{dT}$ can be calculated to be

$$\frac{dG}{dT} \simeq \frac{\Delta G}{\Delta T} = -2.81 \times 10^{3} \text{ psi/}^{\circ}\text{F} \tag{25}$$

Assuming a reasonable operating temperature of 250°F, the relative error on twist angle due to the thermal change in modulus of rigidity is found to be

$$\frac{d\theta}{\theta} \quad -\left(\frac{1}{G} \cdot \frac{dG}{dT}\right) \cdot dT \tag{26}$$

$$2.58 \times 10^{-4} \; dT \tag{27}$$

For a temperature determined within 10°F, the relative percentage error due to thermal effect on modulus of rigidity is around 0.258 percent.

Since the thermal effects on the three quantities discussed herein are deterministically predictable, the total inaccuracy of these three factors combined should therefore be the algebraic sum of the three individual errors:

$$\therefore \frac{d\theta}{\theta}\bigg|_{total} \quad \left(\frac{1}{L} \; \frac{dL}{dT} - \frac{1}{J} \cdot \frac{dJ}{dT} - \frac{1}{G} \; \frac{dG}{dT}\right) \cdot dT \tag{28}$$

$$2.36 \times 10^{-4} \; dT \tag{29}$$

For a 10°F uncertainty in temperature measurement of the shaft, the total combined error due to the three items discussed will be around 0.236 percent.

TABLE IV. TEMPERATURE EFFECT ON MODULI OF ELASTICITY AND RIGIDITY OF AM355 STAINLESS STEEL

| Temperature (°F) | Modulus of Elasticity E | Modulus of Rigidity G |
|---|---|---|
| 80 | 29.3 | 11.4 |
| 400 | 27.3 | 10.5 |
| 600 | 26.0 | 9.9 |
| 700 | 25.3 | 9.6 |
| 800 | 24.6 | 9.4 |

## ENVIRONMENTAL INFLUENCES ON SENSOR PERFORMANCE

Generally, in terms of sensor performance degradation, the operating environment tends to change the inductance and resistance of the coil of the magnetic pickup or of the eddy-current probe. The effect of this change in sensor parameters is to introduce a corresponding change in the time constant of the output circuit. And finally, the uncertainty in the time constant will then be reflected as an error to the time delay needed to reach the given triggering level.

## Effect on Coil Inductance

The inductance of a long solenoidal type of coil is given by

$$L = \frac{\mu N^2 A}{l} \tag{30}$$

where L = inductance of the coil

N = number of turns

$\mu$ = permeability of the core material

A = cross-sectional area

l = length of the coil

Taking the natural logarithm of both sides of Equation (30) and then differentiating the terms with respect to an environmental parameter X (either temperature, vibration, or shock) yields

$$\frac{1}{L}\left(\frac{dL}{dX}\right) = \frac{1}{\mu}\left(\frac{d\mu}{dX}\right) + 2\,\frac{1}{N}\left(\frac{dN}{dX}\right) + \frac{1}{A}\left(\frac{dA}{dX}\right) - \frac{1}{l}\left(\frac{dl}{dX}\right) \tag{31}$$

For a given amount of dX change, the percentage change in inductance becomes

$$\frac{dL}{L} = \frac{d\mu}{\mu} + 2\,\frac{dN}{N} + \frac{dA}{A} - \frac{dl}{l} \tag{32}$$

In the case of a magnetic pickup, the major contributor to the percentage change of the coil inductance is the $\frac{d\mu}{\mu}$ term. The term $\frac{dN}{N}$ is zero, since the number of turns N is a constant. The terms $\frac{dA}{A}$ and $-\frac{dl}{l}$ partially cancel each other (besides, their individual contribution is very small--in the range of 0.001 to 0.002 percent). The temperature, shock, or vibration changes the residual magnetism of the core material and consequently changes the permeability $\mu$. Figure 12 shows the temperature effect on the residual magnetism for various Alnico alloys. For a typical core material Alnico V of the magnetic pickup, a 2.5 percent reduction in residual magnetism results from a 500°F temperature increase. The reduction of residual magnetism of the core material due to shock or vibration is shown in Figure 13. For Alnico II, a reduction of 2 percent is caused after the application of 1000 impacts to the material. For Alnico V material, the reduction will

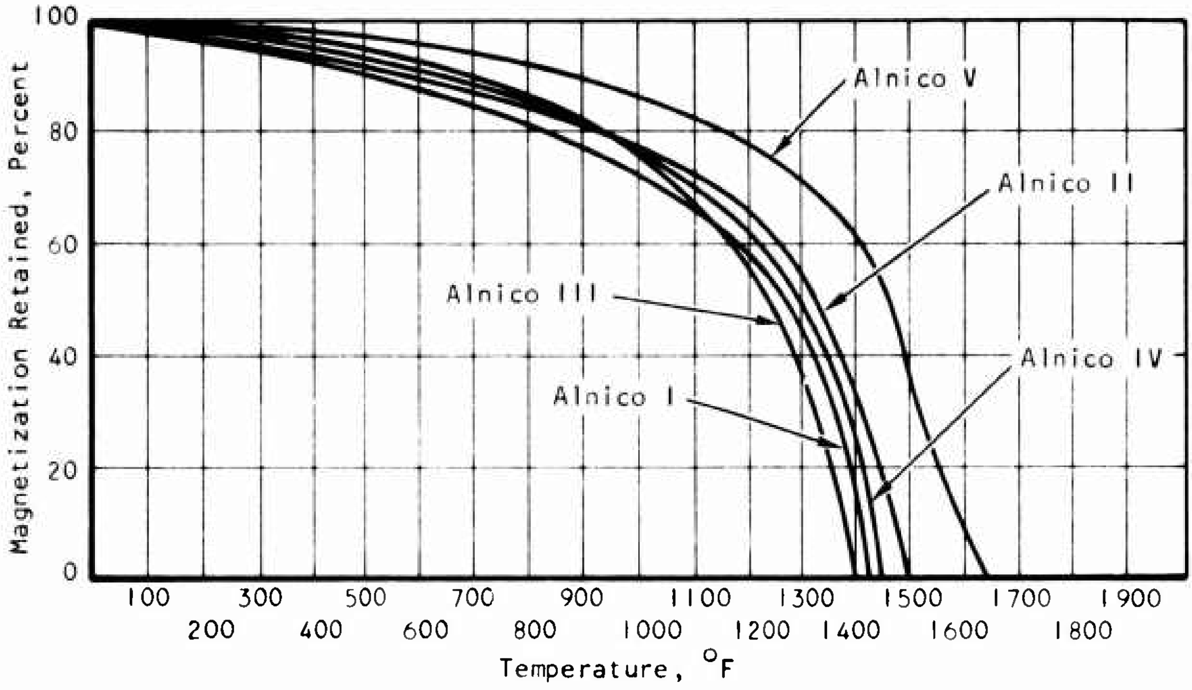

Figure 12. Residual Magnetism vs Temperatures for Various Grades of Alnico.

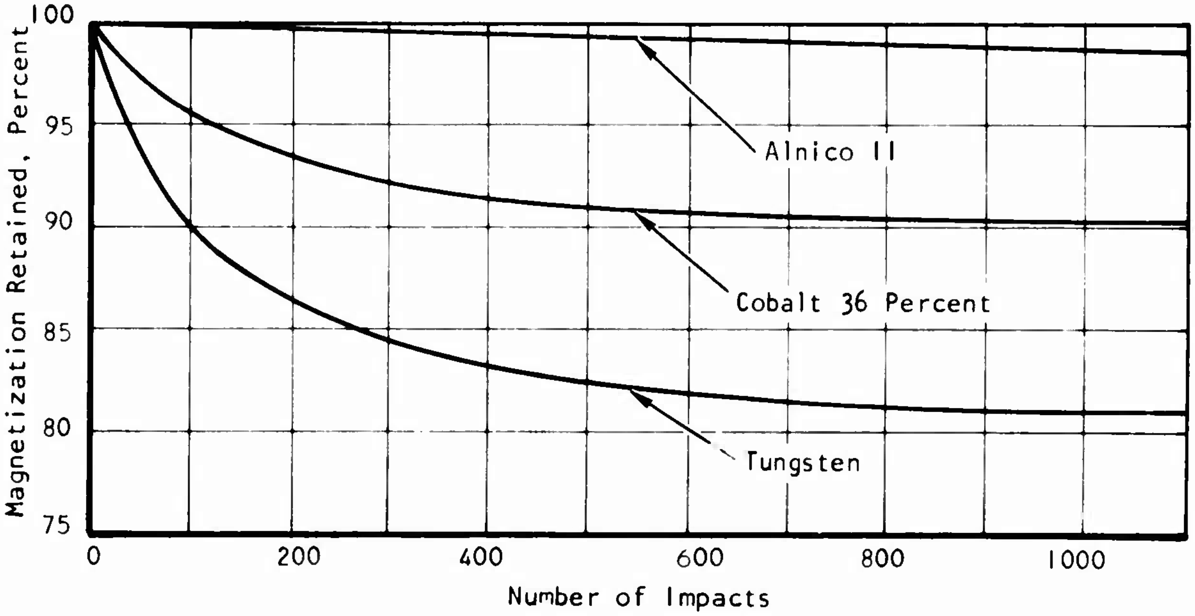

Figure 13. Magnetic Resistance to Impact.

probably be of the same magnitude. The influence of combined temperature and shock/vibration effects could create a worst-case reduction in residual magnetism of 5 percent. The influence of the reduction in residual magnetism on the change of permeability $\mu$ can be found by use of the demagnetization curve of a specific permanent magnet core material as shown in Figure 14. A new demagnetization curve can be constructed by subtracting the amount of reduction (5 percent in this case) from the original demagnetization curve. This new curve is shown as the dashed line in Figure 14. Usually, the magnet will be operated to the right of line AO. The permeability of the core material before and after the reduction can then be found by measuring the average slope along curves BE and CD, respectively. For Alnico V material, a 5-percent reduction in residual magnetism results in a change of approximately 5 percent in permeability $\mu$ also (and, consequently, a 5-percent change in inductance).

In the case of an eddy-current probe, the core has the same permeability $\mu_o$ as air. Temperature change will cause only a very minute change in $\frac{dL}{L}$ through thermal expansion $\frac{dA}{A}$ and $\frac{dl}{l}$. This variation will be the same in the magnetic pickup case--on the order of 0.001 to 0.002 percent. The shock/vibration effects would introduce noise to the output, but cannot change $\frac{dL}{L}$ through any of the parameters listed in Equation (32).

Effect on Coil Resistance

The only parameter that has an effect on the coil resistance is the operating temperature. Temperature changes in many cases will cause a significant variation in the coil resistance of a magnetic pickup or an eddy-current probe. For a 500°F temperature variation, this change could amount to 85 percent of the coil resistance. However, the effect of this resistance change on the time constant is rather small, because the coil resistance contributes only a very small part of the total resistance involved in the time constant equation. For example, an 85-percent change in the resistance of a 500-$\Omega$ copper coil caused by a 500°F temperature variation contributes only a 0.425-percent change to the time constant because of the large, 100 k$\Omega$ load resistance used.

## INACCURACIES DUE TO UNCERTAINTY IN SIGNAL DELAY TIME

There are four major contributors to the uncertainty in the delay time associated with the phasing pulse signals generated by magnetic pickups. Since the twist angle of the shaft is measured as the time differential between the phasing pulses from two pickups, the constant part of the delay time causes no error and only the uncertain part of the delay time introduces inaccuracy. These four major contributors are: (1) uncertainty due to variations in inductance $\frac{dL}{L}$, (2) uncertainty due to variations in resistance $\frac{dR}{R}$, (3) uncertainty due to variations in emf delay time, and

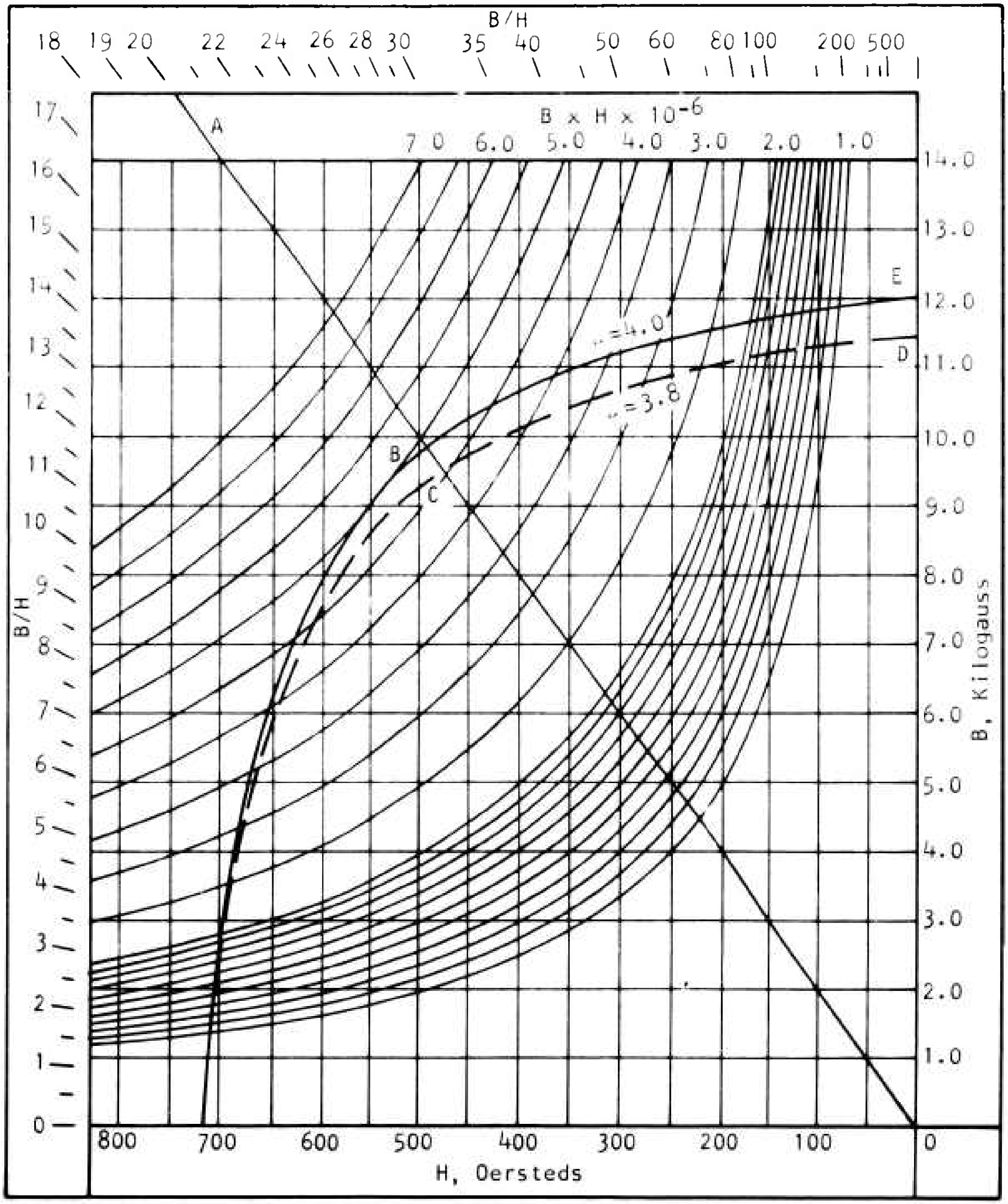

Figure 14. Demagnetization Curve--Energy Product and B/H Values for Alnico VA.

(4) uncertainty due to variations in triggering level of the pulse shaping circuit. Items (1) and (2) act on the delay time due to the L/R time constant of the pickup circuit; Item (3) acts on emf delay time alone; and Item (4) acts on both the delay time due to the time constant and the delay time due to emf rise. In order to simplify the analysis, all four items are assumed to affect both delay times. This assumption will result in a more conservative estimate of these types of inaccuracies, which will further strengthen the findings in relation to the actual situation.

As pointed out under Environmental Influences on Sensor Performance, the variation in inductance over a 500°F temperature range and shock/vibration condition is approximately 5 percent; i.e., $\frac{dL}{L} \approx 5$ percent. The variation in coil resistance is small in comparison to the value of the load resistance $R_L$. However, because of the manufacturing tolerances and the effect of aging, the variation in load resistance $\frac{dR_L}{R_L}$ could become significant, assuming it also is 5 percent. The uncertainty in emf delay time depends upon the fabrication precision achievable with the phasing pole piece. This uncertainty is on the order of 20 percent (10-mil uncertainty caused by a 50-mil cutter). The uncertainty of the triggering level is ±4 mv of a 20-mv level. Therefore the uncertainty (4) is also 20 percent. Assuming these uncertainties occur randomly and that they affect the delay time linearly, the total effective uncertainty on delay time can be obtained by taking the RSS value of these four factors. This turns out to be

$$\frac{dt_{delay}}{t_{delay}} = 29.2 \text{ percent} \tag{33}$$

The output amplitude of a monopole pickup decreases linearly with the rotational speed. The rise time of the signal reaching to its peak increases linearly with the decrease in speed. Therefore, the worst-case effect of $\frac{dt_{delay}}{t_{delay}}$ to reach a fixed triggering level will occur at the low-speed end, i.e., 6000 rpm. The peak amplitude of a typical monopole pickup at this speed is around 5 volts. The delay time from true signal-zero level to the 20-mv triggering level will be approximately 600 nsec by linear proportioning. The uncertain amount of this delay time becomes $dt_{delay} \simeq 175$ nsec. For a 5-deg full scale or an equivalent of 139 μsec, this uncertainty in delay time to reach the triggering level will amount to 0.126 percent.

## INACCURACIES DUE TO ELECTRONIC CIRCUITRY

Under this category, the major contributors are: (1) instability of clock pulses, (2) inaccuracy of the counters, (3) inaccuracy of the computation modulus, and (4) inaccuracy due to the coincidence-interpolation circuits.

The stability of the clock oscillator frequency has been made to be accurate within 0.002 percent for frequencies up to 30 MHz. Since the phase angle is measured by counting the number of cycles of such clock pulses passing through the opening period of the timing gate, the same percentage inaccuracy will be transmitted to the measured phase angle; i.e.,

$$\frac{d\theta}{\theta}\bigg|_{\text{clock pulse instability}} = 0.002 \text{ percent} \qquad (34)$$

Because the counters used to count the clock pulses may either add or miss one count due to the transient of the trigger pulse, the accuracy of the counters is generally ±1 count per number of counts actually measured. If the clock frequency used is high enough (say 30 MHz to 50 MHz) or the coincidence-interpolation method is used so that more pulses can be counted even with a lower clock frequency, the accuracy of the counters can be expected to be 0.2 percent or better.

The truncation error in computation will be the major inaccuracy contributed by the computation module.

Assuming a 6-tooth phasing gear is to be used, the equation for phase angle becomes

$$\theta = \left[\left(\frac{N_2}{N_4}\right) N_3 - N_1\right] \times 60 \qquad (35)$$

Let

$$F = \left(\frac{N_2}{N_4}\right) N_3 - N_1 = F_o \pm \Delta F \qquad (36)$$

where $F_o$ is the true fraction and $\Delta F$ is the computation error,

then

$$\theta = (F_o \pm \Delta F)\ 60 = 60\ F_o \pm 60\ \Delta F = \theta_o \pm \Delta\theta \qquad (37)$$

Therefore

$$\theta_o = 60\ F_o \text{ and } \Delta\theta = 60\ \Delta F \qquad (38)$$

Then

$$\frac{\theta}{\theta_o} = \frac{\theta_o \pm \Delta\theta}{\theta_o} = 1 \pm \frac{\Delta\theta}{\theta_o} = 1 \pm \frac{\Delta F}{F_o} \qquad (39)$$

Assume $\theta_o = 5$ deg is the full-scale value of $\theta$, then

$$F_o = \frac{5}{60} = 0.083333333\text{-------} \qquad (40)$$

If the decimal point is set at $D_4$, then the truncation error will be

$$\Delta F \leq 0.0001 = 1 \times 10^{-4} \qquad (41)$$

and the percentage error due to truncation at 5th digit after the decimal point becomes

$$\frac{\Delta F}{F_o} = 0.12 \text{ percent} \tag{42}$$

and $\frac{\Delta\theta}{\theta_o}$ should also be 0.12 percent.

The inaccuracy introduced by the counters used in the coincidence-interpolation circuits has already been accounted for in the estimate of the accuracy of the counters. The other remaining source of inaccuracy in the coincidence-interpolation circuit part is the uncertainty in the triggering level of the AND gates used for coincidence checking. This inaccuracy will show up as a variation in the switching time of the gate. This variation can be as large as 20 percent of the switching time. For a typical AND gate with a 30-nsec switching time, this variation could amount to 6 nsec. In terms of the minimum full-scale time-phase of approximately 64 μsec, the maximum inaccuracy of this type will result in an error in measured twist angle of 0.01 percent. The total effective accuracy due to electronic components can be calculated by using the RSS rule over the individual inaccuracies just discussed and is found to be around 0.233 percent.

By summing up the inaccuracies due to residual thermal inaccuracy on shaft twist angle, uncertainty in signal delay time and inaccuracy of electronic circuitry in RSS fashion, the total effective system accuracy capability can then be assessed. This total system accuracy is found to be 0.355 percent. This represents an estimate of the typical accuracy the system would have.

# PHASE ANGLE SENSOR SELECTION AND DESIGN CONSIDERATIONS

## EVALUATION OF CANDIDATE PHASE ANGLE SENSORS

Three basic types of sensors were evaluated for performing the phase angle sensing function: variable capacitance proximity transducer, eddy-current proximity transducer, and variable reluctance magnetic pickup.

The variable capacitance proximity measurement approach is based on frequency modulation of a carrier wave. The proximity probe is designed such that its capacitance varies with displacement from metal objects (such as gear teeth). This variable capacitance forms part of a resonant circuit that controls the frequency of an oscillator. Hence, a change in the proximity of the probe to metal is converted, via a change in capacitance, into a frequency change which in turn is converted into an analog dc voltage by a reactance converter.

The eddy-current proximity probe operates on the inductive proximity principle. The probe contains a flat coil which serves both excitation and sensing functions. The excitation generates an alternating magnetic field. As the probe nears a conductor, eddy currents are induced in the conductor due to the alternating magnetic field. The flow of eddy current in the conductor will be reflected to the coil as an increase in loss to the probe excitation source. This loss is a function of the distance between the coil and the conductor and certain material properties of the conductor, such as resistivity and core loss, if it is ferromagnetic. Because of the small absolute changes normally associated with these eddy-current losses at different distances, a general method of sensing this change in loss is the use of a tuned oscillator circuit. The eddy-current coil serves as the inductance of the tuned circuit. The increase in loss reduces the Q of the tuned circuit and thereby reduces the amplitude of oscillation. By rectifying the oscillation amplitudes, a dc voltage proportional to the distance or other material properties can be obtained. The eddy-current method works even at zero speed. However, its transduction will involve the use of more complicated electronic circuits.

The variable reluctance magnetic pickup is a self-excited probe. It employs a permanent magnet for excitation and a coil for sensing. It requires relative motion between the probe and, in this case, a ferromagnetic object, or armature. The arrangement is similar to an electromagnet and its armature, except that a permanent magnet is used and the coil, instead of being excited, is a sensing coil. As the separation between the probe and armature is changed, the reluctance of the magnetic circuit changes, and a corresponding change in magnetic flux takes place, generating a voltage in the sensing coil. Where the armature is gear-shaped and rotating at high rpm, several hundred volts typically can be generated by the sensing coil. The permanent magnet could be replaced by an electromagnet, if demanded by environmental considerations.

The phase-angle sensor candidates were evaluated with respect to the following factors:

1. Temperature capability
2. Vibration capability
3. Capability to withstand contamination
4. Rise time of the signal transduced
5. Repeatability of signal
6. Speed range capability
7. Signal conditioning complexity required

### Temperature Capability

As far as temperature capability is concerned, the capacitive sensor and the eddy-current sensor types are about equally capable. Both can operate under a temperature up to 1200° to 1300°F. The temperature capability of the off-the-shelf magnetic pickup type is around 550°F. The main limiting factor is the Alnico V permanent magnet material used. The temperature capability of this third type of sensor possibly could be pushed up to around 800° or 900°F if high-temperature soft magnetic material were used and the electromagnet approach were adopted to replace the permanent magnet. Of course, this would slightly increase signal conditioning complexity.

### Vibration Capability

The vibration capabilities of the three types of sensors appear to be more or less the same. Both the capacitive and the eddy-current types have been used on a J57 turbojet engine with vibration environments that are significantly more severe than those specified. Figure 15 shows a typical vibration spectrum under which the aforementioned sensors were located. The magnetic pickup type sensor has been used on the AiResearch T76 turboshaft engines for torque measurement. Currently, this measurement system is under qualification test for Navy logistic aircraft applications. The vibration levels of the 1250-hp T76 engine are comparable to those of the J57 engine.

### Capability to Withstand Contamination

The eddy-current and the magnetic pickup types of sensors can withstand typical contamination at the selected shaft location such as oil mist, grease, and dust or sand, with little or no problem. The sensors of these two types can be totally encapsulated in hermetical seals. The sensing mechanism will not be hampered by the contaminants since they are nonmetallic and have approximately unity relative permeability (similar to that of

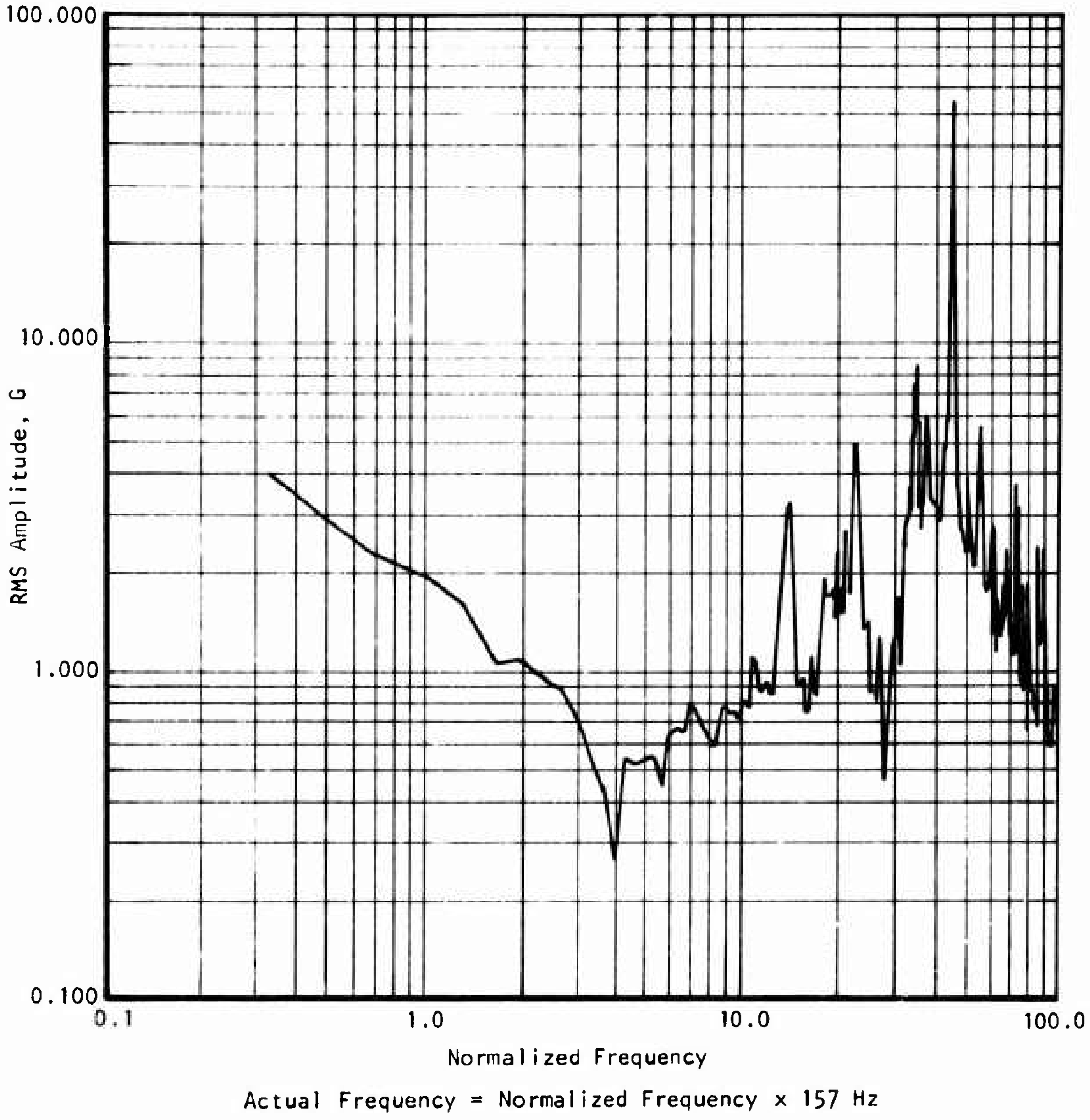

Figure 15. A Measured Vibration Spectrum From J57 Turbojet Engine.

the air gap). On the other hand, the sensing mechanism of the capacitive sensor depends on the dielectric constant of the air gap. The presence of oil mist or grease tends to perturb this dielectric constant and consequently causes noise to appear in the sensor output. If these perturbations are of the high-frequency type, however, they can be removed electronically and again the sensing function of the capacitive sensors probably will not be impaired by the contaminants.

### Rise Time of the Signal Transduced

Because of the small capacitance needed in a capacitive sensor and/or the high frequency level at which the sensor normally operates, capacitive probes are potentially faster than the other two types (i.e., eddy-current and magnetic). Additional lengthening of the rise time of a capacitive sensor, however, is introduced by the reactance conversion circuits if an FM transduction scheme is used in generating the phasing pulses. The rise time of an eddy-current probe is limited by the amount of inductance and resistance needed for the probe to operate. The ability to quicken the signal electronically is also affected by the relatively low sensor output. The sensor rise time of a magnetic pickup is limited by the same factors as the eddy-current sensor; however, due to the relatively large signal output generated by a magnetic pickup, the rise time of the pulse signal can be shortened significantly by electronic means.

### Repeatability of Signal

In terms of the signal repeatability of the sensor output over an extended period of time and under a cyclically varying temperature environment, the magnetic pickup is inferior to the other two types because of a certain irreversible process of a permanent magnet. This signal repeatability drawback of a magnetic pickup can be improved, however, if an electromagnet is used instead of the permanent magnet. In view of the fact that the signal processing approach adopted for the digital torque measurement system does not utilize the quantitative amplitude information of the sensor output signal, the repeatability of the sensor output signal does not appear to be a dominant factor in determining the sensor type selection.

### Speed Range Capability

Both the capacitive and the eddy-current types of sensors operate on a tuned-frequency resonant circuit principle that theoretically works at zero shaft speed. Therefore, they can be used over a very wide range of shaft speeds from almost stationary to the maximum of 26,000 rpm. The magnetic pickup type sensor operates on a principle that depends upon the rate of cutting the magnetic flux by the sensor coil. Consequently, the amplitude of the output signal will be in direct proportion to the shaft speed. This type of sensor is not suitable for extremely low speed applications. In view of the relatively high shaft speeds involved, a minimum surface speed of 600 ips (at which the coil cuts the magnetic flux lines) can be accomplished easily. With this level of surface speed, a significantly large signal amplitude can be expected from a magnetic pickup. The speed range capability for the present application of the magnetic pickup appears to be as good as that of the other two types of sensors.

## Signal Conditioning Complexity

The signal conditioning complexity of the three types of sensors considered is in the following order: capacitive, eddy-current, and magnetic. The signal conditioning required for the capacitive sensor is the most complex because of the employment of the FM scheme. This involves the use of a high-frequency FM oscillator, a reactance conversion module to change the information contained in the frequency modulation into analog pulses, and special designs to stabilize the oscillator against temperature and vibration under an operational environment. The use of the operational amplifier transduction scheme for capacitive probes could eliminate the need for the reactance conversion circuits, but in return, would add an operational amplifier. The other requirements of this latter scheme will remain the same as the FM scheme. Additionally, the operational amplifier scheme will be more susceptible to noise interference from other sources. The dc-excited scheme could get rid of the delicate FM oscillator and the precisely tuned reluctance converter altogether; however, the high dc excitation voltage required may become objectionable from an RFI point of view.

The signal conditioning required for the eddy-current type sensor is of about the same complexity as the operational amplifier transduction scheme for the capacitive sensor. It requires the use of an oscillator to induce eddy currents into the phasing pole piece; however, the stability of the oscillator used for eddy-current sensors need not be as critical as that of the FM oscillator used for capacitive sensors. This allows a certain relaxation of the hardware complexity.

The simplest signal conditioning required is that of a permanent magnet sensor. It requires practically no electronics. The signal conditioning for the electromagnet type magnetic pickup sensor is nearly as simple, requiring only a reasonably well-regulated dc source to supply the needed magnetomotive force (MMF).

From the signal conditioning requirement point of view, the magnetic pickup (permanent or electromagnet) appears to be the most desirable choice.

Table V provides a summary of the aforementioned comparisons. On the basis of these comparisons, it was concluded that the permanent magnet pickup is clearly superior, provided that its temperature capability is sufficient for the application.

To further confirm the environmental capability of the magnetic sensors, a search through specifications of related sensors to establish their typical characteristics was performed. The following composite environmental characteristics were extracted from those sources.

TABLE V. SUMMARY OF COMPARISONS

| Capability | Sensor Type<br>Capacitive Sensor | <br>Eddy-Current Sensor | <br>Magnetic Pickup |
|---|---|---|---|
| Temperature capability | High | High | Medium |
| Vibration capability | High | High | High |
| Contamination capability | Low | High | High |
| Rise time | Fastest | Medium | Fast |
| Signal repeatability | Good | Good | Good |
| Speed adaptability | High | High | Adequate |
| Signal conditioning | Complex | Moderate | Simple |

### Magnetic Pickup Environmental Capabilities

| | |
|---|---|
| Temperature | -100°F to +800°F |
| Altitude | 0 to 50,000 ft |
| Humidity | 95 percent ±5 percent per MIL-E-5009D |
| Fungus | Compatible with MIL-E-5009D |
| Sand and dust | Compatible with MIL-E-5009D |
| Vibration | 5g from 15 Hz to 100 Hz |
| | 5g to 20g from 100 Hz to 150 Hz |
| | 20g from 150 Hz to 500 Hz |
| Shock | 30g for a duration greater than 10 msec |
| Reliability | 200,000 hr MTBF |

Compared with the required temperature of $-35^{\circ}F$ to $500^{\circ}F$ and the required vibration of 1 to 10 g from 10 to 10,000 Hz, the magnetic sensors should have sufficient environmental tolerance capability for the subject application. Further supporting this conclusion is the fact that permanent magnet generators in the form of tachometers for control, instrumentation, and power applications are commonly used on aircraft gas turbine engines.

## MAGNETIC PICKUP AND PHASING GEAR DESIGN CONSIDERATIONS

The design problem is to achieve the fastest rise time and highest voltage output for the gear-pickup combination. Because of the wide variety of commercially available pickups, it should not require a special design.

From a theoretical viewpoint, this problem is extremely difficult because of the problems in analytically deriving expressions that will adequately describe the reluctance of the applicable magnetic circuits. However, the problem is not too difficult if approached empirically.

A wide variety of magnetic pickups and phasing gear configurations can be used. All of these possibilities may be simply represented, however, by Figure 16, which shows the flux paths for a generic configuration.

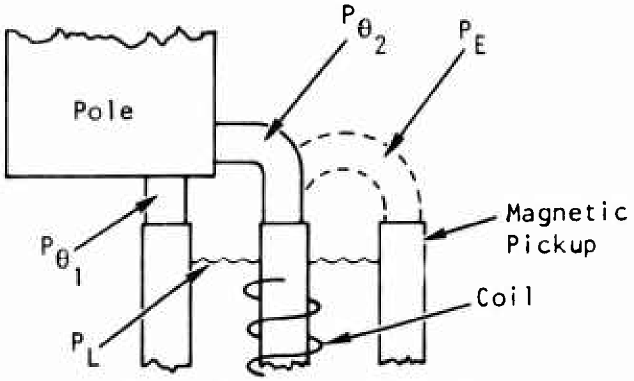

(Only Principal Paths Shown)

Figure 16. Magnetic Pickup Flux Paths.

In Figure 16, the permeances, $P_{\theta 1}$ and $P_{\theta 2}$, are functions of θ and change as the phasing pole sweeps by the probe. The rise time of the output is proportional to rates at which these permeances change; i.e.,

$$e = N \frac{d\phi}{dt} \tag{43}$$

$$\phi = F_m P \tag{44}$$

Since $F_m$ is relatively constant for this circuit (and is the magnetomotive force supplied by the permanent magnet), then

$$e = -N\ F_m \frac{dP}{dt} \tag{45}$$

$$= N\ F_m \frac{dP}{d\theta} \cdot \frac{d\theta}{dt} \tag{46}$$

where $\frac{d\theta}{dt}$ = rotational speed.

This may also be seen in Figure 17, which is the electrical analog of the magnetic circuit (where resistance is proportional to 1/P). $P_L$, the permeance of the leakage paths, and $P_E$, the permeance of the external flux paths not associated with the phasing pole, are relatively constant. The current in this circuit (the flux analog) increases as the permeances, $P_{\theta 1}$ and $P_{\theta 2}$, increase.

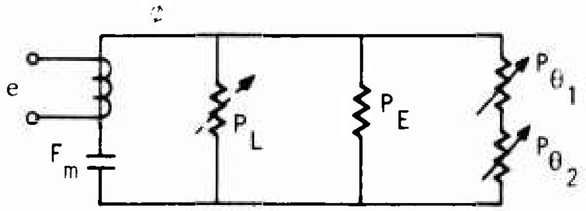

Figure 17. Magnetic Circuit for Pickup.

Figure 18 shows the characteristic output of the probe as the leading edge of a phasing pole sweeps by. This figure also shows that, all other things remaining constant, the smaller the probe diameter, the sharper the output pulses.

The following paragraphs discuss the key factors in selecting a probe-phasing gear design.

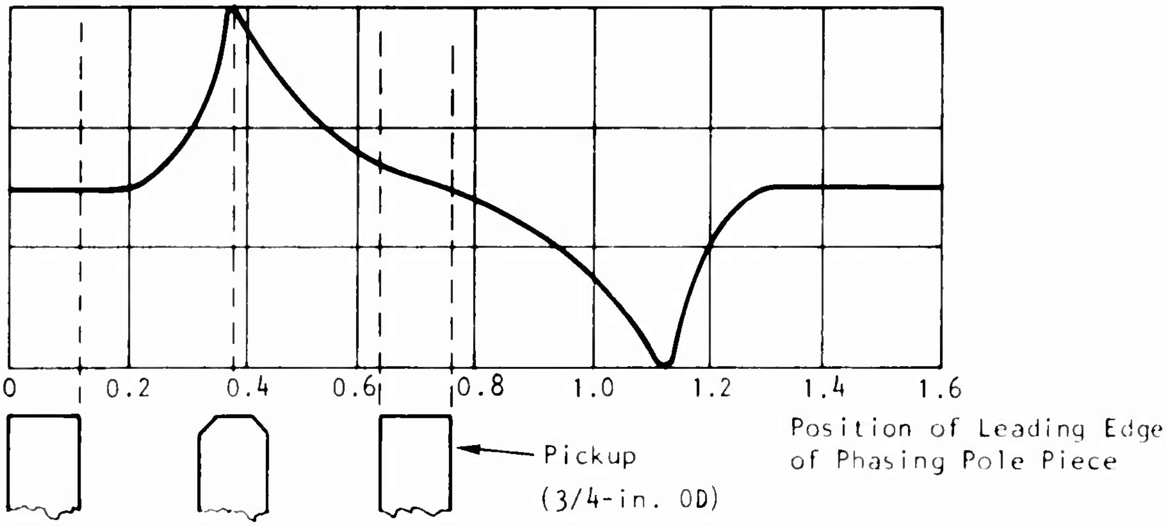

Figure 18. Correlation of Sensor Output With Probe Geometry.

### Relative Velocity

As shown by Equation 46, the pickup output is directly proportional to the velocity of the phasing pole as it sweeps by. In relative terms,

$$\frac{E_1}{E_2} = \frac{r_1\dot{\theta}_1}{r_2\dot{\theta}_2} \qquad (47)$$

where r is the radius of the phasing gear. This shows that for a given probe and pole geometry, the output can be increased by increasing the rotational speed or the radius of the phasing gear.

### Gap Distance

When a phasing gear is directly centered over the probe, the permeance is approximately proportional to 1/g where g is the separation between the pole and probe, or the gap distance. Thus, the total flux change during a cycle is also proportional to 1/g, and

$$\frac{E_1}{E_2} = \frac{g_2}{g_1} \qquad (48)$$

That is, the output is inversely proportional to the gap distance. To illustrate, one probe under consideration provides a 200-volt peak-to-peak output at a gap distance of 0.005 in. and a speed of 1000 in./sec. For the same speed and a gap distance of 0.025 in., which is considered desirable for the torque sensor due to other considerations, the output will be approximately

$$200 \frac{0.005}{0.025} = 40 \text{ v p-p} \tag{49}$$

This is considered an adequate output.

### Probe Size

The smaller the probe is in diameter, the faster will be its rising time (see Figure 3). However, the smaller probes deliver, in general, a smaller output voltage. Since a high output voltage is also desired for triggering, the criterion used in this area was to maximize voltage output/rise time in the selection of pickups.

### Phasing Gear Configuration

The optimum phasing gear configuration, apart from diameter, is related to the pickup geometry. The "gear" teeth should change abruptly with $\theta$, should have approximately the same area as the total pickup tip area, and should be spaced such that adjacent teeth have essentially no effect on the change in reluctance provided by the tooth sweeping across the face of the pickup.

In general, this is satisfied by a gear having a pitch value of 8 or less, where

$$\text{Pitch} = \frac{\text{no. of teeth} + 2}{\text{gear diameter}} \tag{50}$$

## TEMPERATURE COMPENSATION

### METHOD TO COMPENSATE FOR THERMAL EFFECT ON TWIST ANGLE

As disclosed in the previous discussion, the error in twist angle due to the various temperature effects could become significant if it is not compensated. This compensation generally requires determination of the temperature of the shaft in operation. Because of the smaller sensitivity of these effects to temperature, however, the temperature of the shaft need not be determined very accurately. A temperature measurement accurate to within 10°F of the actual temperature should yield no more than 0.236 percent relative error due to all the thermal effects on the shaft. In view of the relatively small range of the shaft temperature variations, about 100°F*, it appears to be possible to measure this temperature accurately within 10°F without using the contact type of sensors such as thermocouples or thermoresistive temperature measurement devices. Four possible methods for noncontacting determination of the shaft temperature were investigated during the program period:

1. Inferential computation method
2. Infrared method
3. Temperature-dependent alternator method
4. Temperature-dependent eddy-current method

The inferential computation method measures the temperature of the stationary parts around the shaft and then computes the temperature of the shaft by using a heat-transfer model. This method requires temperature measurements at several fixed locations, and needs an accurate heat transfer model. It also demands that a small amount of complicated computation capability be designed into this temperature measurement subsystem. In view of the existence of the main rotor downwash and the engine inlet airflow at the selected shaft location, it may be difficult to accomplish the 10°F measurement accuracy without knowledge of the downwash and engine inlet airflow.

The infrared method is a method of measuring the temperature of an object without contact by sensing the infrared radiation emitted from that object. Commercial infrared temperature measurement devices have been developed to measure low temperature (0° to 300°F, or 200° to 600°F) with an accuracy of ±2 percent at a distance of from 6 inches to several feet. The problem with

---

*Extrapolated from the input quill temperature data of UH-1 helicopters included in USAAVLABS Technical Report 70-46, DESIGN CRITERIA FOR AN INSPECTION AND DIAGNOSTIC SYSTEM FOR THE UH-1D HELICOPTER, Eustis Directorate, U.S. Army Air Mobility Research and Development Laboratory, Fort Eustis, Virginia, November 1970, AD 879623.

this type of device for the application discussed herein is the inherent low environmental temperature capability (around 120°F) of this type of device.

The temperature-dependent alternator method utilizes a specially designed electric generator with permanent magnet poles mounted on the shaft and emf-generating coils in the surrounding stator housing. The magnetic induction of the permanent magnet poles changes with temperature. Consequently, the induced emf in the stator coil also will be a function of temperature. This function can be obtained by calibration and the compensation can be done by using a single variable function generator. The alternator design itself, however, could be quite an effort. In addition, the irreversible hysteresis loop of the permanent magnet traced out by the temperature variation also may cause difficulty in accomplishing the ±10°F accuracy objective.

The temperature-dependent eddy-current method utilizes the temperature-dependent nature of the resistivity of a nonferromagnetic metal or the core loss of a ferromagnetic metal to indicate the temperature of the metalic body being tested. In this case, an equivalent transformer is formed by the eddy-current probe coil and the conductive sink material, with the coil being the primary and the sink being the secondary of the equivalent transformer. When the temperature of the sink material changes, the energy loss due to the sink material will be reflected to the primary as a change of the coil Q--the required energy for excitation. By properly measuring this reflected circuit change, a noncontacting temperature measurement of the sink material can be obtained. Both ferromagnetic and nonferromagnetic metals can be used in the sink. However, the temperature characteristics of the core loss of a ferromagnetic material are more complex than those of the resistivity of a nonferromagnetic metal. The amount of change due to temperature change depends upon the particular sink metal material selected. This temperature-dependent eddy-current method for noncontacting temperature measurement for the rotating shaft would require a stationary eddy-current probe and a soft magnetic eddy-current energy sink mounted on the shaft. This eddy-current energy sink can be designed in such a way that it will appear as a homogeneous surface to the eddy current and provide good heat conduction from the shaft, but will be subject to very little stress caused by the applied torque. The variations in core loss then can be limited to those caused by the temperature changes only. The geometry and the stress level then will have very little influence on the resultant core loss change. Among the four possible compensation methods investigated, the temperature-dependent eddy-current method appears to be the most promising one. It requires only a rather simple and reliably built sensing probe and energy sink. The signal conditioning and computation electronics are also the lowest for the eddy-current approach for noncontacting measurement of shaft temperature. The compensation of nonlinear output relationship versus temperature can be accomplished with a single variable function generator. However, if the temperature measurement is used for digital compensation such as in the subject case, the compensation of nonlinear relationship can be implemented easily in the analog-to-digital converter by employing a read-only-memory (ROM) for the nonlinear digitization.

## TEMPERATURE COMPENSATION BY USE OF EDDY-CURRENT PROBES

In view of the greater potential and the relative ease in implementation of the eddy-current probe method for noncontact temperature sensing over the other three methods, more refined analyses were performed on this method during the program period to substantiate its feasibility for the intended application. These analyses covered the following four areas: (1) theoretical derivations, (2) evaluation of supporting data, (3) the effect of flux-cutting due to shaft rotation, and (4) the effect of stress in the eddy-current sink. In items (3) and (4), not only the effects or their influences were investigated, but solutions to minimize such effects or to compensate for them by computational corrections were recommended.

### Theoretical Derivations

The equation that governs the operation of an eddy-current probe is the electric-curl equation of the well-known Maxwell's equations of the electromagnetic theories; i.e.,

$$\nabla \times \vec{E} = -\mu \frac{\partial \vec{H}}{\partial t} \tag{51}$$

where $\nabla$ = the vector gradient operator "nabla"

$\vec{E}$ = the vector electric field in the eddy-current sink

$\mu$ = the permeability of the sink material

$\vec{H}$ = the vector magnetic field in the eddy-current sink

The vectors $\vec{E}$ and $\vec{H}$ are to be sinusoidally excited; therefore, they can be rewritten as follows to isolate the time-varying part:

$$\vec{E} = \vec{E}_o e^{j\omega t} \tag{52}$$

$$\vec{H} = \vec{H}_o e^{j\omega t} \tag{53}$$

where $e^{j\omega t}$ represents the sinusoidally time-varying part, and $\vec{E}_o$ and $\vec{H}_o$ are now spatial vectors only.

Substituting $\vec{E}$ and $\vec{H}$ from Equation (52) into Equation (51), gives

$$\nabla \times \vec{E}_o = -j\omega\mu\vec{H}_o \tag{54}$$

or

$$\vec{H}_o = -\frac{1}{j\omega\mu} \nabla \times \vec{E}_o \tag{55}$$

Since the current density flowing in the eddy-current sink is related to the electric field by

$$\vec{E}_o = \rho \vec{J}_o \tag{56}$$

where $\rho$ is resistivity of the sink material and is a function of temperature T, Equation (55) becomes

$$\vec{H}_o = -\frac{\rho}{j\omega\mu} \nabla \times \vec{J}_o \tag{57}$$

Considering the case where the nonmagnetic metal is used as the sink material, then

$$\frac{\partial\vec{H}_o}{\partial T} = -\frac{\nabla \times \vec{J}_o}{j\omega\mu_o} \times \frac{\partial\rho}{\partial T} \tag{58}$$

and the relative magnitude of this magnetic field variation becomes

$$\frac{\left|\frac{\partial\vec{H}_o}{\partial T}\right|}{\left|\vec{H}_o\right|} = \frac{\left(\frac{\partial\rho}{\partial T}\right)}{\rho} \tag{59}$$

For a given temperature variation $\Delta T$, this gives

$$\frac{|\Delta\vec{H}_o|}{|\vec{H}_o|} = \frac{\Delta\rho}{\rho} \tag{60}$$

Thus, the variation in the resistivity of the sink material due to temperature changes will cause a corresponding variation in the magnetic field. Since this magnetic field is established by the electric energy supplied to the probe coil, the variation in the current or voltage supplied to the probe becomes an indication of the variation of the temperature-dependent resistivity of the sink material.

In order to determine whether such a resistivity change will result in any measurable output, the theoretical relation and values of two typical nonmagnetic metals (i.e., copper and aluminum) are used to provide an estimate. The temperature-resistivity relationship is as follows:

$$\rho = \rho_o (1 + \alpha T) \tag{61}$$

where $\rho_o$ is the resistivity at a reference temperature, $\alpha$ is the temperature coefficient of the resistivity, and T is the temperature measured from that reference point. Taking the natural logarithm of both sides of Equation (61) yields

$$\ln \rho = \ln \rho_o + \ln (1 + \alpha T) \tag{62}$$

Differentiating with respect to T and transposing the dT term gives

$$\frac{d\rho}{\rho} = \frac{\alpha dT}{(1 + \alpha T)} \tag{63}$$

For copper, $\alpha \cong 0.0035$ per $^{o}F$. At T = $300^{o}F$, and for a dT = $100^{o}F$, the percentage change in resistivity becomes

$$\left.\frac{d\rho}{\rho}\right|_{copper} = 17.1 \text{ percent} \tag{64}$$

Similarly, for aluminum,

$$\left.\frac{d\rho}{\rho}\right|_{aluminum} = 14 \text{ percent} \tag{65}$$

with a temperature coefficient $\alpha \cong 0.00239$ per $^{o}F$. Assuming an operating voltage of 10 v, a 14 to 17 percent resistivity change would produce an output variation of 1.4 to 1.7 v, which is definitely measurable with present-day electronics.

## Evaluation of Supporting Data

In order to support the theoretical prediction, experimental data existing in-house at AiResearch were evaluated to verify the predicted magnitude of output variation with temperature change for different sink materials (see Figures 19 through 23). The data are expressed as plots of eddy-current probe signal conditioner output voltage versus displacement for different operating temperatures. Since the output voltage is proportional to the eddy current, which, in turn, is proportional to the resistivity, the variation in output voltage is representative of the resistivity change of the sink material. The output voltage percentage change for a temperature change of $100^{o}F$ from an operating temperature of approximately $300^{o}F$ is listed in Table VI for the various sink materials evaluated.

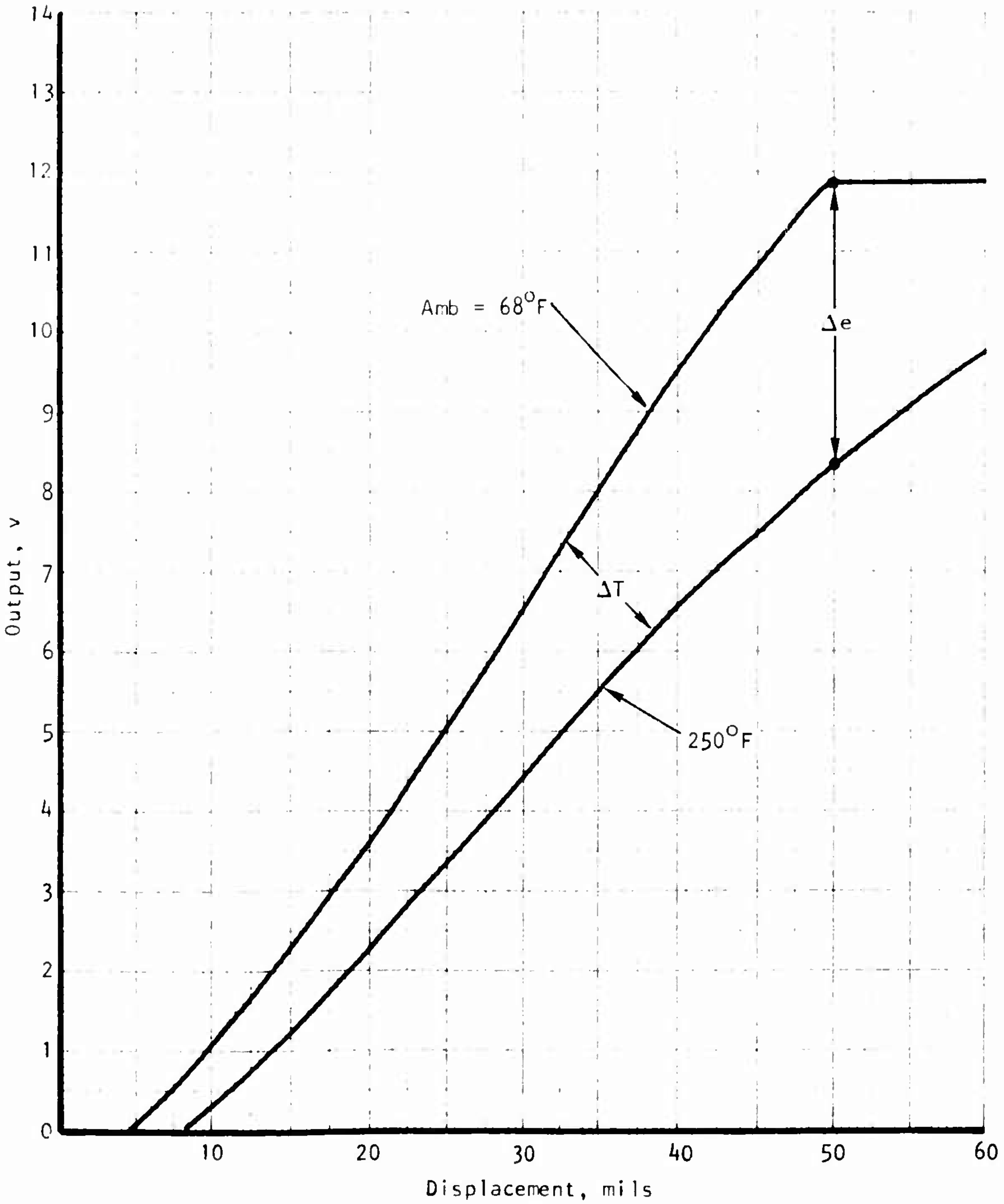

Figure 19. Test Data Plot for Al 2024 Sink Material.

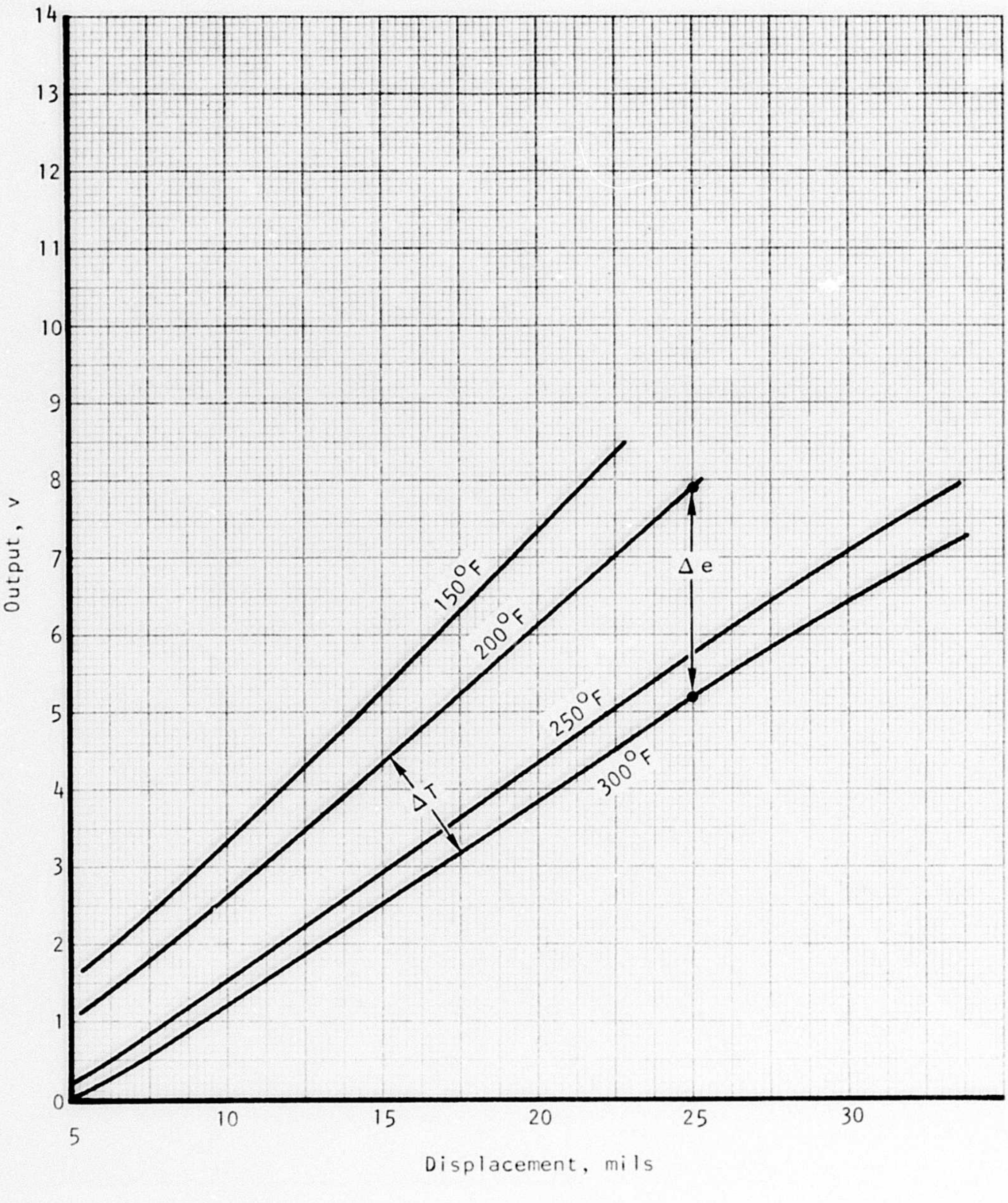

Figure 20. Test Data Plot for M-50 Steel Sink Material.

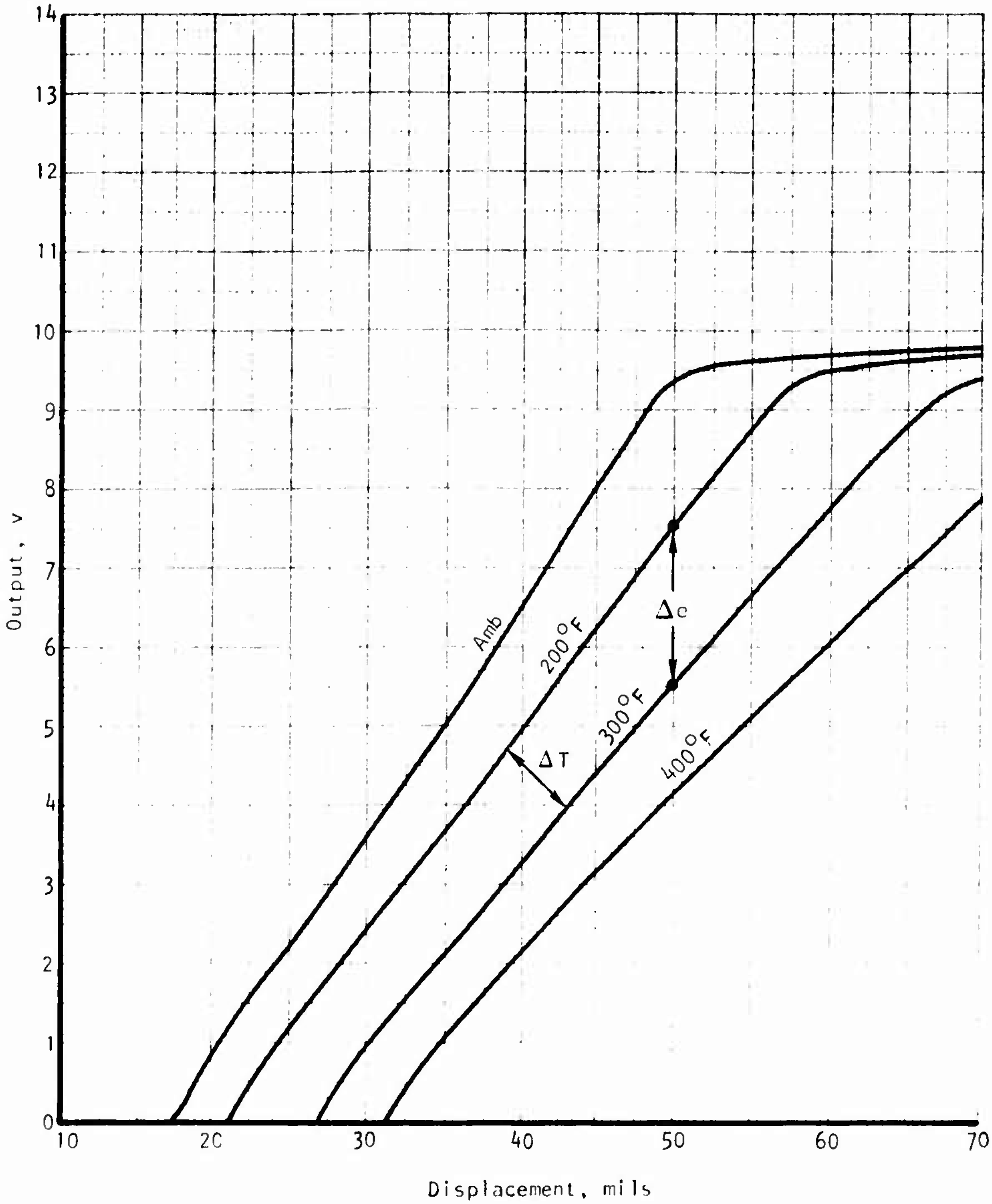

Figure 21. Test Data Plot for 4340 Steel Sink Material.

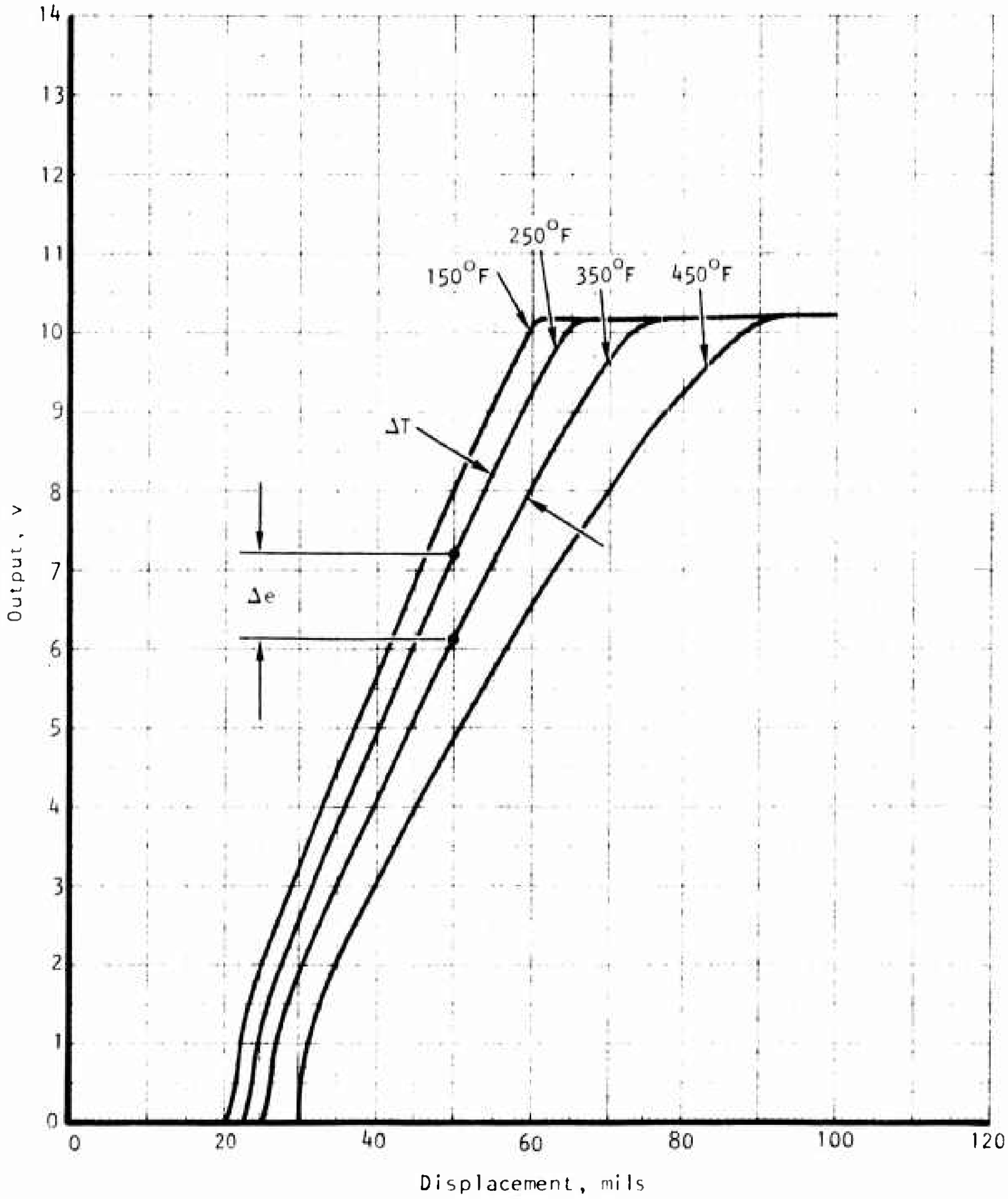

Figure 22. Test Data Plot for AMS-5659 Stainless Steel Sink Material.

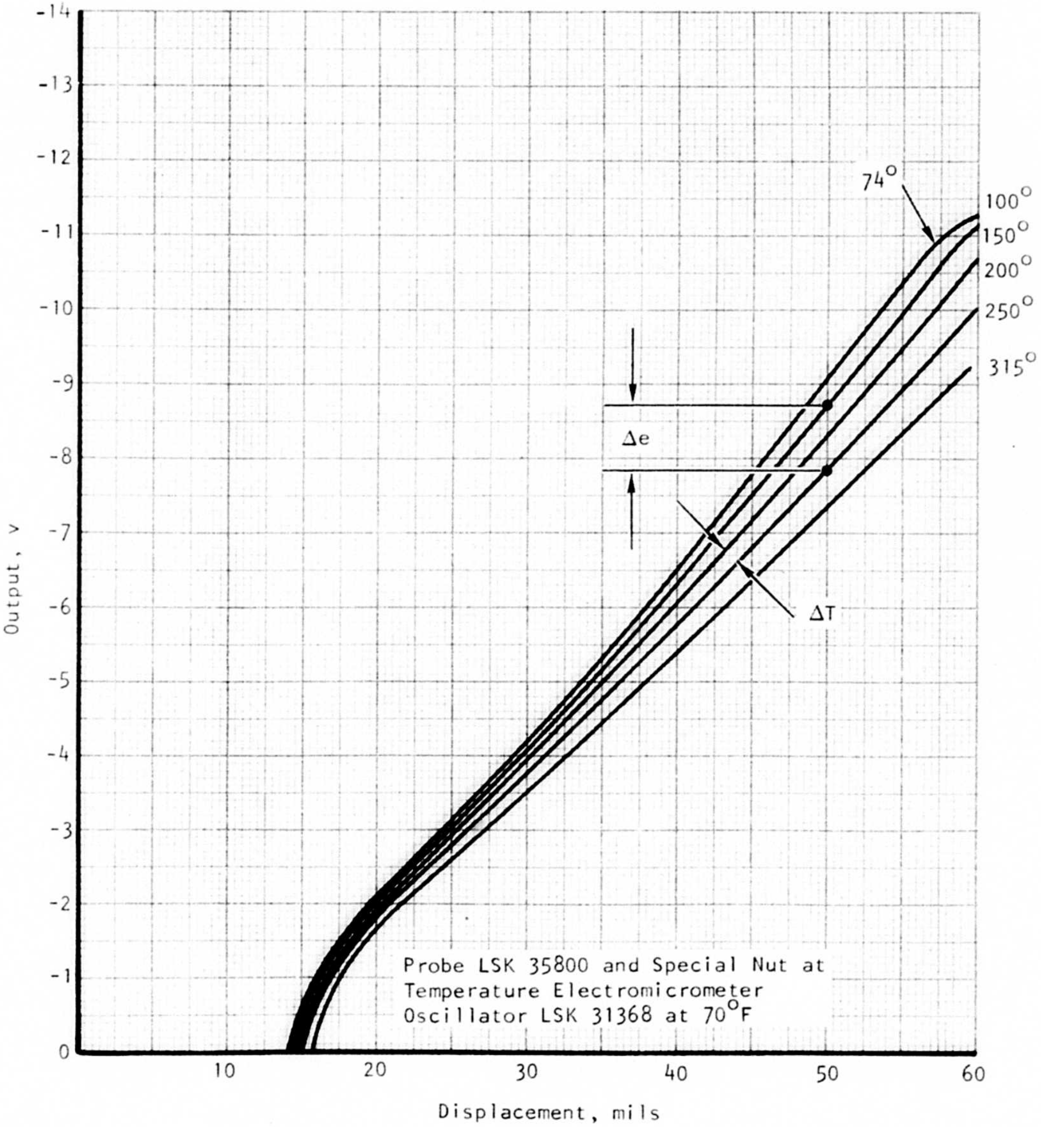

Figure 23. Test Data Plot for 17-4PH Stainless Steel Sink Material.

TABLE VI. MEASURED OUTPUT VOLTAGE CHANGE DUE TO 100°F TEMPERATURE CHANGE

| Sink Material Used | Output Voltage Percentage Change | Remarks |
|---|---|---|
| 2024 Al alloy | 23 | - |
| M-50 steel | 52 | Highly nonlinear with temperature change |
| 4340 steel | 38 | Fairly linear |
| AMS-5659 stainless steel | 17 | Fairly linear |
| 17-4 PH stainless steel | 10.8 | Fairly linear |

NOTE: Operating temperature ≈ 300°F

The experimentally obtained output change for aluminum appears to be higher than the expected theoretical value (23 percent actual, versus 14 percent predicted). The deviation is considered to be attributable to (1) insufficient data curves, (2) error introduced due to interpolation, (3) nonlinearity of the eddy-current probe output, and (4) difference between an aluminum alloy and a pure aluminum material. Table VI also shows that a significantly larger output change is obtained from certain ferrous metals; e.g., M-50 and 4340 steel. Although this larger percentage output change permits easier measurement, the accompanying large change in magnetic properties generally complicates the problem.

### Effect of Flux-Cutting Due to Shaft Rotation

The previous analyses were based on a static condition in which the current generated in the material was by induction only. When the probe is used on a rotating shaft, an additional current flow in the sink material could be caused by the flux-cutting generator effect due to the motion of the metallic surface beneath the probe coil. This following discussion analyzes such an effect and determines whether such a current component can be minimized or corrected by computation. Figure 24 depicts such a dynamic condition. The probe coil is assumed to be rectangular in cross section to simplify the analytical manipulations. The normal component

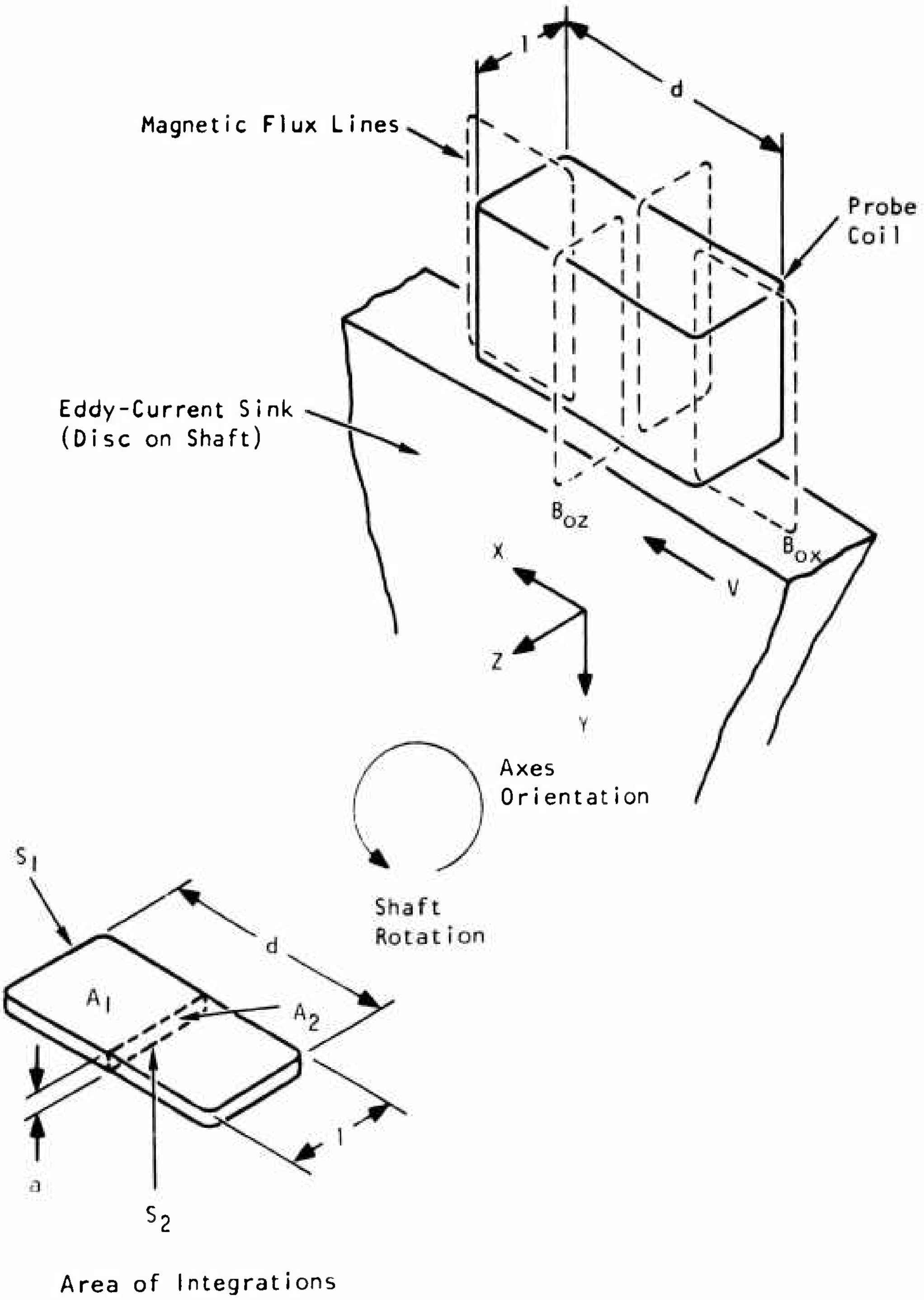

Figure 24. Magnetic Field at the Surface of an Eddy-Current Sink.

$B_y$ at the air-metal boundary surface is zero because of the boundary condition of a magnetic field after entering a metallic medium. Letting $\vec{B} = \vec{B}_o e^{j\omega t}$ be the sinusoidal magnetic induction, then

$$\vec{B} = \vec{B}_o e^{j\omega t} = (B_{ox} \vec{i}_x + B_{oz} \vec{i}_z) e^{j\omega t} \tag{66}$$

The induced voltage in the material can be calculated from the curl equation; i.e.,

$$\nabla \times \vec{E} = -\frac{\partial \vec{B}}{\partial t} = -j\omega \vec{B}_o \tag{67}$$

and

$$e_{ind} = \oint_{S_1} \vec{E} \cdot d\vec{s} = \iint_{A_1} \nabla \times \vec{E} \cdot d\vec{a} \tag{68}$$

$$= -j\omega \iint_{A_1} \vec{B}_o \cdot d\vec{a} \tag{69}$$

Assuming $B_o$ is more or less uniformly distributed over the cross-sectional area $A_1 = 1d$, then

$$e_{ind} = -j\omega 1d |B_o| \tag{70}$$

where $|B_o|$ is the magnitude of $\vec{B}_o$, which is $\sqrt{B_{ox}^2 + B_{oz}^2}$. Therefore,

$$|e_{ind}| = \omega 1d \sqrt{B_{ox}^2 + B_{oz}^2} \tag{71}$$

The flux-cutting emf can be calculated from the generator equation

$$\vec{E}_{vel} = \vec{v} \times \vec{B} = v\vec{i}_x \times \left[B_{ox} \vec{i}_x + B_{oz} \vec{i}_z\right] e^{j\omega t} \tag{72}$$

or

$$\vec{E}_{vel} = -v B_{oz} e^{j\omega t} \vec{i}_y \tag{73}$$

and

$$e_{vel} = \oint_{S_2} \vec{E}_{vel} \cdot d\vec{s} = 2av\, B_{oz}\, e^{j\omega t} \tag{74}$$

or

$$|e_{vel}| = 2av\, B_{oz} \tag{75}$$

where a is the skin depth.

The magnitude ratio of these two emf's then becomes

$$\frac{|e_{ind}|}{|e_{vel}|} = \frac{ld\omega\sqrt{B_{ox}^2 + B_{oz}^2}}{2av\, B_{oz}} \tag{76}$$

In order to minimize the emf due to flux-cutting, three parameters can be used: l, d, and $\omega$. The maximization of l is not recommended because the residual magnetic component $B_{oy}$ due to a finite conductivity may still interact with this length to cause a certain flux-cutting emf in the sink material. Both d and $\omega$ can be maximized to increase the ratio. The frequency $\omega$ is the most desirable parameter to optimize, because it reduces the value of the skin depth, a, when it is increased. For a typical coil operating under a frequency of 10 kHz or more, the ratio of the magnitude of the induced emf to the magnitude of the flux-cutting emf will be on the order of 1000 to 1 or better. This means that the error caused by the flux-cutting emf will probably be less than 0.1 percent of the temperature measured. In the worst case, even if such a small error were to become intolerable, the flux-cutting emf error could be corrected by computation, because the magnitude of such an emf changes directly with the shaft rotational speed and the speed information can be readily extracted from the phasing pulse signals. However, additional electronics will be needed to extract such information.

## Effect of Stress in Eddy-Current Sink

Changes in the stress levels existing in the eddy-current sink material also tend to change the resistivity and the core loss parameters of the material used. Such changes obscure the changes caused by the temperature variations; the occurrence of such changes will, therefore, cause an error in the measurement of the temperature of the shaft. There are two ways to minimize this temperature measurement error: (1) design the eddy-current sink in such a way that it provides good thermal conduction from the shaft but is not subject to the same torsional stress, and (2) compensate for the error during the computation of torque. Approach (1) can be accomplished by mounting the eddy-current sink on spring contacts to allow freedom of rotation of the sink with respect to the shaft. Approach (2) can be carried out once the necessary relationships are established as discussed below. It is known that

$$\theta = 57.3 \frac{\tau L}{JG} \tag{77}$$

where $\theta$ = twist angle

$\tau$ = torque

J = polar moment of inertia of shaft

L = shaft length

G = modulus of rigidity

The values of L and J change only slightly with temperature and consequently can be regarded as constants. The modulus of rigidity G decreases linearly with temperature increase; therefore, it can be expressed as follows:

$$G = G_o (1 - K_2 T) \tag{78}$$

where $G_o$ is a constant reference value, $K_2$ is the temperature coefficient of the modulus of rigidity, and T is the temperature. By substituting this expression for G into Equation (77), the twist angle becomes

$$\theta \cong \frac{K_1 (1 + K_2 T)}{G_o} \cdot \tau \tag{79}$$

And the true torque can be calculated as

$$\tau = \frac{\theta G_o}{K_1 (1 + K_2 T)} \tag{80}$$

Since T is measured by a voltage representing the eddy-current flow which is influenced by both the temperature and the stress (or twist angle $\theta$) of the shaft,

$$e_{eddy} = K_3 T + f(\theta) \tag{81}$$

or

$$T = \frac{1}{K_3}\left[e_{eddy} - f(\theta)\right] \tag{82}$$

Finally, the true torque that is applied to the shaft can then be expressed in terms of the two measured quantities θ and $e_{eddy}$:

$$T = \frac{K_3 \theta G_o}{K_1 \left\{K_3 + K_2\left[e_{eddy} - f(\theta)\right]\right\}} \tag{83}$$

The constants $K_1$, $K_2$, $K_3$ and the functional relationship f(θ) can be obtained experimentally. Therefore, the true value of the applied torque can be either computed or calibrated in terms of θ and $e_{eddy}$ without too much difficulty.

## EXPERIMENTATION ON SELECTED SINK MATERIAL

A considerable amount of experimental effort was spent on the noncontacting eddy-current temperature sensor to evaluate the temperature sensitivity and the measurement repeatability of some of the most promising eddy-current sink materials and probes. The 4340 steel and the pure copper were selected for additional experimental evaluations. The 4340 steel sink material showed the highest signal sensitivity and linearity with respect to temperature change among the ferrous metals investigated. The pure copper was the best of the practical pure conductive type materials. Five samples of each kind of sink material were prepared for the tests. Two designs of eddy-current probes were used; the type 314-L30 probe is good to 500°F, while the type 306-3348 probe is good to 1300°F. The probes are about 1/4 to 1/3 in. diameter, with inductances of approximately 35 μh.

The experimental data indicated that the 4340 steel was relatively less stable. Figure 25 shows a plot of output versus gap distance with temperature as a third parameter for a 4340 steel sample before it was specially temperature cycled. High temperature sensitivity as evidenced by the wide separation of the curves was observed (as was anticipated). However, a significant amount of temperature hysteresis was also observed when the metal sample temperature was reduced to 350°F after reaching a high level of 605°F. Figure 26 shows a test plot of the same steel sample under identical test conditions after the sample had been temperature cycled from ambient to 700°F several times before the test. A drastically different set of curves was observed. Temperature sensitivity decreased sharply; however, the temperature cycling did reduce the hysteresis and improve the repeatability of the measurement. By proper adjustment of two circuit parameters of the eddy-current probe signal oscillator, temperature sensitivity was improved. Figure 27 shows the improved set of curves and Figure 28 shows the output-voltage-to-temperature relationship at a gap distance

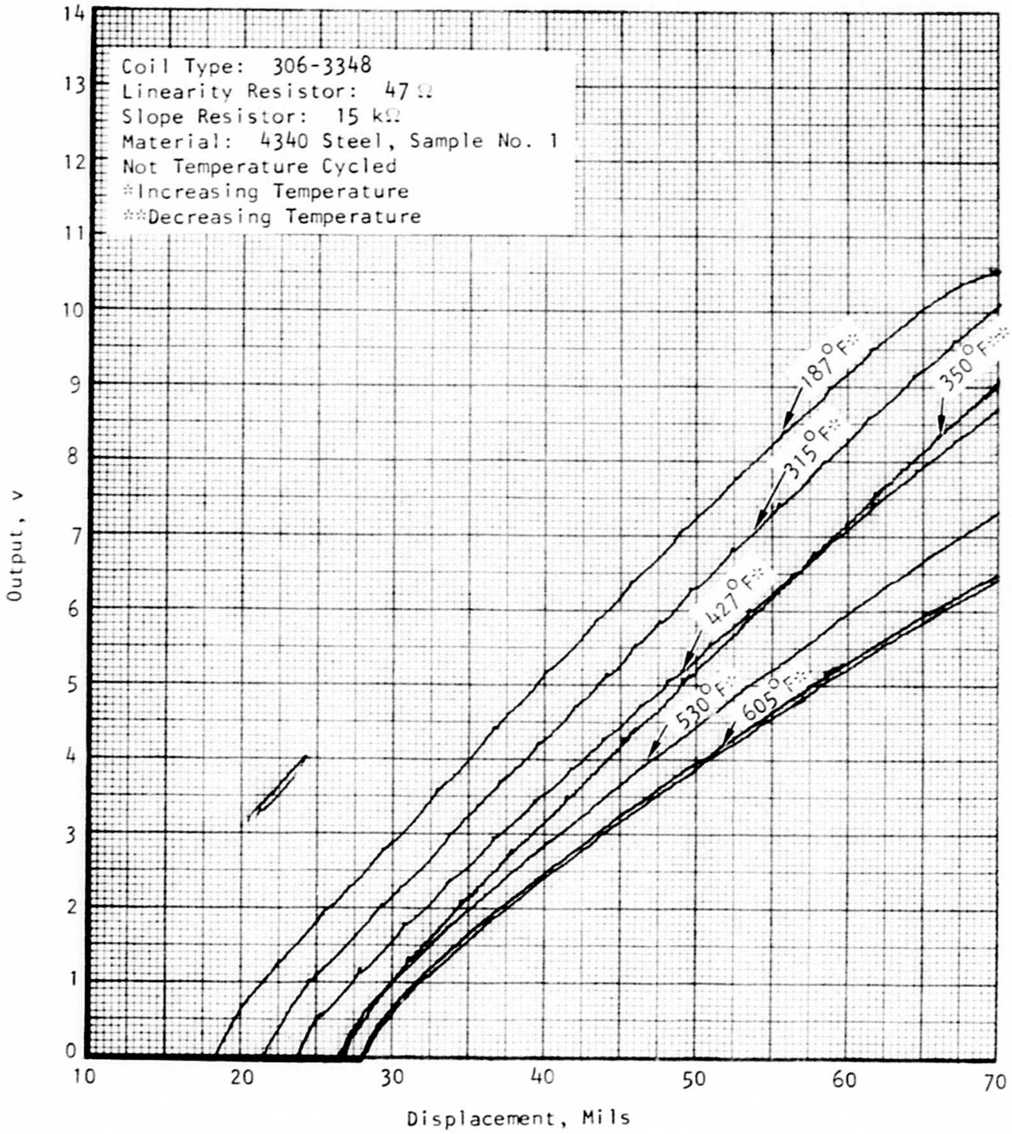

Figure 25. Test Data for 4340 Steel--Not Temperature Cycled.

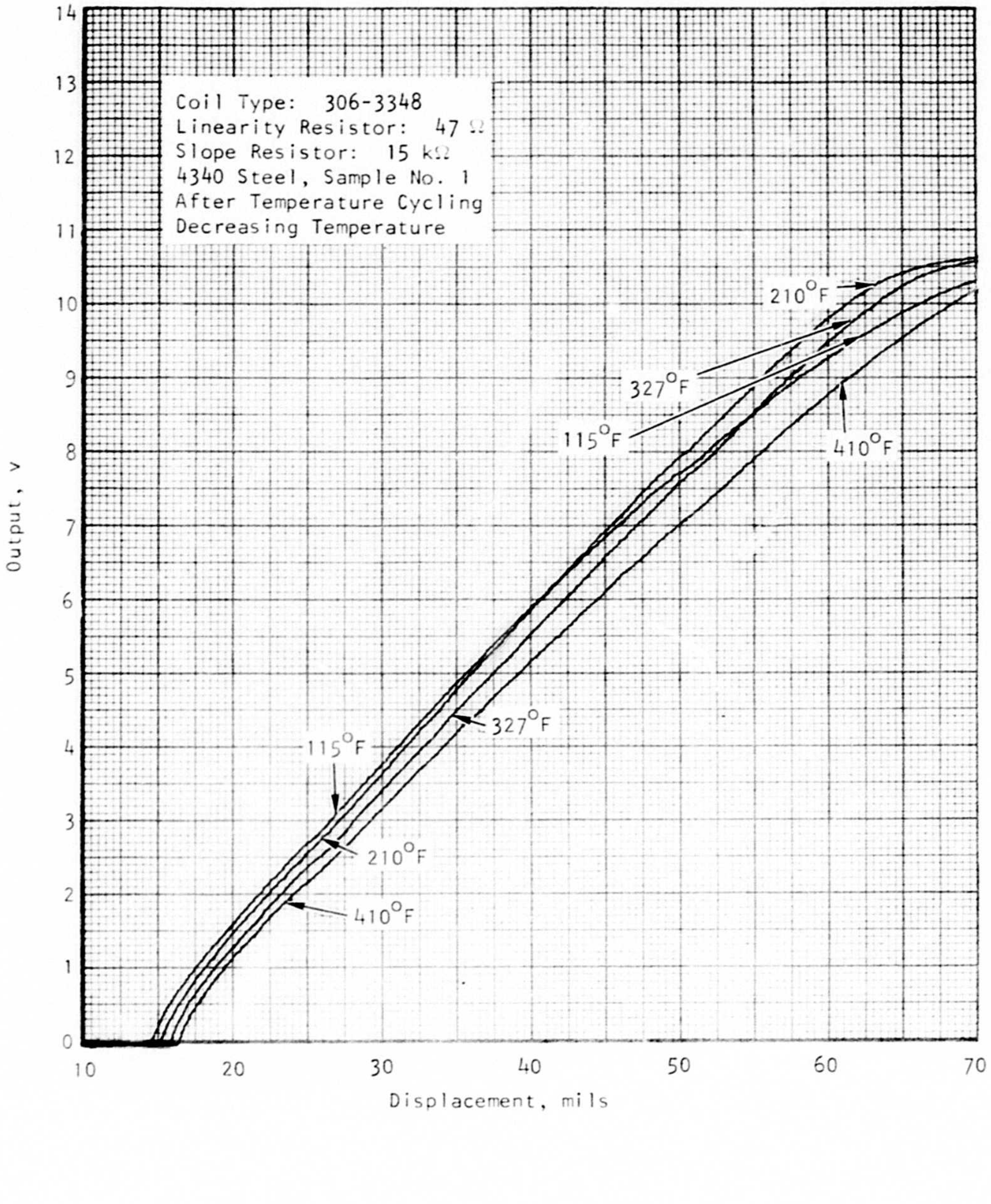

Figure 26. Test Data for 4340 Steel--After Temperature Cycling.

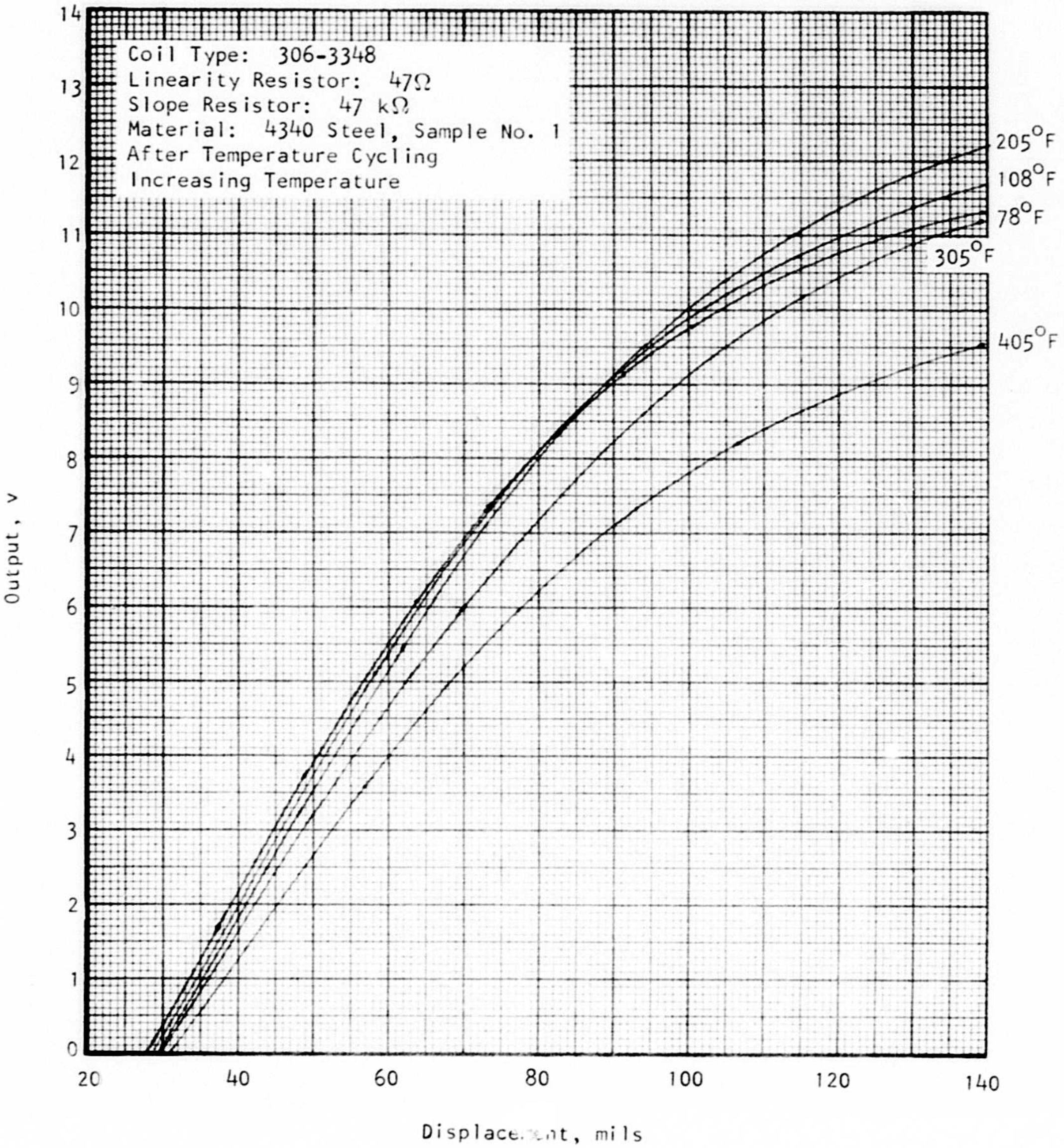

Figure 27. Improved Test Data for 4340 Steel.

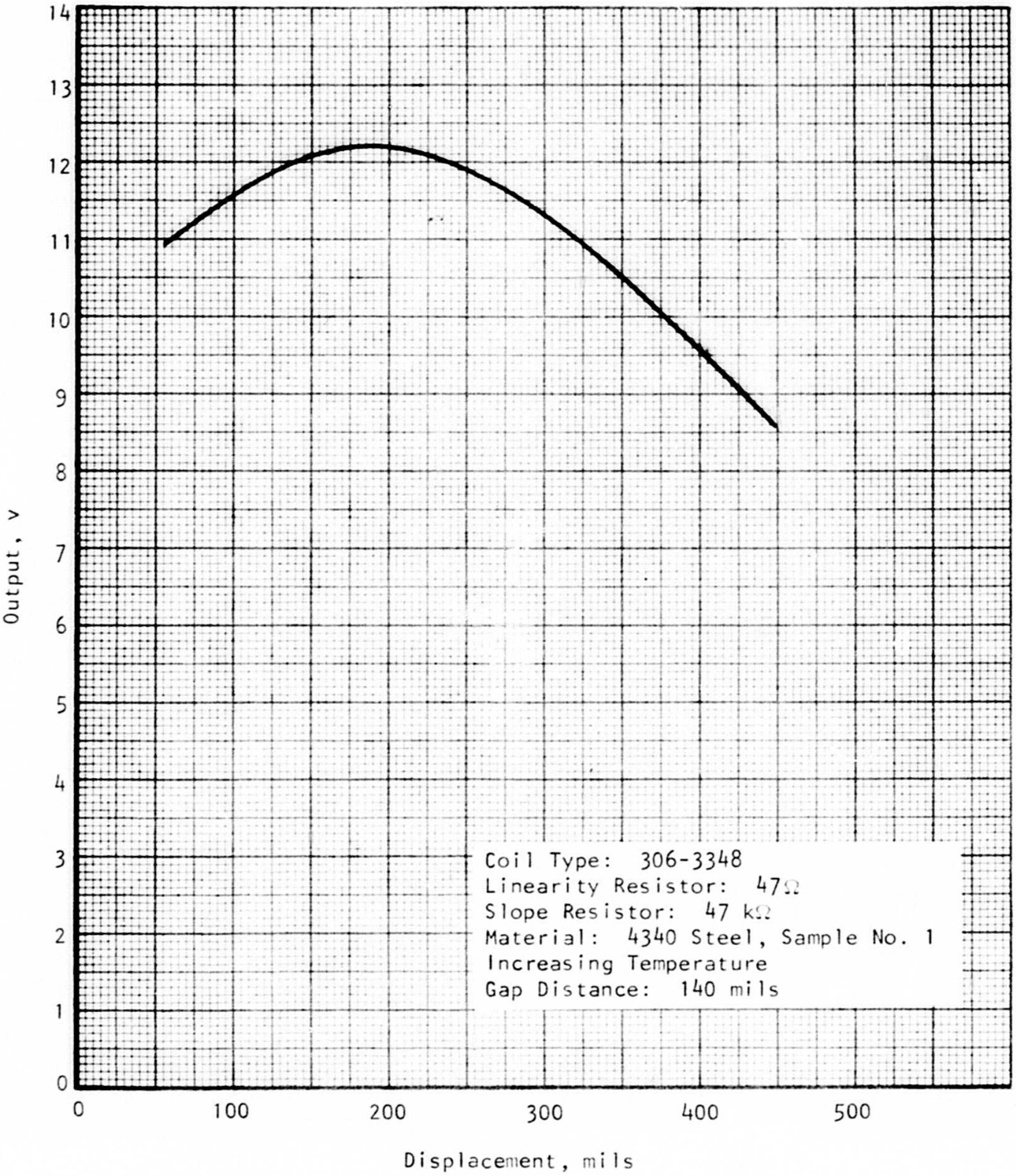

Figure 28. Improved Output vs Temperature Data for 4340 Steel.

of 140 mils. As shown in Figure 28, the output-voltage-to-temperature relationship does not show a 1-to-1 correspondence between the output and the temperature--there are two possible temperature readings for a given output voltage level. The temperature sensitivity was reduced to 16.4 percent per 100°F at 300°F, as contrasted to 38 percent per 100°F temperature change from other tests. The primary reduction in sensitivity was caused by the rise in dc level at the 300°F operating point.

The experimental data on the pure copper sink material showed much more promising results. The data from these five copper samples (of which samples Nos. 1 through 3 were temperature cycled, and samples Nos. 4 and 5 were not temperature cycled) showed that the results were highly repeatable and the temperature sensitivity was close to the predicted value of 17 percent. Figure 29 shows a set of curves made for sample No. 5 during an increasing temperature sequence. Figure 30 shows the results of an identical test on the same sample, but during a decreasing temperature sequence. Figure 31 shows the test results on a temperature-cycled sample, (No. 3) under an identical test condition, but performed on a different day. Figure 32 gives an example of the repeatability of the data from the five samples at a metal temperature of 203°F. The deviation from the average of these curves is about 0.05 v. Considering the resolution limitation and the accuracy limitation of the rudimentary test setup and the data plotting equipment, the actual repeatability of the data should be better than 0.05 v. It was frequently observed during the tests that even a temperature difference of about 1°F could consistently be indicated by the eddy-current temperature sensor when a better display device such as a digital voltmeter was used. By plotting the output voltage versus the metal temperature under a constant gap distance, the temperature output relationship can thus be established (see Figure 33). The temperature sensitivity evaluated at 300°F is 14.6 percent as contrasted to the predicted value of 17 percent per 100°F change in temperature. This temperature sensitivity decreases at the lower end of the temperature scale. Fortunately, the use of the proper probe with the proper combination of oscillator parameters will allow the temperature sensitivity to be increased for the lower end of the temperature scale at the sacrifice of high-end sensitivity. Figure 34 shows such a set of experimental data and Figure 35 shows the temperature output relationship when evaluated at an air gap of 160 mils. The temperature sensitivity of the low-temperature end is approximately 23.7 percent per 100°F change evaluated at 200°F. Consequently, by switching the sensor at the appropriate output level, it appears to be possible to measure the metal temperature by eddy-current means with sufficient sensitivity for a full temperature range from below ambient to a high temperature of well over 500°F. The ability to operate at a larger air gap (beyond 100 mils) will offer the advantage of lowering the influence of vibrations during sensor operation. The deviation of the measured sensitivity from the predicted value is believed to be caused by the nonlinear effects of the material and of the oscillator circuit, which was not accounted for in the initial modeling.

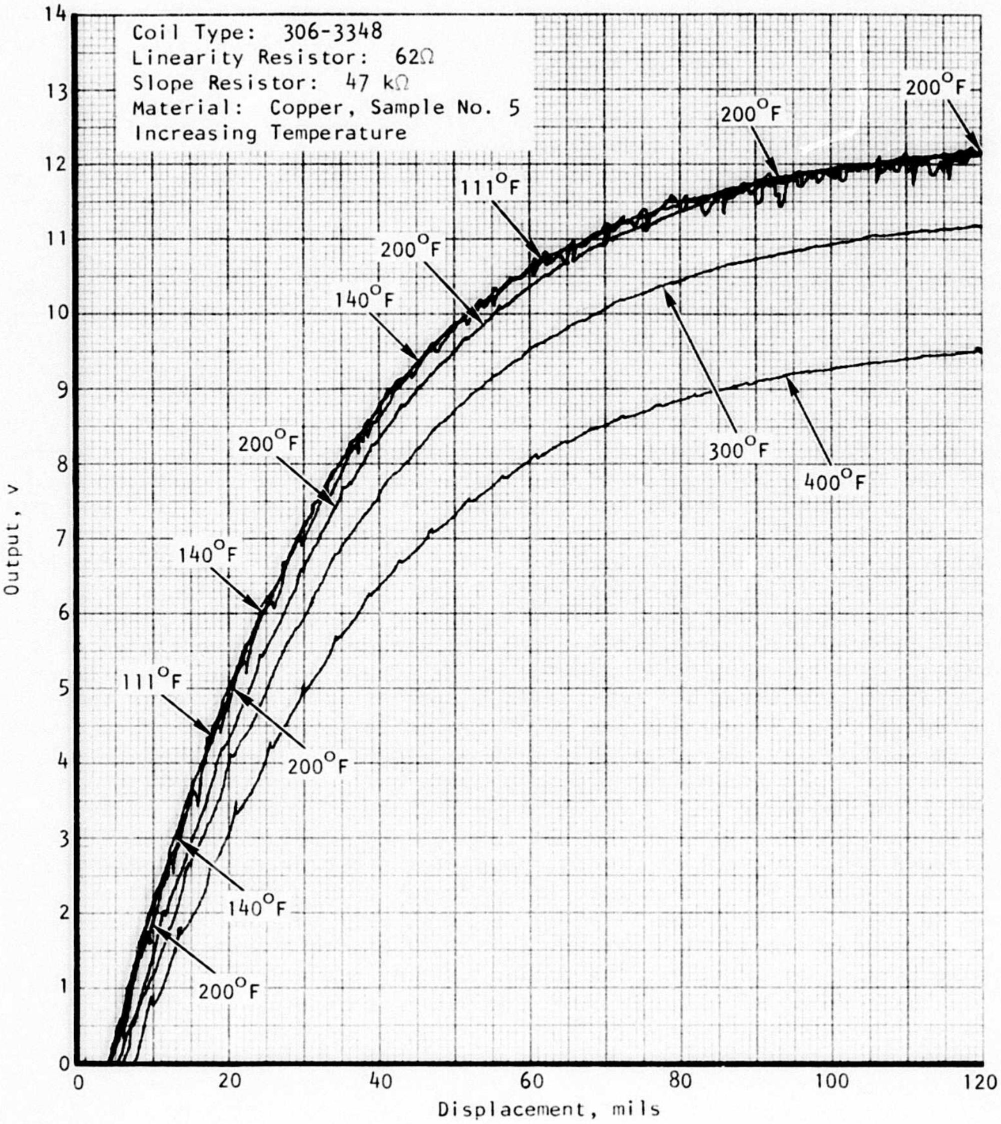

Figure 29. Test Data for Copper--Sample No. 5, Increasing Temperature.

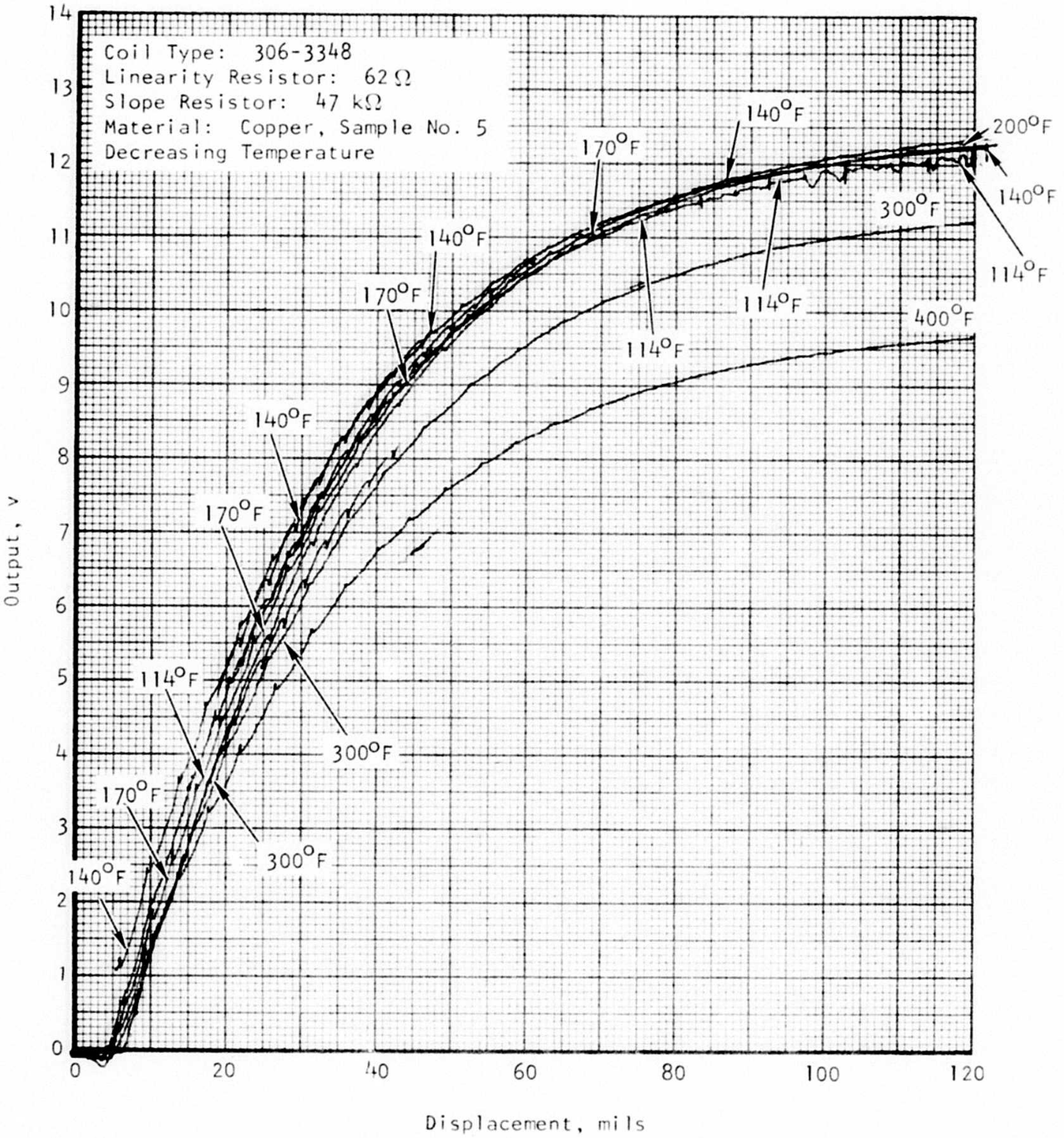

Figure 30. Test Data for Copper--Sample No. 5, Decreasing Temperature.

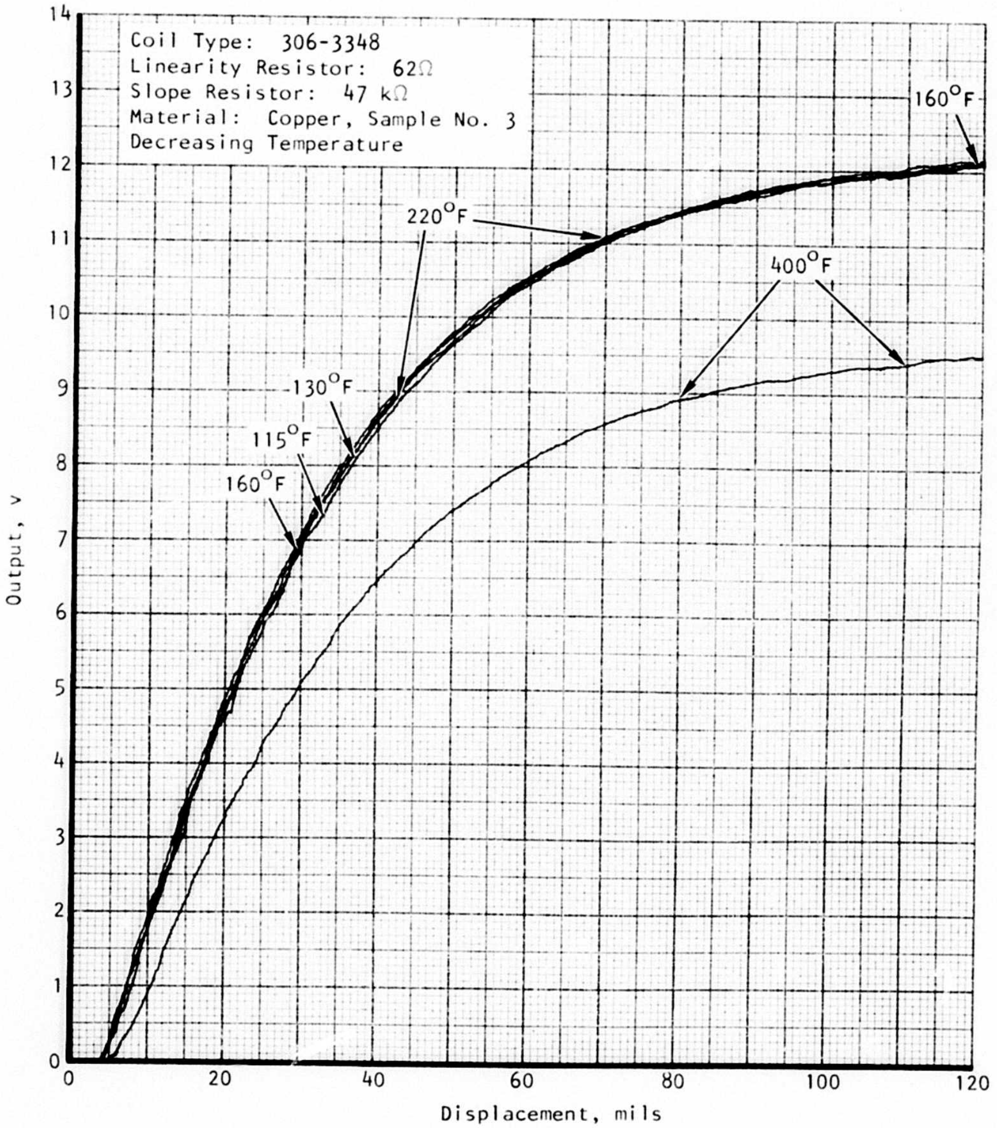

Figure 31. Test Data for Copper--Sample No. 3, Decreasing Temperature.

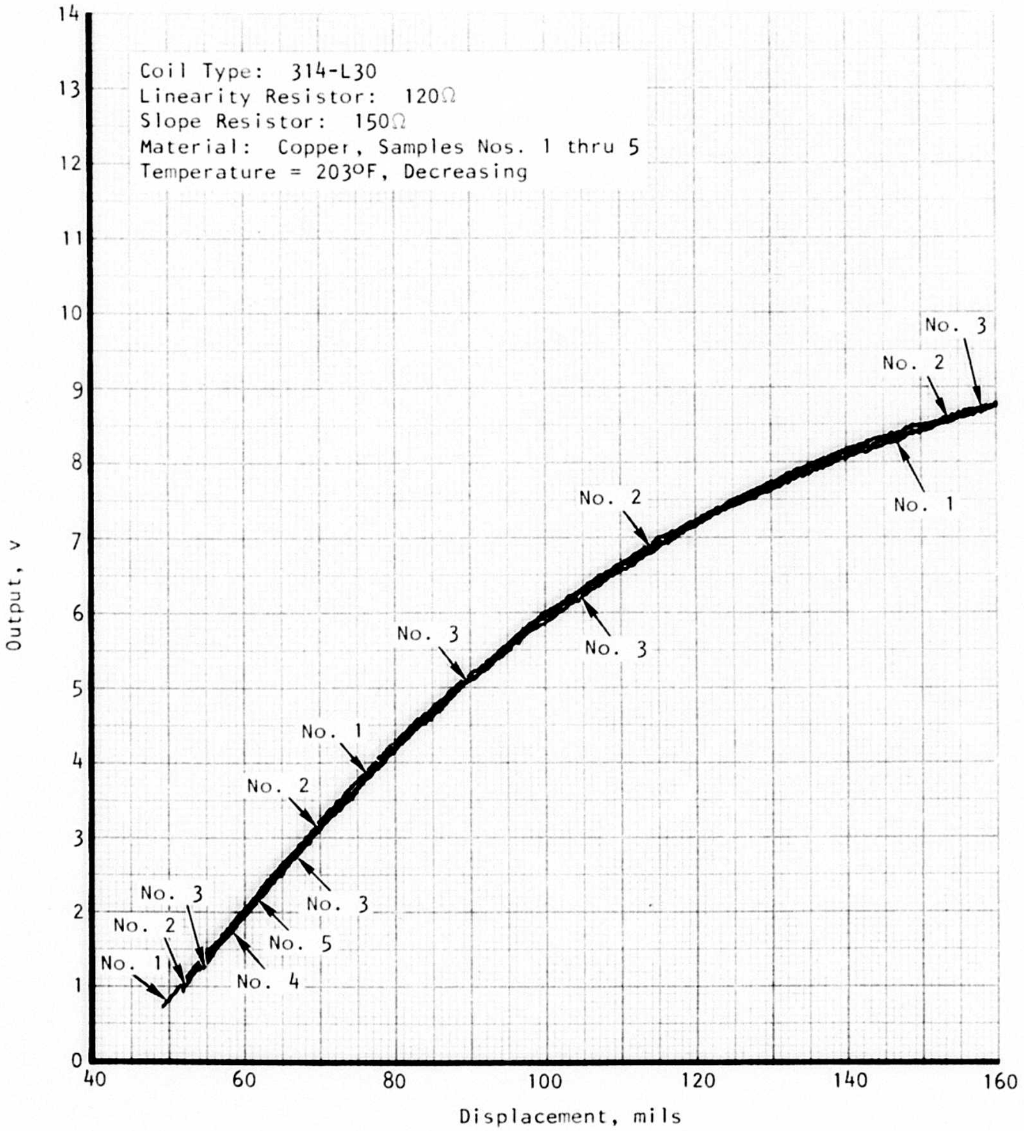

Figure 32. Repeatability of Copper Samples--Temperature 203°F, Decreasing.

Figure 33. Output vs Temperature for Copper--With 306-3348 Probe Type.

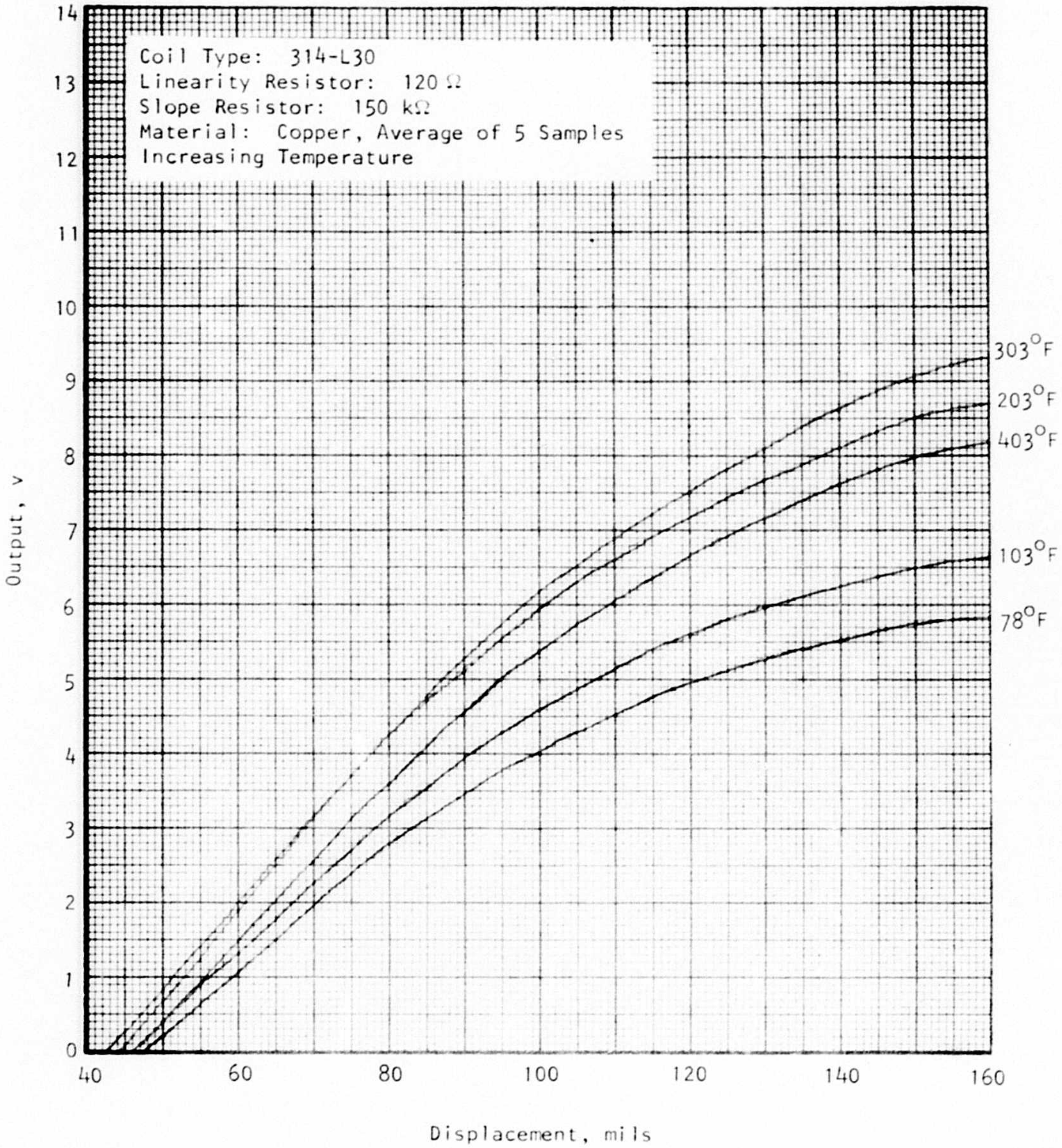

Figure 34. Test Data for Copper--With 314-L30 Probe Type.

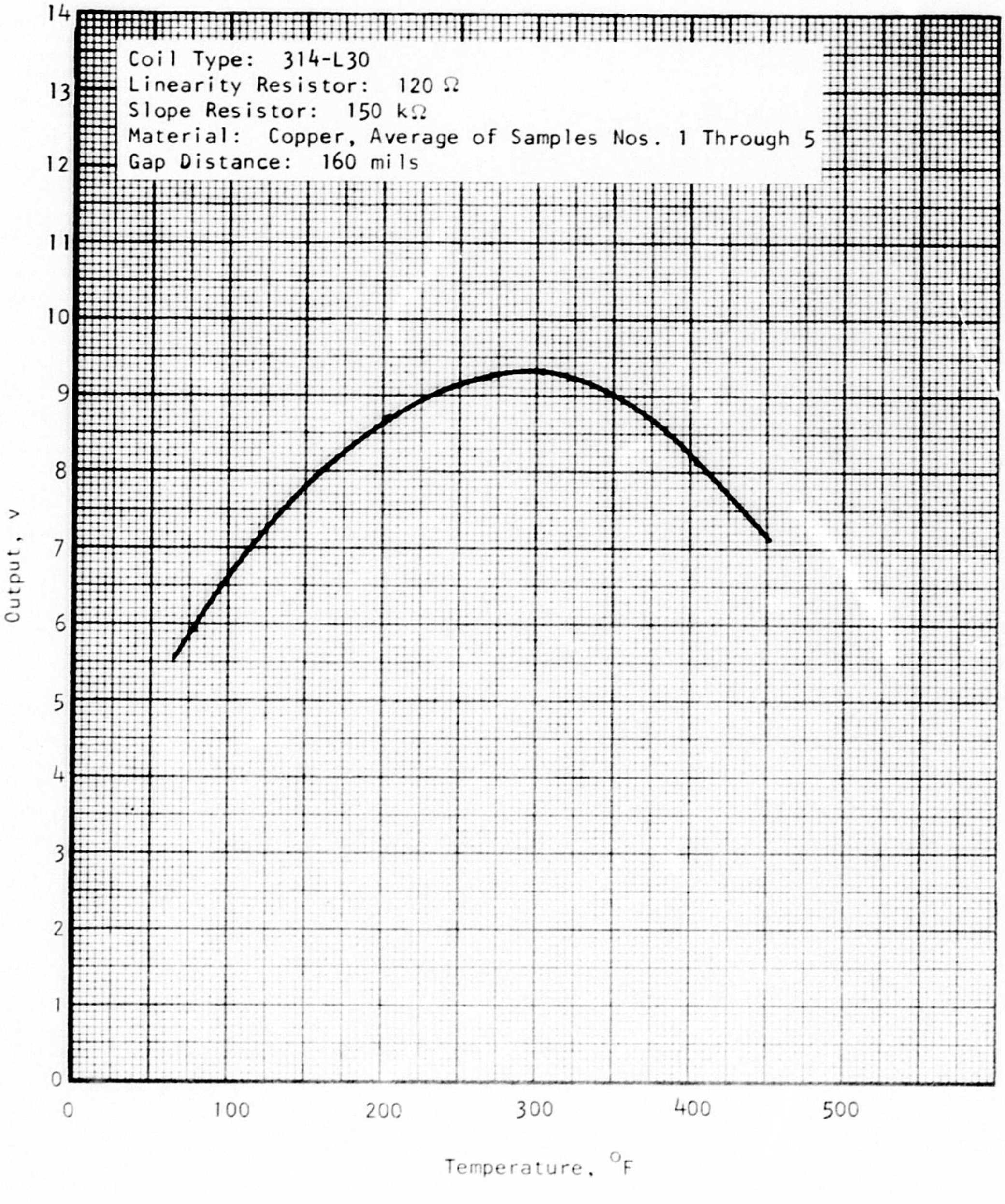

Figure 35. Output vs Temperature for Copper--With 314-L30 Probe Type.

Because of fabrication considerations, temperature tests of the plated copper samples were conducted to determine the characteristics and differences of the plated copper used as a substitute for the pure copper eddy-current sink material. Three steel samples plated with 10 mils of copper were prepared. Temperature tests using the same eddy-current probes were conducted on these samples. Although the quantitative relationships among the output voltage level, sample temperature, and air gap distance changed from that of a pure copper sample, the new characteristic curves still exhibit the complementary nature of the probe sink-material arrangement as originally exhibited by the pure copper material. The repeatability of the temperature measurement appears to be acceptable and the hysteresis due to temperature cycling seems to be negligible. Figures 36 and 37 show the characteristic curves of the two probes with 10 mils of plated copper as the new sink material.

## EDDY-CURRENT NONCONTACTING TEMPERATURE SENSOR CONFIGURATION

It has been pointed out that, with two probes and different circuit parameters, a complementary temperature-output relationship can be accomplished with eddy-current probes with copper sinks. Figure 38 shows a circuit design that will allow measurement of the full range of temperature by the use of two complementary probes, with probe No. 1 being of the 314-L30 type (Figure 35) and probe No. 2 of the 306-3348 type (Figure 33). The automatic switchover point can be set anywhere between 200°F and 300°F. When the output from probe No. 2 exceeds the threshold value that corresponds to the switchover temperature, the output voltage from probe No. 1 will be used to provide the low-temperature information (otherwise, output from probe No. 2 will be used for indication). To make an ever-decreasing output-to-temperature relationship, the output from probe No. 1 will be subtracted from a fixed reference voltage to achieve the needed inversion. If an ever-increasing output-to-temperature relationship is desired, the subtractor and the reference voltage circuitry should then be included in the output of the No. 2 probe conditioner path. The two solid-state switches will provide a fully open (nearly zero-volt) or a fully closed (whatever actual probe output) path for the corresponding probe output according to the control signal. The control of these two switches will always be 180 deg out of phase (i.e., one is fully open while the other is fully closed) so that at any given temperature there will be only one probe selected. The reference voltage selects the switchover temperature, while the gain adjustments in the adder circuit allow the matching of slopes of the two output temperature segments.

Figure 39 shows an overall output-to-temperature relationship of the two complementary types of probes. The switchover temperature is selected to be 250°F and the reference voltage is 20.8 v. The gain settings on the adder are both unity. A one-to-one correspondence between the output voltage and the temperature can thus be achieved. For a temperature change of 300°F, a voltage swing of 4.65 v can be obtained. Consequently, an average output change of 0.155 v per 10°F temperature change is realized.

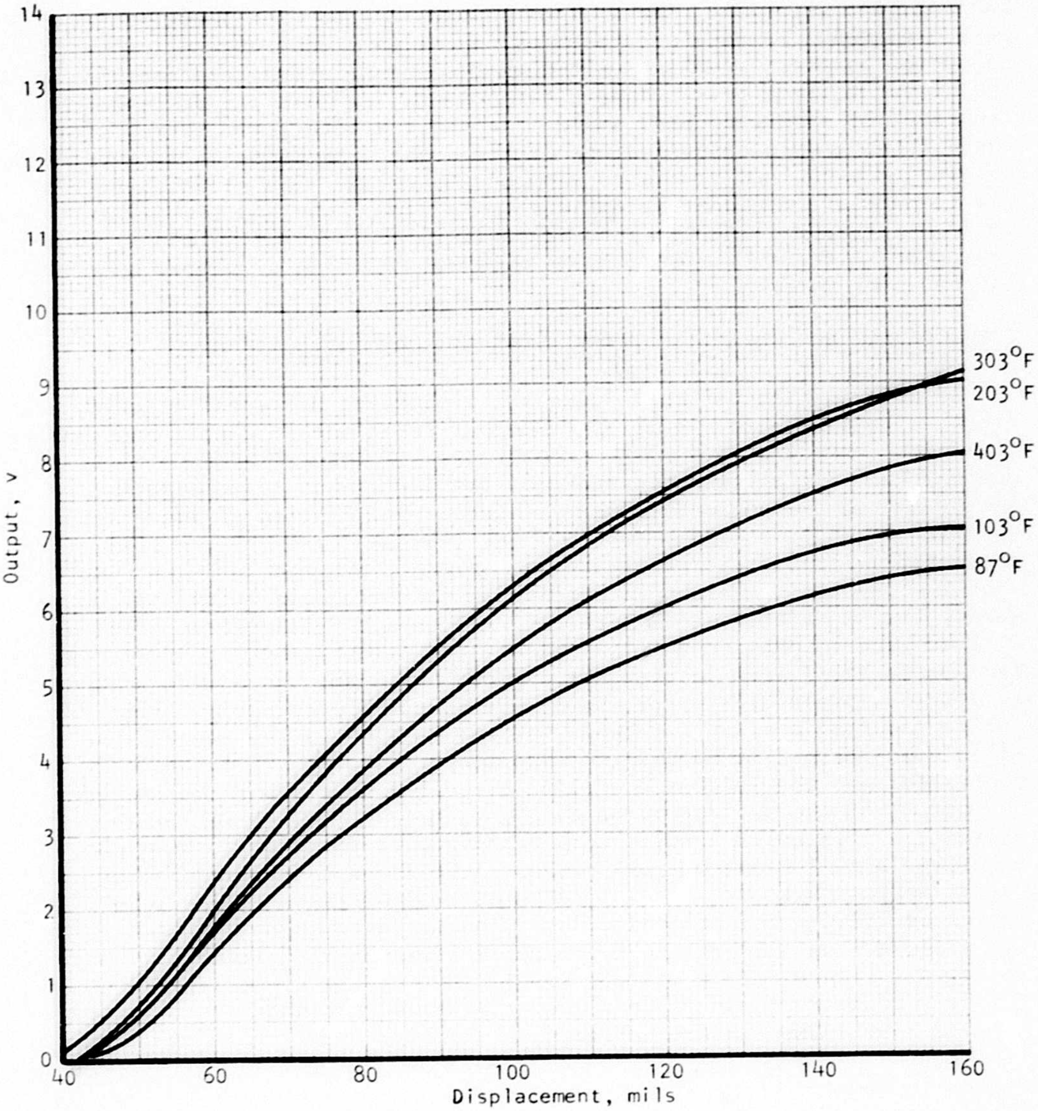

Figure 36. Eddy-Current Characteristic Curve for Probe 314-L30 Copper-Plated Sample.

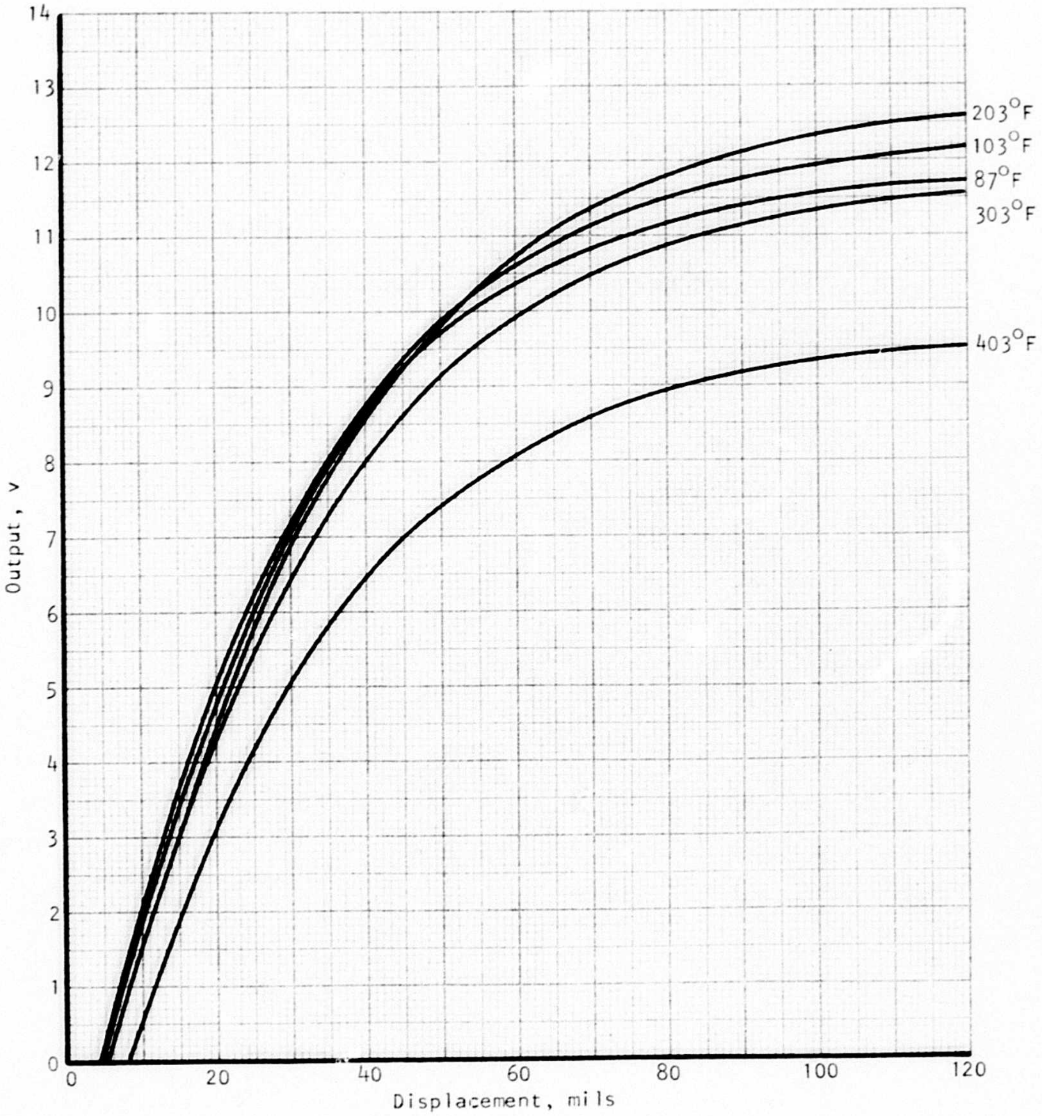

Figure 37. Eddy-Current Characteristic Curve for Probe 306-3348 Copper-Plated Sample.

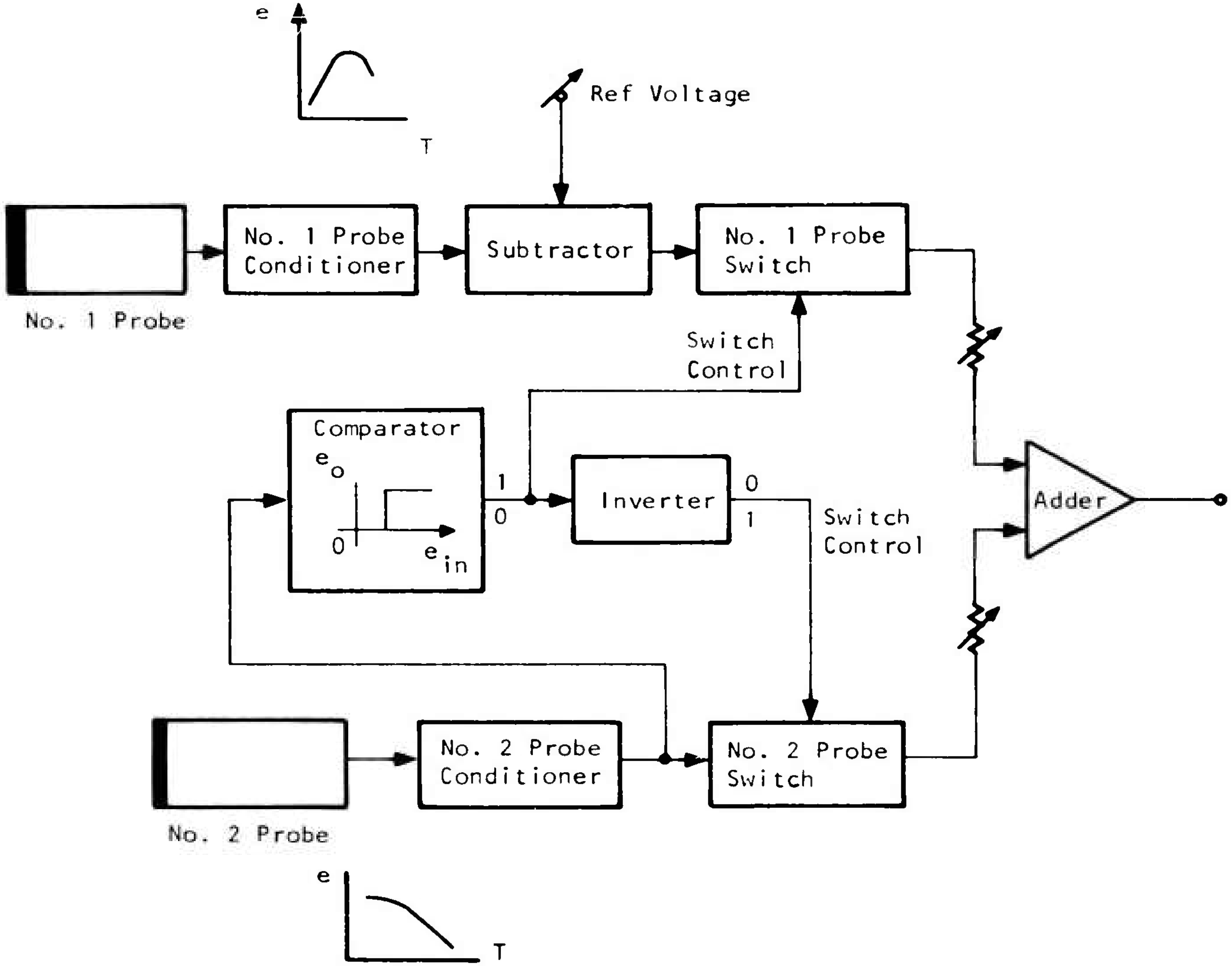

Figure 38. Block Diagram of Noncontacting Complementary Eddy-Current Temperature Sensor Design.

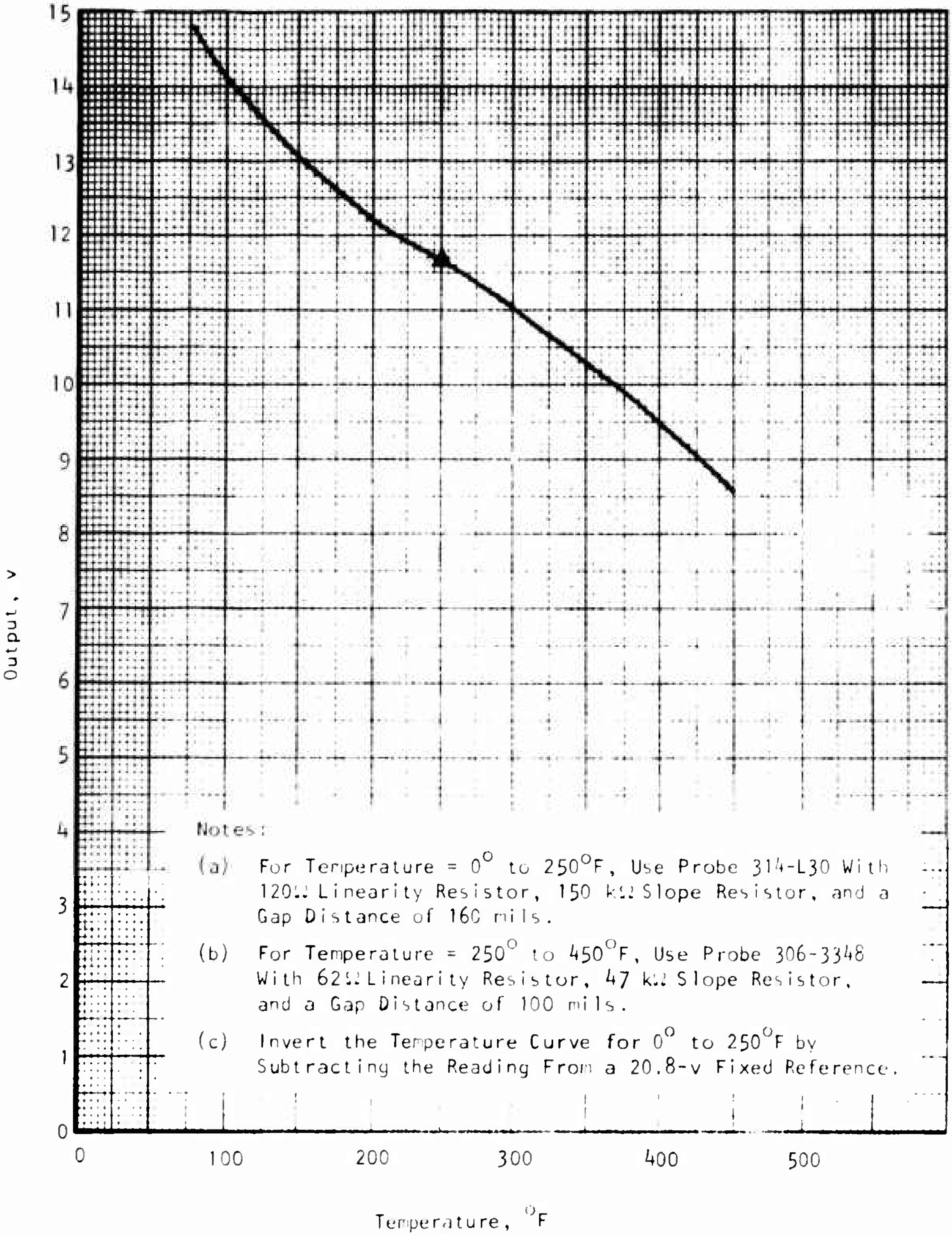

Notes:

(a) For Temperature = 0° to 250°F, Use Probe 314-L30 With 120Ω Linearity Resistor, 150 kΩ Slope Resistor, and a Gap Distance of 160 mils.

(b) For Temperature = 250° to 450°F, Use Probe 306-3348 With 62Ω Linearity Resistor, 47 kΩ Slope Resistor, and a Gap Distance of 100 mils.

(c) Invert the Temperature Curve for 0° to 250°F by Subtracting the Reading From a 20.8-v Fixed Reference.

Figure 39. Overall Output vs Temperature Relationship for the Complementary Probe Design.

## RECOMMENDED REFINEMENTS

Although a noncontacting temperature sensing unit that will measure the metal temperature of a shaft to within 10°F (or better) can be developed, the effort to accomplish this development was considered to be beyond the scope of the program. Because these refined investigations could also benefit other applications, such as noncontacting monitoring of critical bearing temperature, or the temperature measurement of a metal buried deeply in a nonmetalic medium, etc., it is recommended that the refined investigations listed below be conducted by a separate effort.

### Sink Material Optimization

This effort should also include investigation of the use of alloys, plating of a thin metal on a thick metal base, and the use of other material deposition techniques such as flame spraying. Different sink materials have demonstrated different influences on temperature sensitivity, output linearity, and measurement repeatability. The use of composite materials could allow the use of the best features of each material.

### Probe Optimization

As the probe becomes larger, the allowable air gap distance increases, and a lower operating frequency can be used. A large air gap distance makes the device less vulnerable to shock and vibration influences. With probe coil inductances on the order of [illegible] mh and coil diameters approaching 1 in., the operating distance can be lengthened to around 1 in. Lowering the operating frequency causes deeper penetration of eddy current into the sink material. Such deeper current penetration could yield a better average temperature of the metal object to be measured.

### Oscillator Circuit Optimization

By properly optimizing the oscillator circuitry, it may be possible to achieve increased temperature sensitivity and to avoid the multiple-correspondence relationship between the temperature and the output voltage. Possibly, only one probe will be needed instead of the two probes presently required for the full range of temperature measurement.

An understanding of the interrelationship among sink material, probe, and oscillator circuit will also furnish the insight needed for other applications.

# DESIGN OF ADVANCED TORQUE MEASUREMENT SYSTEM

Design effort performed during the program included the system design, the test sensing unit design, the processor design, the design of related peripheral electronics that are needed for testing or for system integration, and the system software development. The design of the test sensing unit differs from that of a regular sensing unit in that this test unit also provides the adjustment for torque simulation and furnishes its own heater elements for temperature control. The torque is simulated by displacing the two phase pickups with respect to each other through a micrometer mechanism.

## SYSTEM DESIGN

System design was performed in terms of the system functional definition, the finalization of computation equations, and the establishment of upper-bounds of coincidence counts.

Figure 40 shows the overall system in block diagram form. This system is composed of a sensing unit, a temperature unit, a digital signal processing and computing unit, and a display unit. The sensing unit measures the phase and temperature information through the monopole pickups and the eddy-current probes. The phase information is further conditioned and evaluated, and the torque value is computed by the digital signal processing and computing unit. The temperature unit conditions and converts the shaft temperature data sensed by the eddy-current probes to a compatible digital format for temperature corrections performed by the computation module of the digital signal processing and computing unit. The resultant torque value is then transmitted to the display unit for outputting the information.

The operation of the system consists of two cycles: the measurement cycle and the computation cycle. The measurement cycle is performed by the coincidence checking logic and data collection counters of the coincidence measurement logic sub-unit, and the computation cycle is performed by a central processor (CP) of the torque computation sub-unit. Results of the computation are displayed through seven-segment fluorescent display devices for a given period of time before the initiation of another computation cycle. This displayed information also can be held for an extended period of time by turning to a manual control position of the system operation mode selection switch.

The measurement cycle is initiated by a "COMPUTATION READY" signal generated by the CP reset control. Upon reception of this reset signal for the CP, all the counters in the coincidence checking logic area will be cleared, all the control flip-flops and latches will be reset to their ground state, and the coincidence checking between the conditioned probe A signal and the clock signal will be activated. The use of coincidence between the probe A and the clock signals will avoid the ±1 count error in $N_1$ and $N_2$ countings. The counting of $N_1$ and $N_2$ will be activated by

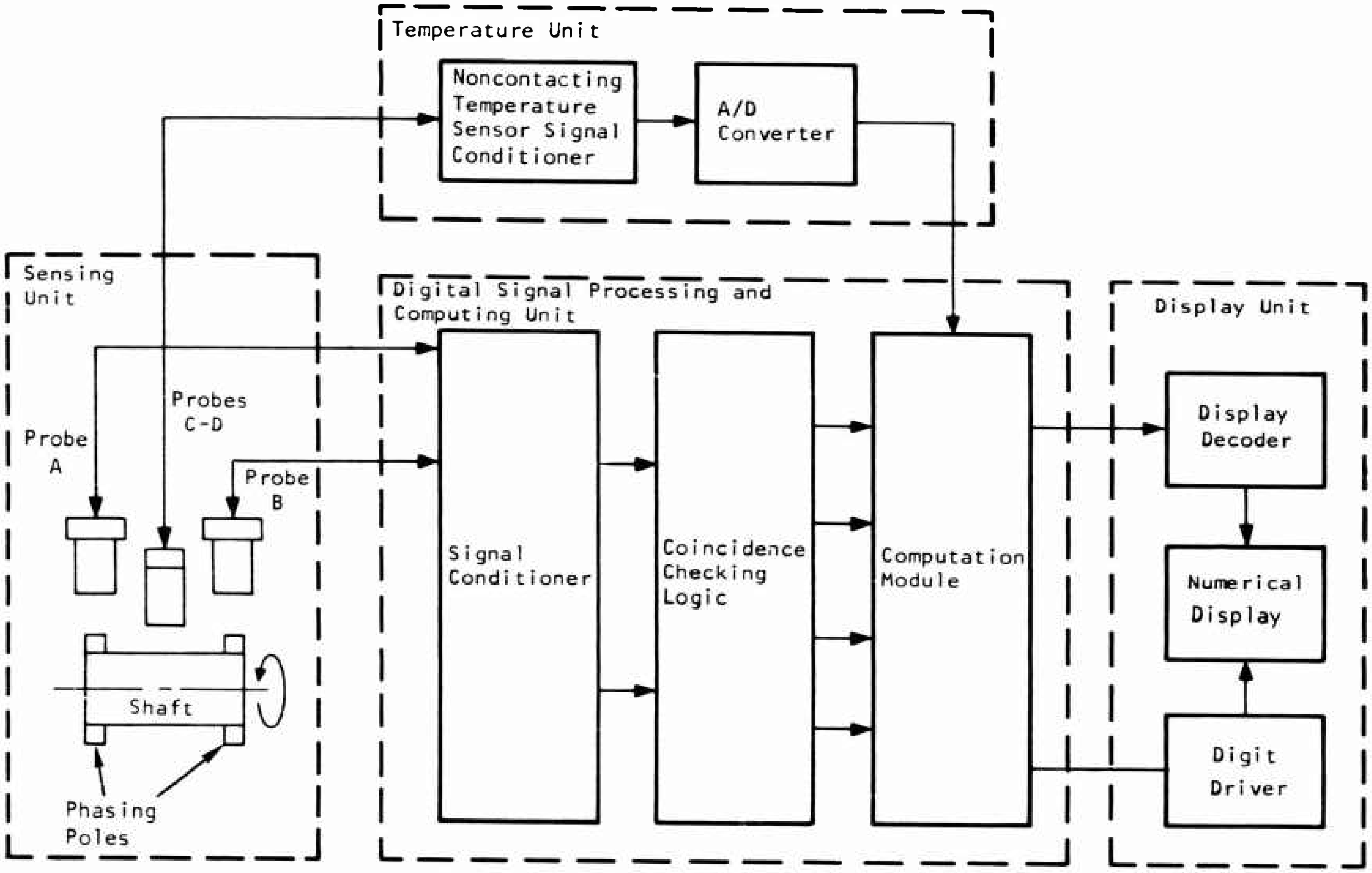

Figure 40. Block Diagram of Torque Measurement System.

the detection of coincidence between the probe A and the clock signals, and it will be terminated by the first coincidence of the probe B and the clock signals. The first coincidence of the probe B and clock signals also will activate the counting of $N_3$ and $N_4$. The termination of this second set of countings will be dependent upon the detection of the second coincidence between the probe B signal and the clock. The measurement cycle will be completed after the detection of the second coincidence of the probe B and the clock signals. All four counts $N_1$, $N_2$, $N_3$, and $N_4$ will be available on the counters for inputting to the CP at the end of the measurement cycle. A "MEASUREMENT READY" signal will be generated by the coincidence checking and measurement logic at the end of this cycle to notify the CP of the availability of data for computation.

The computation cycle will be initiated by the "MEASUREMENT READY" signal from the coincidence checking and measurement logic. The computation is controlled by a program counter and a solid-state read-only-memory (ROM) programmer. The coincidence counts and the temperature data of the shaft are sequentially input into the CU through the input multiplexers under the control of the ROM programmer. After completion of the computation, the programmer will remain in a "NO OP" state and the program counter will be locked out from further incrementing its count. The program counter will be reset to a ground state after a given period of data display time by the reset control logic. In addition, a "COMPUTATION READY" reset signal will be sent to the coincidence checking and measurement logic to initiate another set of measurement data.

## Computation Equations

Three steps are involved in the computation of the torque value from the measured coincidence counts and the shaft temperature: the computation of shaft twist angle, the temperature correction for change in modulus of rigidity, and the final computation of torque value with the proper scale factors injected:

### Equation for Computation of Twist Angle

The following equation is used to compute the shaft twist angle from the measured coincidence counts:

$$\theta = 60 \left[ \left(\frac{N_2}{N_4}\right) N_3 - (N_1 - 1) \right] \tag{84}$$

where $\theta$ = the shaft twist angle in mechanical degrees for a 6-tooth phasing gear

$N_1$ = the number of probe B pulses counted between the coincidence of the probe A signals and the clock and the first coincidence of the probe B signal and the same clock signal

$N_2$ = the number of counts of the clock signal during the same time period as for $N_1$

$N_3$ = the number of probe B signals counted between the first and the second coincidence of the probe B signal and the clock

$N_4$ = the number of counts of the clock signal during the same time period as for $N_3$

The $(N_1-1)$ term used instead of $N_1$ in the phase angle computation Equation (76) is a corrected term to compensate for the extra counting of the $N_1$ counter of the coincidence detection logic. This counter, when triggered by the coincidence of the probe A timing signal and the clock, will register the initial phase delay as a full count also. The subtraction of 1 from the content of this counter removes this extra partial count and makes $(N_1-1)$ represent the original $N_1$ term.

Equation for Temperature Compensation

For most of the shaft material, the effect of temperature on the modulus of rigidity can be represented by a linear relationship as indicated by Equation (85) over the temperature range of the subject application:

$$G = G_o \ (1 - K_2' \ T) \tag{85}$$

where $G_o$ = the value of the modulus of rigidity at a reference temperature of $T_o$

$K_2'$ = normalized temperature coefficient of G

T = the differential temperature measured with respect to a reference temperature $T_o$

With reference temperature $T_o$ setting to 225°F, the normalized temperature coefficient of G (i.e., $K_2'$) is approximately equal to 0.000263593 and the value of $G_o$ is equal to 10.99219 for AM355 stainless steel.

The temperature information is sensed by a pair of eddy-current probes. Since the relationship between eddy-current sensor output voltage and the temperature to be measured is, in general, nonlinear, G also will be related to the eddy-current sensor output in a nonlinear manner.

Since the temperature of the shaft need only be measured to within ±10°F of the true temperature, the digitization of the temperature data and the correction for temperature effect can be greatly simplified by dividing the output voltage range of the eddy-current sensor into bands corresponding to 10°F wide and utilizing the position-index, $I_T$, of these bands as an indication of the shaft temperature.

This arrangement again will allow the use of a linear relationship for temperature compensation for the change in modulus of rigidity due to temperature variations. The new equation for temperature compensation becomes

$$G = G_o \left| 1 - K_2 \left( I_T - I_o \right) \right| \tag{86}$$

With the temperature range as defined in Table VII, the values of $K_2$ and $I_o$ become 0.0029661 and 27, respectively.

## Equation for Torque Computation

The equation for computing the torque from the measured twist angle is

$$\tau = \frac{JG}{(57.3)\ L} \cdot \theta \tag{87}$$

where $\tau$ = the torque transmitted through the shaft, in.-lb

$J$ = the polar moment of the shaft, $\text{in.}^4$

$G$ = the modulus of rigidity of the shaft, $\text{lb/in.}^2$

$L$ = the length of the shaft, in.

With the quantized temperature scheme used, the final torque equation becomes

$$\tau = K_s \left| 1 - 0.00229661 \left( I_T - 27 \right) \right| \cdot (60) \left[ \left( \frac{N_2}{N_4} \right)^{N_3} - \left( N_1 - 1 \right) \right] \tag{88}$$

where $K_s = \frac{JG_o}{57.3L}$ and is established for each of the intended applications listed in Table VIII.

## Establishment of Coincidence Upper Bounds

This effort was performed to facilitate the determination of the counter size needed for $N_1$, $N_2$, $N_3$, and $N_4$.

In this analysis, two clock frequencies (1.5 MHz and 375 kHz) were used to evaluate using either a faster or a slower clock. The window size of the coincidence gate is 20 nsec in order to allow a good measurement resolution at high speed.

## TABLE VII. DEFINITION OF TEMPERATURE QUANTIZATION BANDS

| Temp Range (°F) | $I_T$ | Temp Range (°F) | $I_T$ | Temp Range (°F) | $I_T$ |
|---|---|---|---|---|---|
| -40 to -30 | 1 | 150 to 160 | 20 | 330 to 340 | 38 |
| -30 to -20 | 2 | 160 to 170 | 21 | 340 to 350 | 39 |
| -20 to -10 | 3 | 170 to 180 | 22 | 350 to 360 | 40 |
| -10 to 0 | 4 | 180 to 190 | 23 | 360 to 370 | 41 |
| 0 to 10 | 5 | 190 to 200 | 24 | 370 to 380 | 42 |
| 10 to 20 | 6 | 200 to 210 | 25 | 380 to 390 | 43 |
| 20 to 30 | 7 | 210 to 220 | 26 | 390 to 400 | 44 |
| 30 to 40 | 8 | 220 to 230 | 27 | 400 to 410 | 45 |
| 40 to 50 | 9 | 230 to 240 | 28 | 410 to 420 | 46 |
| 50 to 60 | 10 | 240 to 250 | 29 | 420 to 430 | 47 |
| 60 to 70 | 11 | 250 to 260 | 30 | 430 to 440 | 48 |
| 70 to 80 | 12 | 260 to 270 | 31 | 440 to 450 | 49 |
| 80 to 90 | 13 | 270 to 280 | 32 | 450 to 460 | 50 |
| 90 to 100 | 14 | 280 to 290 | 33 | 460 to 470 | 51 |
| 100 to 110 | 15 | 290 to 300 | 34 | 470 to 480 | 52 |
| 110 to 120 | 16 | 300 to 310 | 35 | 480 to 490 | 53 |
| 120 to 130 | 17 | 310 to 320 | 36 | 490 to 500 | 54 |
| 130 to 140 | 18 | 320 to 330 | 37 | 500 to 510 | 55 |
| 140 to 150 | 19 | | | | |

TABLE VIII. SCALE FACTORS

| Application Case | Shaft Speed (rpm) | Full-Scale Torque (ft-lb) | Full-Scale Twist Angle (deg) | Scale Factor $K_s$ (ft-lb/Mech. deg) |
|---|---|---|---|---|
| I | 6000 | 250 | 5 | 50 |
| II | 6600 | 725 | 5 | 145 |
| III | 26,000 | 300 | 10 | 30 |

### The 1.5-MHz Clock

The maximum number of counts of $N_1$ and $N_3$ is bounded by the maximum possible time differential between the clock and the probe B signal, divided by the size of the coincidence checking window. Because of the repetitive nature of the clock signal, the maximum possible differential time between the clock and the probe B signal will be just one period of the clock frequency, which is 667 nsec at 1.5 MHz. Consequently, the bounds for $N_1$ and $N_3$ become

$$N_1 \leq 34 \text{ counts}$$

$$N_3 \leq 34 \text{ counts}$$

Because of the fixed clock frequency for all speed levels, the maximum count of $N_2$ and $N_4$ will occur at 6000-rpm speed. The maximum count of $N_4$ will be dependent upon the number of clock pulses within one cycle of the probe B frequency and the number of probe cycles needed to achieve a coincidence. At 6000 rpm, there are 2498 cycles of clock pulse in one cycle of probe B frequency. Therefore, the maximum bound for $N_4$ becomes

$$N_4 \leq 84{,}932 \text{ counts}$$

To obtain the upper bound for $N_2$, the number of cycles of clock pulses during the maximum twist angle should be added to the upper bound of $N_4$. Thus the following relationship is obtained:

$$N_2 \leq 84{,}932 + 167 = 85{,}099 \text{ counts}$$

### The 375-kHz Clock

Should a slower clock frequency such as 375 kHz be selected, the upper bounds for $N_2$ and $N_4$ will remain about the same; however, the upper bounds for $N_1$ and $N_3$ will be increased. In the case of 375 kHz clock frequency, the new bounds are found to be

$N_1 \leq 134$ counts

$N_2 \leq 83{,}792$ counts

$N_3 \leq 134$ counts

$N_4 \leq 83{,}750$ counts

Using a slower clock allows a better resolution in $N_1$ and $N_3$ counts; on the other hand, it requires a longer time to achieve the coincidence. Reducing the clock frequency from 1.5 MHz to 375 kHz will require four times longer to accomplish a measured cycle.

Since the selected CP takes data in binary coded decimal (BCD) format, the size of the BCD counters needed for $N_2$ and $N_4$ will be five digits long, and the size needed for $N_1$ and $N_3$ will be two to three digits long, depending upon the clock frequency selected.

To allow for the possible skipping of coincidence detection due to the inadequate overlapping in actual signals and also to facilitate the design of data multiplexer for CP interface, the length for $N_1$ and $N_3$ is to be six digits. The clock frequency is determined to be 1.5 MHz.

## SENSING UNIT DESIGN

Two major design areas were performed: sensing unit electrical design and sensing unit mechanical design. In order to facilitate the testing, special designs that are part of the test functions were also performed.

### Sensing Unit Electrical Design

The electrical design of the sensing unit includes primarily the definition of the pickup output level desired, the selection of the pickup source and load impedances, the specification of the circuit time constant, and the determination of the output signal rise time that is actually achievable.

#### Magnetic Monopole Phase Pickups

Generally speaking, the higher the pickup output, the more desirable it becomes for the sensing unit application. An increased output from the pickup will not only improve the signal-to-noise ratio, but also will reduce the time required to reach a given triggering level (delay time). The output level is generally limited by the manufacturing and environmental tolerance considerations. For the present application, an output voltage of 100 v peak-to-peak under the rated condition is considered to be a practical choice.

Since the pickup is used as a voltage source, it is desirable to have a low source impedance and a high load impedance to realize the maximum voltage from the pickup. However, the source impedance is dependent on the number of turns per unit volume that are required to generate the desirable output level, and the load impedance depends on the amount of distributed cable capacitance that can be tolerated before causing extraneous oscillations in the output signal. A coil resistance of 300 ohms is typical for a pickup that will satisfy the requirements of the subject application. The typical value of the pickup load impedance has been determined experimentally to be around 1 MΩ. This value allows a reasonably small circuit time constant, yet produces almost 100-percent voltage output with a total distributed capacitance of 300 pf without causing excessive oscillations.

The time constant of the pickup circuit with an inductance of 100 mh and a load resistance of 1 MΩ is only 0.1 μsec. From preliminary research analysis and experiment, this time constant was found to contribute very little to the actual signal rise time, which is dominated primarily by the emf rise time of the flux-cutting action. The 0.1 μsec time constant from a coil with 100-mh inductance represents almost the minimum achievable value, since further reduction of this time constant would require an increase of the load resistance to a value such that the distributed capacitance might become influential.

### Eddy-Current Temperature Probes

Based on the results of the preliminary research phase of the program, the following electrical characteristics were established for the eddy-current probes to be used:

| | |
|---|---|
| Coil Inductance | 30 μh to 40 μh |
| Coil Q | 30 to 50 |
| Coil DC Resistance | 50 Ω to 100 Ω |

### Heater Elements

Heater elements should have enough power to heat up the sensing unit to 500°F steady-state temperature. It was estimated that a total of 1kw of electrical power would be needed. Consequently, two 500-watt heater elements were used to provide the temperature adjustment capability. These heater elements are not the regular components of the torque measurement system. They were incorporated in the design merely to facilitate the temperature tests.

## Sensing Unit Mechanical Design

The sensing unit mechanical design included the design of the phasing gear assembly, the provision of mounting posts for the installation of phase monopole pickups and temperature-sensing eddy-current probes, the design of the micrometer adjustment mechanism, and the design of the housing structure to incorporate the aforementioned functions.

Figure 41 shows the design of the test sensing unit. To accommodate testing at high speed and high temperature, the phasing gear is supported directly by the drive shaft. The phasing gear assembly is made of two parts: the gear body and the gear adapter shaft. This adapter shaft can be replaced by a smaller shaft to accept air-motor drive in case the electrical drive motor causes excessive noise interference on electronic logic circuits. Two heater elements can be attached to the unit for the temperature tests. These heater elements are capable of heating the entire test sensing unit to a temperature of more than 500°F. They can also be removed from the unit when performing the other tests, such as contamination and vibration tests. The twist angle is simulated by displacing one monopole pickup slightly with respect to the other pickup. Micrometer mechanisms are added to the test unit to allow for precision adjustment of twist angle up to a full scale of ten mechanical degrees. After a specific twist angle is selected, the micrometer set bolt will be used to prevent the angular setting from being changed by vibration. Thermal insulators are incorporated in the test unit to minimize the angular inaccuracy due to thermal expansion of the micrometer mechanism itself. A spring-loading design is used to furnish the needed pressure on the phasing arm to eliminate backlash and hysteresis that may occur during the twist angle setting.

The detailed construction and dimensions of the phasing gear assembly are shown in Figure 42. The dimensions of the phasing monopole pickups and the eddy-current temperature probes are shown in Figures 43 and 44, respectively. The air-motor drive design configuration and the electrical drive design configuration are shown in Figures 45 and 46, respectively.

## PROCESSOR DESIGN

Three major areas were performed for the processor design. These areas are (1) design of the coincidence interpolation and measurement logic, (2) selection of CP, and (3) design of CP interface and control.

### Design of Coincidence Interpolation and Measurement Logic

The coincidence interpolation and measurement logic circuit of the processor system is required to perform three functions. The first function is the generation of extremely narrow timing markers from the probe signals and the clock signal to achieve a coincidence resolution of the required value, i.e., 20 nsec. The second function is to check the coincidence of these timing markers. The third function is to properly register or measure the corresponding counts under different states of the coincidence condition.

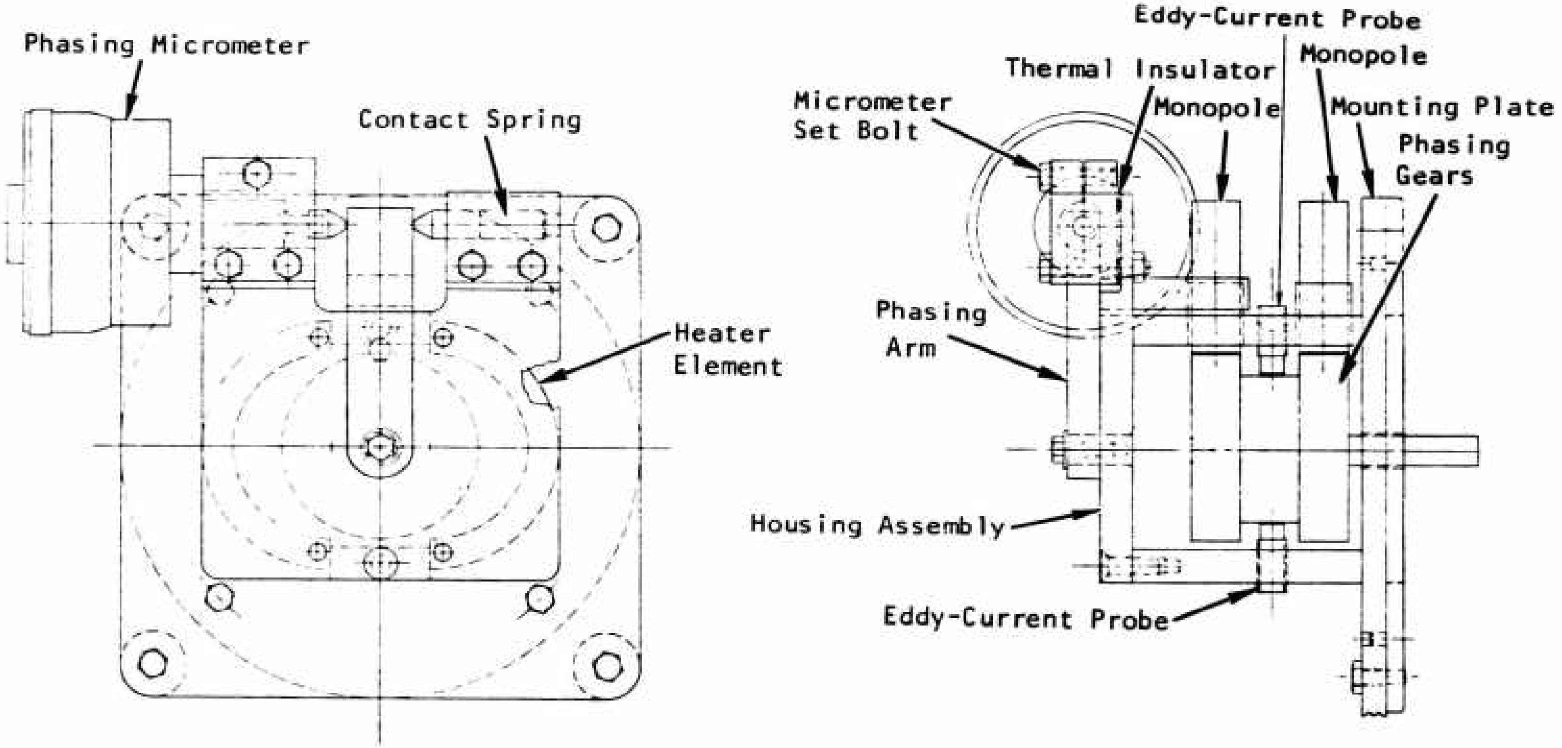

Figure 41. Test Sensing Unit Design.

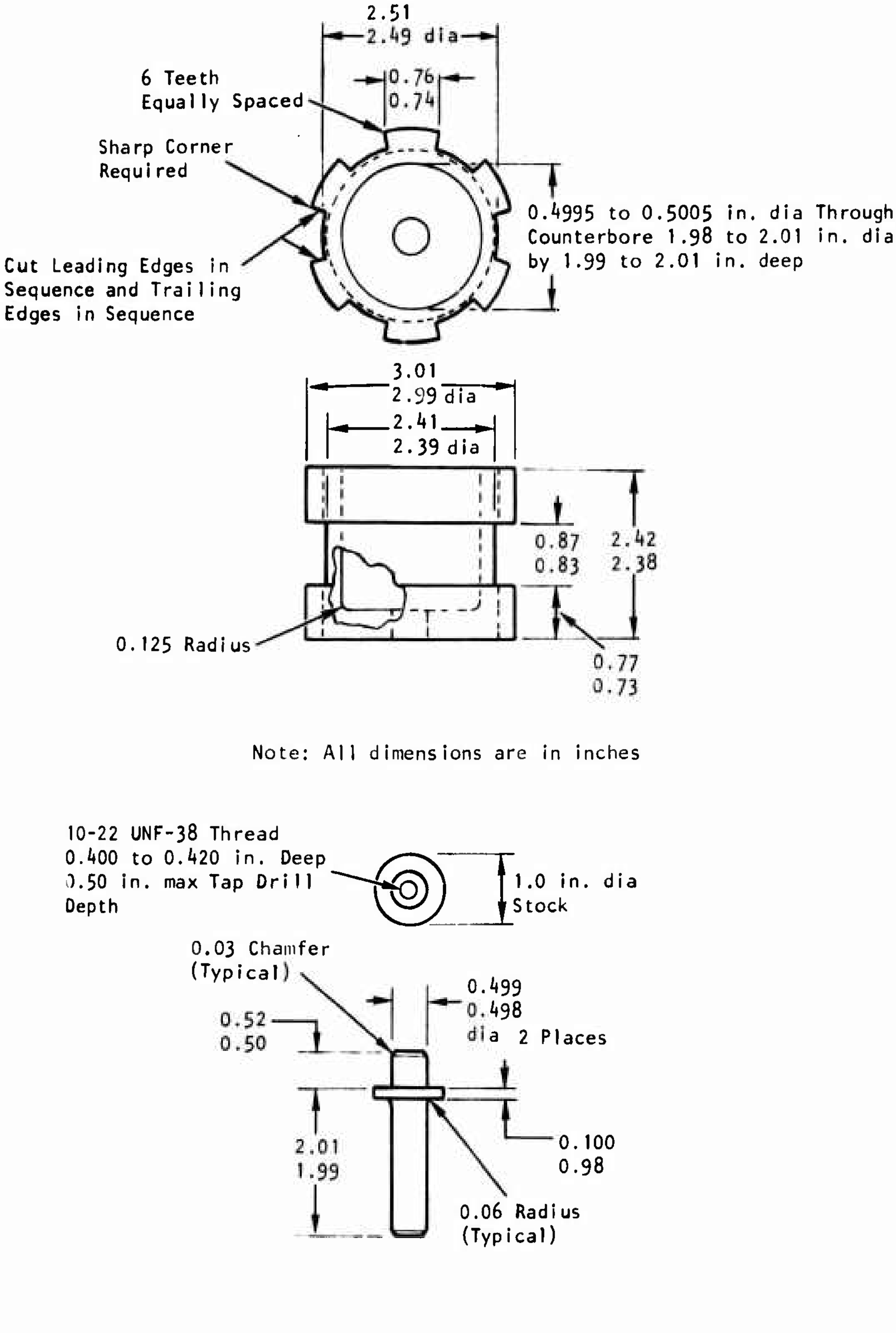

Note: All dimensions are in inches

Figure 42. Phasing Gear Assembly.

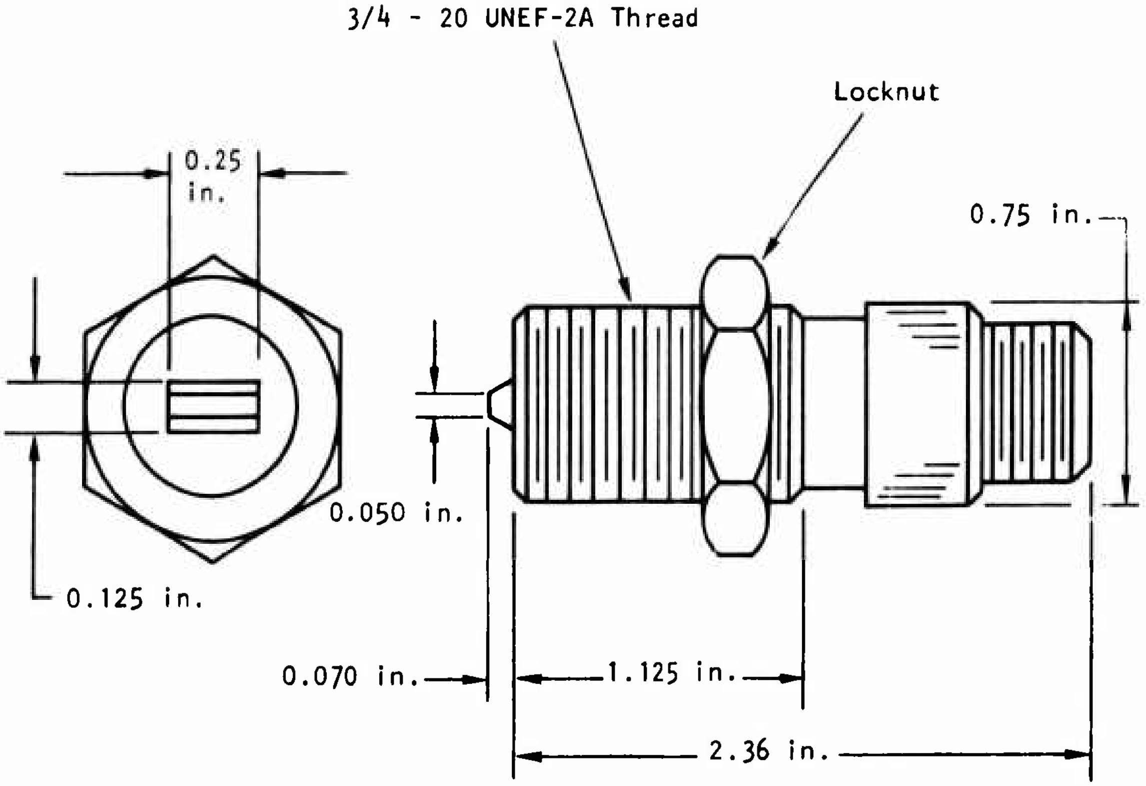

Figure 43. Modified AIRPAX Model 1-0046 Monopole Pickup.

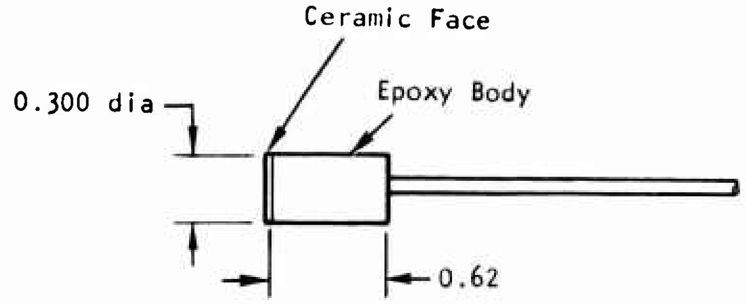

Bentley Nevada Model 314 Probe

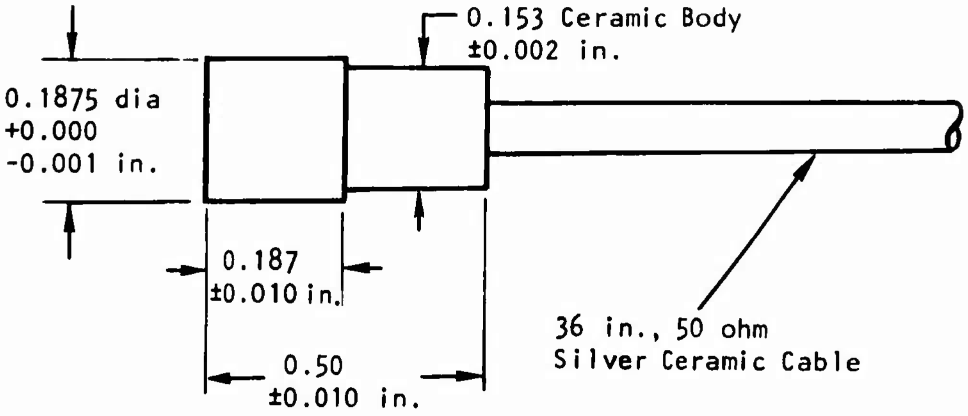

Bentley Nevada Model 306-3348 Probe

Figure 44. Dimensions of Eddy-Current Temperature Probes.

Note: All Dimensions are in Inches

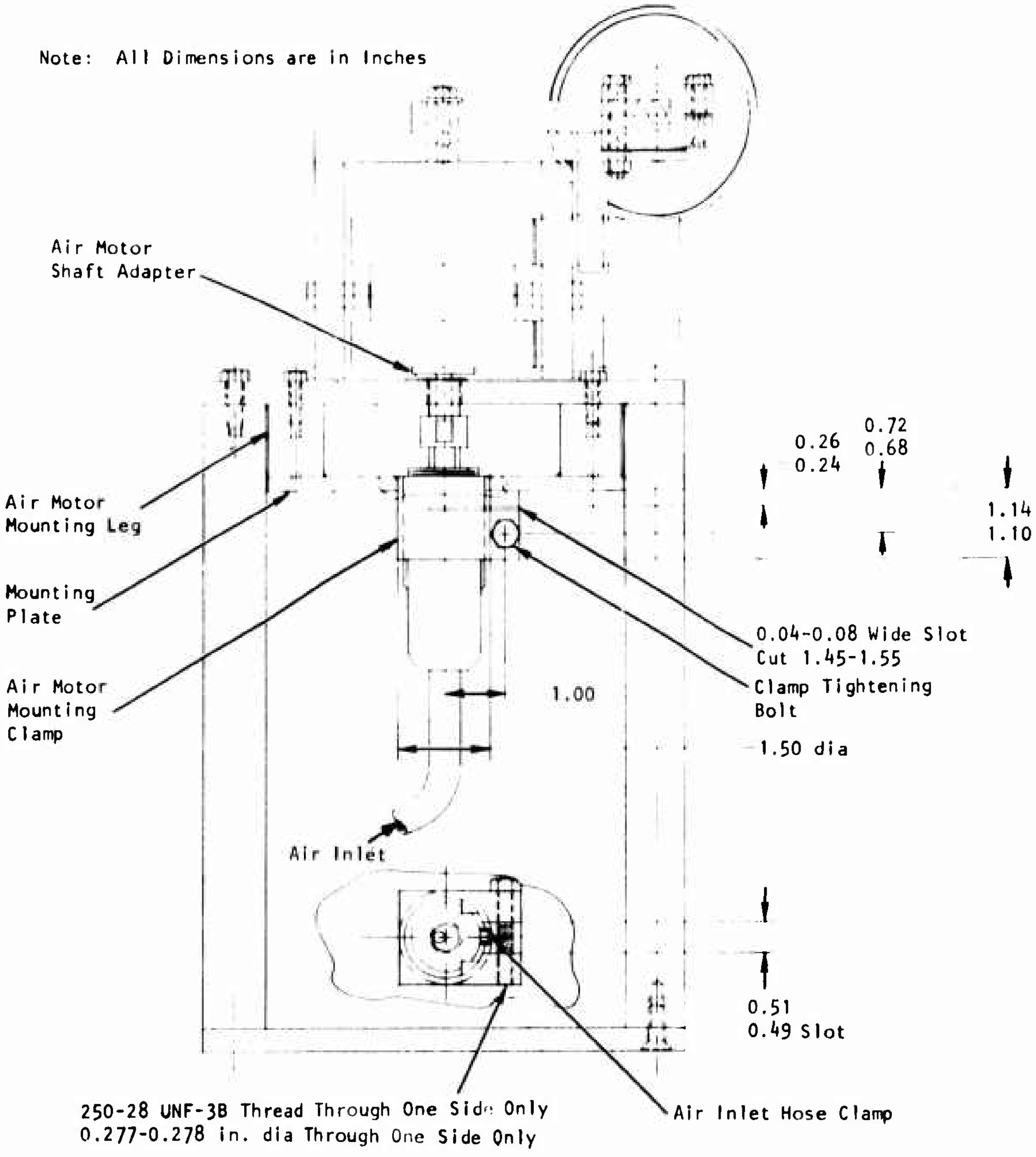

Figure 45. Design of Air Motor Drive.

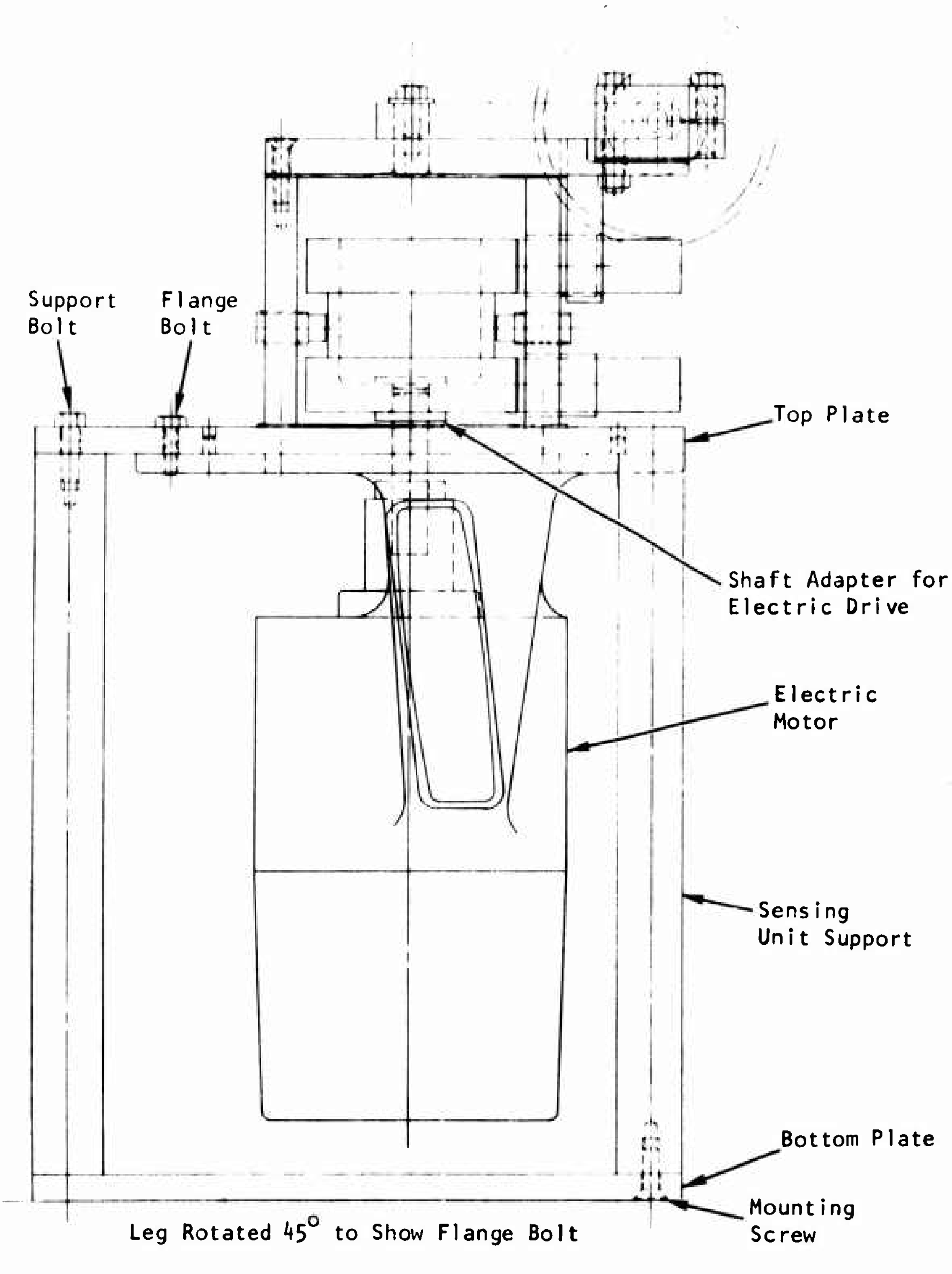

Figure 46. Design of Electrical Drive.

Figure 47 shows the design drawing of this coincidence interpolation and measurement logic. The narrow timing pulse is generated by the delay between the two signals arriving at the inputs of a 3-nsec, high-speed, NAND gate. The regular one-shot multivibrator cannot be used for this purpose because the narrowest pulse thus generated will be around 60 to 100 nsec, which is much wider than the required 20-nsec pulses. The coincidence detection is done by another high-speed NAND gate on inverted timing pulses. A pulse stretch circuit is used to allow the transition from the high-speed logic circuits to low-speed logic circuits. Two flip-flops and a coincidence status counter are used to control the proper measurement of $N_1$, $N_2$, $N_3$, and $N_4$. Upon receiving the "COMPUTATION READY" signal from the processor reset control logic, the coincidence status counter will be set to a ground state. After the detection of the first coincidence between the probe B signal and the clock, the coincidence status counter will advance one count. This output state signal will then be used to turn off the counting of $N_1$ and $N_2$ and to turn on the counting of $N_3$ and $N_4$. Upon detection of the second coincidence between probe B and the clock, the output state of the coincidence status counter again will advance one more count to a higher state. The counting of $N_3$ and $N_4$ will be terminated by the end state output. In the meantime, a "MEASUREMENT READY" signal is generated to initiate the computation by CP. The data registered in the four counters will be locked out for CP interrogation until cleared by the "COMPUTATION READY" reset signal generated by the CP reset control logic. A latch is employed to provide a memory of the detection of the coincidence between the probe A signal and the clock signal, as well as a means for resetting the measurement/computation cycle.

### Selection of CP

The CP selected is a calculator type I.C. Package manufactured by Texas Instruments and designed as TMS 0117 NC, Decimal Arithmetic Processor (DAP). This CP is essentially an electronic calculator with modifications to facilitate input/output interface and to speed up system operation. These modifications include the removal of the keyboard de-bouncing circuits associated with the calculators to speed up the processor cycle time; the addition of special operation codes (such as INCREMENT, DECREMENT, SHIFT RIGHT, SHIFT LEFT, and EXCHANGE OPERANDS) to allow more flexible processor operations; the provision of processor BUSY or READY signals for external interface; and the availability of a digit clock signal from the CP to allow synchronization of data input and output. Data input is entered into the machine serially in BCD format one digit at a time, with the MSD first through five terminals $A_1$, $A_2$, $A_3$, $A_4$, and $A_5$. The $A_5$-bit is used to identify whether the input is a data number or an operation code. Output is also expressed in BCD format and is available at four output pins, $S_A$, $S_B$, $S_C$, and $S_D$, in a digit-serial form. Output digits can be extracted at the corresponding digit time from $D_1$ to $D_{10}$. The CP BUSY/READY signal plus other status signals can be extracted at $D_{11}$ time from pins $S_E$, $S_F$, and $S_G$.

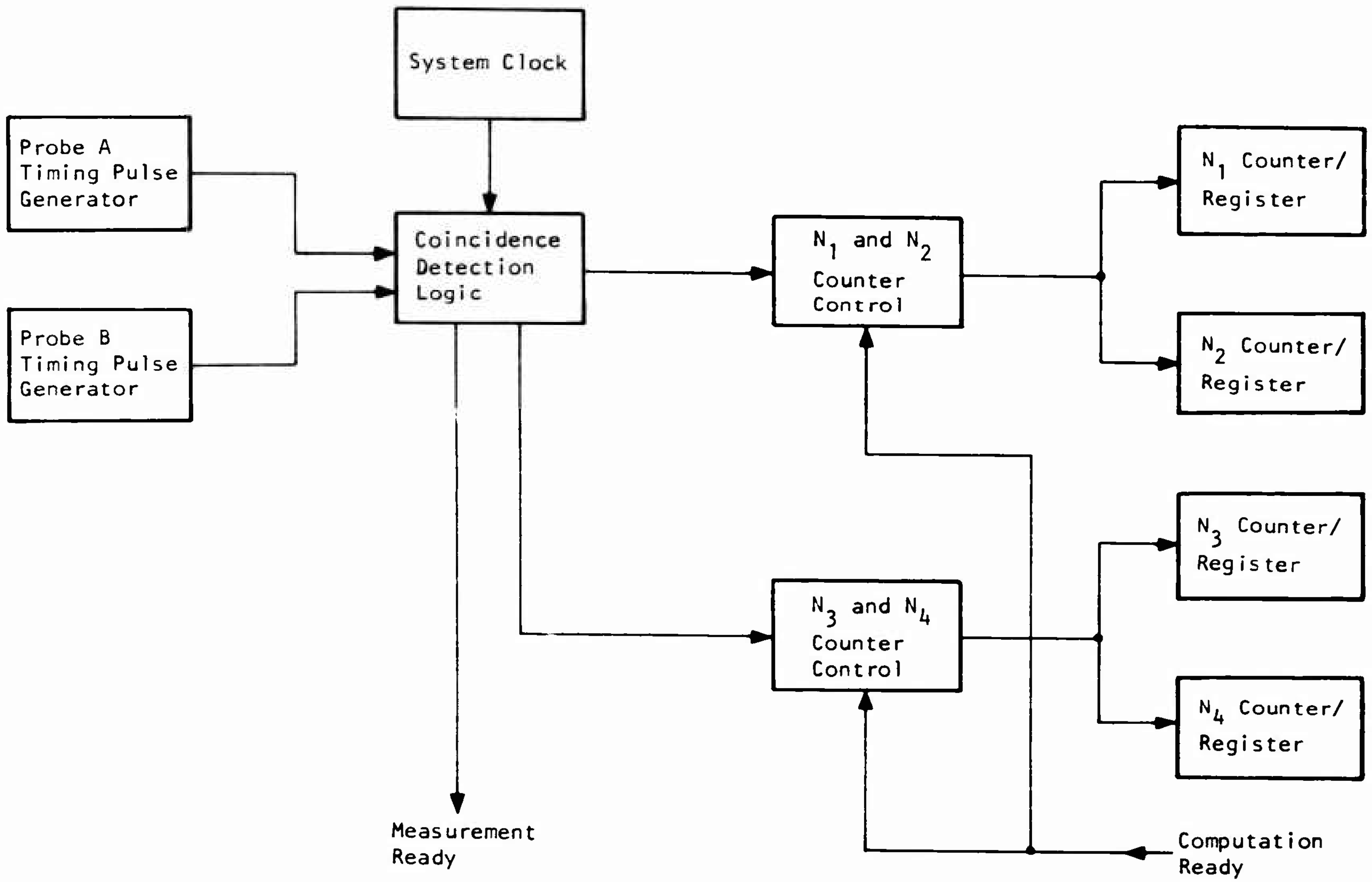

Figure 47. Coincidence Interpolation and Measurement Logic.

Table IX shows the set of operation instructions available from this processor. Table X shows the coding format of input data and operation codes. Table XI shows the coding format for output data and status signals.

TABLE IX. PROCESSOR INSTRUCTION SET

- CLEAR
- ADD
- SUBTRACT
- MULTIPLY
- DIVIDE
- EQUAL
- INCREMENT
- DECREMENT
- SHIFT RIGHT
- SHIFT LEFT
- EXCHANGE OPERANDS
- ADD TO OVERFLOW
- SUBTRACT TO ZERO

This calculator type of CP is most suitable for the subject application because of its low cost and simplicity in programming. The minicomputer type of CP was not selected because its price in general is much (20 to 200 times) higher and because of the excess capability that the subject application does not need.

### Design of CP Interface and Control

The interface of design of the CP for the subject application includes the data input control from phase and temperature measurement channels, the programming increment control of the CP operations, the CP enable control, the means to reset CP and measurement logic in case of CP error or counter overflow, and the system operation cycle control.

Figure 48 shows the design for the CP interfaces as discussed above. The input of data or operation codes will be selected by the use of three layers of digital multiplexers. These multiplexers will be controlled by the program instructions stored in the system programmer. Because of the requirements for selecting data input from two sources, and for treating the stored constant as data input, two additional bits are added to the machine code to provide these data selection and indirect addressing capabilities.

The system programming control will be done by two 4-bit program counters together with two 256 x 4-bit programmable read only memories (PROM). The program counter will be activated by the "MEASUREMENT READY" signal generated by the coincidence interpolation and measurement logic circuitry. At the end of computation, the CP will be left in a NO-OP state for a given period of time to allow the proper display of the computed result to the user. This display also can be held for an indefinite length of time by a manual request. After the given fixed display period or the removal of the manual request, the program counter will be set into an initial state ready for another measurement/computation cycle. A 64-bit, random-access memory (RAM) was also added to the design to provide an intermediate read-write storage, which will be needed in programming the CP to mechanize the torque computation.

The system operation cycle control will be performed by three networks: ENABLE CONTROL LOGIC, RESET CONTROL LOGIC, and PROGRAM COUNTER SYNCHRONIZATION AND CONTROL LOGIC. These three logic networks together will activate the measurement or computation cycle, generate the CP BUSY or READY signal, and control the system program cycling.

The operation of the CP is shown in Figure 49. The timing of the various controls associated with the CP operation is shown in Figure 50. The logic equations from which the controls are derived are given in Table XII.

## DESIGN OF PERIPHERAL ELECTRONIC CIRCUITS

This area of the program was to provide the designs of the miscellaneous electronic circuits that were needed in order to allow the overall processor system functioning. These design efforts included the design of system clock generator, the design of probe signal conditioner, the system power supply modifications, CP display decoder/driver circuit design, and the design of programming aid circuit to facilitate the software programming.

### Design of System Clock Generator

Figure 51 shows the design of the system clock generator. Two inverters out of a hex-inverter I.C. package are used as high gain amplifiers. The remaining four inverters can be used for other purposes. This clock generator is crystal controlled to ensure the stability and precision needed for the coincidence interpolation application. The output of the clock is fed into a frequency divider to provide 1/2, 1/4, 1/8, and 1/16 of the fundamental frequency. The 1/2 and 1/4 frequencies can be used for the clocking of the coincidence checking logic. The 1/16 frequency can be used as clock pulses for the CP.

### Design of Probe Signal Conditioner

A signal conditioner design that will provide a nonlinear circuit element to damp out the ringing signal in the monopole pickup, that will clip the negative half cycle of the signal, and that will prevent input signal level rising beyond the TTL limit is shown in Figure 52. In addition, this circuit will not saturate the output of the comparator due to charging effect of the input capacitor of the comparator. A potentiometer is provided to allow the adjustment of the triggering level of the comparator.

## TABLE X. INPUT CODING FORMAT

| | | (8) | (4) | (2) | (1) | |
|---|---|---|---|---|---|---|
| | $A_5$ | $A_4$ | $A_3$ | $A_2$ | $A_1$ | Number/Operation |
| Data | 0 | 0 | 0 | 0 | 0 | 0 |
| | 0 | 0 | 0 | 0 | 1 | 1 |
| | 0 | 0 | 0 | 1 | 0 | 2 |
| | 0 | 0 | 0 | 1 | 1 | 3 |
| | 0 | 0 | 1 | 0 | 0 | 4 |
| | 0 | 0 | 1 | 0 | 1 | 5 |
| | 0 | 0 | 1 | 1 | 0 | 6 |
| | 0 | 0 | 1 | 1 | 1 | 7 |
| | 0 | 1 | 0 | 0 | 0 | 8 |
| | 0 | 1 | 0 | 0 | 1 | 9 |

0 = Key open, Transistor off or TTL Logic 1
1 = Key closed Transistor on or TTL Logic 0

| | $A_5$ | $A_4$ | $A_3$ | $A_2$ | $A_1$ | Number/Operation |
|---|---|---|---|---|---|---|
| OP Code | 1 | 0 | 0 | 0 | 0 | CLEAR |
| | 1 | 0 | 0 | 0 | 1 | = |
| | 1 | 0 | 0 | 1 | 0 | X |
| | 1 | 0 | 0 | 1 | 1 | ÷ |
| | 1 | 0 | 1 | 0 | 0 | + |
| | 1 | 0 | 1 | 0 | 1 | ADD ONE |
| | 1 | 0 | 1 | 1 | 0 | − |
| | 1 | 0 | 1 | 1 | 1 | SUBTRACT ONE |
| | 1 | 1 | 0 | 0 | 0 | ADD ONE TO OVERFLOW |
| | 1 | 1 | 0 | 0 | 1 | SUBTRACT ONE TO ZERO |
| | 1 | 1 | 0 | 1 | 0 | SHIFT RIGHT |
| | 1 | 1 | 0 | 1 | 1 | SHIFT LEFT |
| | 1 | 1 | 1 | 0 | 0 | EXCHANGE OPERANDS |
| | 1 | 1 | 1 | 0 | 1 | NO OP |
| | 1 | 1 | 1 | 1 | 0 | |
| | 1 | 1 | 1 | 1 | 1 | |

0 = Key open, Transistor off or TTL Logic 1
1 = Key Closed Transistor on or TTL Logic 0

## TABLE XI. OUTPUT CODING FORMAT

The numerical output data is extracted during $D_1$ through $D_{10}$.

| | $S_A$ | $S_B$ | $S_C$ | $S_D$ | $S_E$ | $S_F$ | $S_G$ | Digit |
|---|---|---|---|---|---|---|---|---|
| | 0 | 0 | 0 | 0 | 0 | 0 | 0 | 0 |
| | 0 | 0 | 0 | 1 | 0 | 0 | 0 | 1 |
| Data | 0 | 0 | 1 | 0 | 0 | 0 | 0 | 2 |
| | 0 | 0 | 1 | 1 | 0 | 0 | 0 | 3 |
| | 0 | 1 | 0 | 0 | 0 | 0 | 0 | 4 |
| | 0 | 1 | 0 | 1 | 0 | 0 | 0 | 5 |
| | 0 | 1 | 1 | 0 | 0 | 0 | 0 | 6 |
| | 0 | 1 | 1 | 1 | 0 | 0 | 0 | 7 |
| | 1 | 0 | 0 | 0 | 0 | 0 | 0 | 8 |
| | 1 | 0 | 0 | 1 | 0 | 0 | 0 | 9 |

Status data is extracted during $D_{11}$ time.

| | $S_A$ | $S_B$ | $S_C$ | $S_D$ | $S_E$ | $S_F$ | $S_G$ | |
|---|---|---|---|---|---|---|---|---|
| Status | 0 | 0 | 0 | 0 | 1 | X | 0 | BUSY |
| | 0 | 0 | 0 | 0 | 0 | X | 0 | READY |
| | 0 | 0 | 0 | 0 | 0 | 0 | 0 | SIGN POSITIVE |
| | 0 | 0 | 0 | 0 | 0 | 1 | 0 | SIGN NEGATIVE |
| | 0 | 0 | 0 | 0 | X | X | 1 | ERROR MUST RESET |
| | | | | | BUSY READY | SIGN | ERROR | |

0 = Output not conducting

1 = Output conducting to $V_{SS}$

X = Either 0 or 1

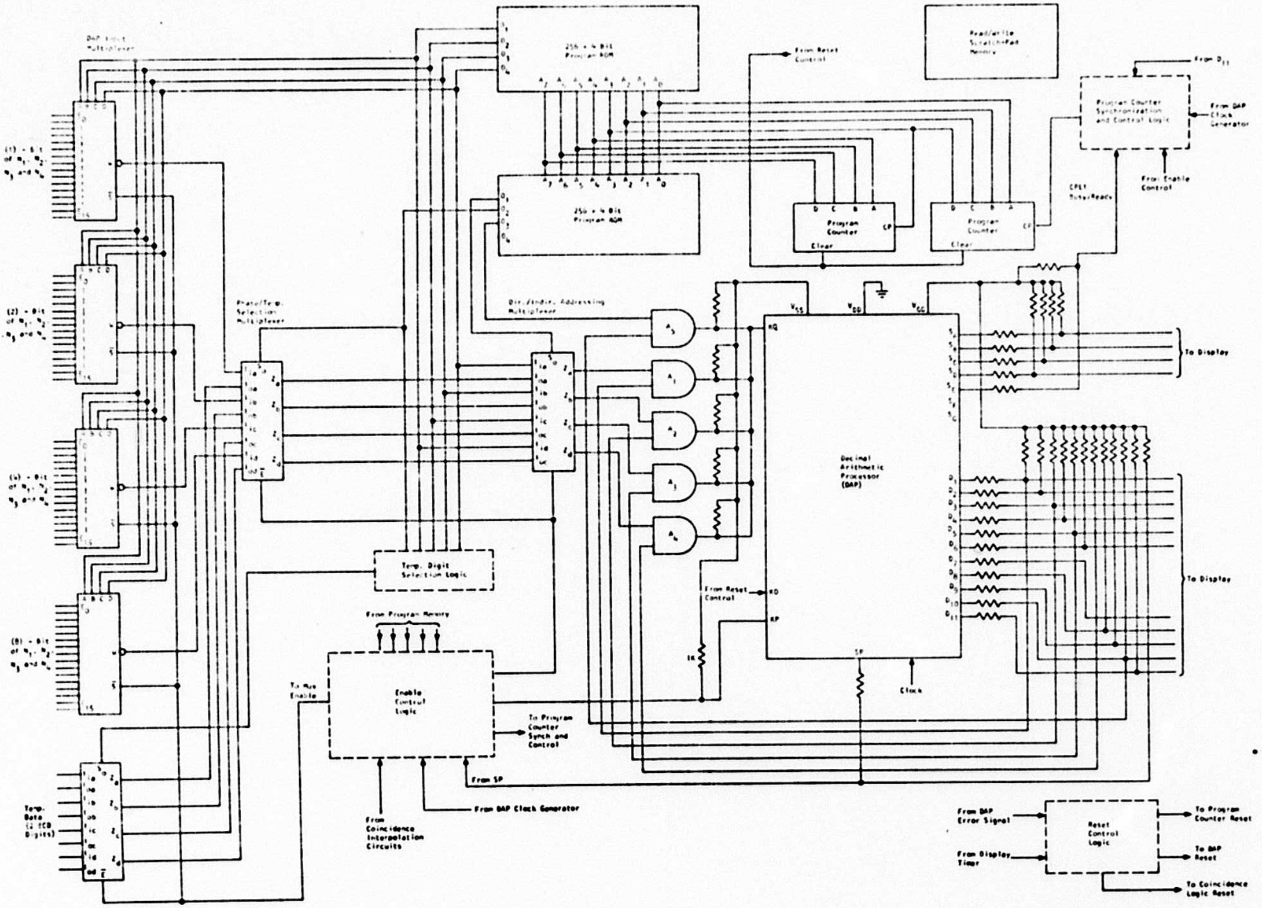

Figure 48. CP Interface and Controls.

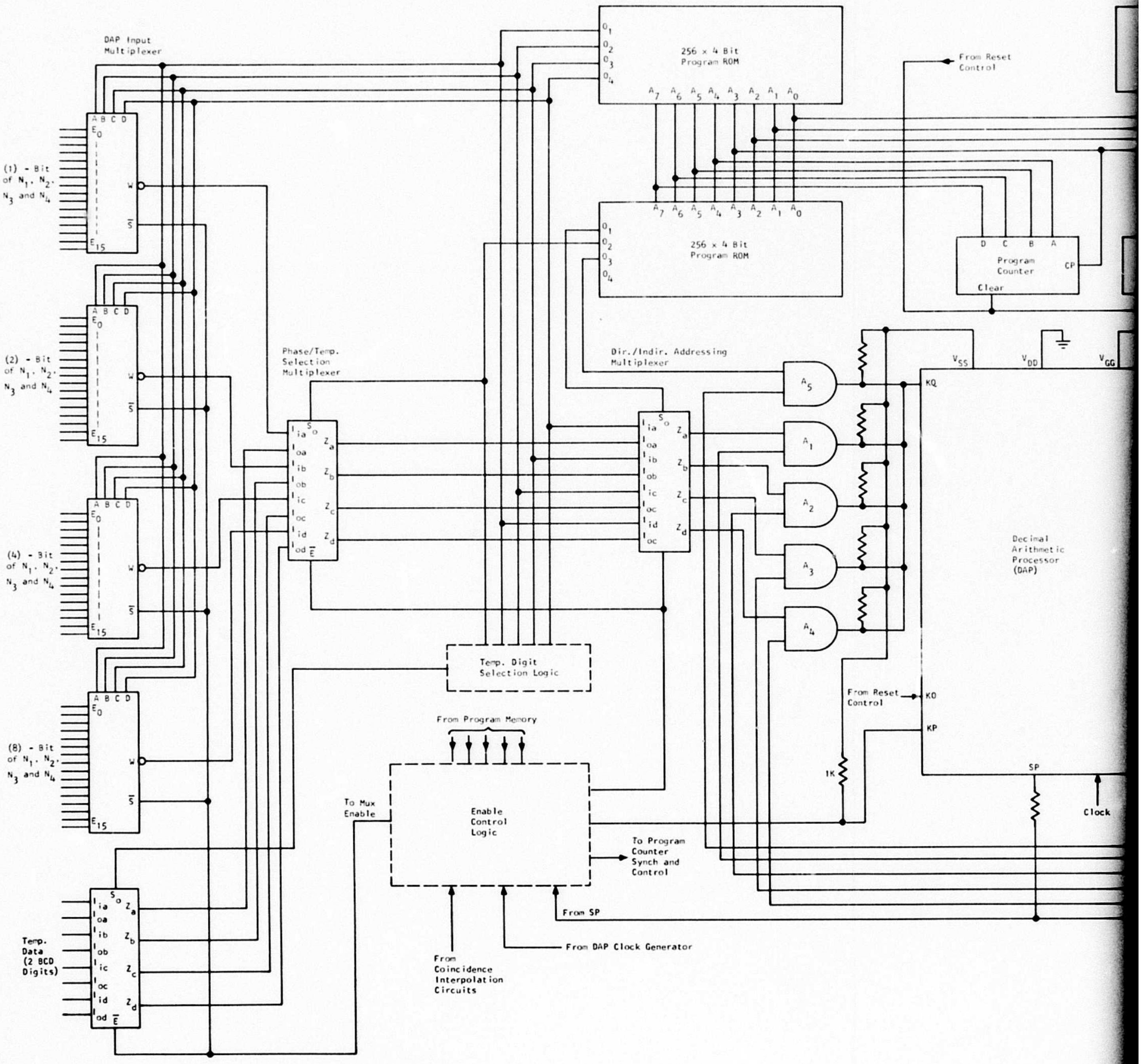

Figure 48. CP Interface and Controls.

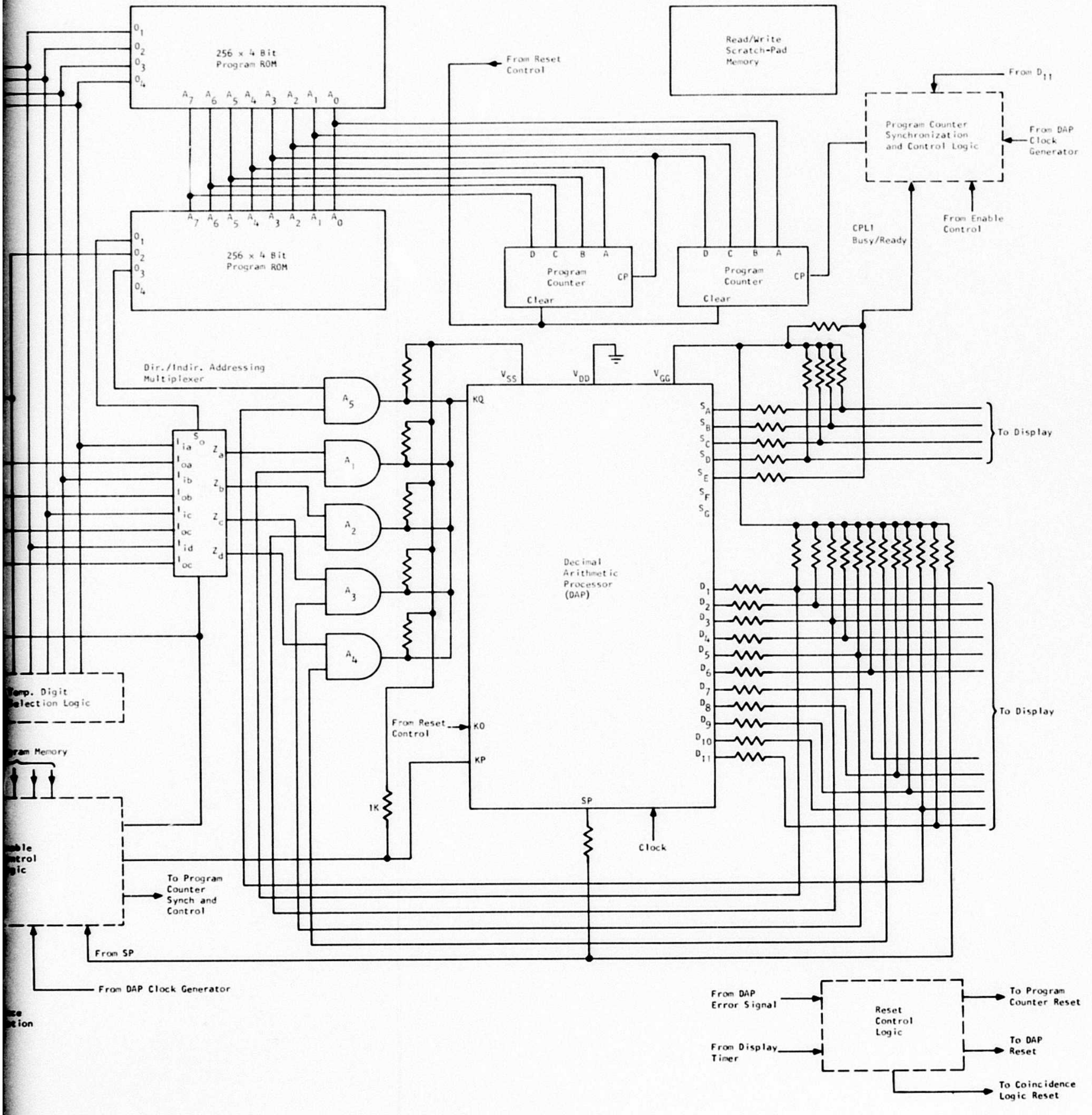
256 x 4 Bit Program ROM
$O_1$ $O_2$ $O_3$ $O_4$
$A_7$ $A_6$ $A_5$ $A_4$ $A_3$ $A_2$ $A_1$ $A_0$
256 x 4 Bit Program ROM
Read/Write Scratch-Pad Memory
From Reset Control
From $D_{11}$
Program Counter Synchronization and Control Logic
From DAP Clock Generator
From Enable Control
CPL1 Busy/Ready
D C B A
Program Counter
CP
Clear
Program Counter
Dir./Indir. Addressing Multiplexer
$A_5$ $A_1$ $A_2$ $A_3$ $A_4$
$S_0$
$I_{ia}$ $I_{oa}$ $I_{ib}$ $I_{ob}$ $I_{ic}$ $I_{oc}$ $I_{id}$ $I_{oc}$
$Z_a$ $Z_b$ $Z_c$ $Z_d$
$V_{SS}$ $V_{DD}$ $V_{GG}$
KQ
KO
KP
SP
Decimal Arithmetic Processor (DAP)
$S_A$ $S_B$ $S_C$ $S_D$ $S_E$ $S_F$ $S_G$
To Display
$D_1$ $D_2$ $D_3$ $D_4$ $D_5$ $D_6$ $D_7$ $D_8$ $D_9$ $D_{10}$ $D_{11}$
To Display
From Reset Control
1K
Clock
mp. Digit election Logic
ram Memory
ble ntrol ic
To Program Counter Synch and Control
From SP
From DAP Clock Generator
ce tion
From DAP Error Signal
From Display Timer
Reset Control Logic
To Program Counter Reset
To DAP Reset
To Coincidence Logic Reset

**nd Controls.**

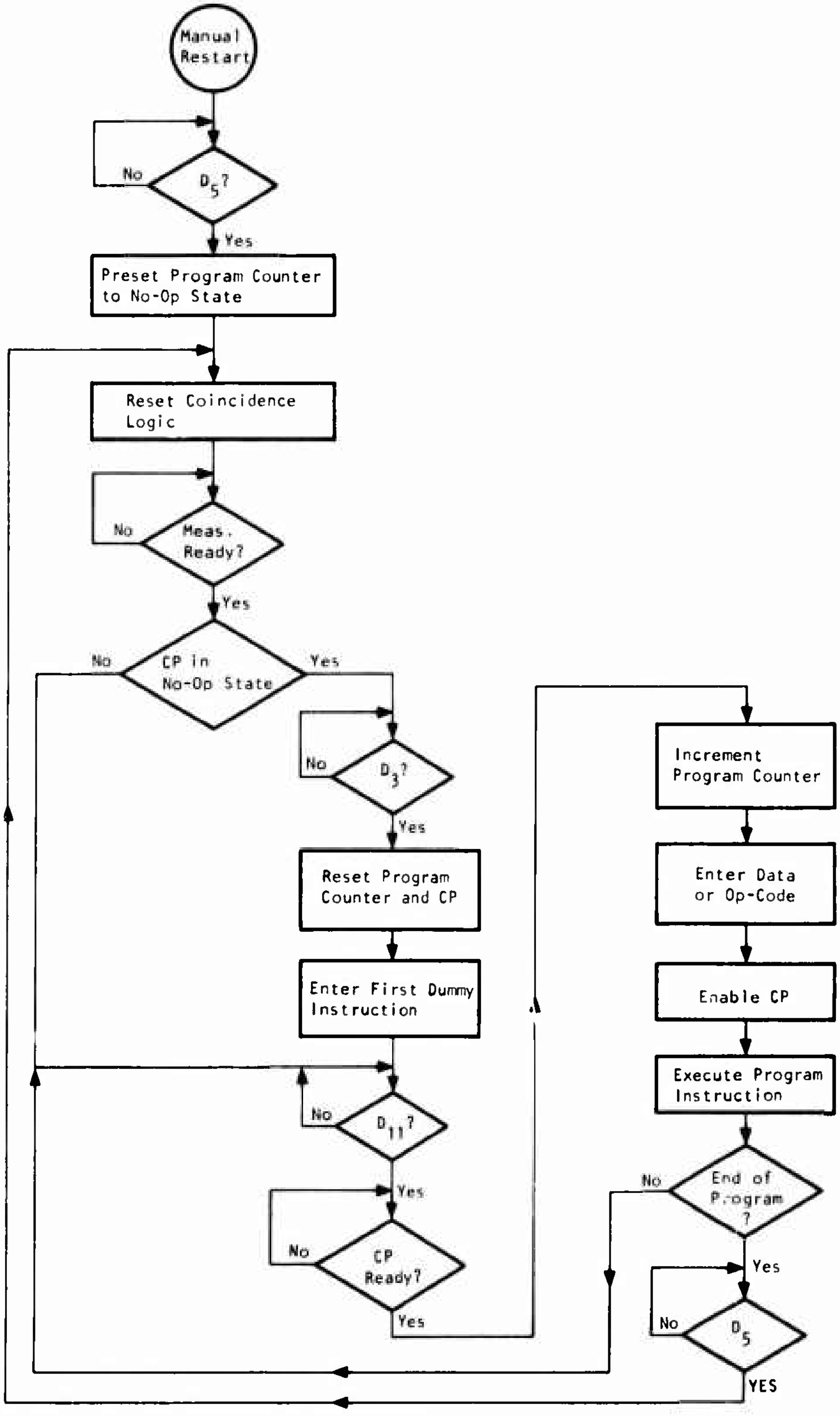

Figure 49. System Operation Flow Diagram of CP.

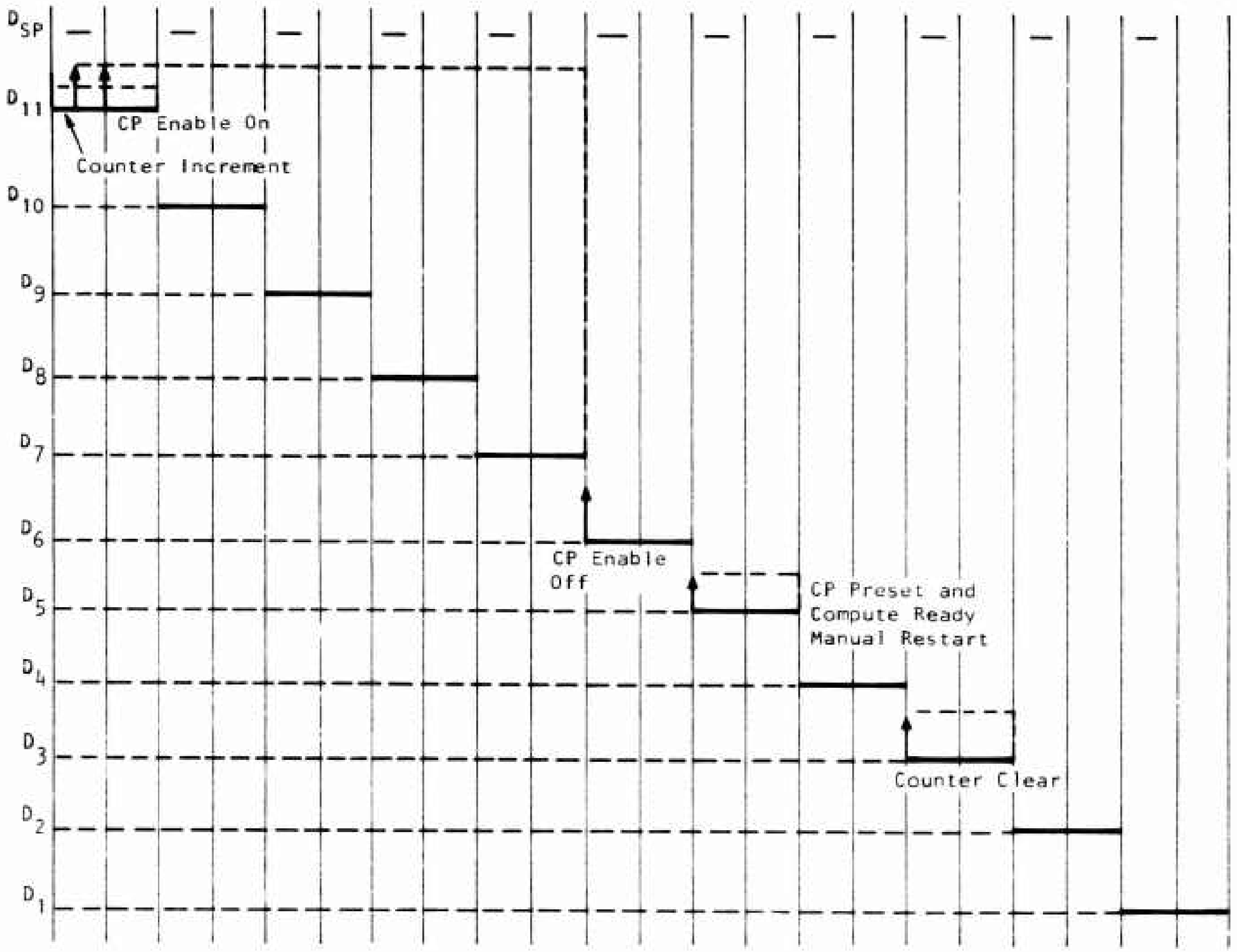

Figure 50. CP Control Timing Diagram.

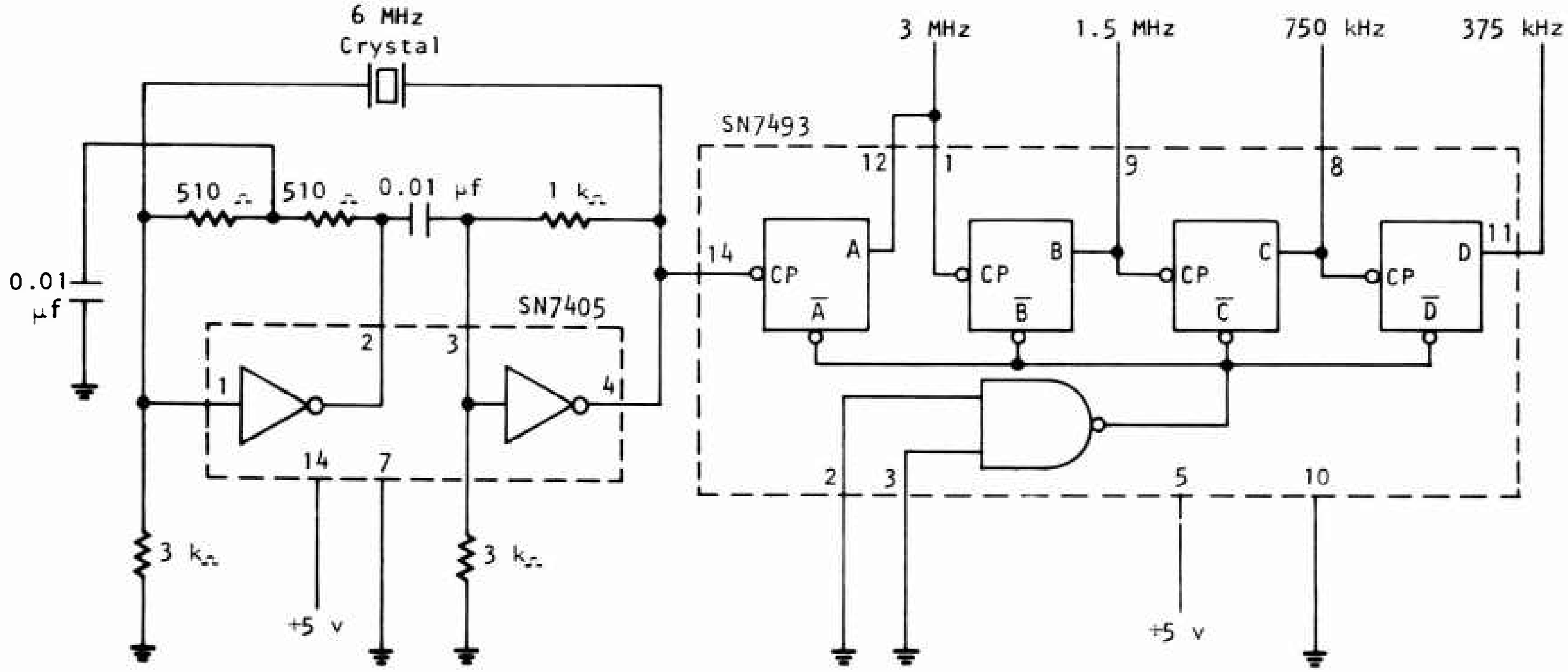

Figure 51. System Clock Generator.

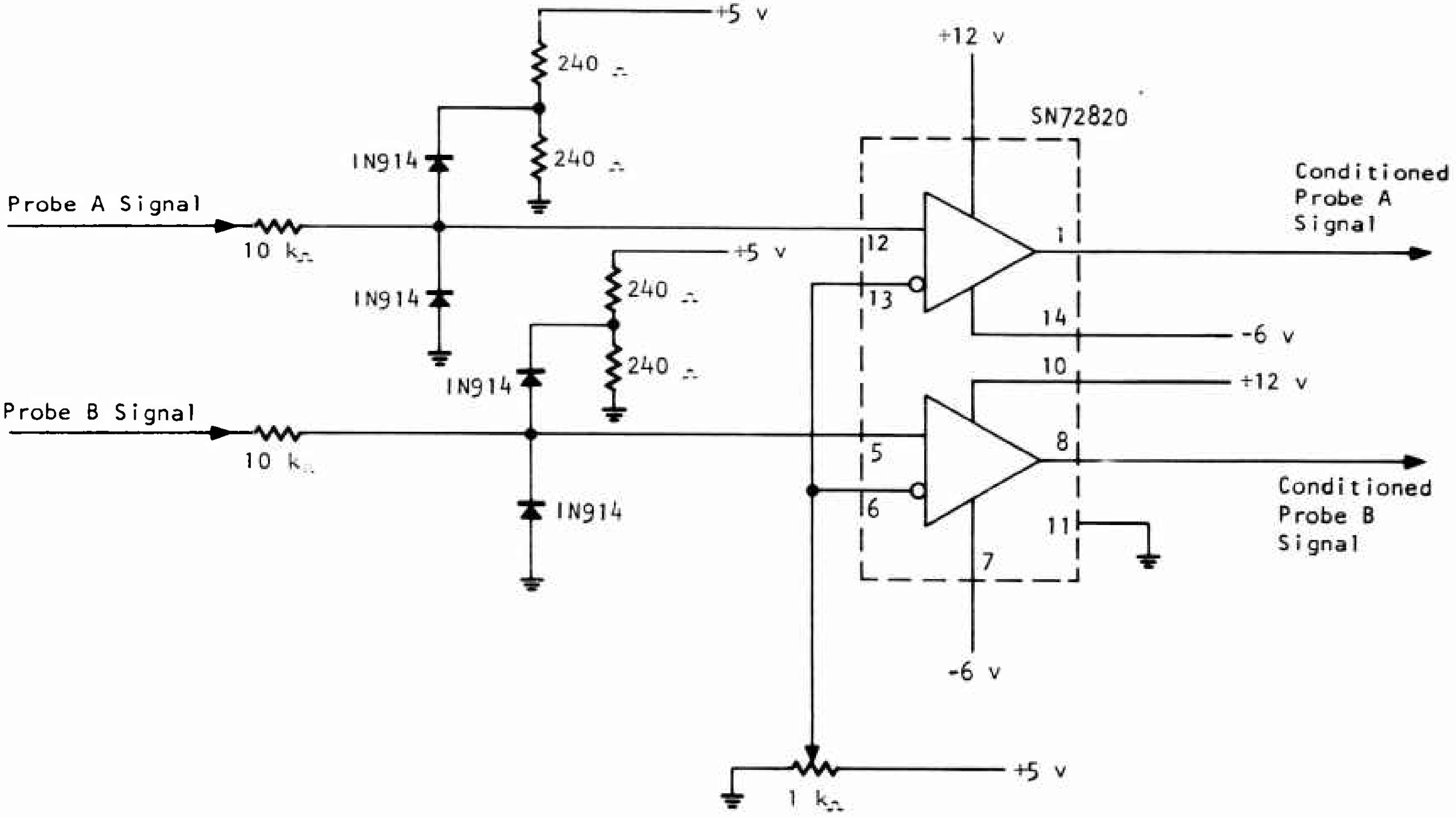

Figure 52. Design of Probe Signal Conditioning Unit.

TABLE XII. LOGIC EQUATIONS FOR CP CONTROLS

| | CP Control | Logic Equation |
|---|---|---|
| 1. | Program Counter Preset | $D_5$ (End of Program) + (Manual Restart) + (CP Err) + (Overflow) |
| 2. | CP Reset/Program Counter Clear | (Measurement Ready) (End of Program) $D_3$ |
| 3. | Program Counter Increment | $D_{11}$ (CP Ready) (Measurement Ready) $\cdot\overline{\text{(End of Program)}}$ |
| 4. | CP Enable | $D_{11}$ $D_{sp}$ (CP Ready) (Measurement Ready) $\cdot\overline{\text{(RAM Write)}}$ $\overline{\text{(Enable Skip)}}$ |

## System Power Supply Modifications

The main system power supply is the RO Associates Model 105 high efficiency power supply which provides the +5 vdc voltage for all TTL packages. The +12 v and ±7 vdc voltages needed by the comparator and the CP are obtained through a modified Servatron Model SE12D100 module. Figure 53 shows the modified circuitry. The power supply needed for the fluorescent display is a full-wave rectifier from a transistor transformer. This circuit is shown in Figure 54.

## CP Display Design

In order to allow larger character size with low cost display devices, the Model DG12-C fluorescent 7-segment display tube manufactured by ISE was selected. These types of display tubes require a filament supply of 0.85 v as well as a plate supply of 40 v. However, because of possible use of non-filtered and nonregulated voltage, the additional power supply does not impose a significant limitation on their application. The display design is shown in Figure 55.

## System Programmer

A programming aid was also designed to allow the manual incrementing of CP instructions during the software programming phase of the system development. Figure 56 shows the circuit design of this manual programmer.

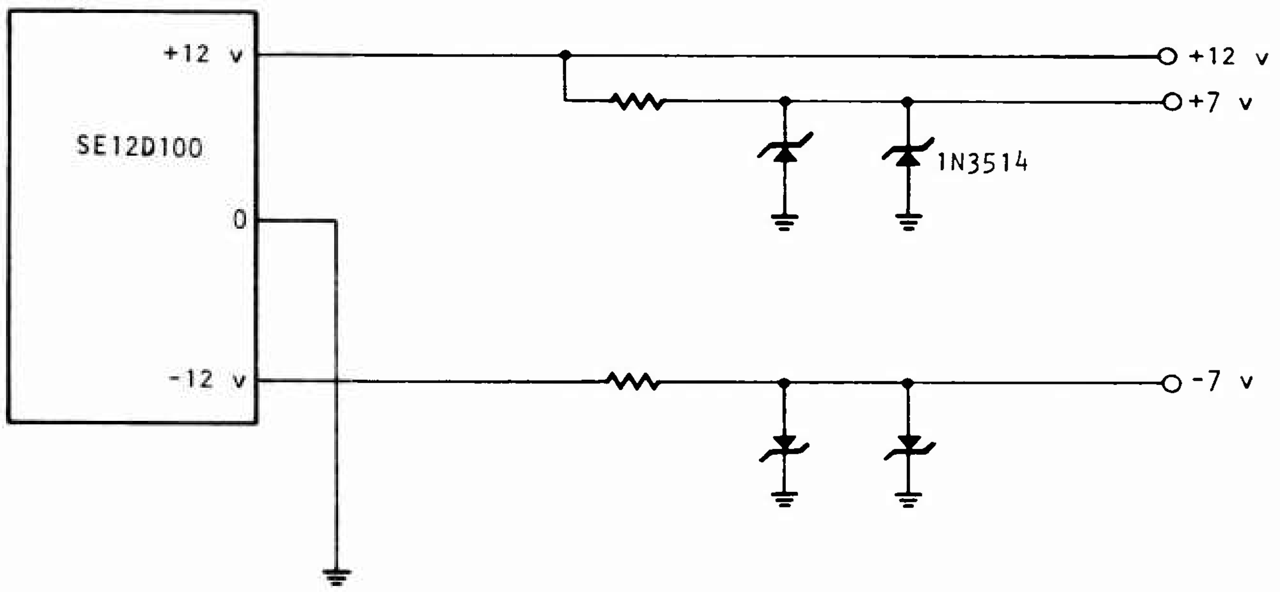

Figure 53. Modified Power Supply.

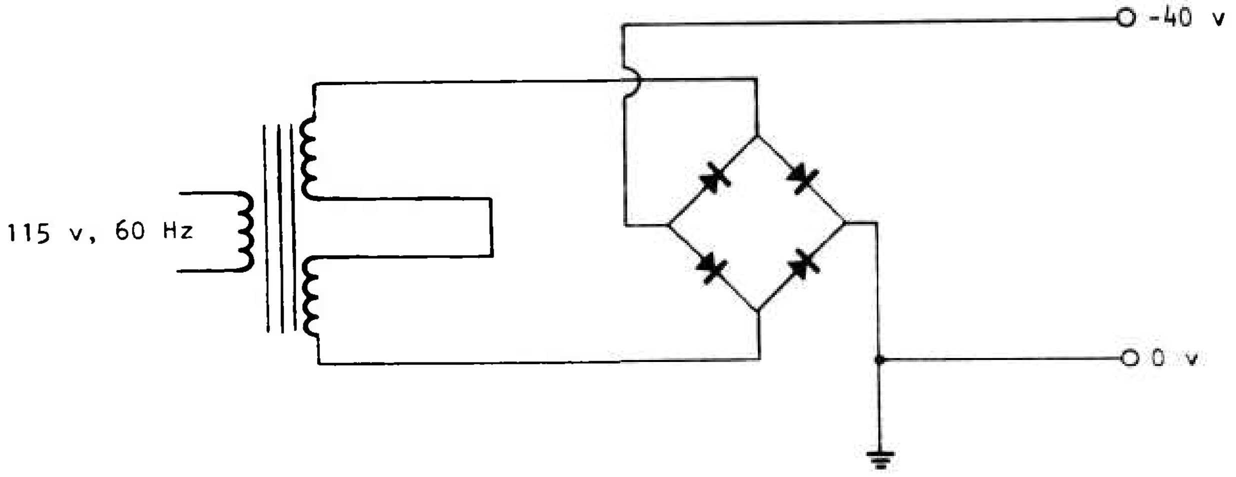

Figure 54. Power Supply for Fluorescent Display Tubes.

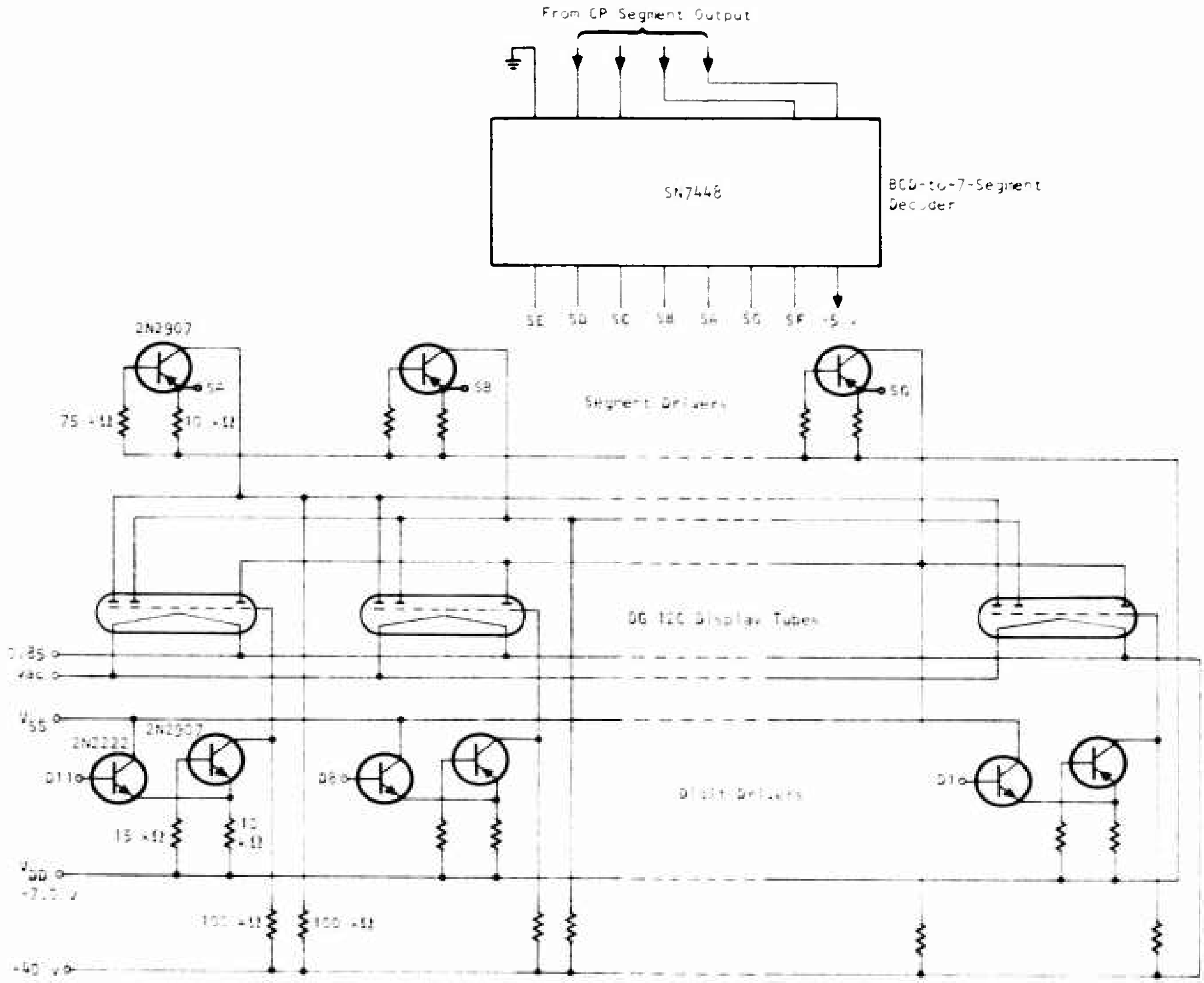

Figure 55. Display Decoder and Drivers.

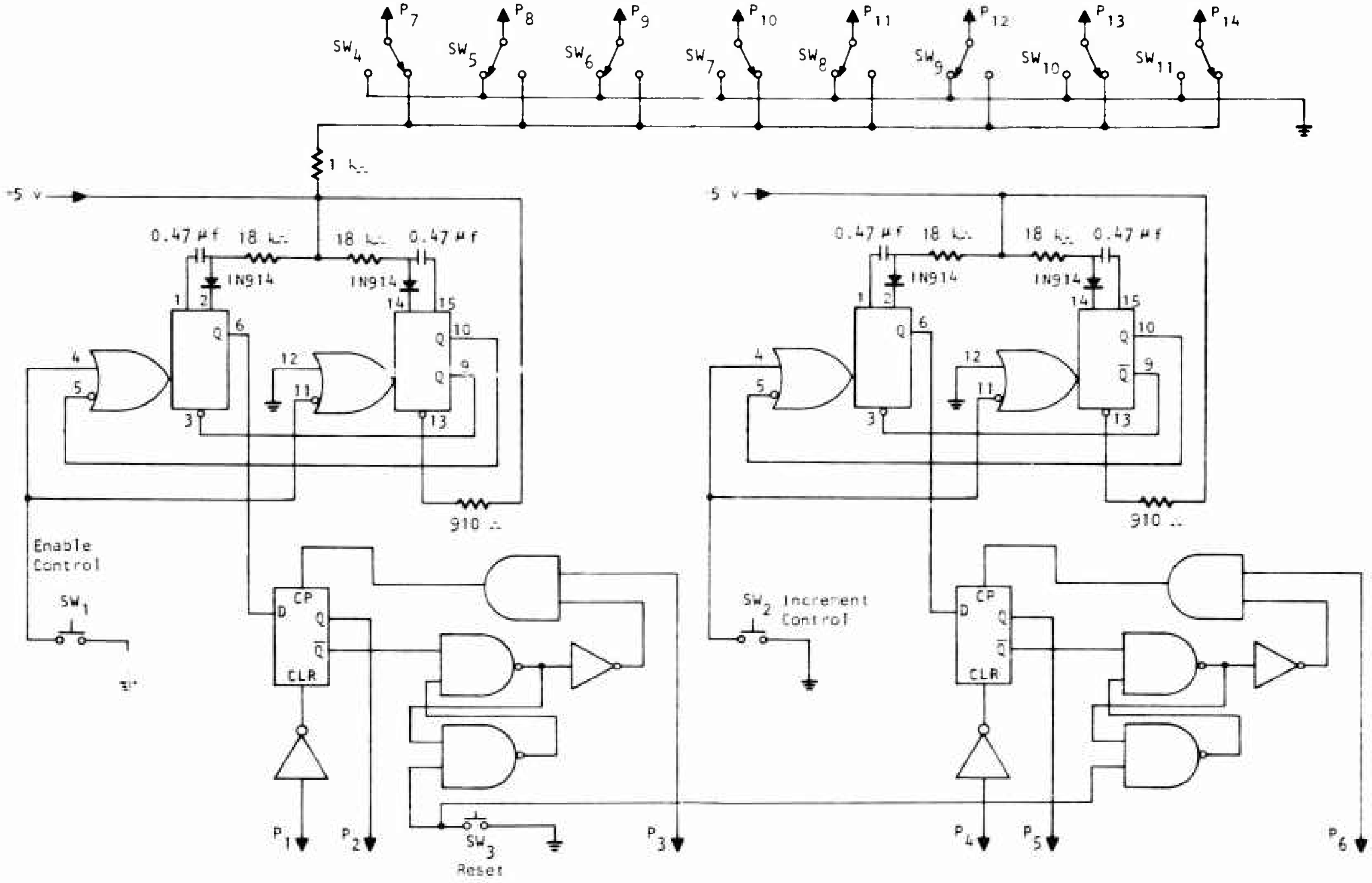

Figure 56. Programming Aid.

## SYSTEM SOFTWARE PROGRAMMING

Four areas of software programming efforts were performed. They are the programming for the computation of twist angle $\theta$, the programming for temperature compensation on modulus of rigidity changes, the programming that allows the selection of any of the three scale factors corresponding to the three torque-speed ranges, and the programming for digital integration of the data points to reduce the effect of transitory noise interference on the system output. The machine language system codes are defined in Table XIII. The complete machine language software program is given in Table XIV. Because of the interferences existing in the programming part that facilitates the selection of the individual scale factor according to the torque-speed ranges, the programmable-read-only-memory (PROM) chips that are used to store these software programs were not burned during the program.

TABLE XIII. SYSTEM PROGRAMMING CODES

| | Programming Instruction | Machine Code | Remarks |
|---|---|---|---|
| 1. | End-of-program mark | 11110101 | - |
| 2. | Preset dummy instruction | 11110101 | - |
| 3. | RAM write | abcdX011 | abcd RAM address |
| 4. | RAM read | abcdX000 | abcd RAM address |
| 5. | Input phase data | ABCD1X10 | ABCD Phase data MUX address |
| 6. | Input temperature data | TXXX0X10 | T = 1 for first digit<br>T = 0 for second digit |
| 7. | Input PROM constant | $C_1C_2C_3C_4$X100 | $C_1C_2C_3C_4$ = PROM constant |
| 8. | CP operations | $P_1P_2P_3P_5$0101 | $P_1P_2P_3P_4$ DAP operational code |
| 9. | Initiate enable skip | 10111101 | |

NOTE: 1 = TTL high, 0 = TTL low

X = Don't care

abcd, ABCD, T, $C_1C_2C_3C_4$, $P_1P_2P_3P_4$ are binary numbers

## TABLE XIV. SYSTEM PROGRAM

| Instruction Number | Program Instruction | Machine Code | Program Counter Address |
|---|---|---|---|
| 1 | Counter preload | 11110101 | 11111111 |
| 2 | CP and counter reset | 01110101 | 00000000 |
| 3 | Buffering instruction | 01110101 | 10000000 |
| 4 | Enter $N_{2-5}$ | 01101110 | 01000000 |
| 5 | Enter $N_{2-4}$ | 10101110 | 11000000 |
| 6 | Enter $N_{2-3}$ | 00101110 | 00100000 |
| 7 | Enter $N_{2-2}$ | 11001110 | 10100000 |
| 8 | Enter $N_{2-1}$ | 01001110 | 01100000 |
| 9 | Shift left | 11010101 | 11100000 |
| 10 | Shift left | 11010101 | 00010000 |
| 11 | Shift left | 11010101 | 10010000 |
| 12 | Shift left | 11010101 | 01010000 |
| 13 | Shift left | 11010101 | 11010000 |
| 14 | CP divide | 11000101 | 00110000 |
| 15 | Enter $N_{4-5}$ | 01111110 | 10110000 |
| 16 | Enter $N_{4-4}$ | 10111110 | 01110000 |
| 17 | Enter $N_{4-3}$ | 00111110 | 11110000 |
| 18 | Enter $N_{4-2}$ | 11011110 | 00001000 |
| 19 | Enter $N_{4-1}$ | 01011110 | 10001000 |
| 20 | CP multiply | 01000101 | 01001000 |
| 21 | Enter $N_{3-2}$ | 10011110 | 11001000 |
| 22 | Enter $N_{3-1}$ | 00011110 | 00101000 |
| 23 | CP subtract | 01100101 | 10101000 |
| 24 | Enter $N_{1-2}$ | 10001110 | 01101000 |
| 25 | Enter $N_{1-1}$ | 00001110 | 11101000 |
| 26 | Shift left | 11010101 | 00011000 |
| 27 | Shift left | 11010101 | 10011000 |
| 28 | Shift left | 11010101 | 01011000 |
| 29 | Shift left | 11010101 | 11011000 |
| 30 | Shift left | 11010101 | 00111000 |

## TABLE XIV - Continued

| Instruction Number | Program Instruction | Machine Code | Program Counter Address |
|---|---|---|---|
| 31 | CP Add | 00100101 | 10111000 |
| 32 | Enter constant 1 | 10001100 | 01111000 |
| 33 | Shift left | 11010101 | 11111000 |
| 34 | Shift left | 11010101 | 00000100 |
| 35 | Shift left | 11010101 | 10000100 |
| 36 | Shift left | 11010101 | 01000100 |
| 37 | Shift left | 11010101 | 11000100 |
| 38 | CP multiply | 01000101 | 00100100 |
| 39 | Enter const. 6 | 01101100 | 10100100 |
| 40 | Shift left | 11010101 | 01100100 |
| 41 | CP add | 00100101 | 11100100 |
| 42 | RAM read $\theta_{-6}$ | 10101000 | 00010100 |
| 43 | RAM read $\theta_{-5}$ | 00101000 | 10010100 |
| 44 | RAM read $\theta_{-4}$ | 11001000 | 01010100 |
| 45 | RAM read $\theta_{-3}$ | 01001000 | 11010100 |
| 46 | RAM read $\theta_{-2}$ | 10001000 | 00110100 |
| 47 | RAM read $\theta_{-1}$ | 00001000 | 10110100 |
| 48 | CP divide | 11000101 | 01110100 |
| 49 | Enter const. 2 | 01001100 | 11110100 |
| 50 | Enter const. 0 | 00001100 | 00001100 |
| 51 | CP multiply | 01000101 | 10001100 |
| 52 | RAM write $D_{11}$ | 00011011 | 01001100 |
| 53 | RAM write $\theta_{-6}$ | 10111011 | 1 001100 |
| 54 | RAM write $\theta_{-5}$ | 00111011 | 00101100 |
| 55 | RAM write $\theta_{-4}$ | 11011011 | 10101100 |
| 56 | RAM write $\theta_{-3}$ | 01011011 | 01101100 |
| 57 | RAM write $\theta_{-2}$ | 10011011 | 11101100 |
| 58 | RAM write $\theta_{-1}$ | 00011011 | 00011100 |
| 59 | Enter const. 1 | 10001100 | 10011100 |
| 60 | Enter const. 9 | 10011100 | 01011100 |
| 61 | CP equal | 10000101 | 11011100 |

## TABLE XIV - Continued

| Instruction Number | Program Instruction | Machine Code | Program Counter Address |
|---|---|---|---|
| 62 | RAM write $D_{11}$ | 00001011 | 00111100 |
| 63 | RAM write $\theta_{-6}$ | 10101011 | 10111100 |
| 64 | RAM write $\theta_{-5}$ | 00101011 | 01111100 |
| 65 | RAM write $\theta_{-4}$ | 11001011 | 11111100 |
| 66 | RAM write $\theta_{-3}$ | 01001011 | 00000010 |
| 67 | RAM write $\theta_{-2}$ | 10001011 | 10000010 |
| 68 | RAM write $\theta_{-1}$ | 00001011 | 01000010 |
| 69 | CP clear | 00000101 | 11000010 |
| 70 | Enter $I_{T-2}$ | 01110110 | 00100010 |
| 71 | Enter $I_{T-1}$ | 11110110 | 10100010 |
| 72 | CP subtract | 01100101 | 01100010 |
| 73 | Enter const. 2 | 01001100 | 11100010 |
| 74 | Enter const. 7 | 11101100 | 00010010 |
| 75 | CP multiply | 01000101 | 10010010 |
| 76 | Enter const. 2 | 01001100 | 01010010 |
| 77 | Enter const. 1 | 10001100 | 11010010 |
| 78 | Enter const. 9 | 10011100 | 00110010 |
| 79 | Enter const. 6 | 01101100 | 10110010 |
| 80 | Enter const. 6 | 01101100 | 01110010 |
| 81 | Enter const. 1 | 10001100 | 11110010 |
| 82 | CP subtract | 01100101 | 00001010 |
| 83 | CP exchange operand | 00110101 | 10001010 |
| 84 | Enter const. 1 | 10001100 | 01001010 |
| 85 | Shift left | 11010101 | 11001010 |
| 86 | Shift left | 11010101 | 00101010 |
| 87 | Shift left | 11010101 | 10101010 |
| 88 | Shift left | 11010101 | 01101010 |
| 89 | Shift left | 11010101 | 11101010 |
| 90 | Shift left | 11010101 | 00011010 |
| 91 | Shift left | 11010101 | 10011010 |
| 92 | Shift left | 11010101 | 01011010 |
| 93 | Shift right | 01010101 | 11011010 |
| 94 | Shift right | 01010101 | 00111010 |

## TABLE XIV - Continued

| Instruction Number | Program Instruction | Machine Code | Program Counter Address |
|---|---|---|---|
| 95 | Shift right | 01010101 | 10111010 |
| 96 | Shift right | 01010101 | 01111010 |
| 97 | RAM read $\theta_{-6}$ | 10111000 | 11111010 |
| 98 | RAM read $\theta_{-5}$ | 00111000 | 00000110 |
| 99 | RAM read $\theta_{-4}$ | 11011000 | 10000110 |
| 100 | RAM read $\theta_{-3}$ | 01011000 | 01000110 |
| 101 | RAM read $\theta_{-2}$ | 10011000 | 11000110 |
| 102 | RAM read $\theta_{-1}$ | 00011000 | 00100110 |
| 103 | Shift right | 01010101 | 10100110 |
| 104 | Shift right | 01010101 | 01100110 |
| 105 | Shift right | 01010101 | 11100110 |
| 106 | CP multiply | 01000101 | 00010110 |
| 107 | Skip X-instructions | 10111101 | 10010110 |
| 108 | No-op No. 14 | 01110101 | 01010110 |
| 109 | No-op No. 14 | 01110101 | 11010110 |
| 110 | No-op No. 14 | 01110101 | 00110110 |
| 111 | No-op No. 14 | 01110101 | 10110110 |
| 112 | Enter const. 0 | 00001100 | 01110110 |
| 113 | Enter const. 5 | 10101100 | 11110110 |
| 114 | Enter const. 0 | 00001100 | 00001110 |
| 115 | CP equal | 10000101 | 10001110 |
| 116 | Skip X-instructions | 10111101 | 01001110 |
| 117 | Enter const. 0 | 00001100 | 11001110 |
| 118 | Enter const. 3 | 11001100 | 00101110 |
| 119 | Enter const. 0 | 00001100 | 10101110 |
| 120 | CP equal | 10000101 | 01101110 |
| 121 | Skip x-instructions | 10111101 | 11101110 |
| 122 | Enter const. 1 | 10001100 | 00011110 |
| 123 | Enter const. 4 | 00101100 | 10011110 |
| 124 | Enter const. 5 | 10101100 | 01011110 |
| 125 | CP equal | 10000101 | 11011110 |
| 126 | No-op No. 14 | 01110101 | 00111110 |
| 127 | No-op No. 14 | 01110101 | 10111110 |

## TABLE XIV - Continued

| Instruction Number | Program Instruction | Machine Code | Program Counter Address |
|---|---|---|---|
| 128 | No-op No. 14 | 01110101 | 01111110 |
| 129 | No-op No. 14 | 01110101 | 11111110 |
| 130 | No-op No. 14 | 01110101 | 00000001 |
| 131 | Shift right | 01010101 | 10000001 |
| 132 | Shift right | 01010101 | 01000001 |
| 133 | End of prog. mark | 11110101 | 11000001 |

# FABRICATION OF ADVANCED TORQUE MEASUREMENT SYSTEM

Three groups of equipment were fabricated during the program: the sensing unit, the processor, and some miscellaneous electronic breadboard circuits needed to facilitate the hardware checkout or the software programming or the laboratory testing efforts of the subject program.

## SENSING UNIT

The sensing unit was first fabricated per design drawing. An adaptor shaft that allowed the use of air motor drive for the sensing unit was also fabricated. However, this shaft was not used during the testing phase of the program because of the following two reasons: first, the air motor drive exhibited excessive resonant vibration due to its pulsed mode of motion; second, the electrical drive motor did not cause any noise interference even though the drive motor was a brush-type motor. The phasing gear was carefully machined so that all the leading edges and all the trailing edges of the gear teeth were precise within ±15 seconds of an arc from the true position. Although the rotating assembly, including the drive shaft of the electrical motor, was balanced at high speed, balance shift of the phasing gear assembly was still observed during the checkout runs of the sensing unit. Phase gear balance and concentricity were reestablished. The shift in balance and concentricity is believed to be caused by the stress relief of the part itself. Considerable efforts were expended for the troubleshooting of this problem. The reworked gear was then temperature-cycled and rotated at high speed to ensure the removal of residual stress. To prepare for the possibility of worst balance and concentricity shift that could exceed the rework limit of the existing shaft, a spare shaft with sufficient gross dimension allowance to compensate for the worst-case shift was also fabricated during the period. This provision allows minimum equipment downtime in case the worst-case balance and concentricity shift does occur. However, tests carried out after the retruing of the phasing gear indicated that such a worst-case possibility appeared to be remote. Two thermocouples were also added to the sensing unit, one inside the hollowed cup of the phasing gear and one outside against the plated copper band. Since the straight part of the phasing gear lies between these two thermocouples, the metal temperature of the phasing gear can be estimated from the temperature readings of these two thermocouples. This provides a calibration means for the eddy-current temperature probes.

Figure 57 shows a close-up of the assembled sensing unit. The sensing unit together with the electrical drive motor is shown in Figure 58. The two heater elements that allow the temperature adjustment from ambient to 500°F are shown in Figure 59. The complete sensing unit with heater elements assembled and metal-temperature thermocouples installed is shown in Figure 60.

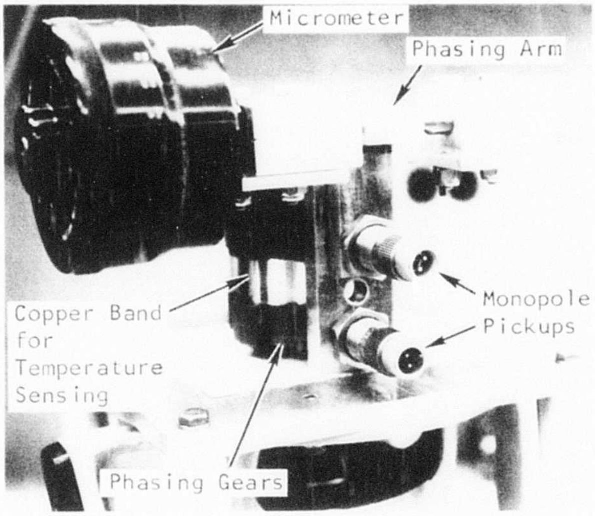

Figure 57. Close-up of the Sensing Unit.

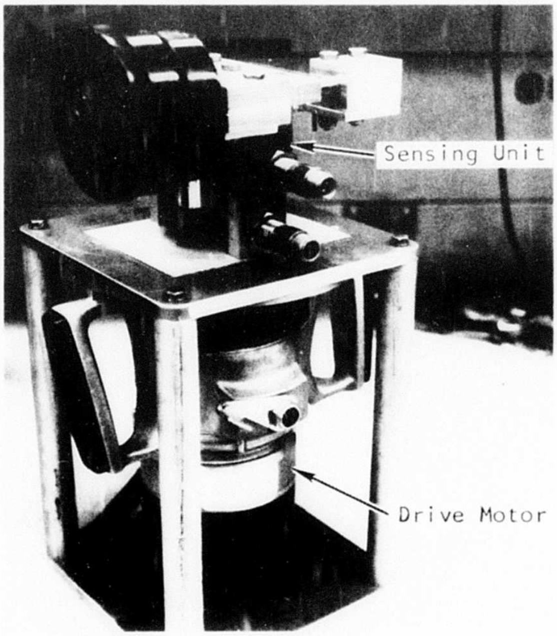

Figure 58. Sensing Unit Together With Drive Motor.

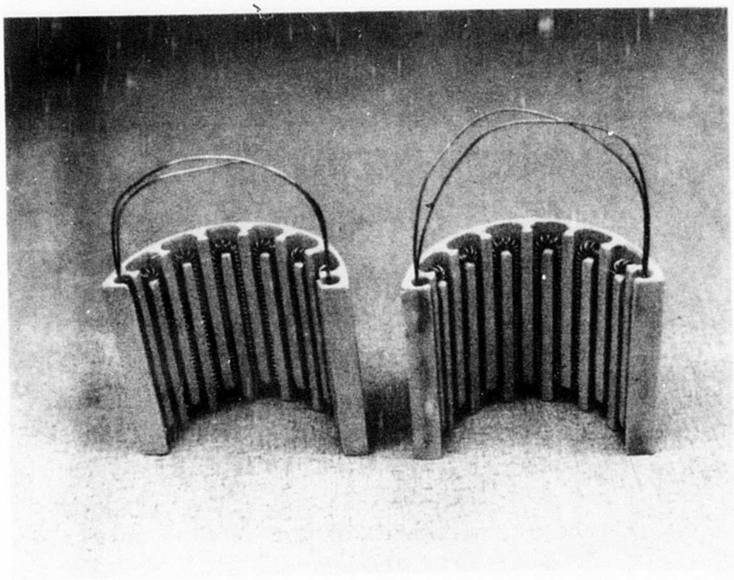

Figure 59. Heater Elements for the Sensing Unit.

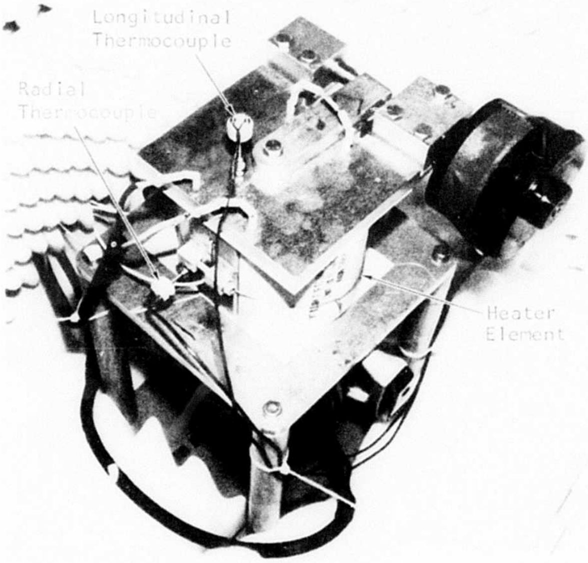

Figure 60. Thermocouple Installations on the Sensing Unit.

## PROCESSING UNIT

The fabrication of the processor included mainly the fabrication of three brassboard circuits for the coincidence interpolation and measurement logic, the CP and interface/controls, and the CP output display, decoder, and drivers. In addition to these main efforts, the inclusion of power supplies to the system, the integration and interconnection of these boards, and the installation of adjustment circuits and system operation control switches were also performed.

The coincidence interpolation and measurement logic brassboard is shown in Figure 61. The circuit board houses the coincidence checking logic, the measurement counter/registers, and digital multiplexers that allow the transmission of the 16 BCD output to the CP through four wires.

The CP and the related interface/control circuit board (Figure 62) houses the 10-digit fluorescent display tubes (Figure 63), the BCD-to-7-segment decoder circuit, the digit drivers, the segment drivers, and also the counter overflow or CP error detecting latches and display drivers. Fluorescent display tubes are used mainly to allow easy viewing at distances. For airborne application, a smaller and more rugged LED-type display device can be used.

The electronics for the temperature channel was not fabricated because it was felt that sensor optimization effort is needed. This channel was set

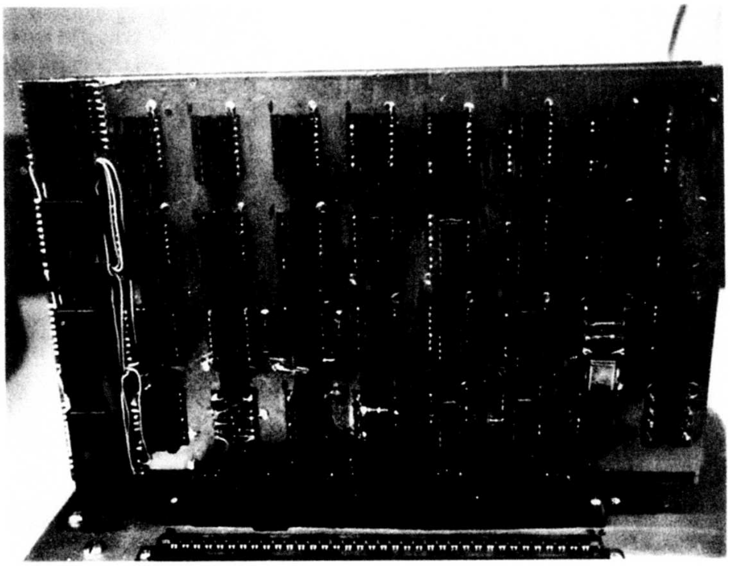

Figure 61. Digital Multiplexers on the Measurement Circuit Board.

up during laboratory testing phase using the existing equipment. Sensor output can be read manually. The quantized index number (i.e., $I_T$) can be input to the processor through a temperature setting switchboard (Figure 64).

Control switches, program selection switches, error signal indicators and display duration adjustment are shown in Figure 65. The program selection switch allows the use of the same electronic processor for the three different applications (6000 rpm, 66,000 rpm, and 26,000 rpm) by single switch action.

The circuit boards and power supplies in installed position are shown in Figure 66.

The input signal sockets and the power connectors are shown in Figure 67.

## MISCELLANEOUS ELECTRONIC BREADBOARDS

Under this category, three breadboard circuits were fabricated.

The one-tube display (Figure 68) for measurement section readout was designed to include the multiplexer address control and interface circuits (Figure 44) so that the results of the coincidence measurements can be read off one digit at a time from the counters. This provision allows evaluation of the sensing unit and measurement electronics before the computation electronics are completed. The results of the coincidence measurement can then be written down, and the resultant phase angle or torque can be manually computed on a separate electronic calculator following the same computation equations.

The second miscellaneous electronic circuit fabricated is the breadboard of the CP without interface and controls (Figure 69). This breadboard allowed the simulation of CP operation before the interface and program controls were completed.

The third item of electronic circuits fabricated is a special programming aid (Figure 70) to facilitate the checkout and the program of the complete system.

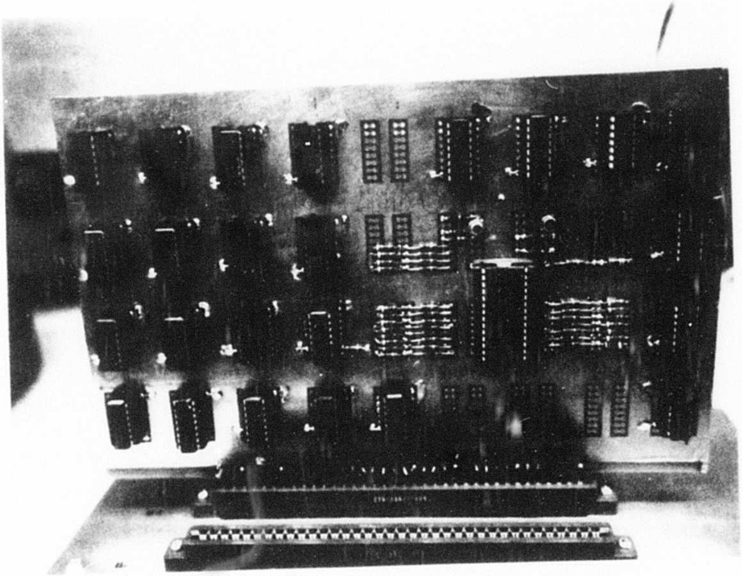

Figure 62. CP and Related Interface/Control Circuits.

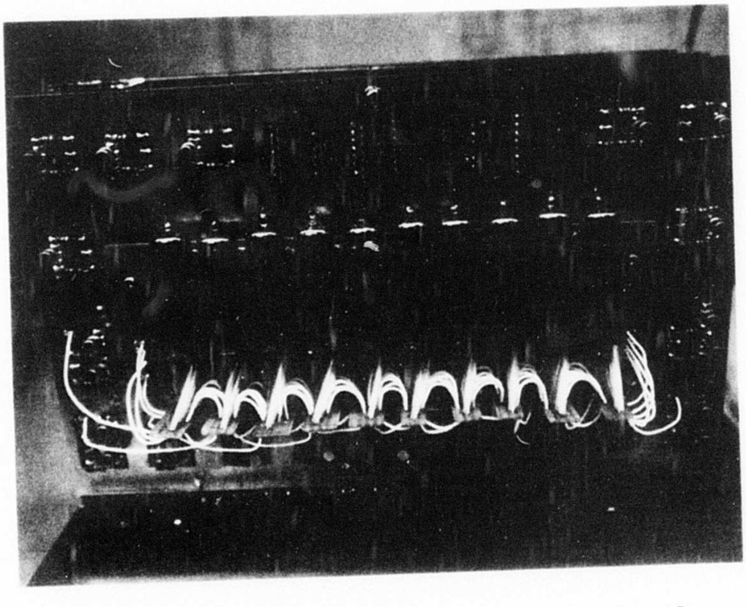

Figure 63. 10-Digit Display Brassboard for CP.

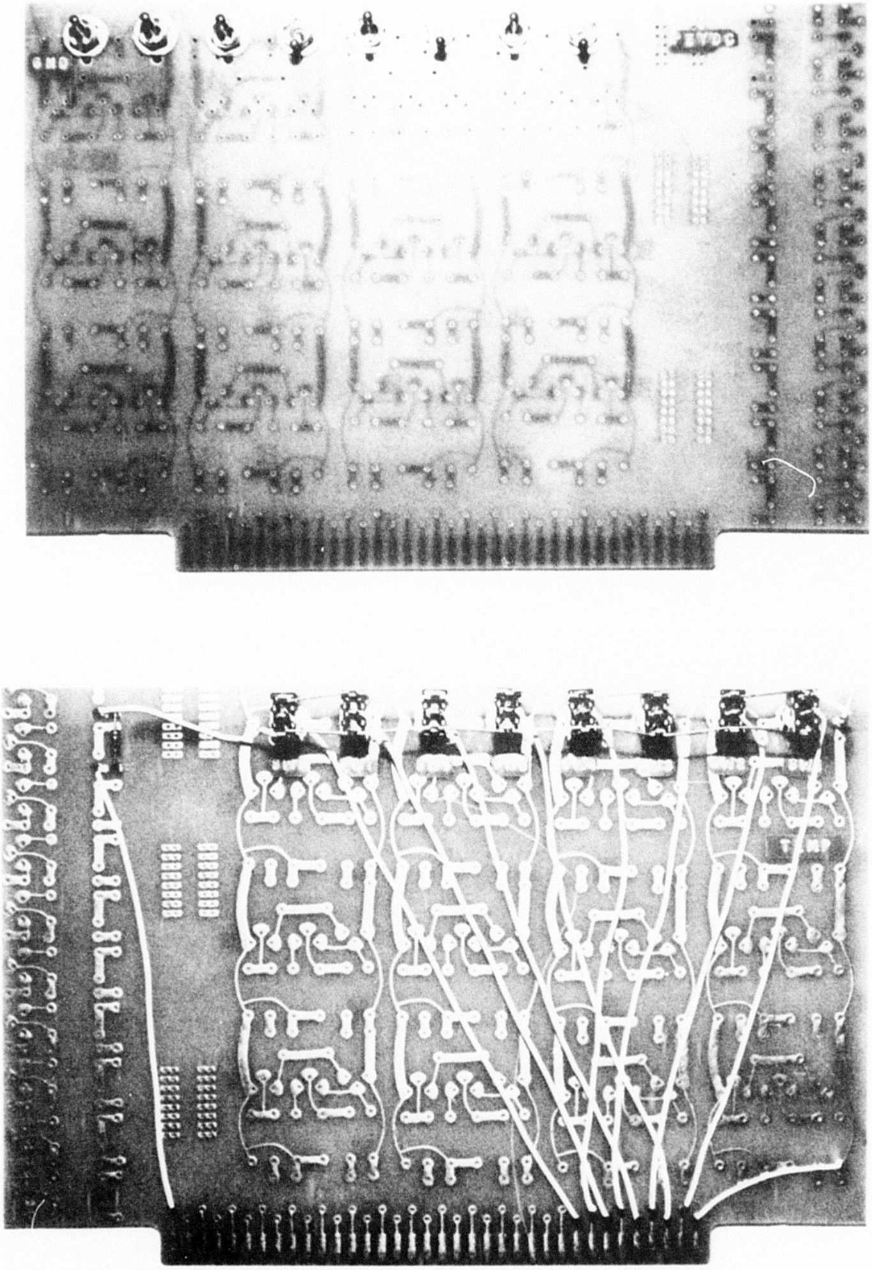

Figure 64. Temperature-Setting Switchboard.

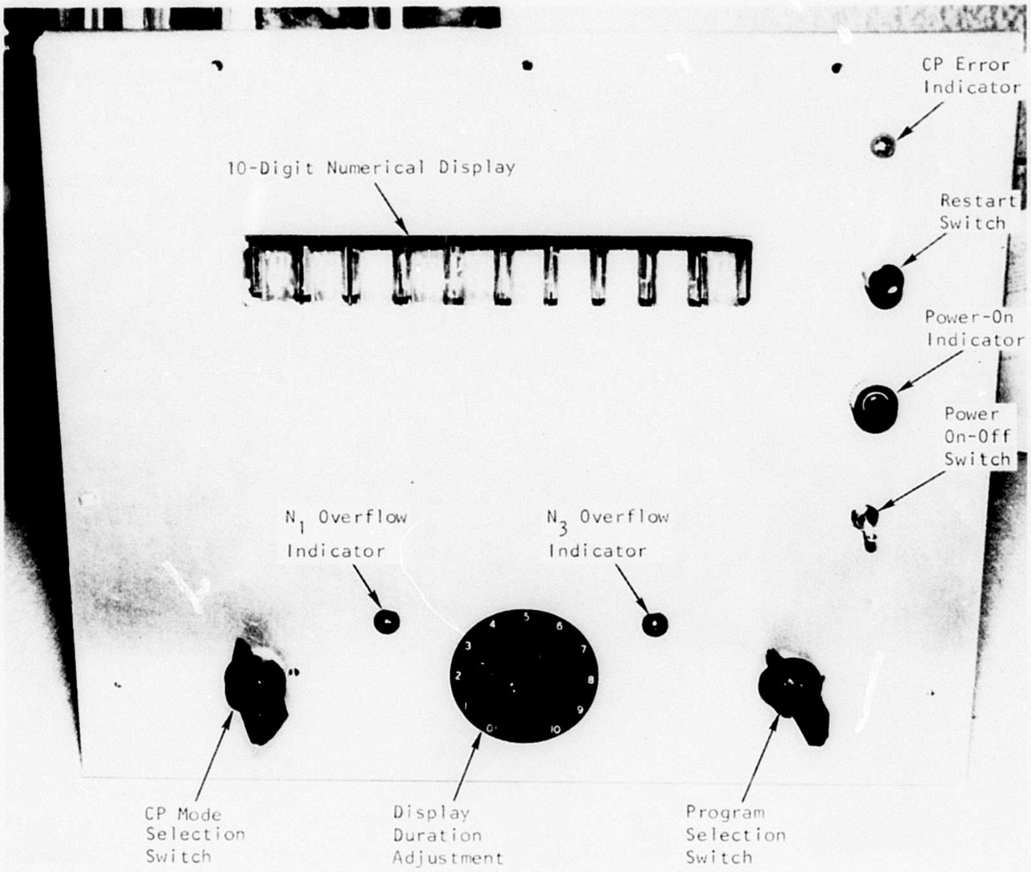

Figure 65. Display and Control Front Panel.

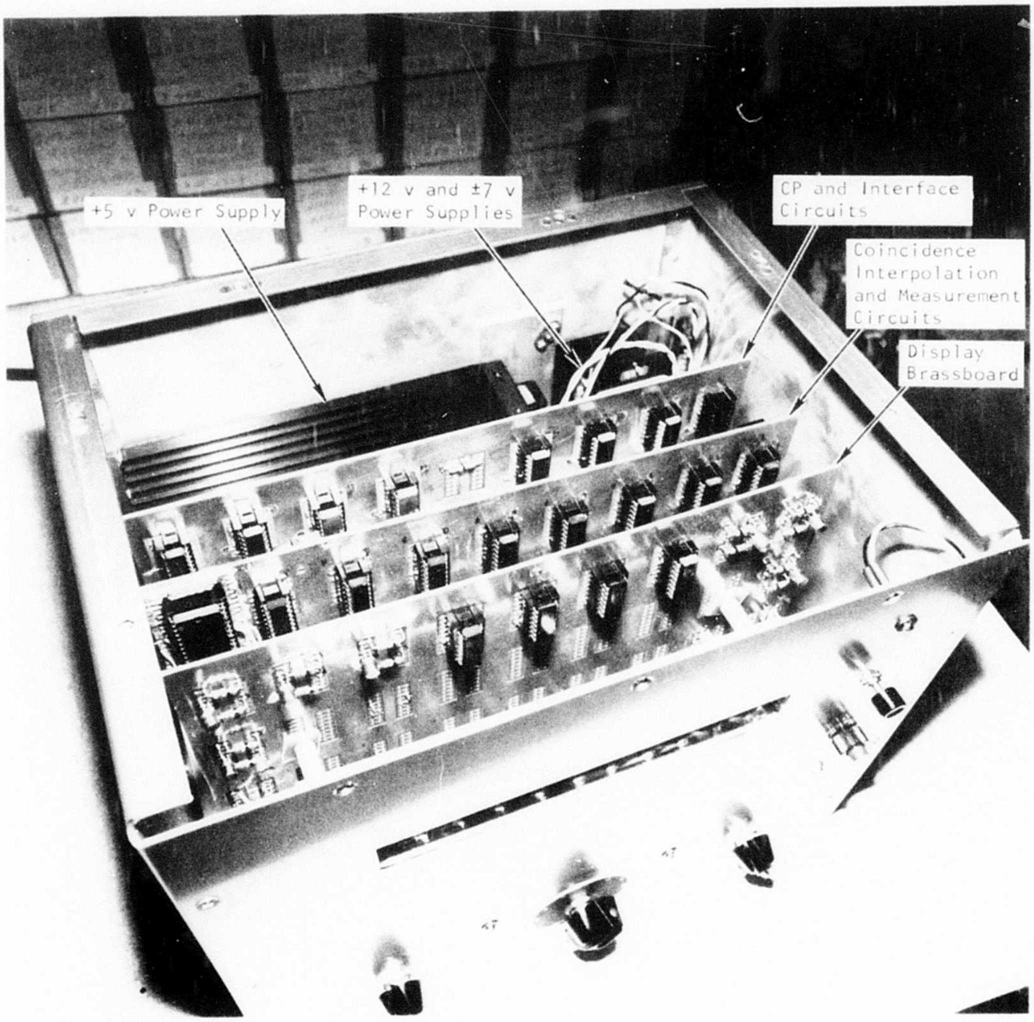

Figure 66. Circuit Boards and Interconnections.

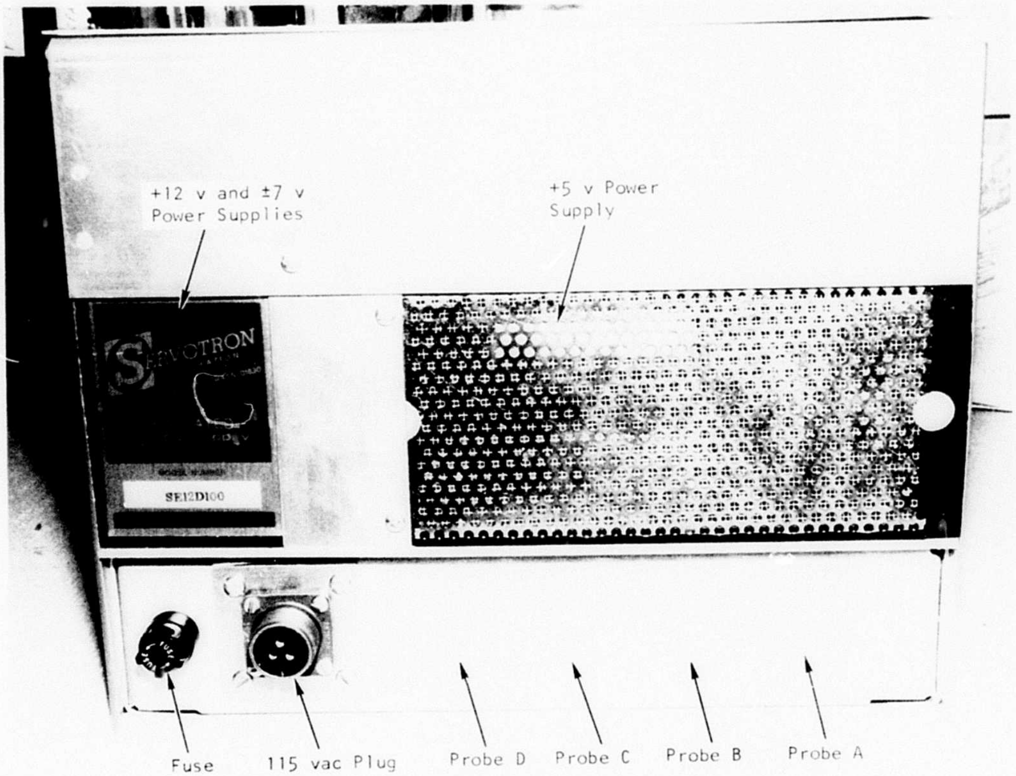

Figure 67. Input and Power Connectors.

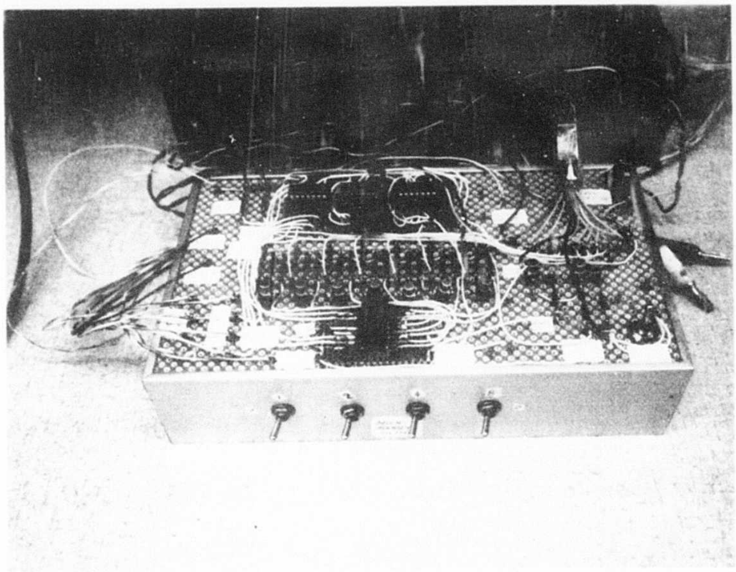

Figure 68. Measurement Output Display.

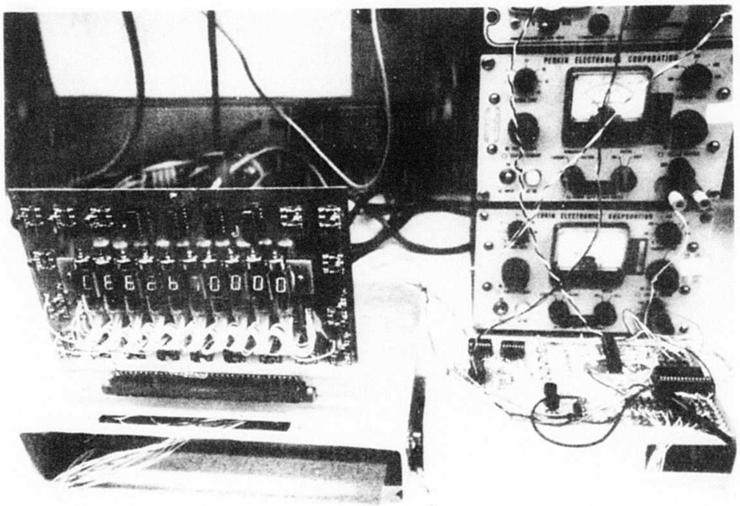

Figure 69. CP Breadboard in Operation.

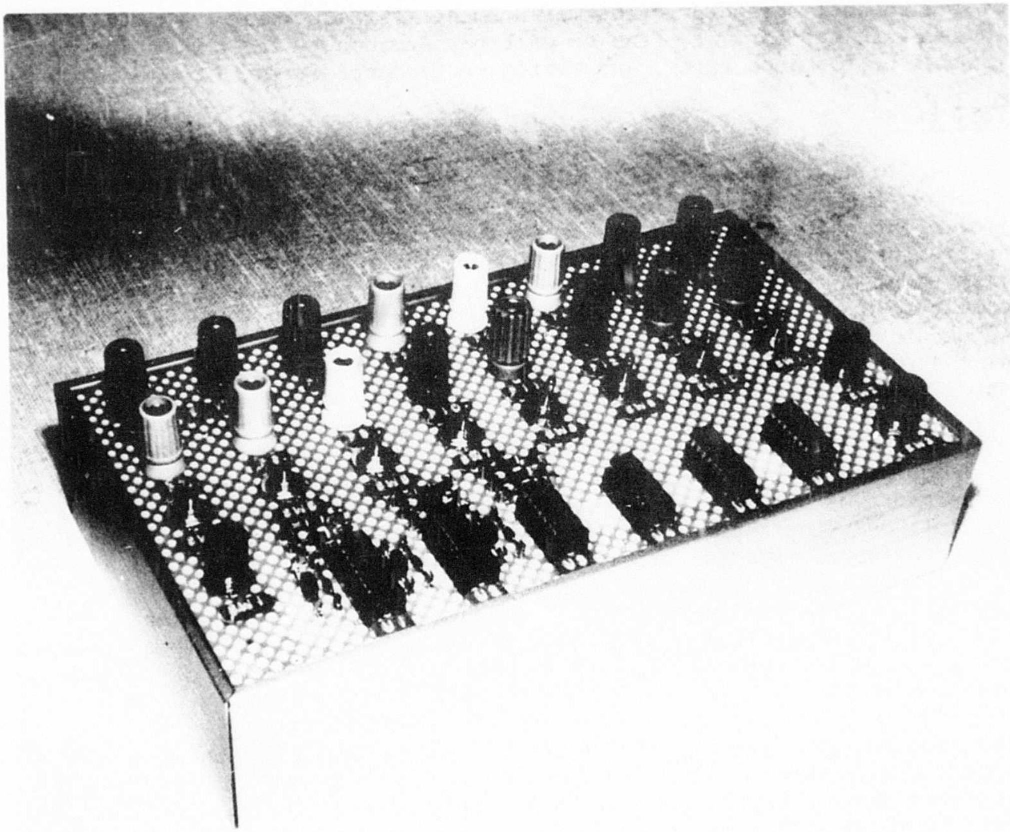

Figure 70. Programming Aid Breadboard Box.

# LABORATORY TESTING

Various tests were performed during the program to evaluate the performance of the subject advanced torque measurement system. These tests fall into three basic categories: sensing unit performance tests, processing electronics performance tests, and system performance tests.

## TEST SETUP

Figure 71 shows a schematic of the setup employed during the tests. Figure 72 shows the installation of the test sensing unit in the temperature control oven. Initially, the self-contained heater elements were used to create the higher temperature environment dictated by the tests. A Colburn Instrument oven was used during the latter part of the tests to provide more precise temperature control and wider range-adjustment capability needed to compensate for the temperature rise caused by frictional heating of the rotating phasing gear element and permit tests at sub-zero temperature levels. The Colburn Instrument oven, when supplied with compressed $CO_2$, provided much quicker control and stabilization of temperature by heating the test object with electricity or cooling it with a burst of $CO_2$. This equipment provided precise and stable temperature control over a low temperature of below -50°F and a high temperature of approximately +400°F. Above +400°F, the mass of the test object and its related heat transfer characteristics made the stabilization difficult.

The test sensing unit was driven by an electric brush-type motor. The speed of the electric motor was controlled by varying the output voltage of the power supply Variac. Because of the voltage limitation of the Variac, the highest speed achieved was 24,000 rpm.

The torquing of the shaft was simulated by displacing one phasing monopole pickup with respect to the other through the micrometer adjustment. For high-temperature tests, the simulated shaft twist angle was first set at a desired value with the use of the micrometer mechanism, then the setting was clamped down so that the micrometer could be removed from the test unit to avoid any possible damage to the micrometer due to excessive heating of its aluminum body. A pushrod was inserted to replace the micrometer so that additional support would be provided to the adjustment arm to prevent the setting from being shaken loose by vibration.

## EQUIPMENT USED

The following equipment were used during the laboratory testing phase of the program:

Test sensing unit

Electronic processing unit

Measurement output display unit

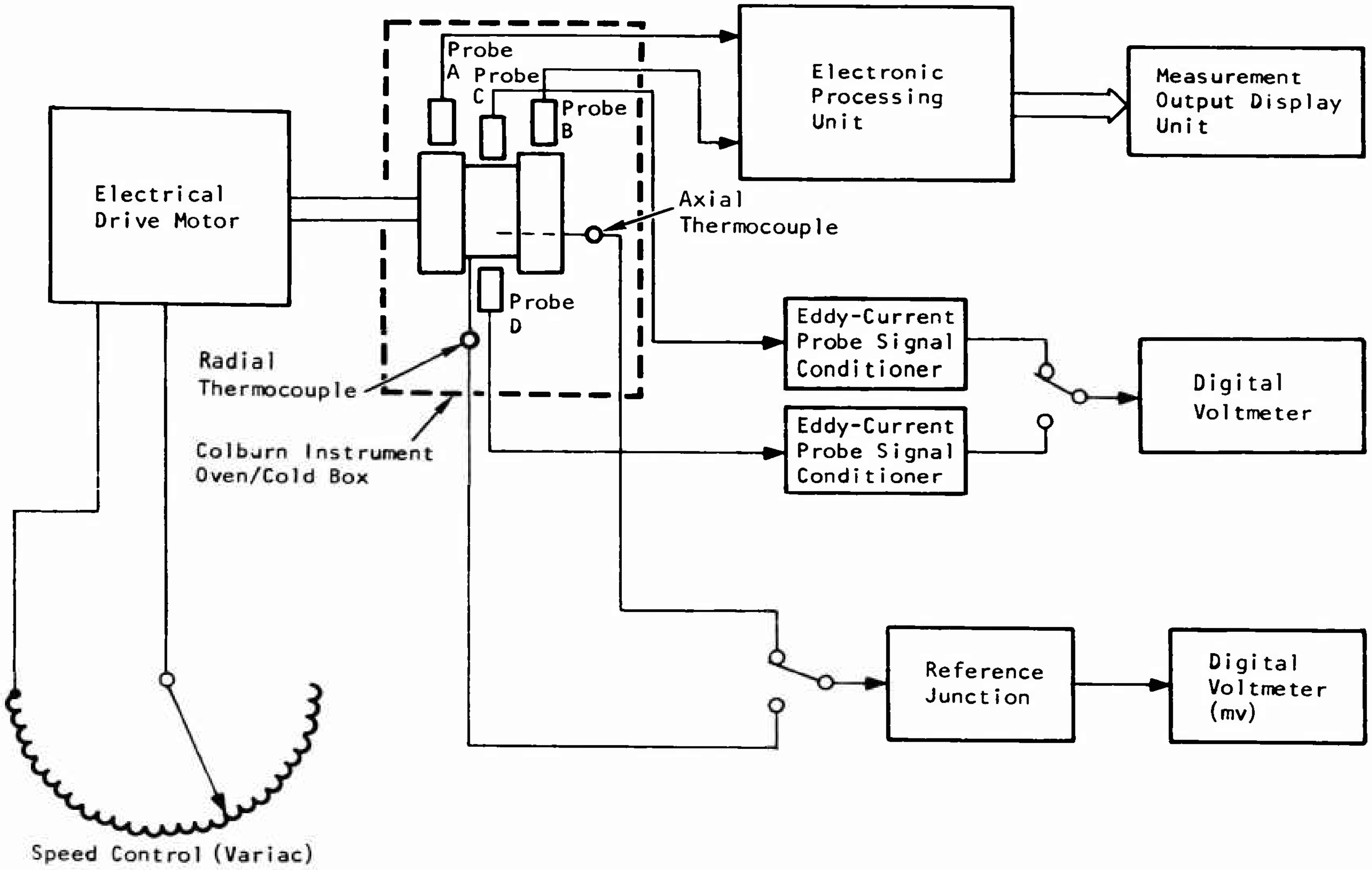

Figure 71. Schematic of Test Setup.

Figure 72. Installation of Test Sensing Unit in Colburn Oven.

Variable-speed drive motor

20 kw Variac speed control

PARAX ac power conditioner, Model P-1405-Q

Eddy-current probe signal conditioners, AiResearch LSK 31367

Colburn Instrument Oven, Model C-106-3600

Variable-frequency strobe light, GR strobotac-1531-A

Oscilloscope, Tektronix Model 454

Oscilloscope camera, Tektronic Model C-31

Pulse generators (2), Contronics lockpulse CPG pulser and Data Pulse Model 110B

Counter, Systron Donner Model 7014 and Dana Model 8130

Voltmeters, Hewlett-Packard Models 412A and 400H

Digital voltmeters (2), Dana Model 5500

Thermocouple bridge

Power supplies

- Systems Research Model 3567
- Power Designs, Inc. Model 5015-S
- Kepco Model SC-150-1

## SENSING UNIT PERFORMANCE TESTS

The purpose of these tests was to determine whether or not appreciable degradation could be caused in the sensing unit by various operating conditions. Many test runs were performed under different speed and temperature conditions. Sensor raw signals were recorded through photographic means. Analyses were performed later to determine if there was a change in terms of waveform and amplitude of the signal.

### Monopole Pickup Under Temperature and Speed

Figures 73 through 77 show a sample set of monopole pickup output signals under different test speeds. The amplitude of the signal varies approximately in proportion to the speed. No distortion or noise was observed at the sensor output. Typical temperature data are shown in Figures 78 through 81. No noticeable effect due to temperature was observed. Both signal amplitude and waveform remain the same under various temperature conditions.

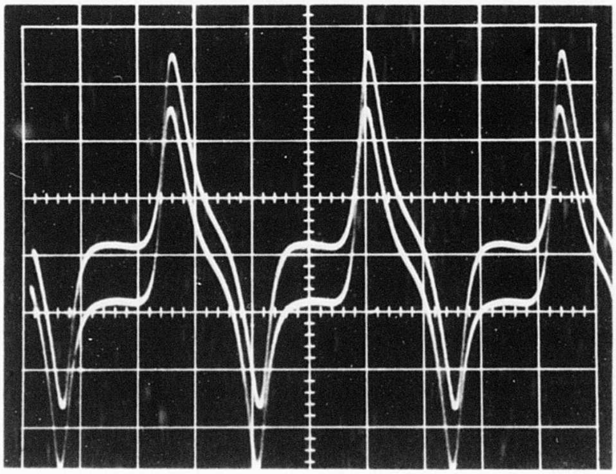

Figure 73. Monopole Output Signals at 6020 RPM.

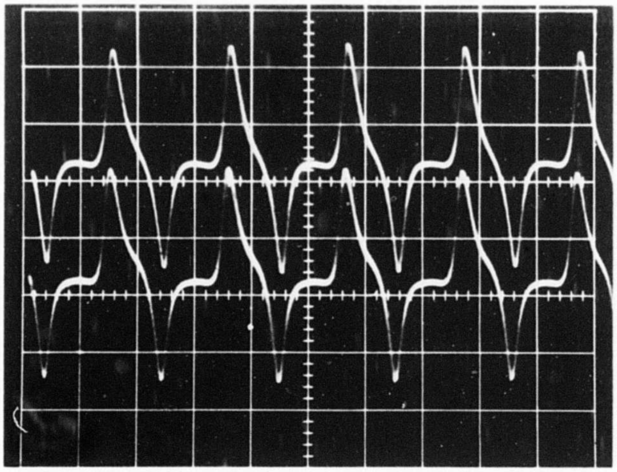

Figure 74. Monopole Output Signals at 10,000 RPM.

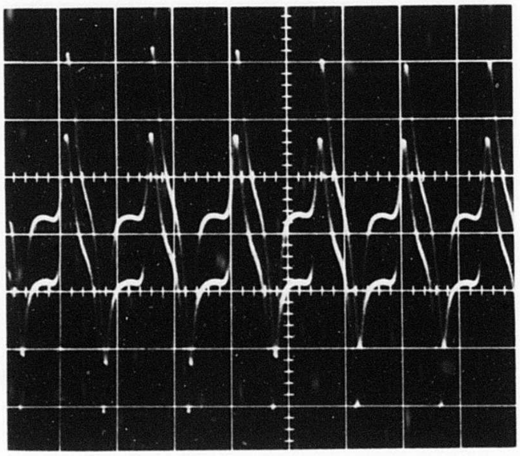

Figure 75. Monopole Output Signals at 14,000 RPM, 200°F; 0.5 ms/cm, 5 v/cm.

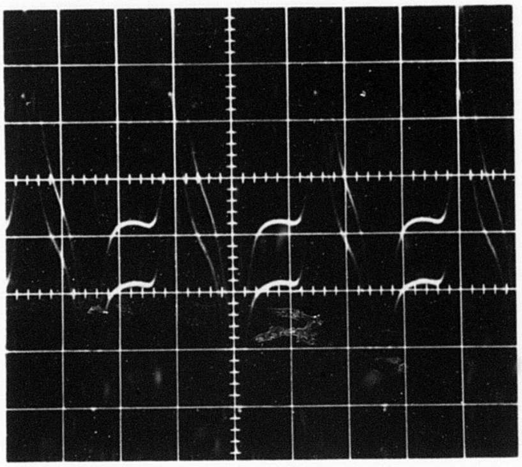

Figure 76. Monopole Output Signals at 20,023 RPM, 200°F; 0.2 ms/cm, 5 v/cm.

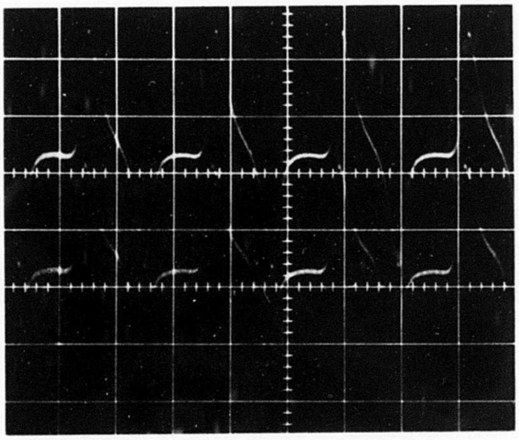

Figure 77. Monopole Output Signals at 23,000 RPM, 200°F; 0.2 ms/cm, 10 v/cm.

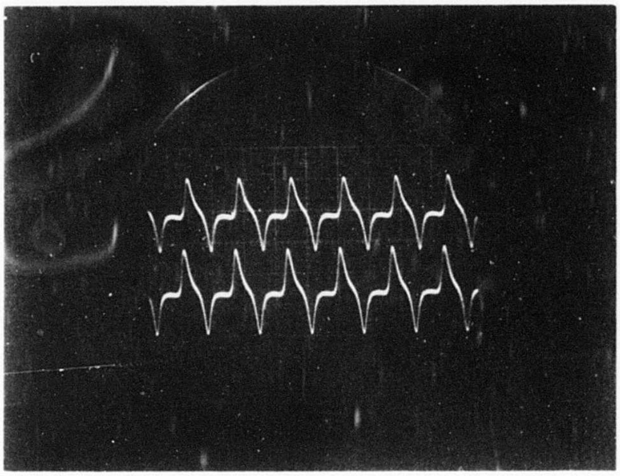

Figure 78. Temperature Data at 6000 RPM, -35°F; 1 ms/cm, 5 v/cm.

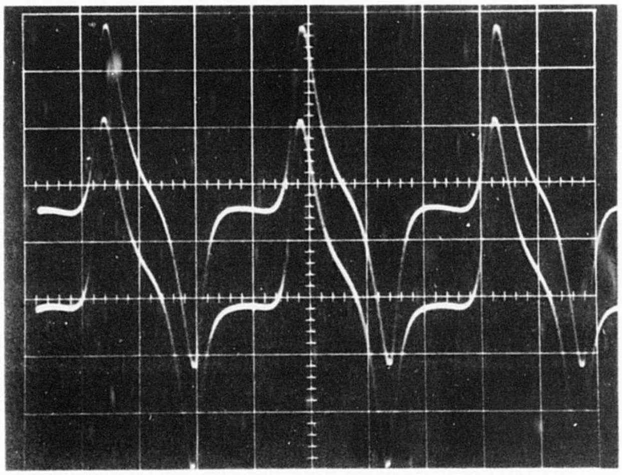

Figure 79. Temperature Data at 6010 RPM, Ambient Temperature; 0.5 ms/cm, 2 v/cm.

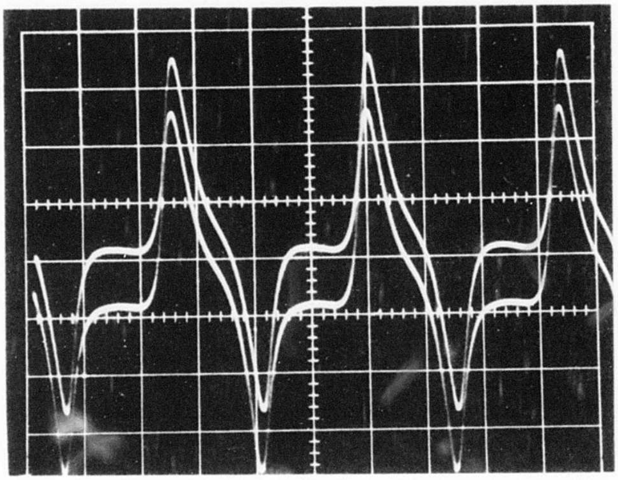

Figure 80. Temperature Data at 6020 RPM, 200°F; 0.5 ms/cm, 2 v/cm.

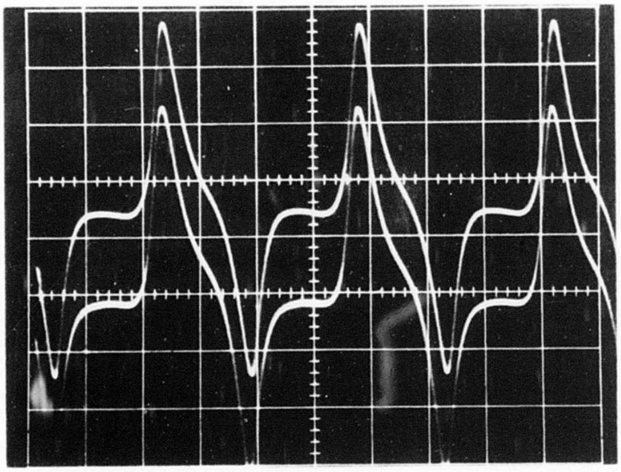

Figure 81. Temperature Data at 6000 RPM, 300°F; 0.5 ms/cm, 2 v/cm.

## Eddy-Current Probe Under Temperature and Speed

The dc output signal from the eddy-current probes was recorded to determine its repeatability. Figures 82 and 83 present the test results for zero shaft speed and 6000 rpm. The shaft metal temperature was obtained by taking the average of the radial and axial thermocouple readings. From Figure 82, almost no change of output over the 30 min test period was observed. From Figure 83, a slow rise in eddy-current probe output was observed. Since the thermocouple readings also indicated a similar slow rise, it was concluded that such a temperature rise was caused by the rotational friction of the phasing gear tooth with the surrounding air. In fact, a temperature rise from ambient to approximately 150°F has been observed during high-speed test at ambient temperature from both the thermocouple indications and the eddy-current probe outputs.

A more extensive temperature run was performed later to establish the temperature relationship of these probes for the full temperature range from -35°F to +500°F. Figures 84 and 85 depict these results. In general, these results agree reasonably well with the static laboratory test results performed during the preliminary research phase of the subject program.

To examine the speed effect on eddy-current probe output, tests were performed on the test sensing unit with the use of the Colburn Instrument oven. The temperature of the test unit was maintained at a preset temperature as constant as possible by feeding in either heat or compressed $CO_2$. Outputs from the eddy-current probe signal conditioners were recorded. The signal conditioner was considered part of the eddy-current sensing unit because of its inseparable function with the probe. Residual temperature effects due to the minute difference caused by temperature control during the test were corrected by use of interpolation according to the thermocouple indications. The summarized test results are plotted in Figures 86 and 87. From these results, there appears to be an increasing trend in signal output with speed, even though this effect was somewhat obscured by the random variation part of the measurement. The speed-induced output components were small compared to the random variation; for probe No. 314, the speed-induced output components were less than 4°F over the intended temperature-application range (up to 300°F). The equivalent temperature variations in probe No. 306 were larger when the switchover temperature was set at 200°F, but with switchover temperature changed to 300°F, the equivalent temperature component due to the speed effect also would be expected to be limited to below 4°F.

Also observed during the tests was the shifting in output level after lengthy dwelling at a higher temperature. This shifting in output level appears to be caused by the insufficient temperature cycling of the core material of the probes. This can be corrected by placing the probes in an oven under a cyclic temperature variation for a long enough period of time to evaporate the trapped moisture and impurities of the core material. The sensor optimization study should also improve this long-term stability of the signal output by proper choice of the operating frequency and geometry, consequently reducing the sensitivity to this type of effect.

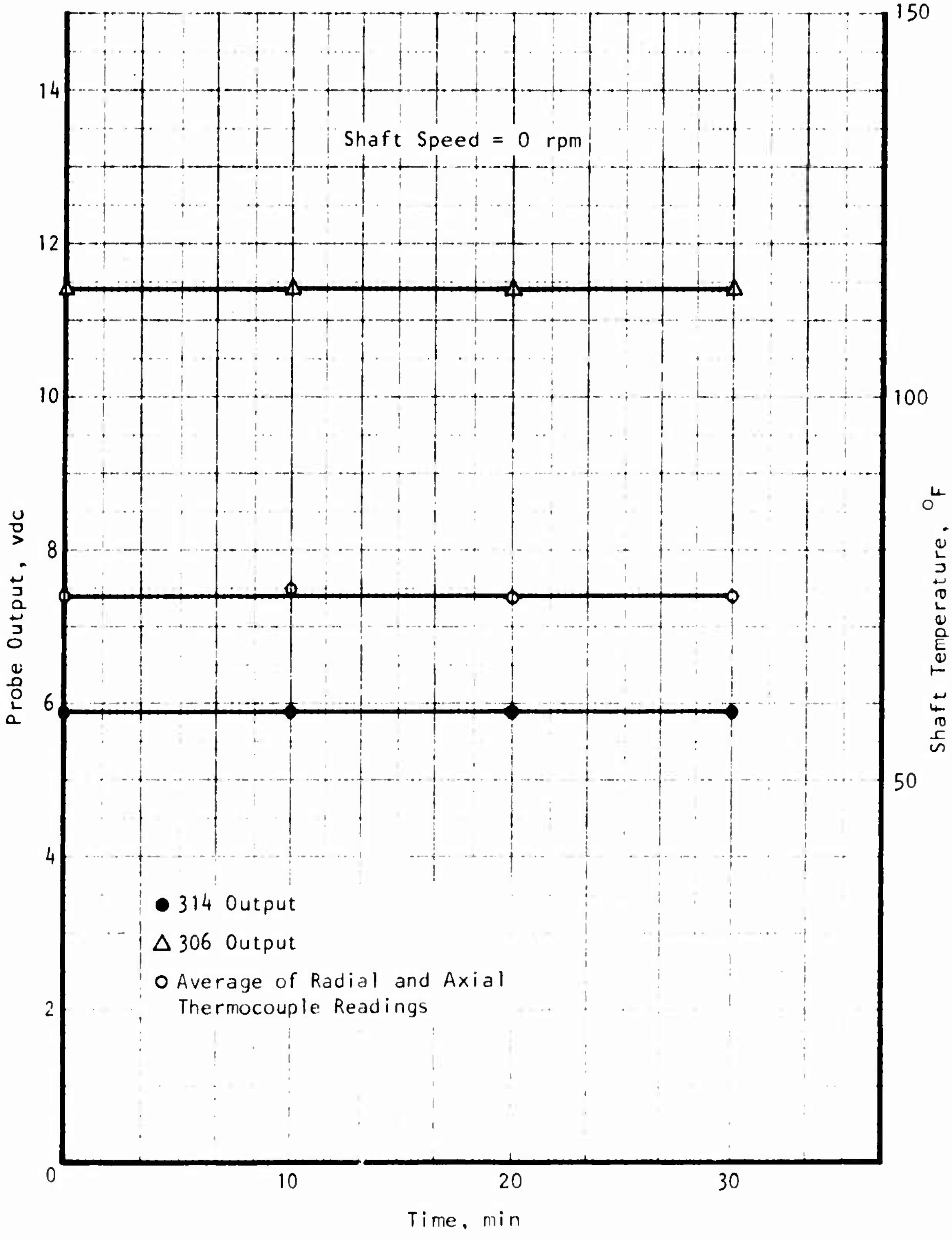

Figure 82. Eddy-Current DC Output (Zero Shaft Speed).

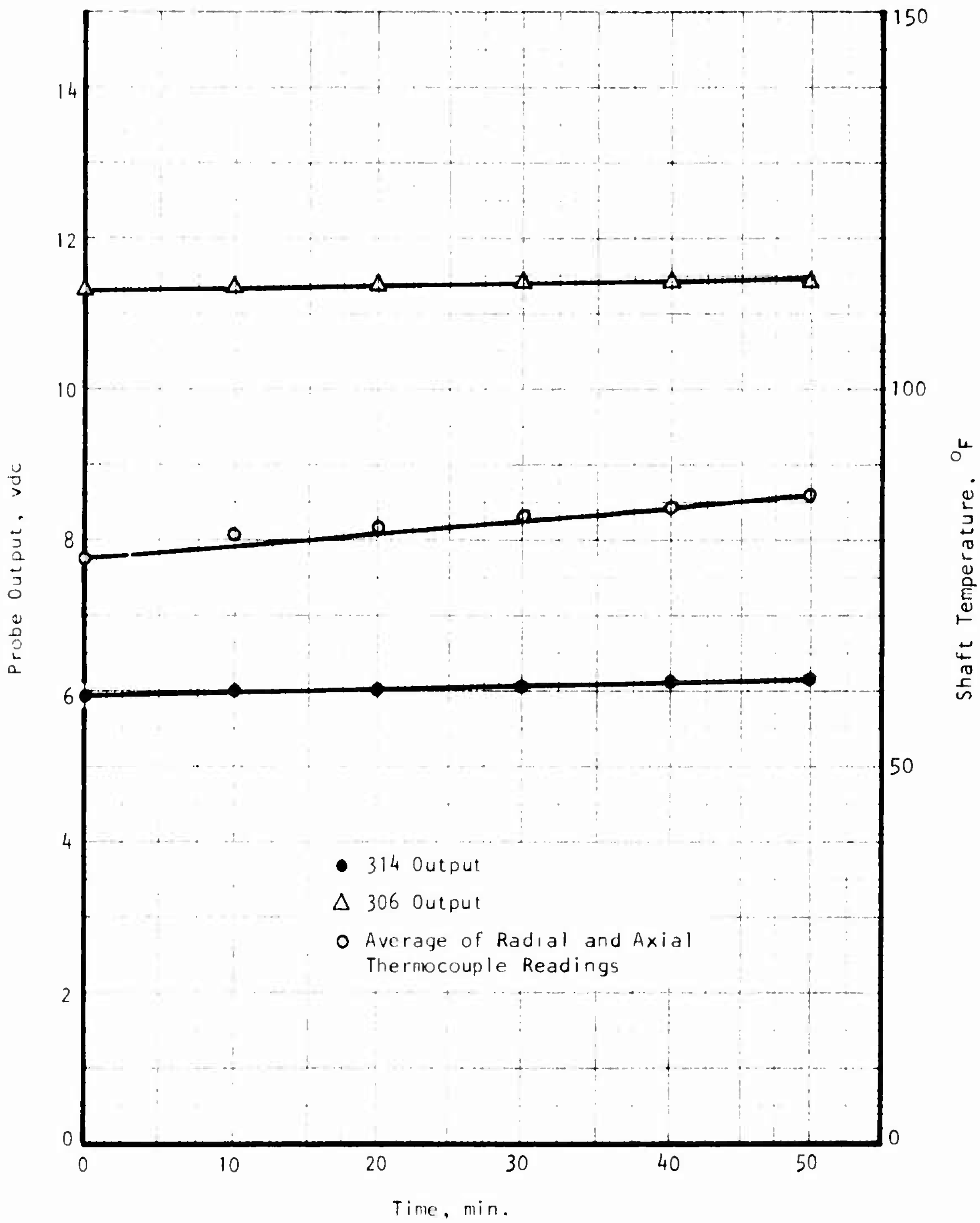

Figure 83. Eddy-Current DC Output (6000 RPM Shaft Speed).

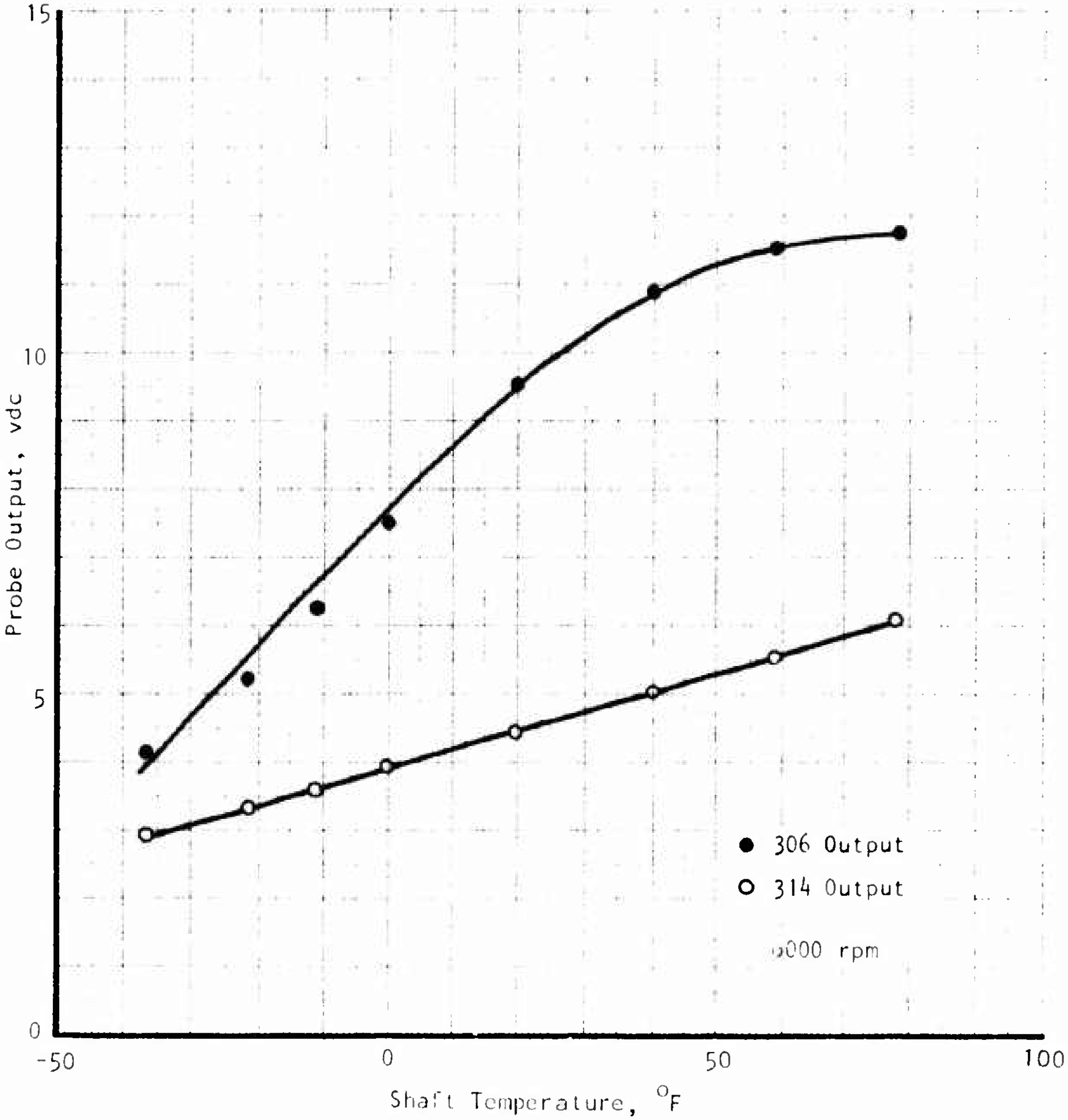

Figure 84. Temperature Relationship (Cold End).

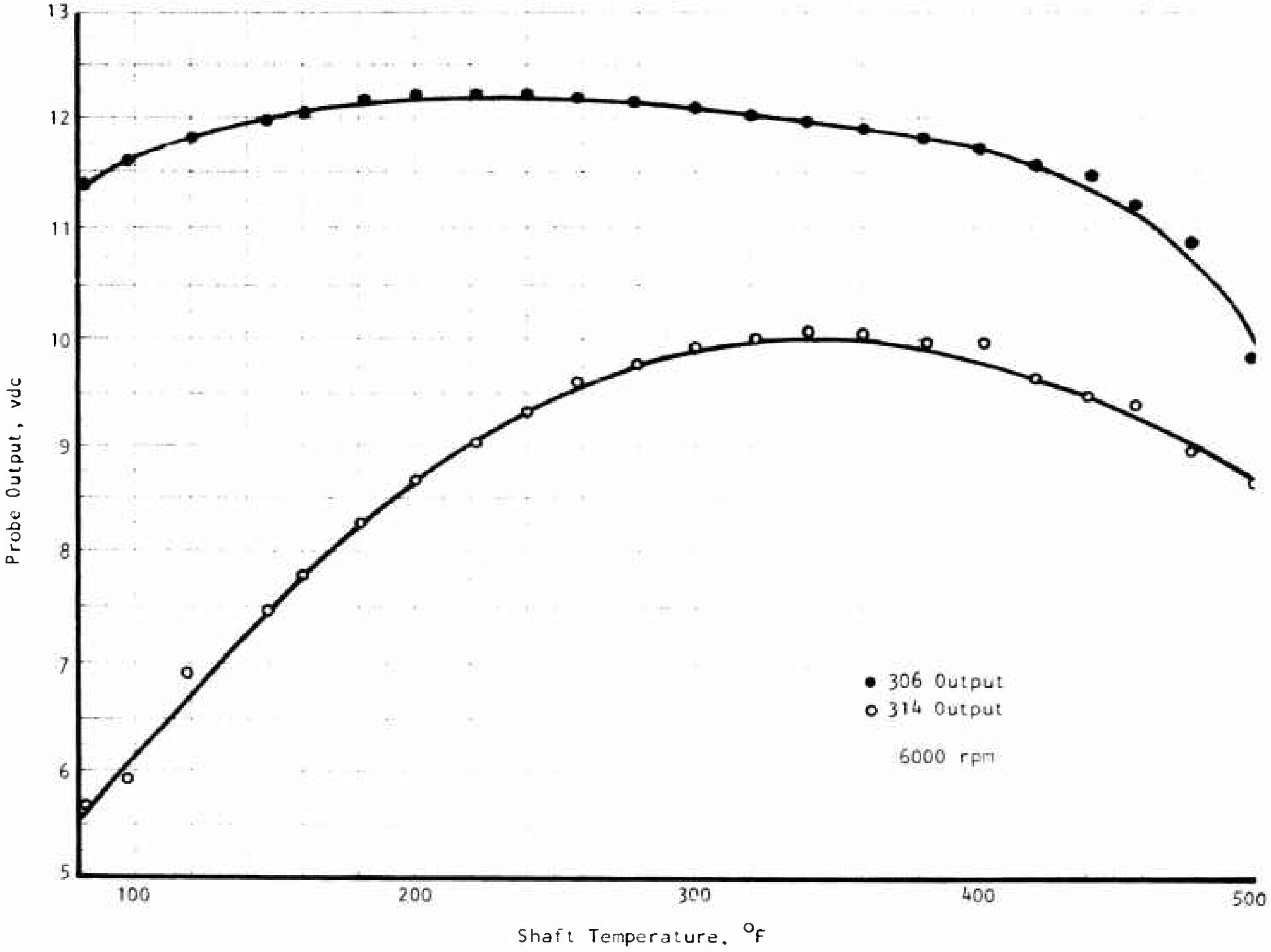

Figure 85. Temperature Relationship (Hot End).

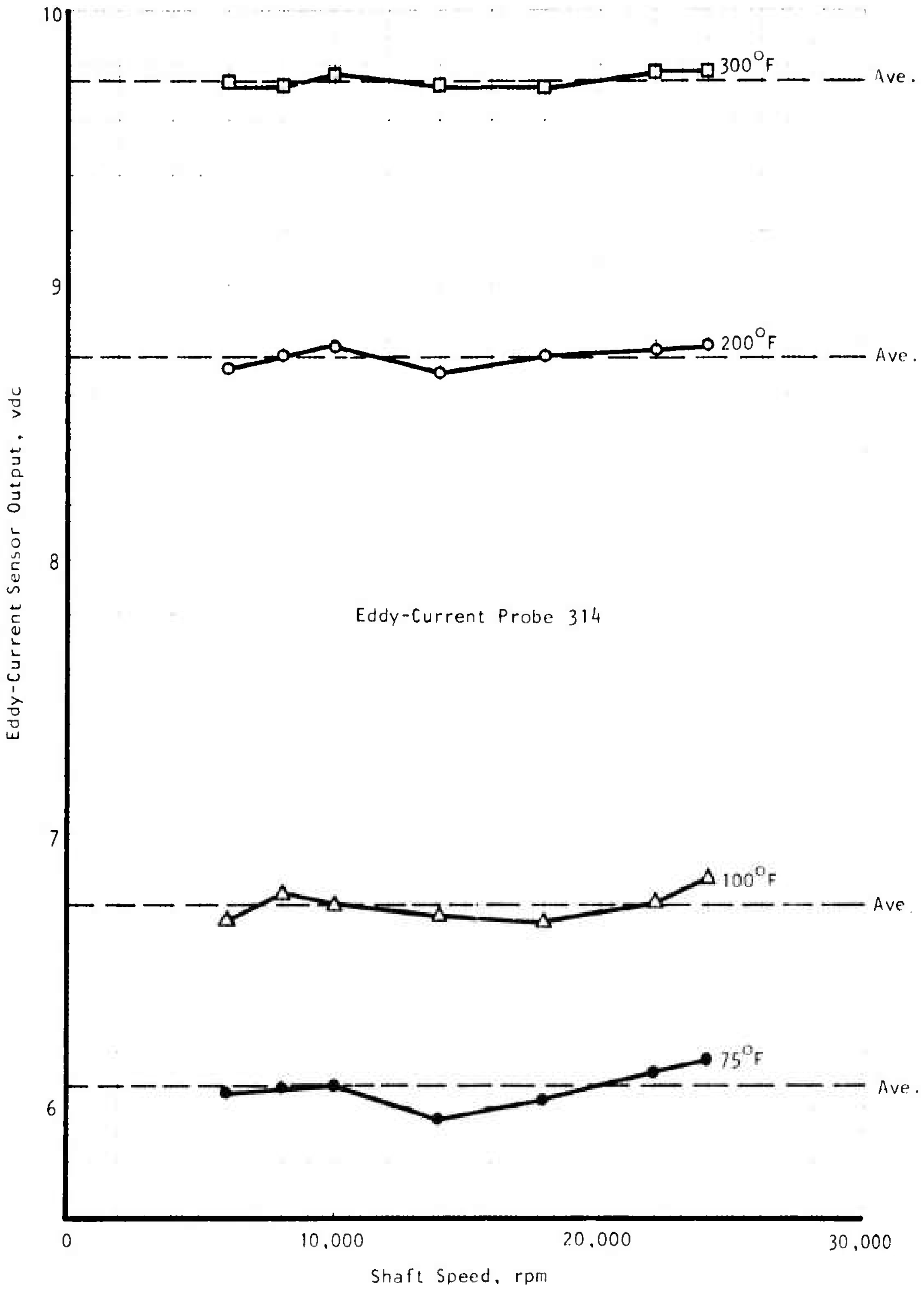

Figure 86. Speed Effect on Eddy-Current Probe Signal--Probe No. 314.

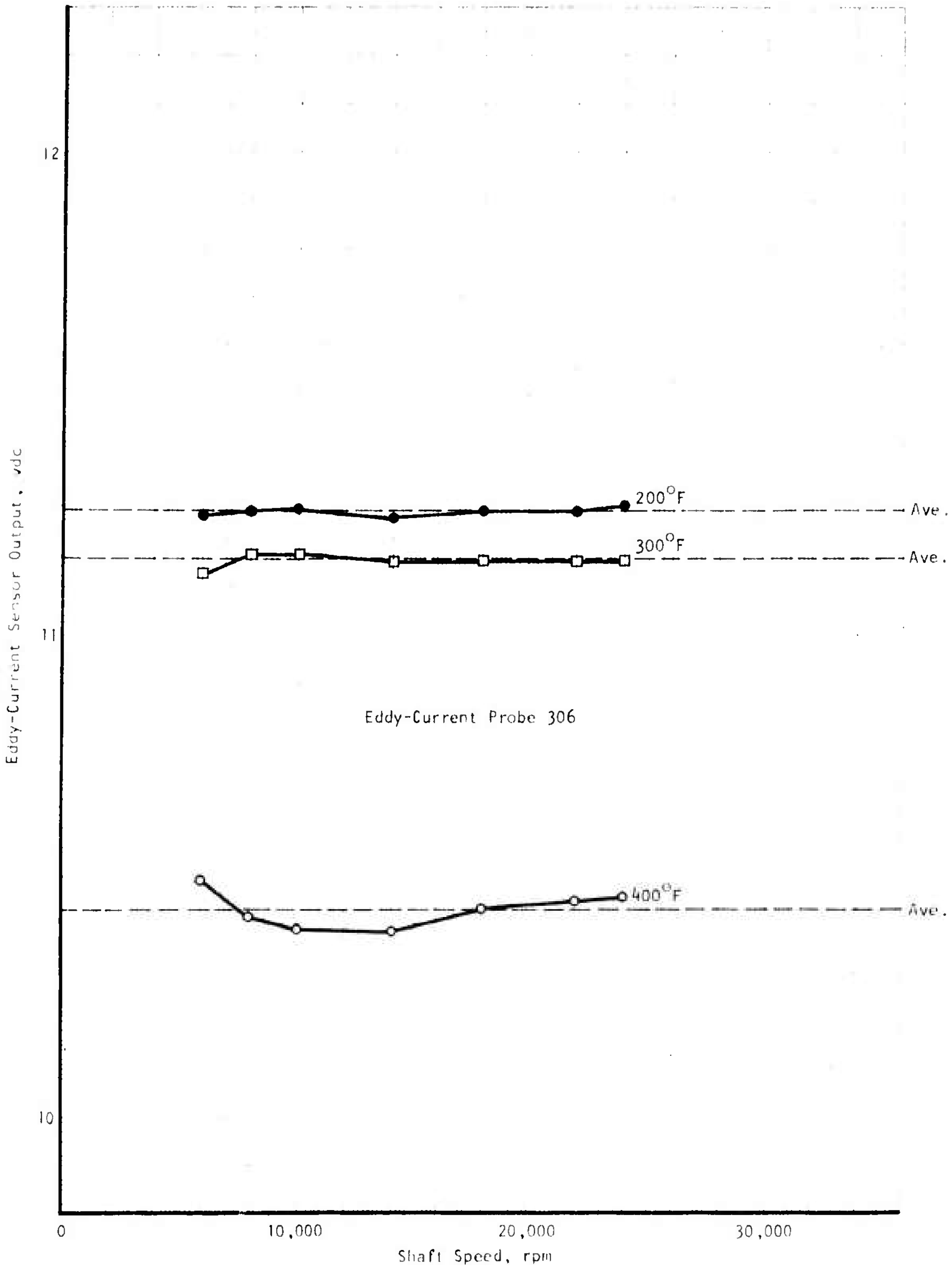

Figure 87. Speed Effect on Eddy-Current Probe Signal--Probe No. 306.

## PROCESSING ELECTRONICS PERFORMANCE TESTS

### Signal Path Delay

To determine the signal delay between the two probe paths, zero phase pulses were applied to the inputs by connecting the same signal to both probe A and probe B terminals. The timing-mark pulses, the coincidence pulses, and the counter control signals were then photographed from the oscilloscope. Figure 88 shows the comparison between timing marks generated by the probe A and probe B signals. The coincidence pulses generated by these two signals and the clock pulse are shown in Figure 89. The counter control pulses triggered by the coincidence pulses are shown in Figure 90. The probe A path is on top and the probe B path is at the bottom. There is practically no delay between the two paths up to the coincidence generation part of the logic circuit. The delay occurs only at the counter control point of the circuit because of the need for proper sequencing of the counters. However, this delay is very small and is of the same magnitude as the resolution of the measurement circuit (i.e., roughly 20 nsec).

### Measurement Accuracy

These tests were aimed at determining the accuracy of the coincidence interpolation and measurement logic circuit. To perform these tests, signals from the electronic pulse generators were used. Signal frequencies of 600 Hz, 660 Hz, and 2600 Hz were set on the pulse generators to simulate the 6000-, 6600-, and 26,000-rpm pulses from the monopole pickups. Full-scale delays that are equivalent to a 5-deg phase difference at 6000 rpm and 6600 rpm and 10 deg at 26,000 rpm were adjusted on the triggered pulse generator. Because of the concurrent software programming effort of the CP brassboard, data were taken directly from the counters through the measurement output display device. Results were then computed from these measured data using a Univac 1108 digital computer following the computation equations developed during the program. Figures 91 through 93 show the results in graphical form. To allow easy visualization of the results, they are presented in percentage form relative to the average value of the measurements performed. The plots were made with the percentage deviation as the ordinate and the test point as the abscissa. The accuracy of all three measurements using electronically generated input signals can be seen to be within ±0.15 percent. This accuracy appears to be in good agreement with the predicted accuracy of the electronic circuitry (approximately 0.12 percent) obtained during the preliminary research phase of the program.

## SYSTEM PERFORMANCE TESTS

These tests were performed to determine the overall performance of the system including the sensing pickups and the measurement electronics. Data were also taken directly from the counters of the coincidence interpolation and measurement logic brassboard through the measurement output display device. Twist angle was adjusted by displacing one pickup with respect to

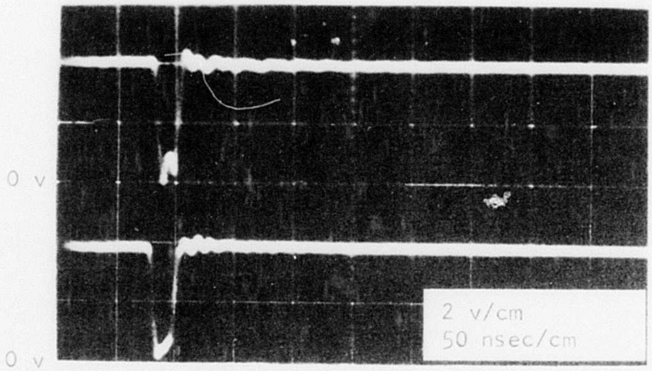

Figure 88. Timing Marks Generated by Probe A and Probe B Signals.

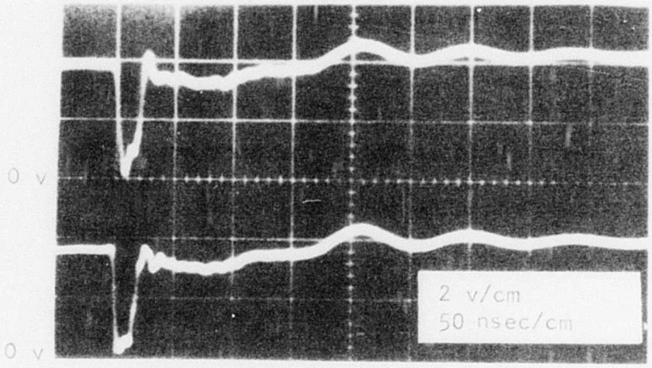

Figure 89. Coincidence Pulses of the Two Signal Paths.

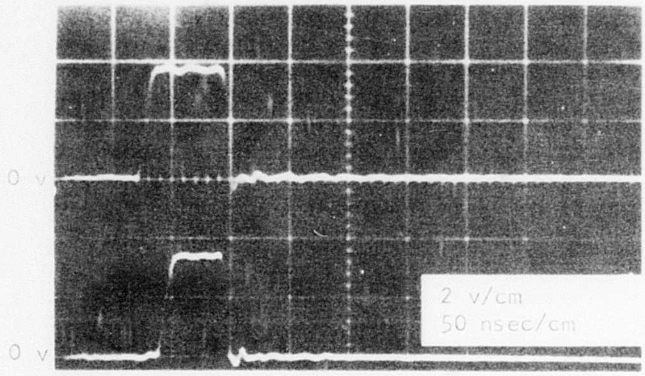

Figure 90. Counter Control Pulses of the Two Signal Paths.

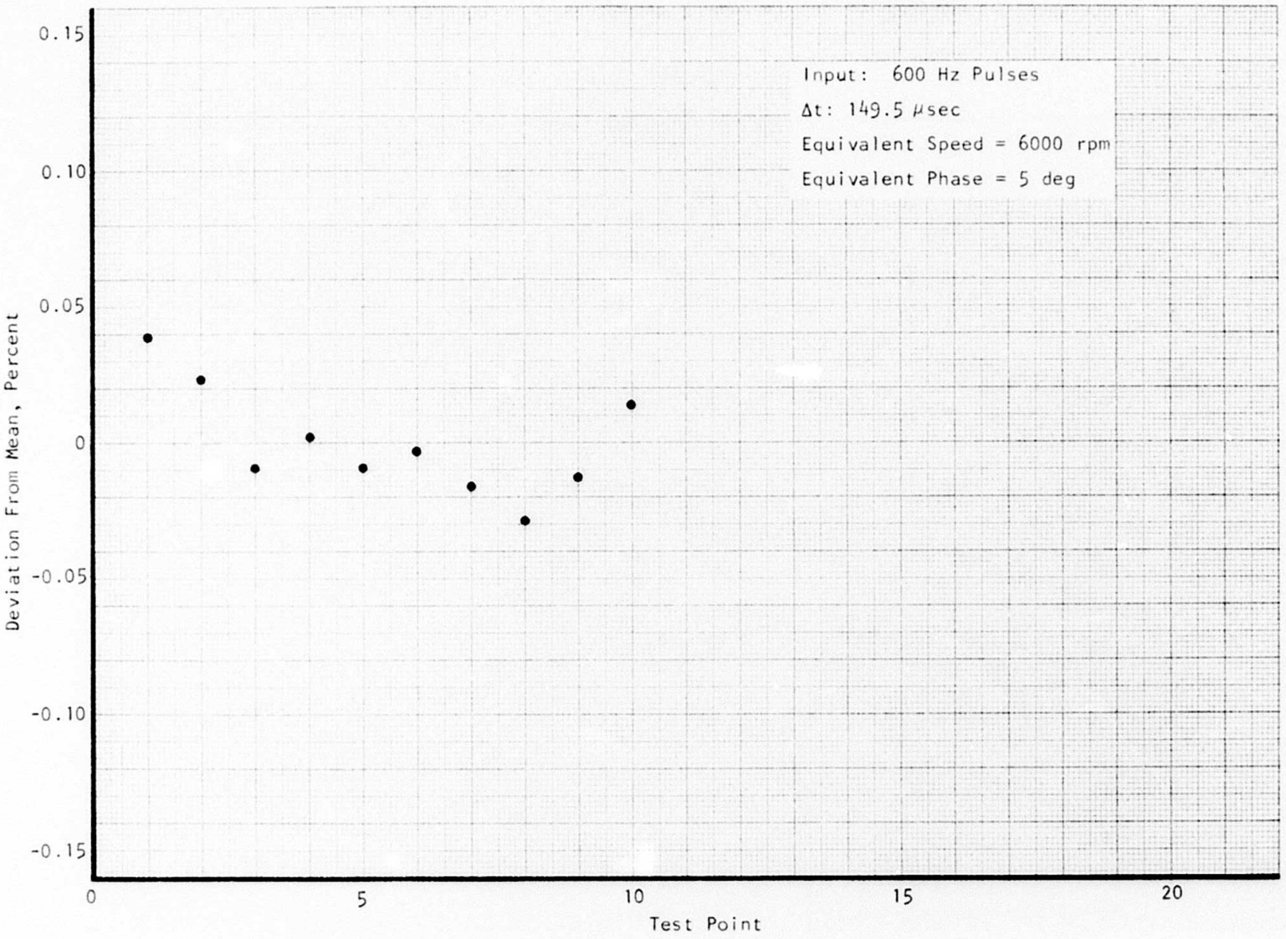

Figure 91. Performance of Electronics at 600 Hz.

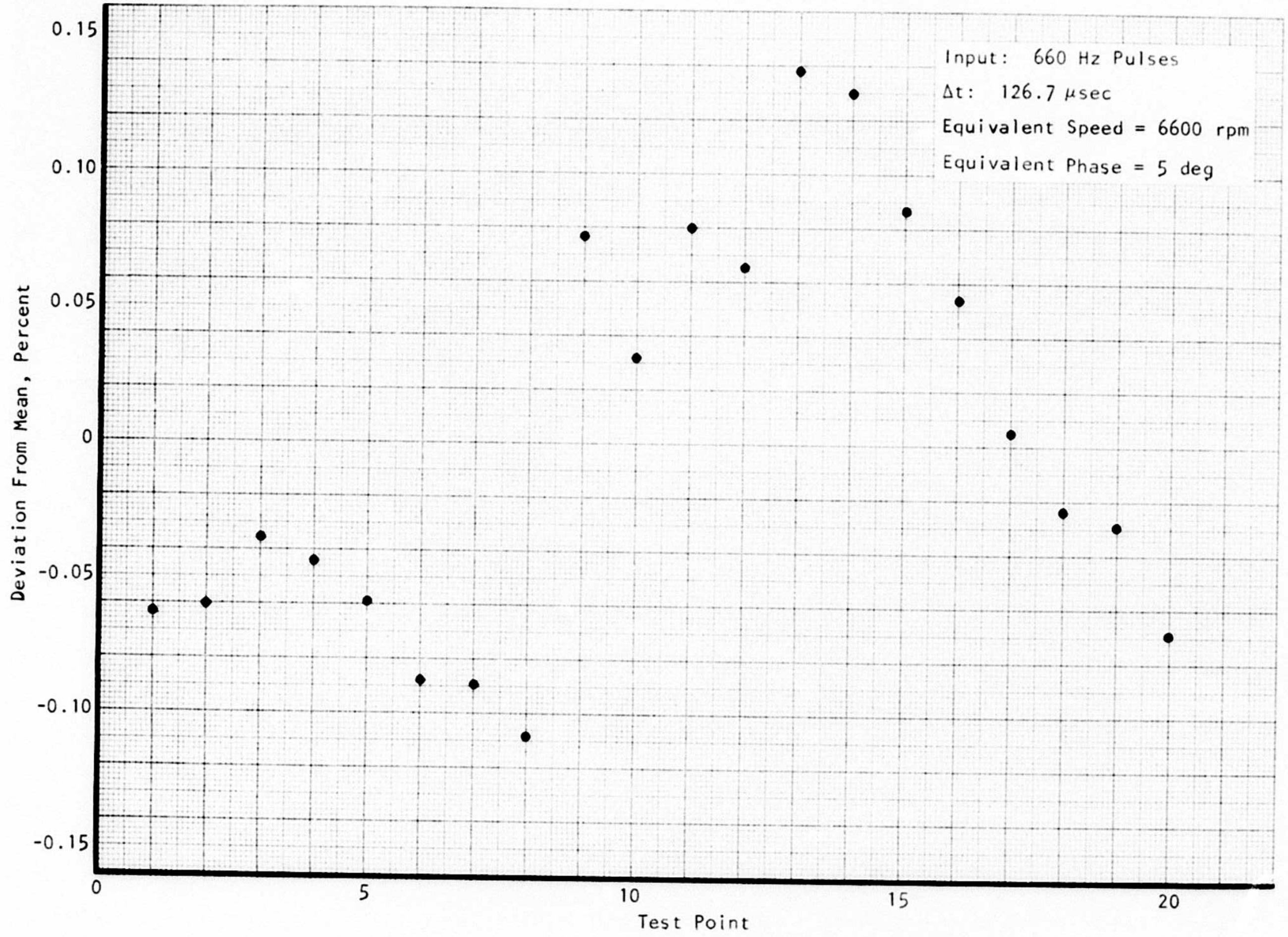

Figure 92. Performance of Electronics at 660 Hz.

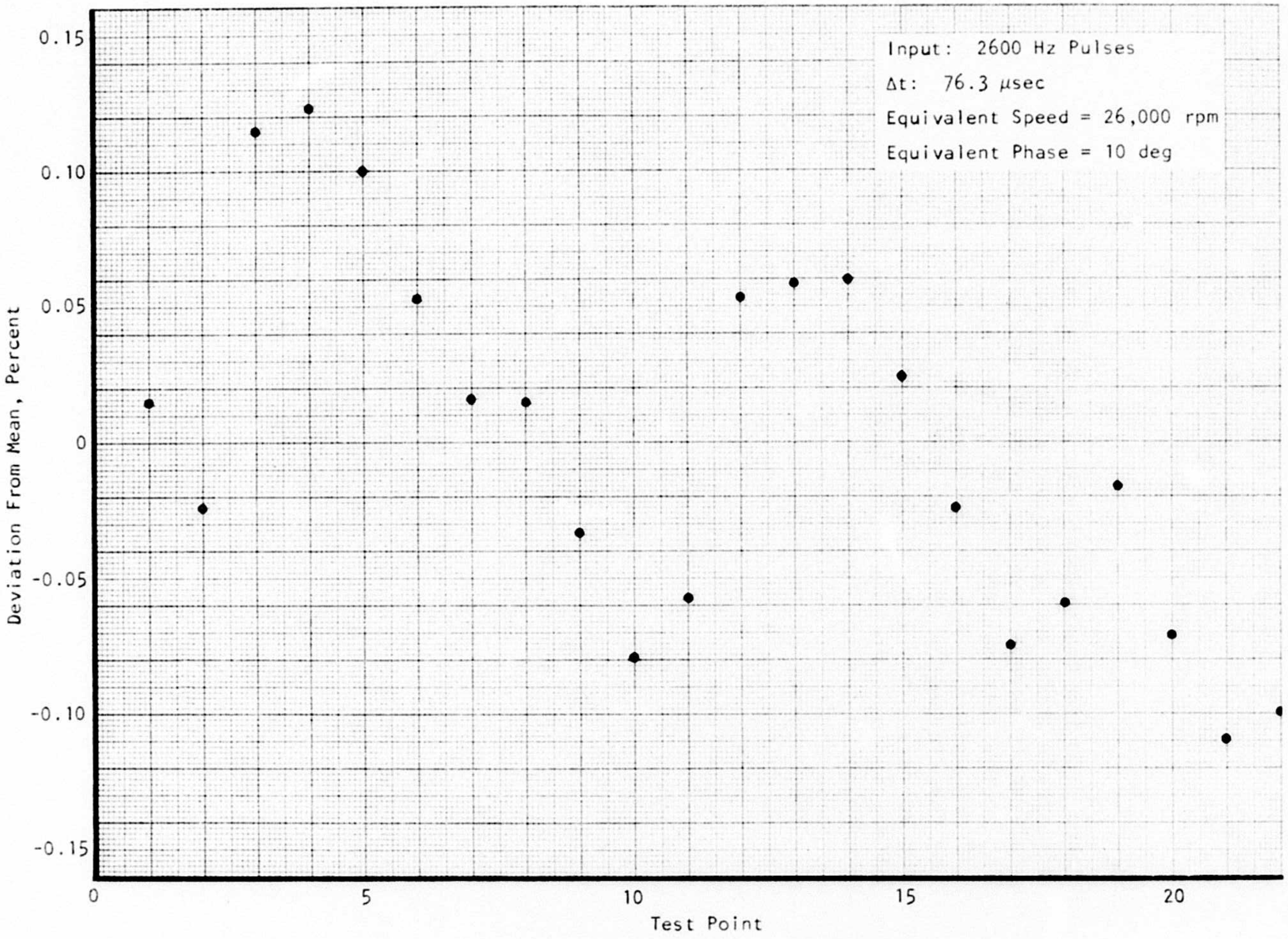

Figure 93. Performance of Electronics at 2600 Hz.

the other through the micrometer mechanism instead of actually torquing the shaft. Twist angle was computed and the digital integration was performed on the Univac 1108 computer following the same computation equations. Table XV shows a sample of the computer printouts. Four basic types of tests were performed under this test sequence. They are: (1) speed tests, (2) temperature tests, (3) performance tests at one-third full scale, and (4) oil contamination tests.

## Speed Tests

Data were taken from the measurement electronics at ambient temperature for various shaft speeds under two phase angle settings: 5 deg, corresponding to the full-scale torque level of external applications, and 9.6 deg, corresponding to the internal application. The value of 9.6 deg was used instead of 10 deg as full scale for internal application because of the limitation of the micrometer adjustment mechanism due to a slightly longer spring in the holder. This limitation can be easily corrected by shortening this contact spring. However, data taken under this setting should also be representative for the 10-deg case. The percentage deviations of the computed phase angle for various speed levels are shown in Figures 94 through 103. The accuracy of the majority of the measurements lies well within the ±1 percent error band (as shown by dotted lines on the plots). Only a few test points in the 10,000-rpm and 14,000-rpm test sequences exceed the ±1 percent band. This exceedance is believed to be caused by the shaft resonant frequency of the test unit, which is found to be in the range from 11,000 rpm to 16,000 rpm. This shaft resonant frequency range is a peculiar property of the test unit. It is anticipated that this resonant frequency range will be outside the normal operating speed range of an actual engine or drive shaft. Therefore, the effect of shaft resonance on system accuracy should be small on a normally torqued shaft.

## Temperature Tests

These tests were performed in a manner similar to the previous speed tests except that temperature became the variable. The shaft speed was held at 6000 rpm and 24,000 rpm for external and internal application cases, respectively. Phase angles of 5 deg and 9.6 deg were used for the external and internal applications, respectively. Test results were computed by the use of the same computer program. Variations of measurement at different test points, but under the same temperature and speed conditions, were plotted on a percentage basis.

Variation of test accuracy at different temperature levels is shown in Figures 103 through 111. Again, the test accuracy is well within the ±1 percent band, except for the high-temperature test at 445°F, where oxidation of the phasing gear was observed. It is suspected that the degradation in measurement accuracy could be due to the oxidation, because it changes the magnetic property of the phasing gear pole piece. However, by using ferromagnetic stainless steel material for the phasing gears, this oxidation problem can be minimized, or removed.

TABLE XV. SAMPLE PRINTOUT - 6000 RPM, 5.06 DEG

```
  I        N1        N2        N3        N4     INTGD DEL T     INTGD PHI
  1      6.00  12640.00      9.00  22374.00     141.310110      5.073891
  2      3.00   5204.00      5.00  12489.00     141.192240      5.070497
  3      5.00  10197.00      6.00  14985.00     141.033600      5.065621
  4      3.00   5230.00      5.00  12549.00     140.996230      5.063834
  5      4.00   7695.00      3.00   7491.00     140.747370      5.055736
  6      4.00   7721.00     11.00  27541.00     140.704920      5.054356
  7      1.00    209.00      1.00   2510.00     140.637320      5.051439
  8      7.00  15248.00      2.00   5014.00     140.473080      5.045377
  9      4.00   7736.00      1.00   2505.00     140.817120      5.057778
 10      3.00   5237.00      6.00  15079.00     140.799460      5.056365
 11      8.00  17732.00      1.00   2503.00     140.793810      5.056443
 12      2.00   2719.00      3.00   7531.00     140.710640      5.052990
 13      3.00   5263.00      2.00   5054.00     140.642750      5.048460
 14      8.00  17755.00      1.00   2506.00     140.711610      5.051025
 15      2.00   2724.00      1.00   2516.00     140.610330      5.046487
 16     20.00  48054.00      1.00   2516.00     141.914320      5.092254
 17      5.00  10317.00      2.00   5055.00     141.719560      5.083339
 18      1.00    211.00      1.00   2530.00     141.667900      5.079370
 19      2.00   2717.00     12.00  30086.00     141.579930      5.076481
 20      1.00    207.00     27.00  67172.00     141.401890      5.072270
 21     10.00  22671.00      3.00   7483.00     141.732830      5.085661

AVE PHI    =      5.063794
SIGMA(PHI)=        .013630
PCT SPREAD=          .2692
```

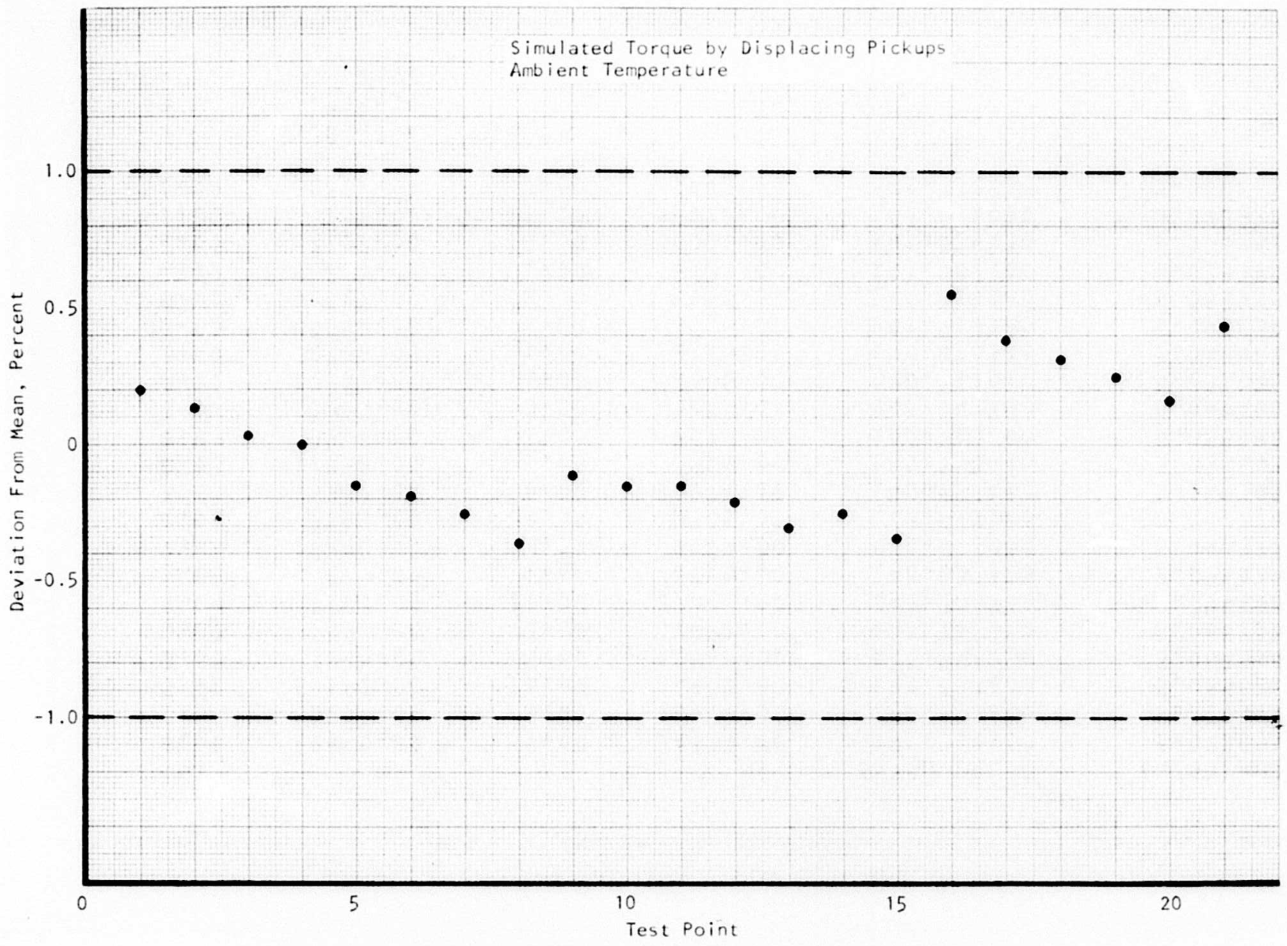

Figure 94. System Performance vs Speed, 6000 RPM, 5 Deg.

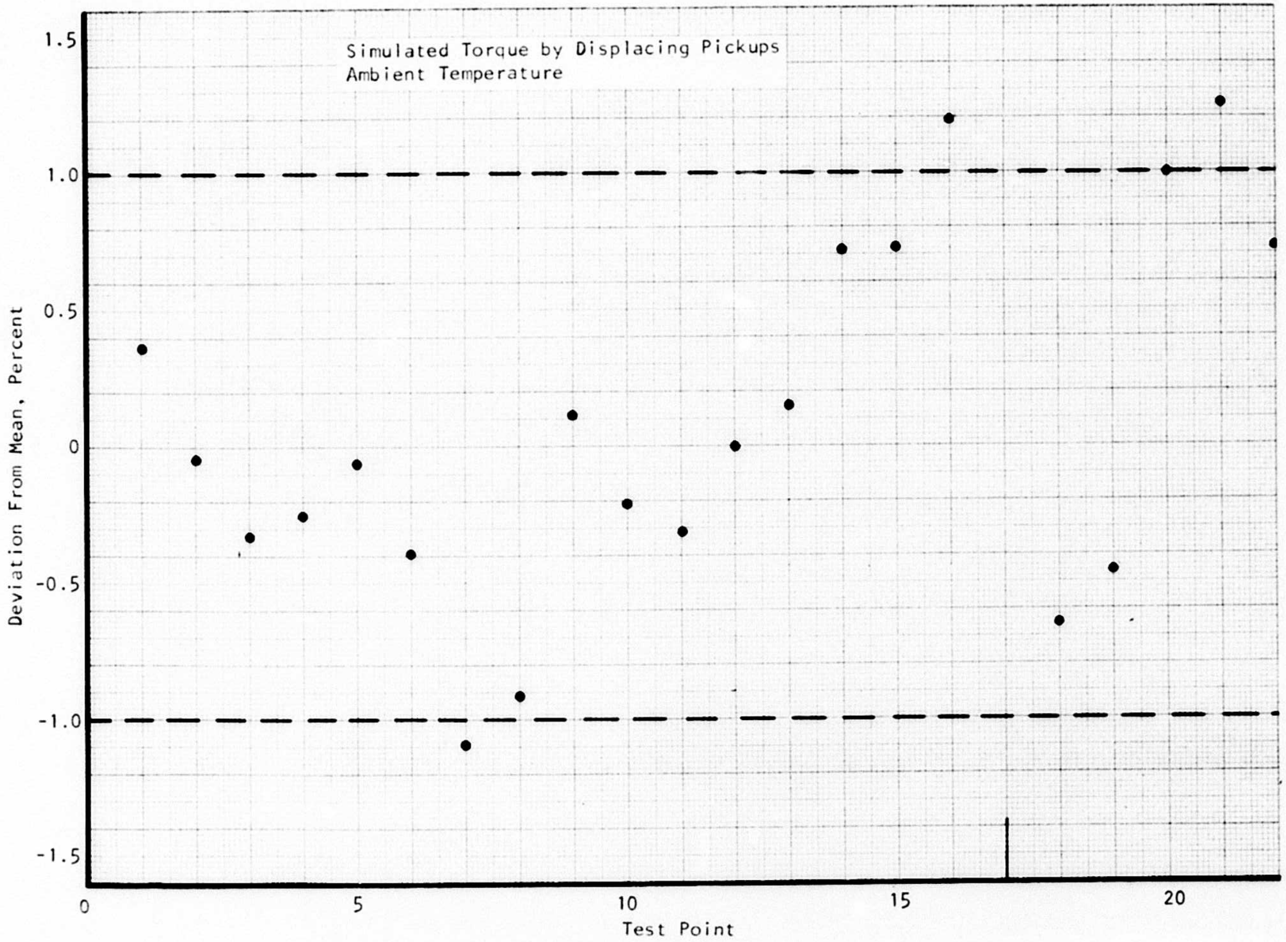

Figure 95. System Performance vs Speed, 10,000 RPM, 5 Deg.

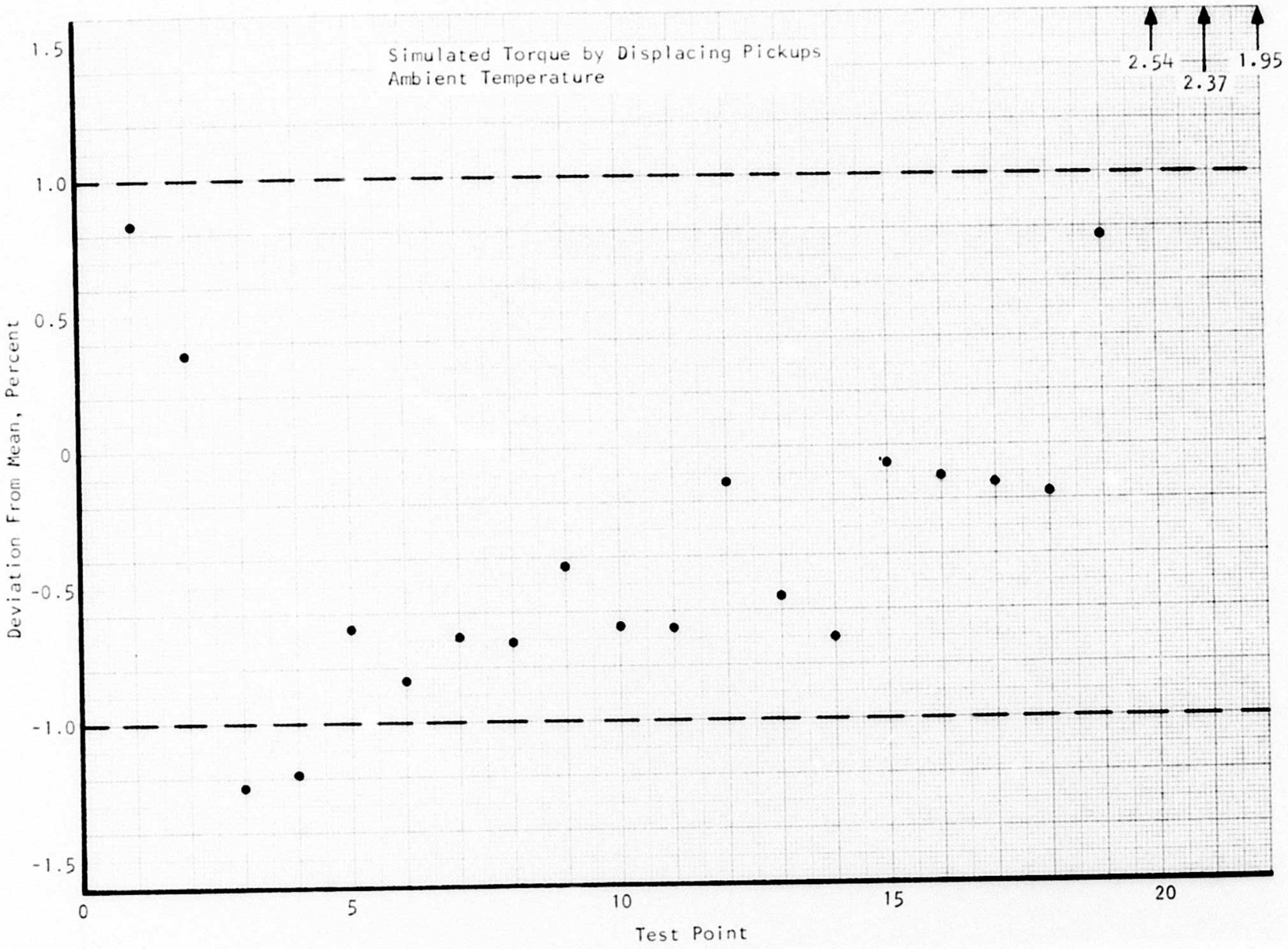

Figure 96. System Performance vs Speed, 14,000 RPM, 5 Deg.

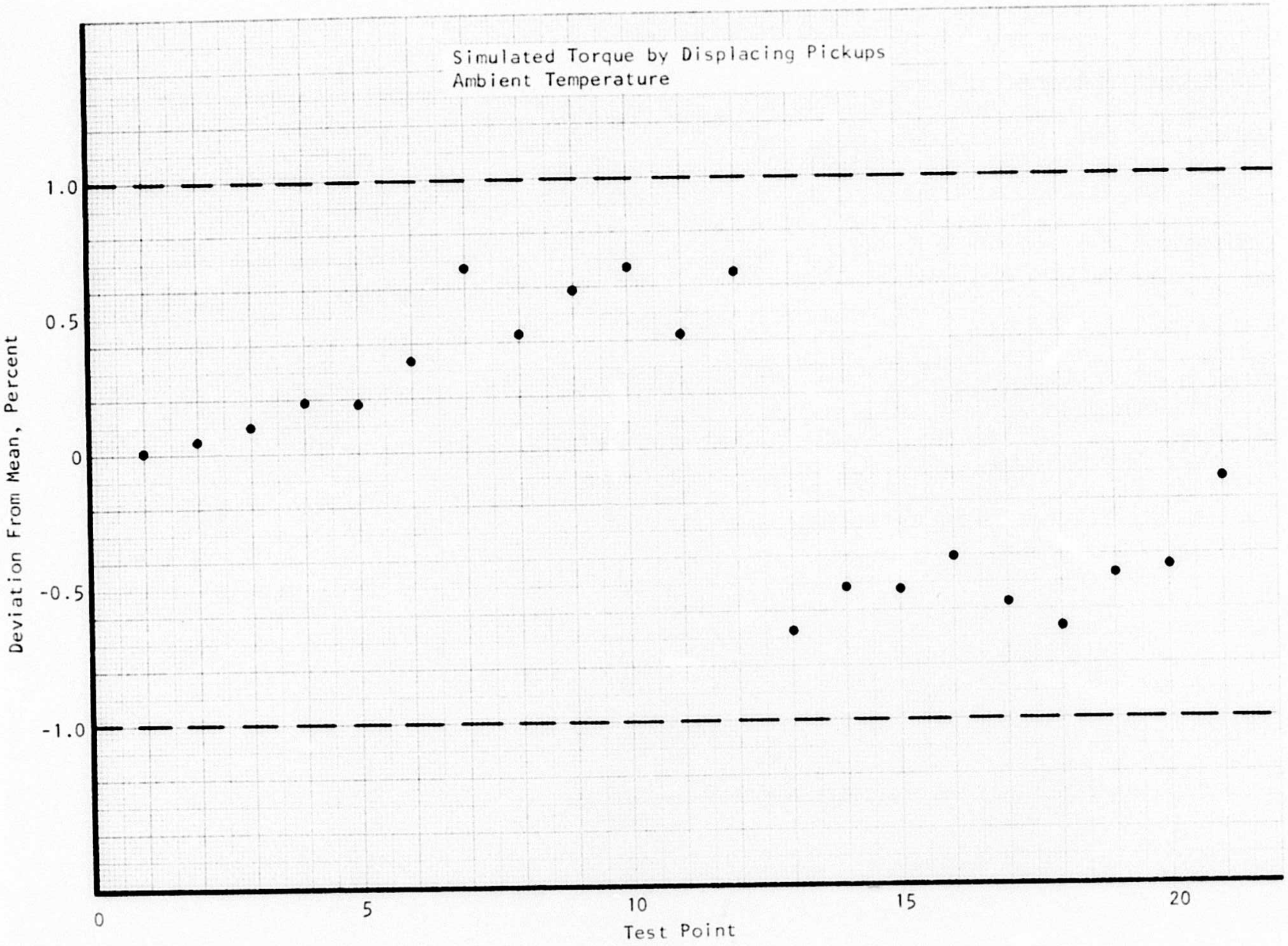

Figure 97. System Performance vs Speed, 18,000 RPM, 5 Deg.

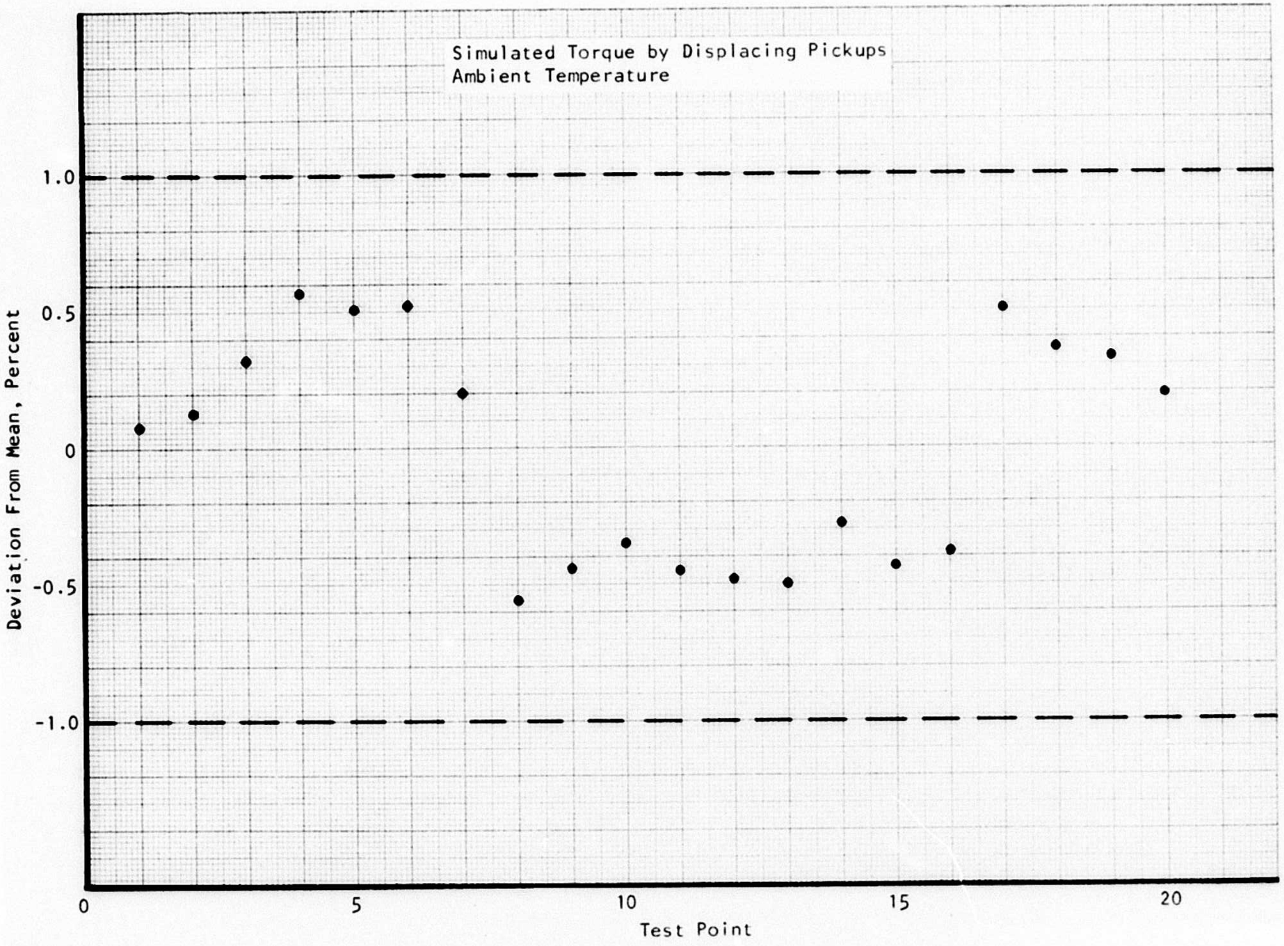

Figure 98. System Performance vs Speed, 22,000 RPM, 5 Deg.

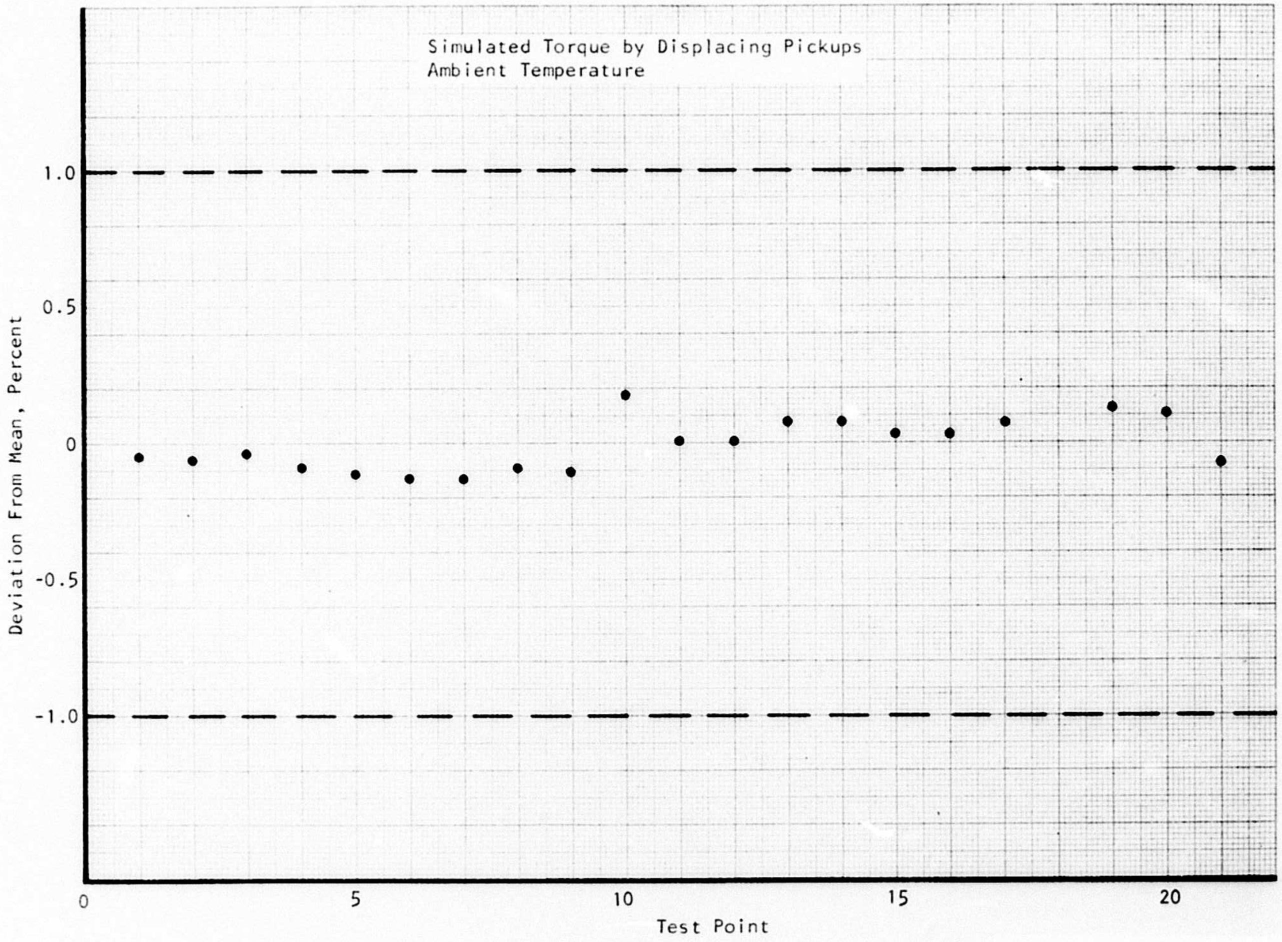

Figure 99. System Performance vs Speed, 6000 RPM, 9.6 Deg.

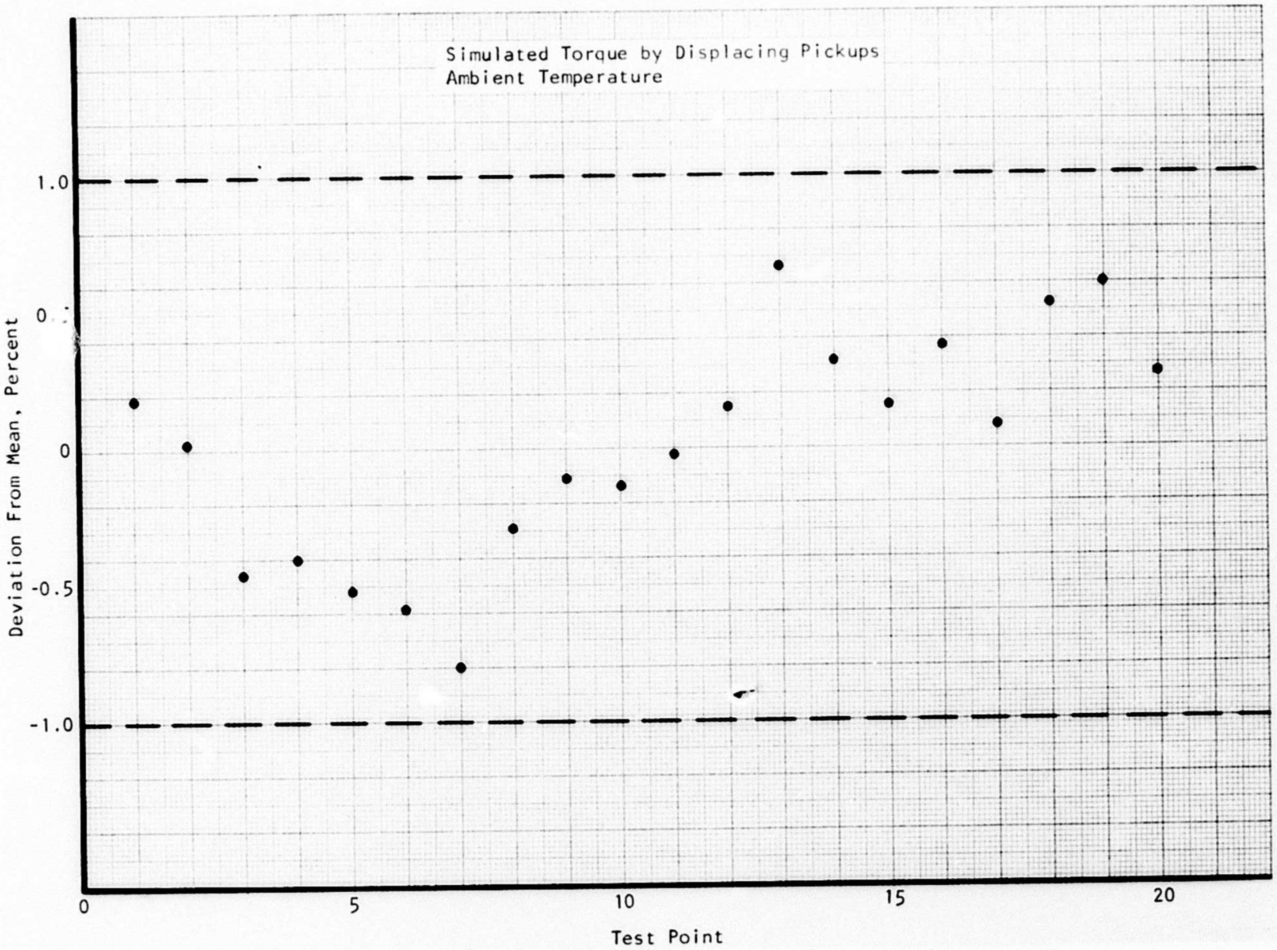

Figure 100. System Performance vs Speed, 10,000 RPM, 9.6 Deg.

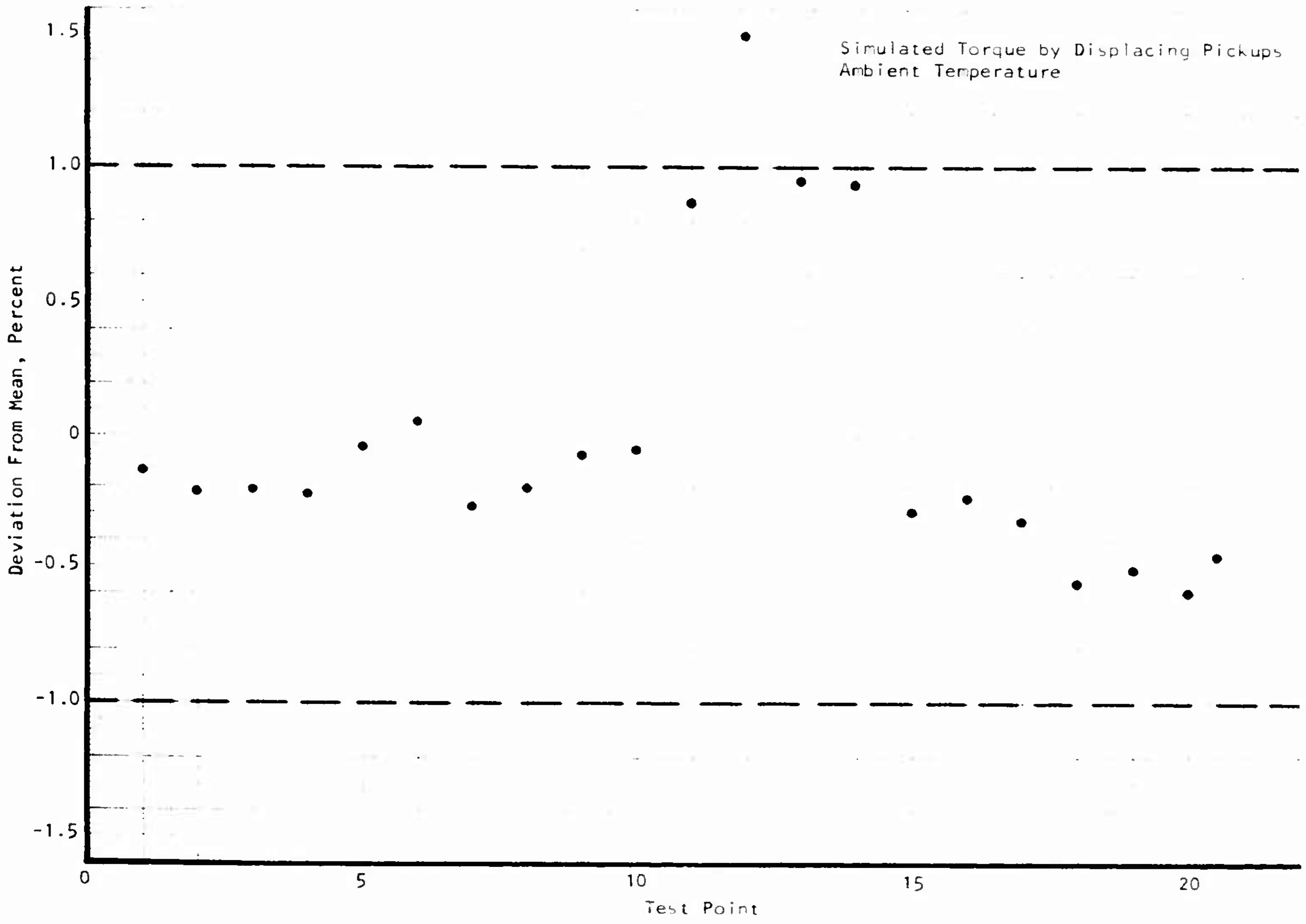

Figure 101. System Performance vs Speed, 14,000 RPM, 9.6 Deg.

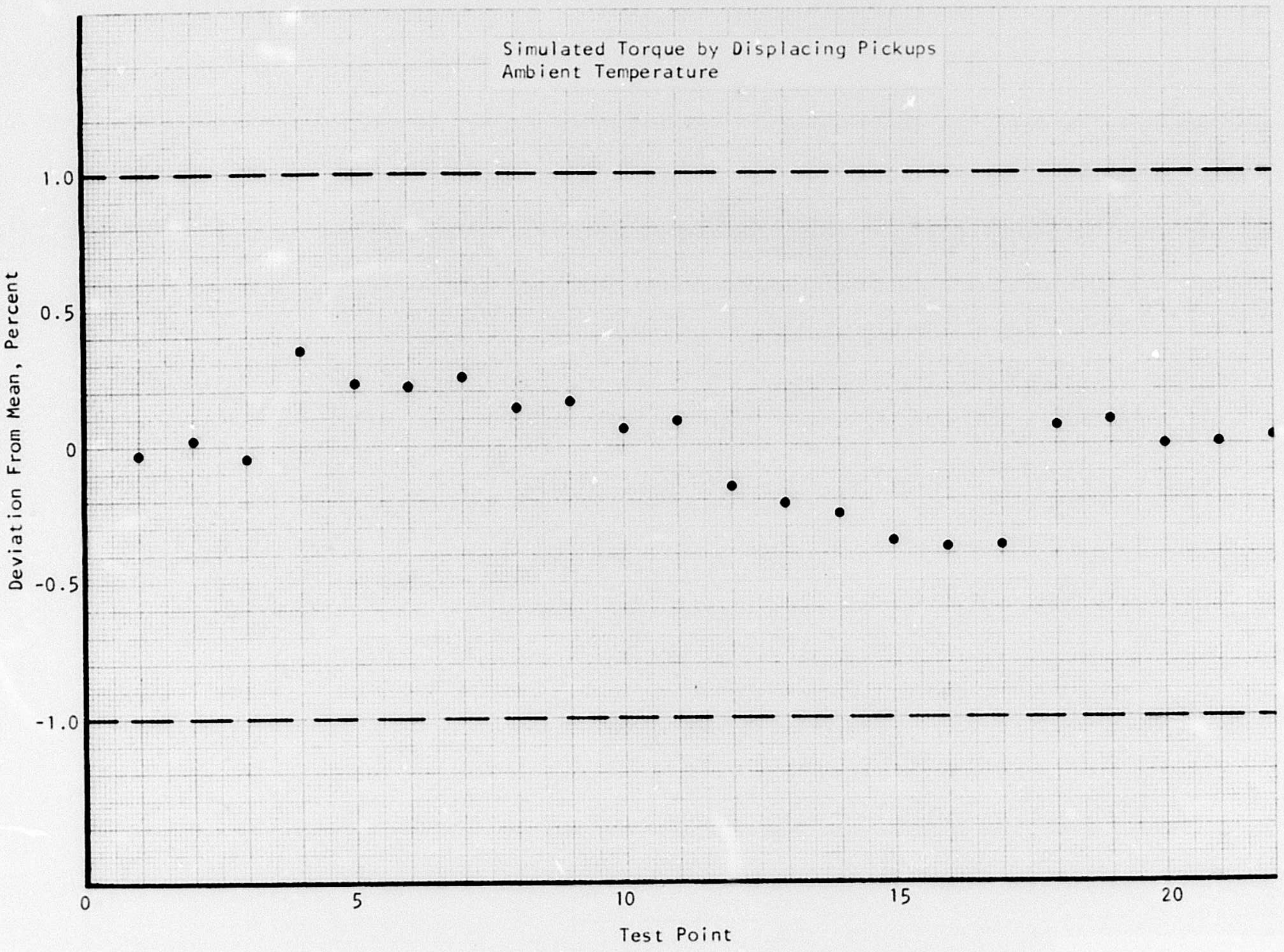

Figure 102. System Performance vs Speed, 18,000 RPM, 9.6 Deg.

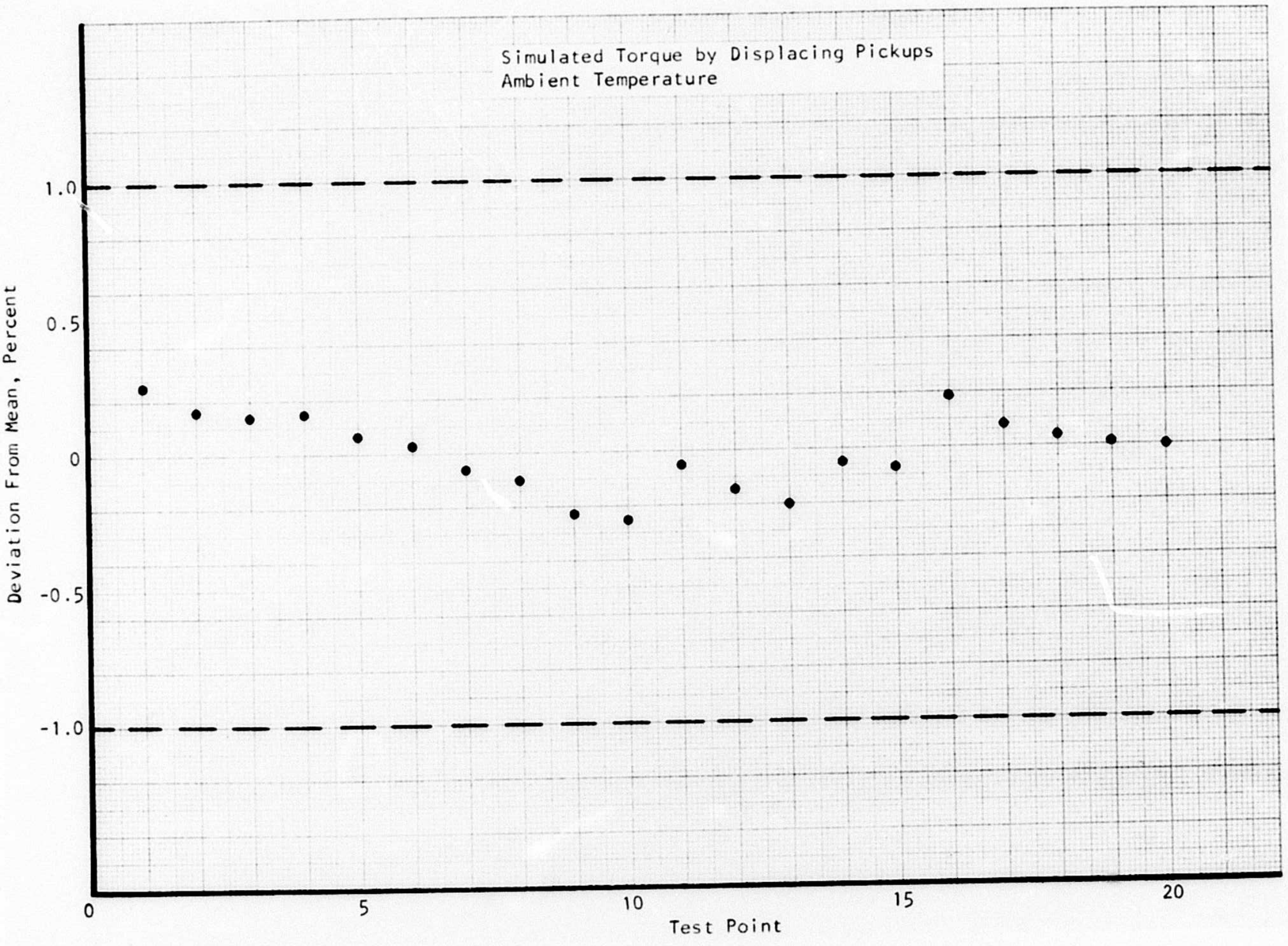

Figure 103. System Performance vs Speed, 22,000 RPM, 9.6 Deg.

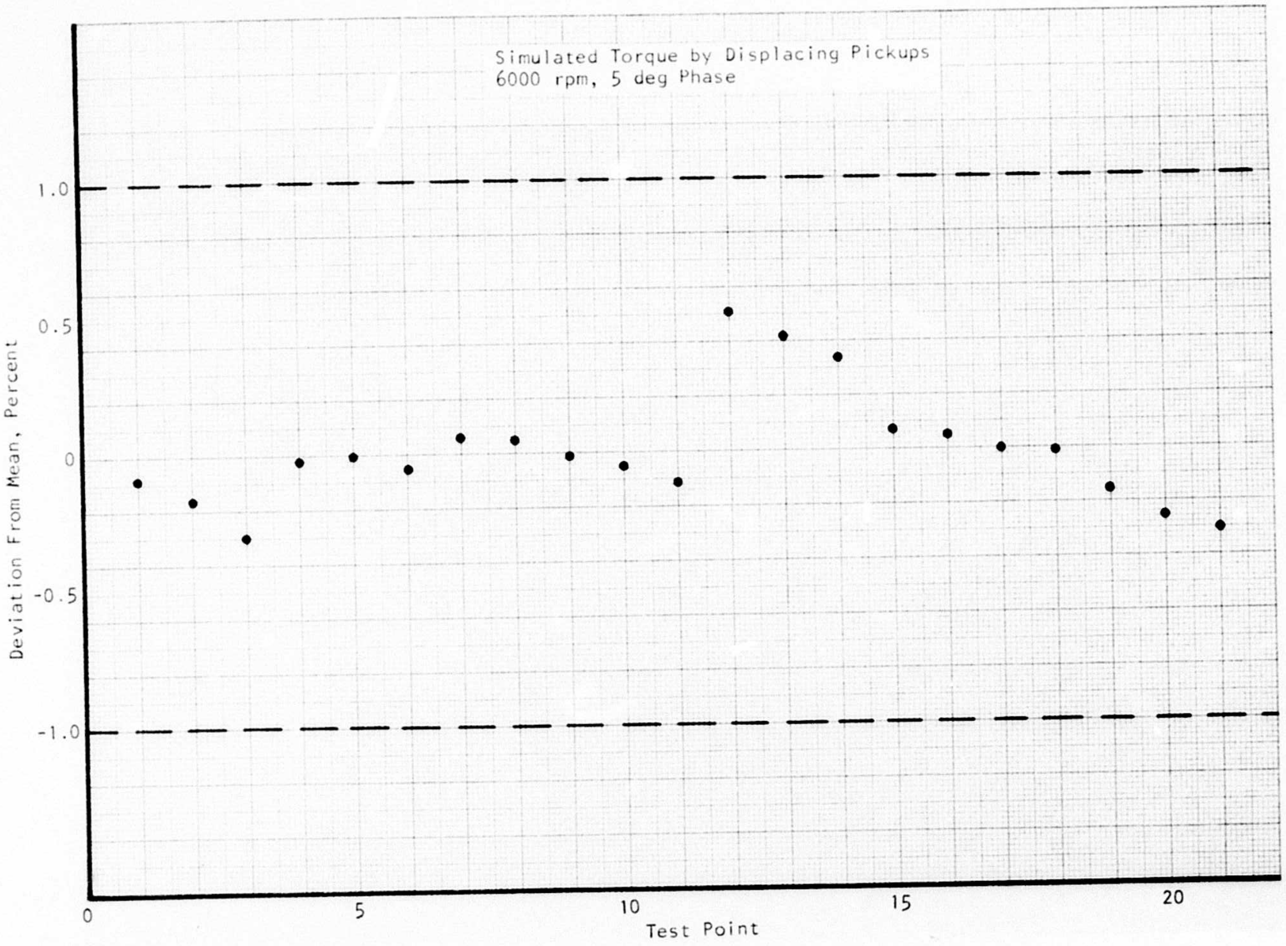

Figure 104. System Performance vs Temperature, -35°F, 6000 RPM.

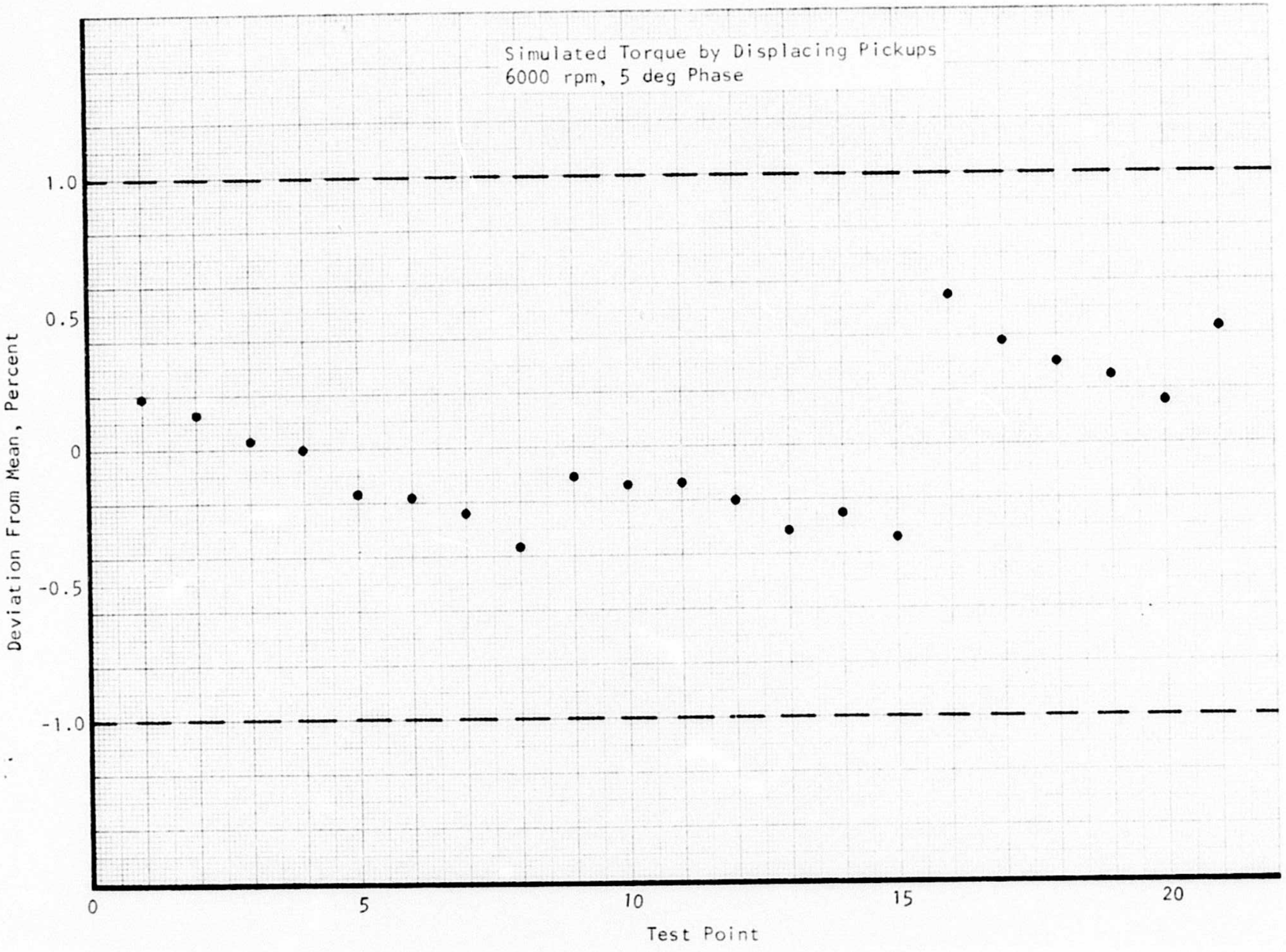

Figure 105. System Performance vs Temperature, 75°F, 6000 RPM.

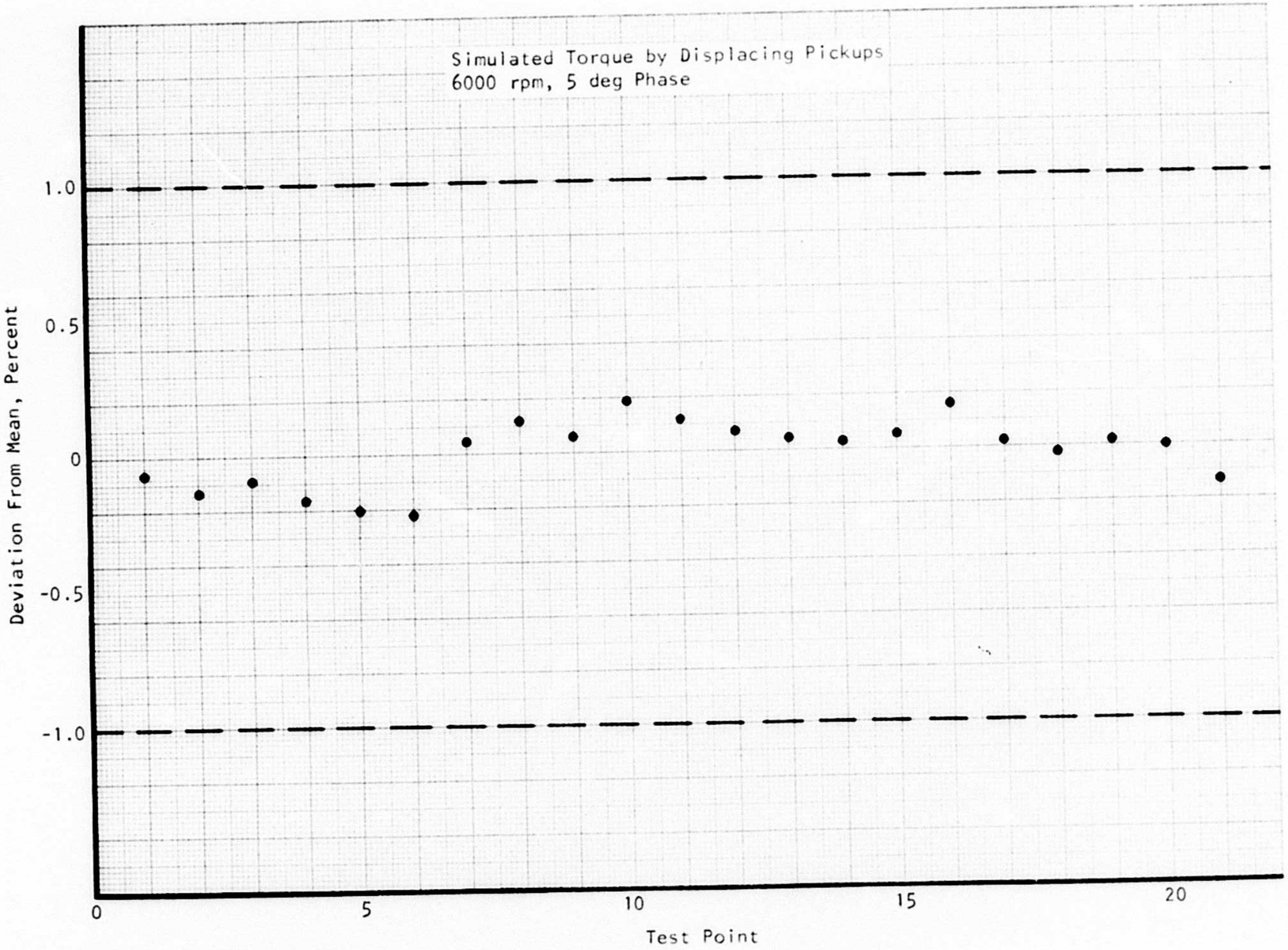

Figure 106. System Performance vs Temperature, $200^{\circ}$F, 6000 RPM.

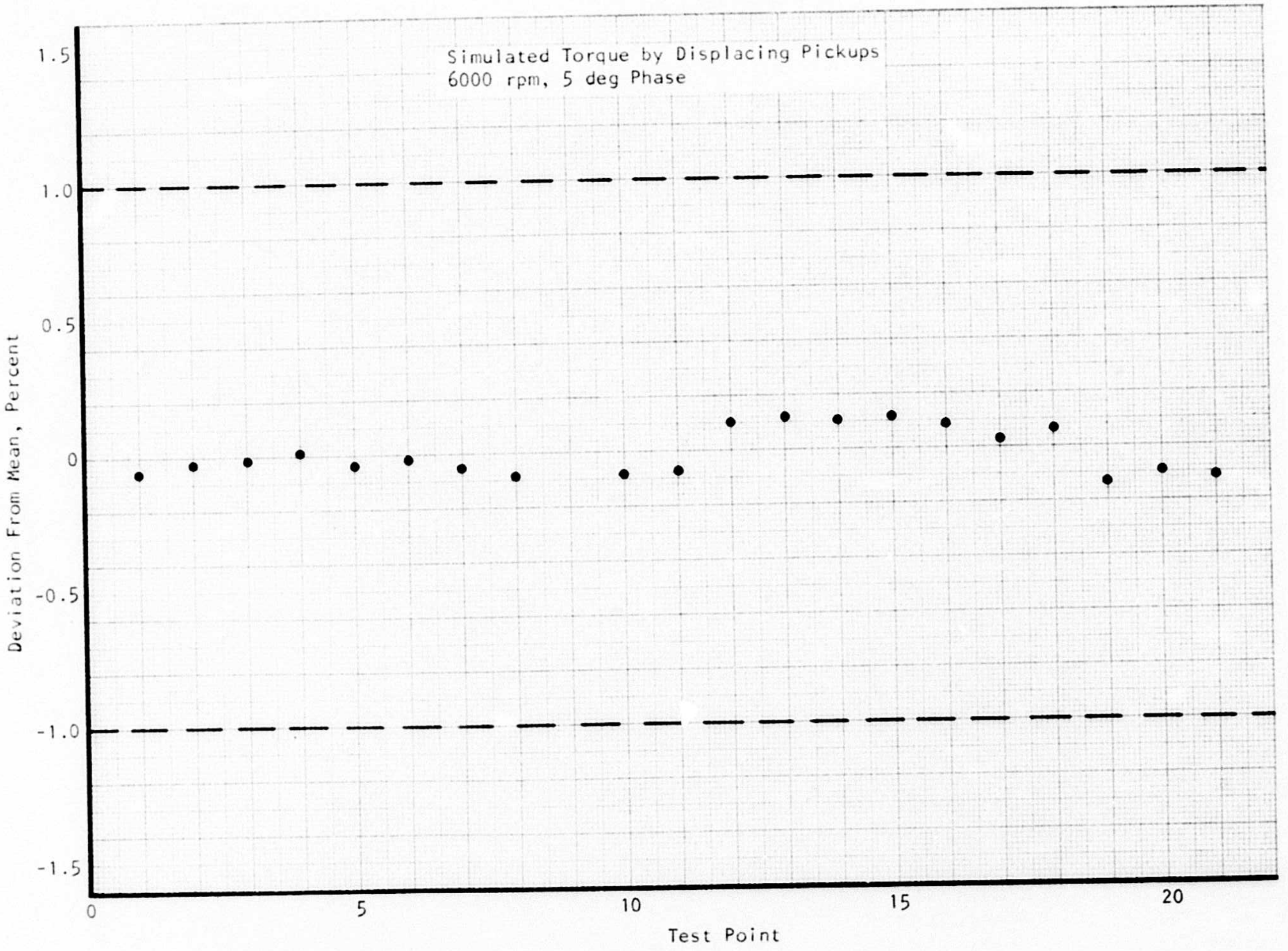

Figure 107. System Performance vs Temperature, 400°F, 6000 RPM.

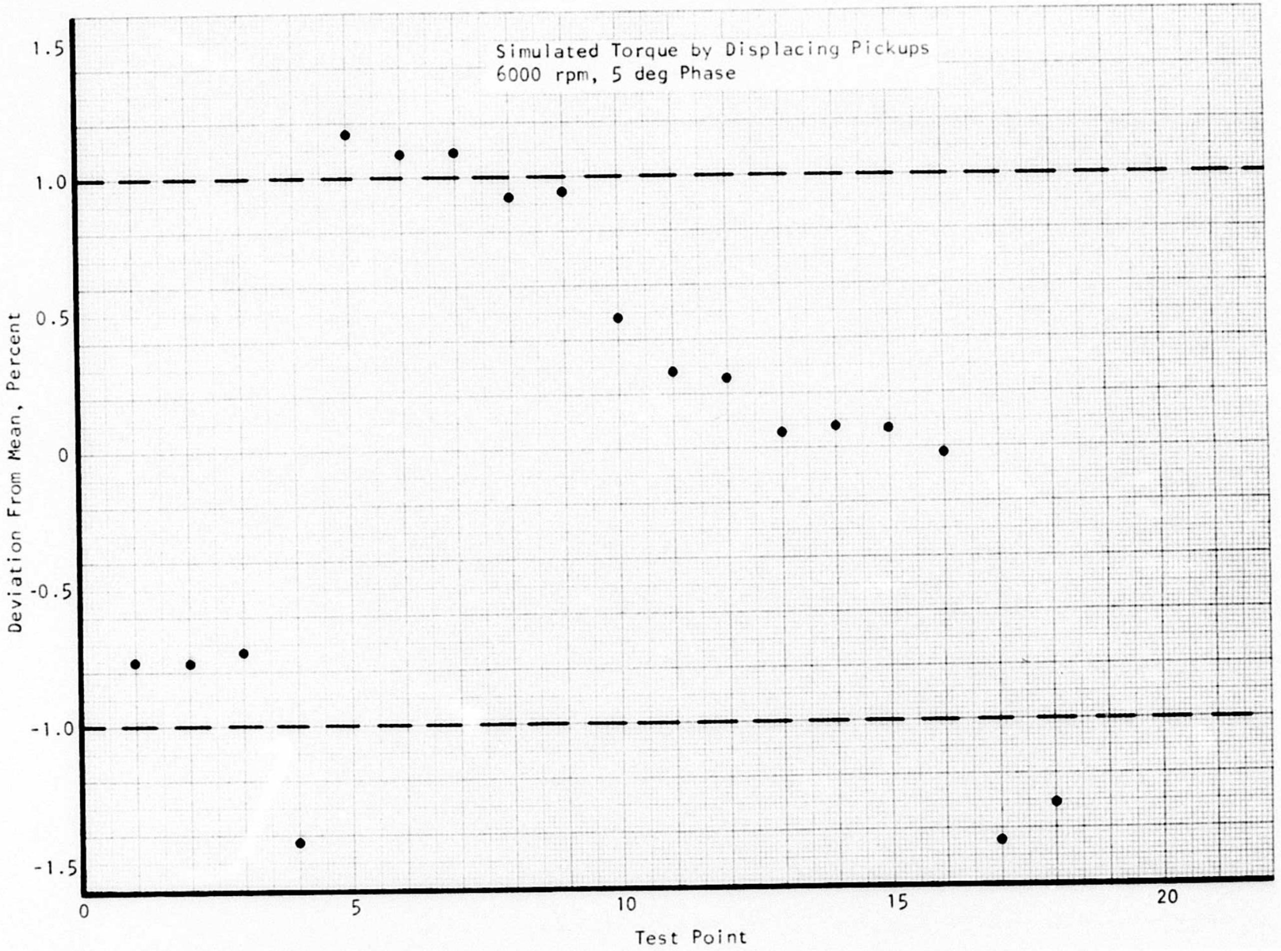

Figure 108. System Performance vs Temperature, 445°F, 6000 RPM.

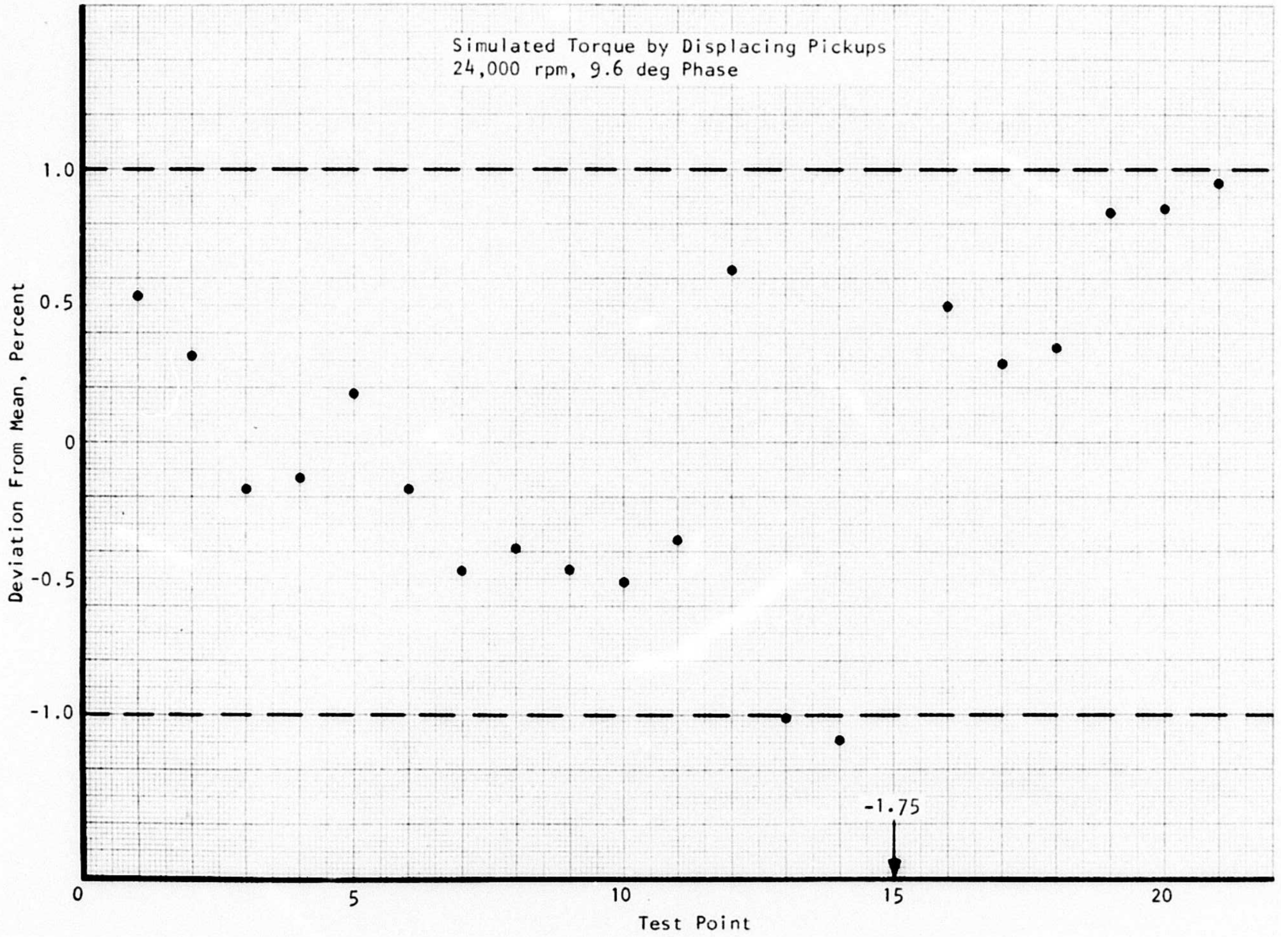

Figure 109. System Performance vs Temperature, $-35^{\circ}F$, 24,000 RPM.

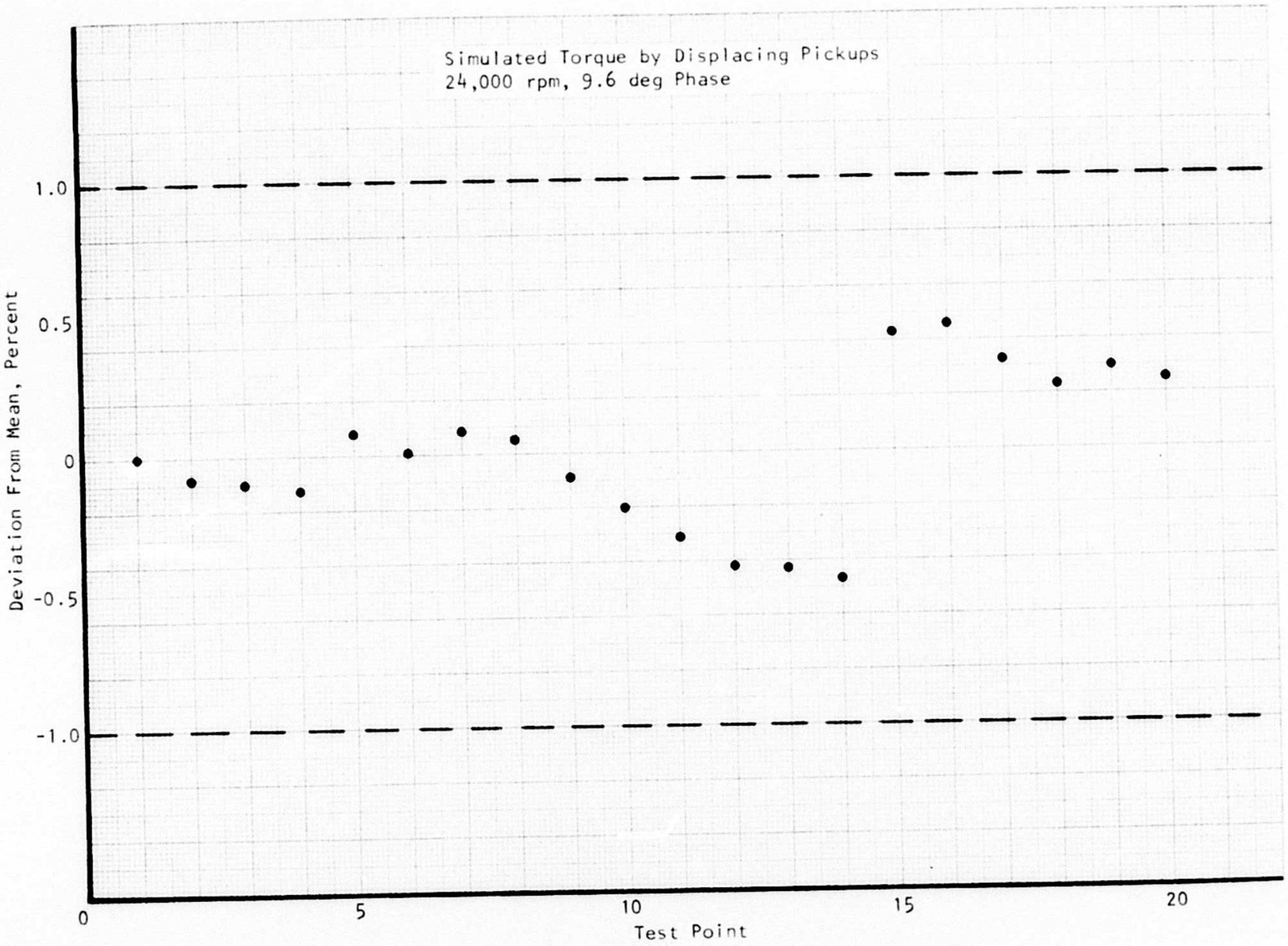

Figure 110. System Performance vs Temperature, 75°F, 24,000 RPM.

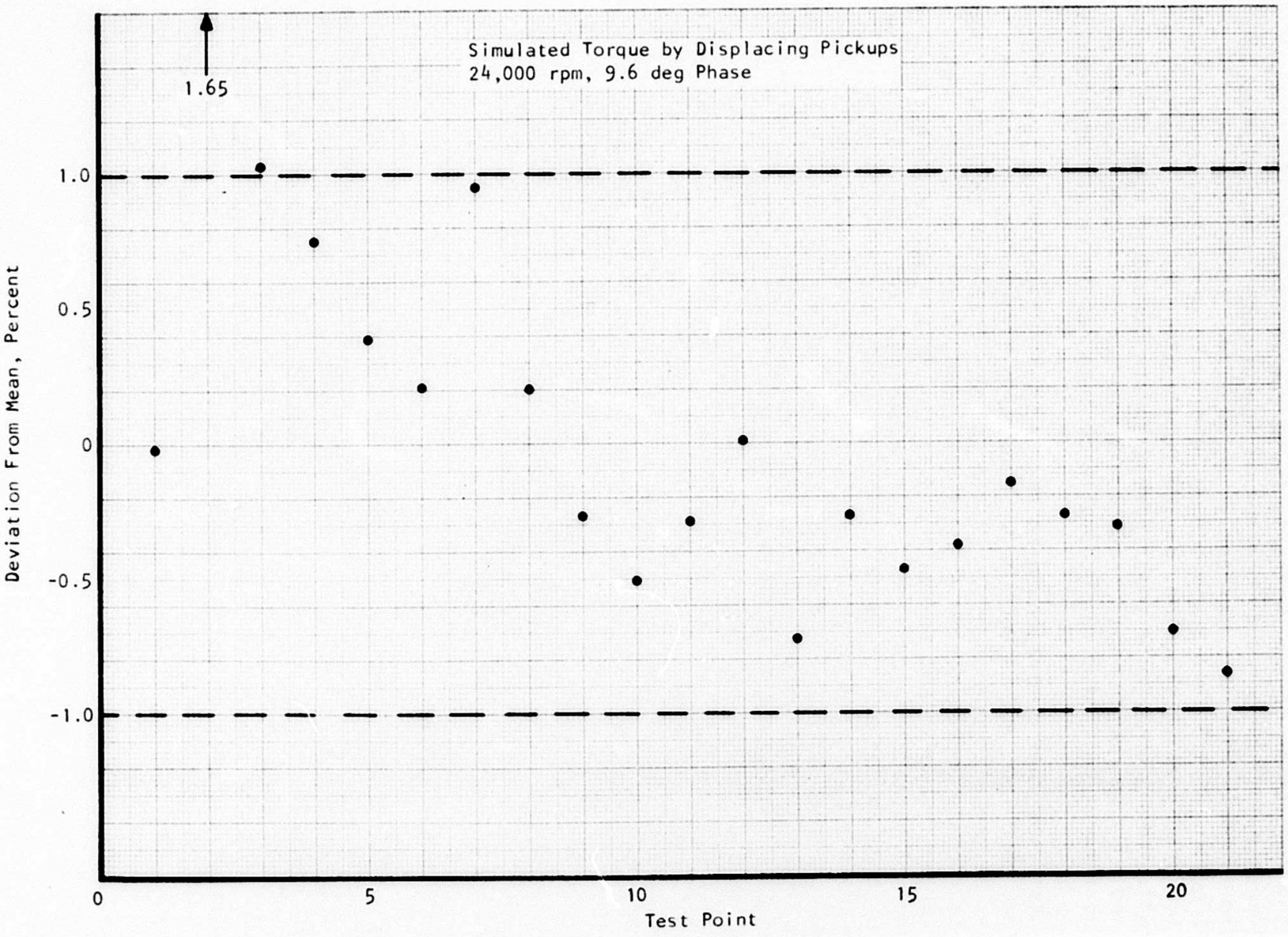

Figure 111. System Performance vs Temperature, $400^{\circ}$F, 24,000 RPM.

## Performance at One-Third of Full Scale

Since the resolution of the system is fixed due to fixed width of the coincidence gate, the percentage error of measurement is anticipated to increase linearly with the decrease in torque level to be measured. Theoretically, at 1/3 full-scale torque level, the percentage error should be three times greater than that of the full scale. However, due to the fact that sensing unit noise amplitudes also are dependent upon the torque level and will be reduced with reduction in torque, a system accuracy better than the theoretical value can generally be obtained in actual application.

Three test runs that corresponded to the 1/3 full-scale torque levels at 6000 rpm, 6600 rpm, and 24,000 rpm were performed to assess the system accuracy at these torque levels. In view of the fact that the actual shaft would be running approximately at constant speed, one-third of the full-scale torque is equivalent to one-third of the full-scale phase angle. In the external application case, this 1/3 phase angle was 1.67 deg. In the internal application case, one-third of full scale was taken as 3.2 deg. The tests were conducted under the ambient temperature environment. Test results were then computed and are plotted in Figures 112 through 114. For the two external application cases at 6000 rpm and 6600 rpm nominal speeds, test results indicate that an accuracy of better than 1 percent can be accomplished at one-third of the full-scale torque levels. For the internal application case, there are a considerable number of exceedances of the 1 percent level during the test run. In view of the fact that good accuracy was achieved at high-temperature runs with the same speed conditions, but with a clamped-down adjustment arm, it was suspected that this deterioration in accuracy at 1/3 full scale for internal application could be caused by the motion of the micrometer due to the vibration at high speed. This will not be a problem of the actual sensing unit because the micrometer mechanism will be eliminated and the twist angle will be created by actual application of torque to the shaft.

## Oil Contamination Tests

Oil contamination tests were performed to determine if there is any deterioration in system accuracy which could be caused by the presence of engine oil at the sensing unit. Clean automobile engine oil was sprayed into the test sensing unit. Both monopole pickups and eddy-current probes were fully soaked. Tests were then conducted at the three nominal speed levels (i.e., 6000 rpm, 6600 rpm and 24,000 rpm) with the corresponding full-scale phase angles set at the sensing unit. Temperature of the test unit was regulated by the Colburn Instrument oven to be close to $75^{\circ}$F. Figures 115 through 117 present the results of the tests. No deterioration in system performance can be noticed from these test results. There was no physical damage to the sensing unit and probes observed during these tests.

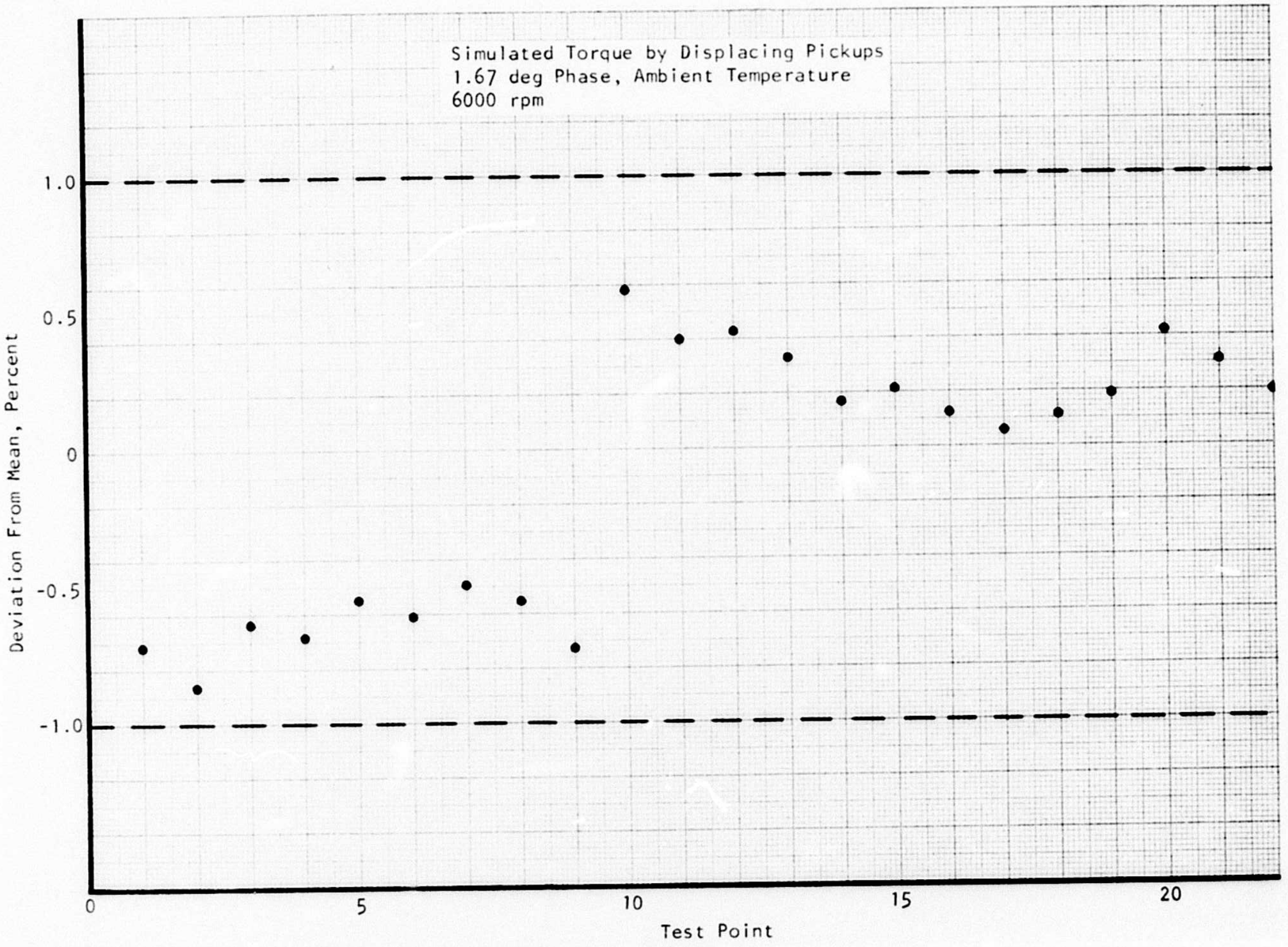

Figure 112. System Performance at 1/3 Full Scale, 6000 RPM.

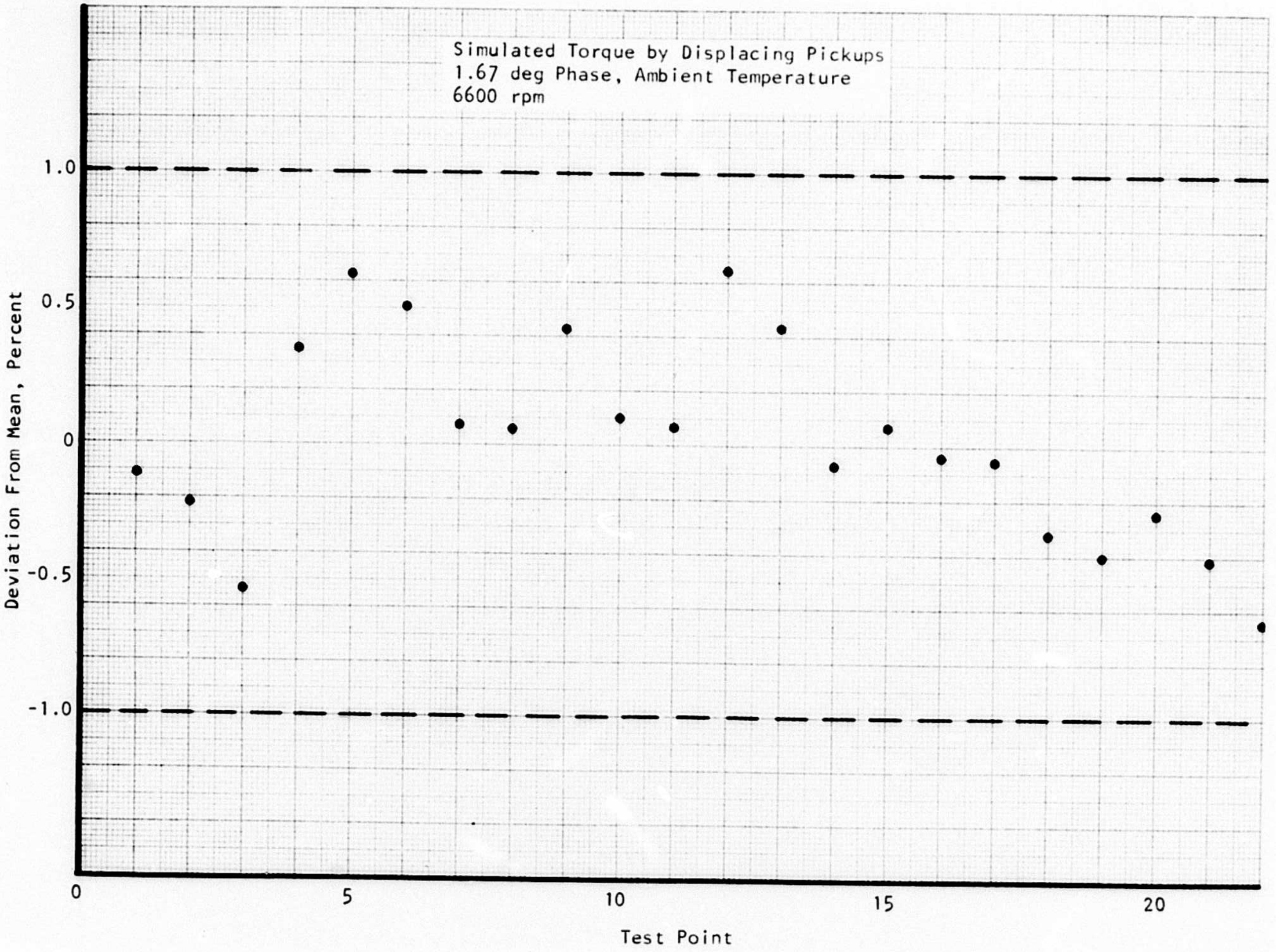

Figure 113. System Performance at 1/3 Full Scale, 6600 RPM.

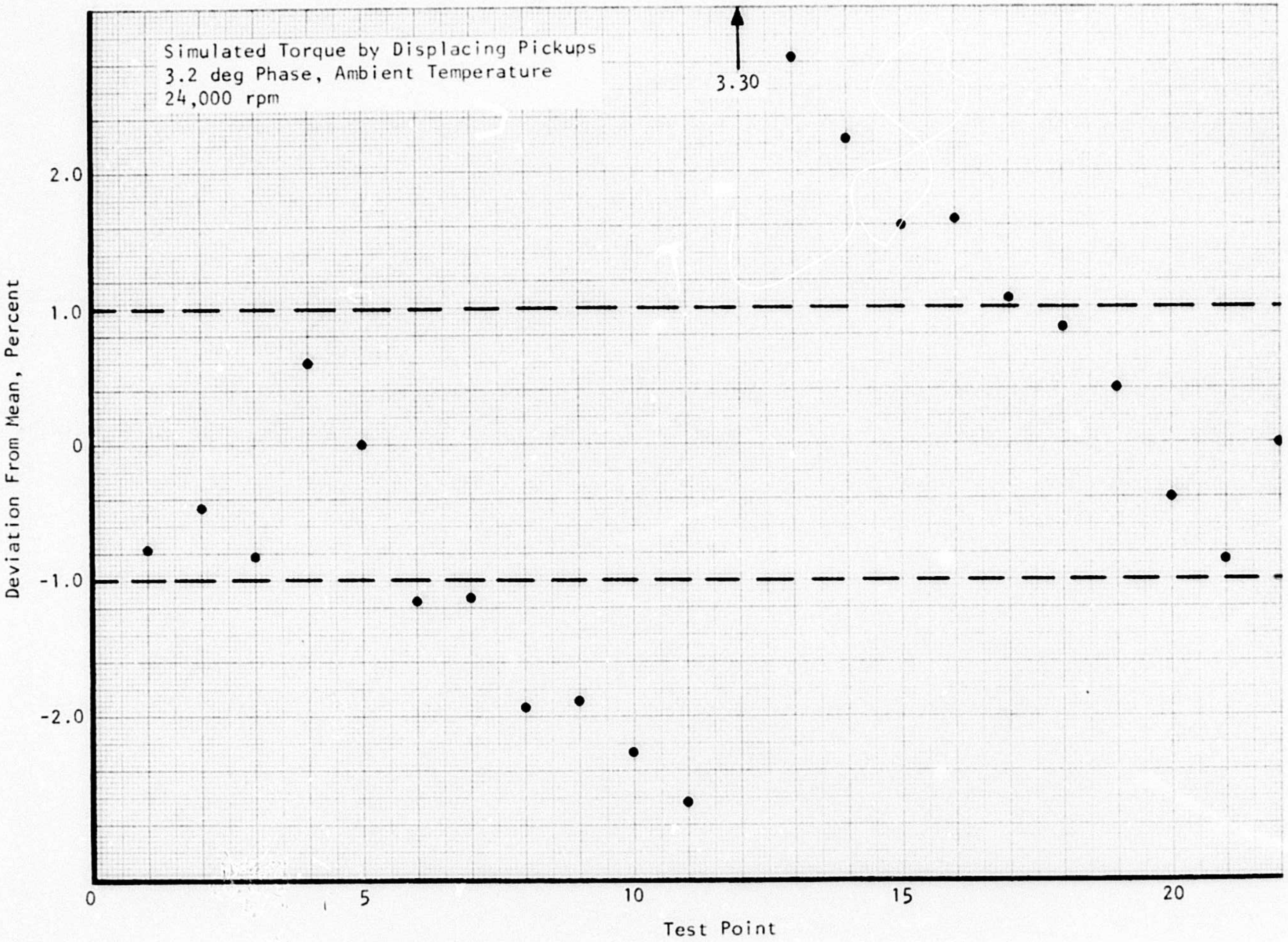

Figure 114. System Performance at 1/3 Full Scale, 24,000 RPM.

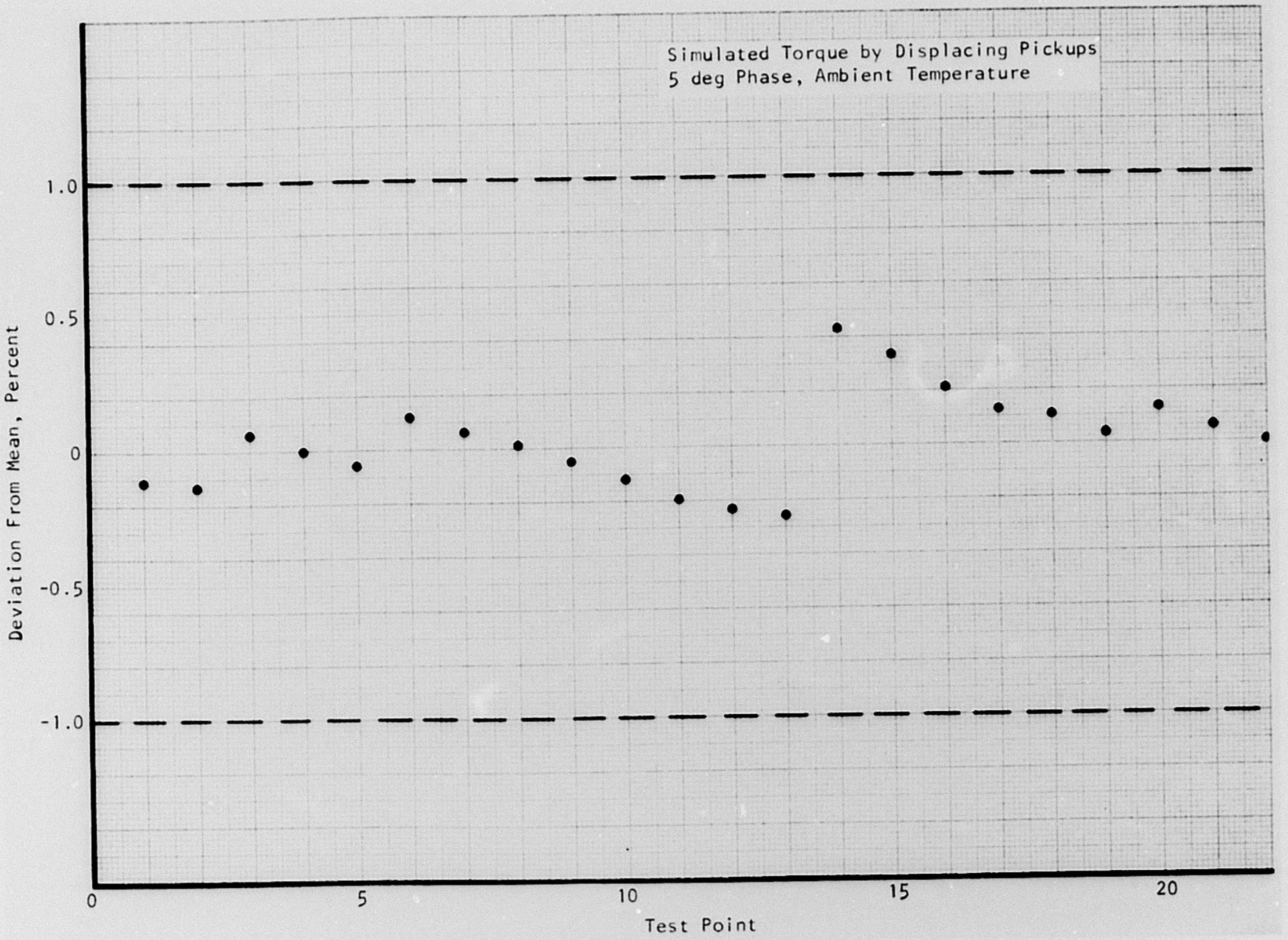

Figure 115. System Performance After Oil Contamination, 6000 RPM.

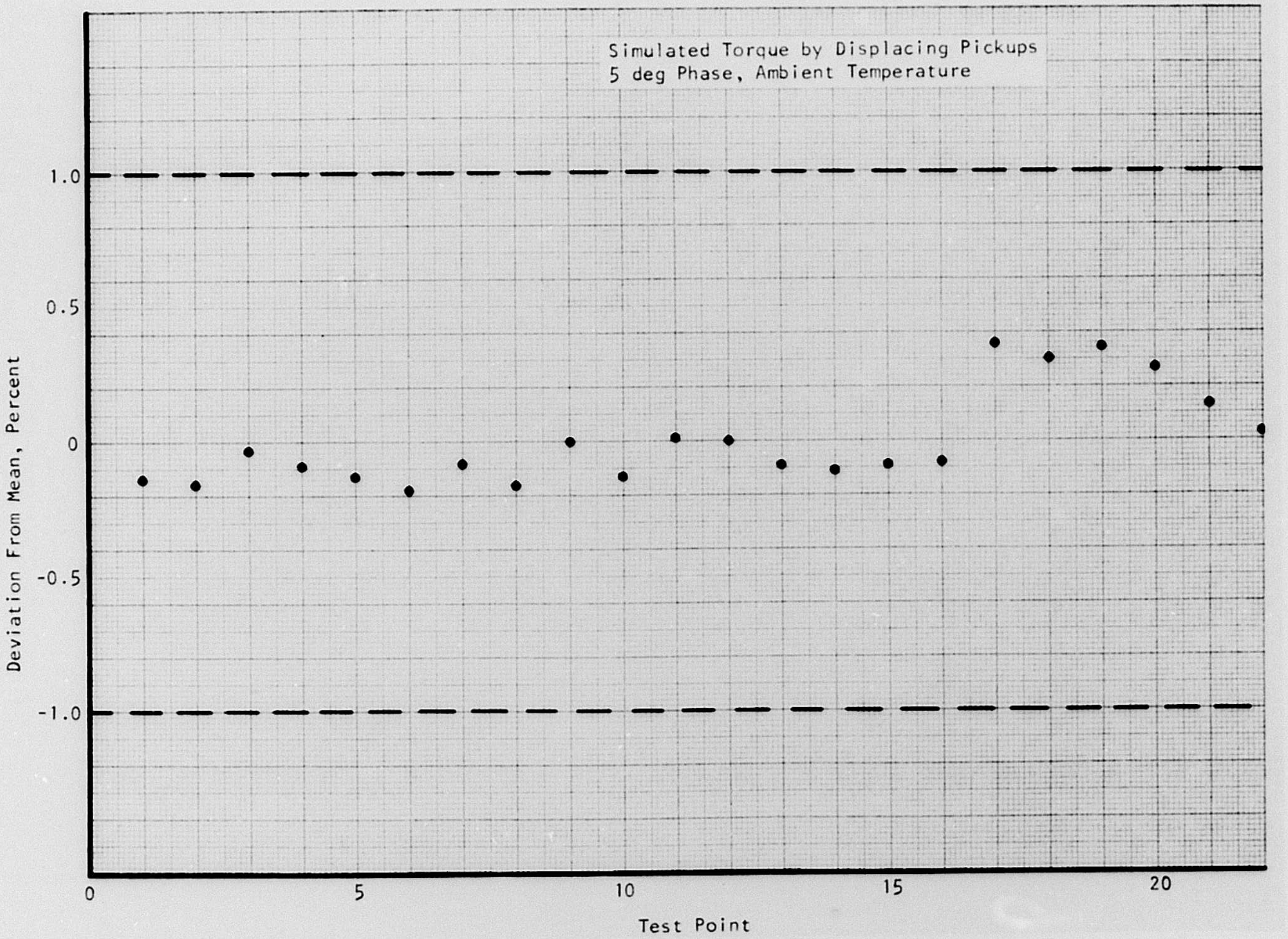

Figure 116. System Performance After Oil Contamination, 6600 RPM.

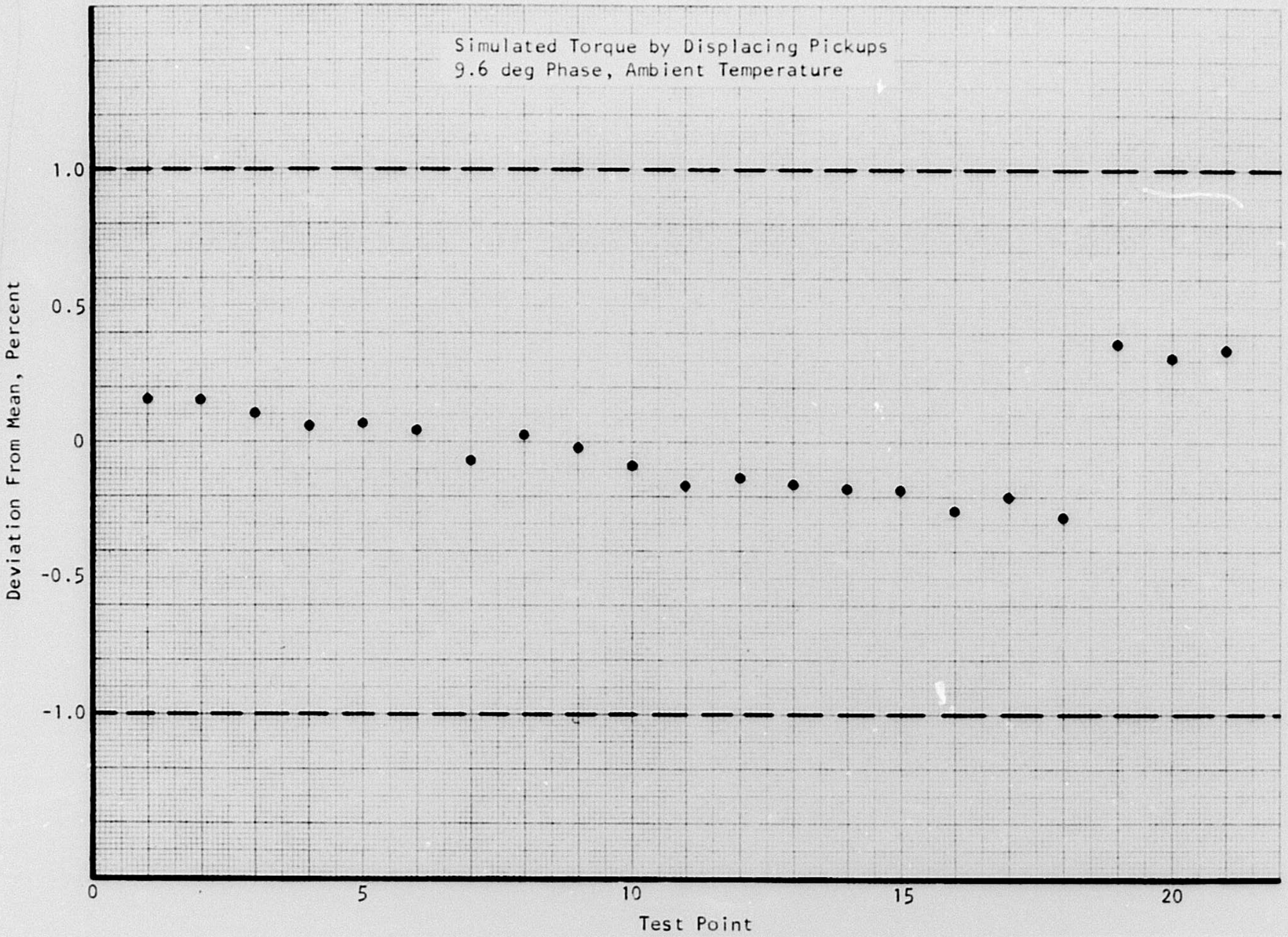

Figure 117. System Performance After Oil Contamination, 24,000 RPM.

## VIBRATION TEST

The experimental monopole pickups used in the laboratory test setup were not purposely subjected to a vibration test. However, a similar unit designed for use in a production engine was tested and qualified. The vibration envelope utilized is given in Figure 118. All three axes of the sensor were subjected to the vibration at a sine sweep of one octave/min. An endurance test of 12 hours per axis was performed at the resonant frequencies. No noticeable mechanical or electrical deterioration occurred.

The laboratory pickups did experience vibration caused by the critical frequency range of the rotating shaft. Although the pickups were exposed to a significant amount of vibration due to the various performance tests performed in this frequency range, no mechanical or electrical changes or damage occurred.

## AMBIENT PRESSURE EFFECT TESTS

As originally scheduled, the purpose of this series of tests was to determine the effect on the sensing unit of ambient pressure changes that would be encountered in actual operation. The ambient pressure effects on the magnetic monopole pickups and the eddy-current probes are known to be negligible, since these types of components are well-sealed and well-temperature-cycled components that have been used quite extensively on aircraft and engine applications for altitudes up to 40,000 ft. The only component that might be affected by the ambient pressure change is the grease-packed housing support bearing if used in an external drive shaft application. The lowering in ambient pressure could conceivably cause grease to seep through the seal; however, grease-packed bearings can be designed to prevent this as are the exposed grease-packed hanger bearings used on many models of helicopters.

Because of the anticipated lack of any detrimental effect of ambient pressure changes on the sensing unit and its components, the ambient pressure tests were considered to be justifiably omitted.

## SHAFT WOBBLE TEST

The influence of shaft wobble was observed and recorded as a consequence of operating the test specimen through the region of the shaft critical frequency. The induced wobbling in the region of interest (10,000 to 15,000 rpm) was quite severe and represented a suitable test. In practice, however, a drive shaft is not expected to be operated at its critical frequency. It was simply a matter of expediency that for the specific test article, the shaft critical speed could be used to excite a pseudo-wobbling.

In theory, shaft wobble causes the sensor pole piece to be rotationally ahead of or behind its nominal position. A time series distribution of individual readings from a specific pole piece then would be centered at the

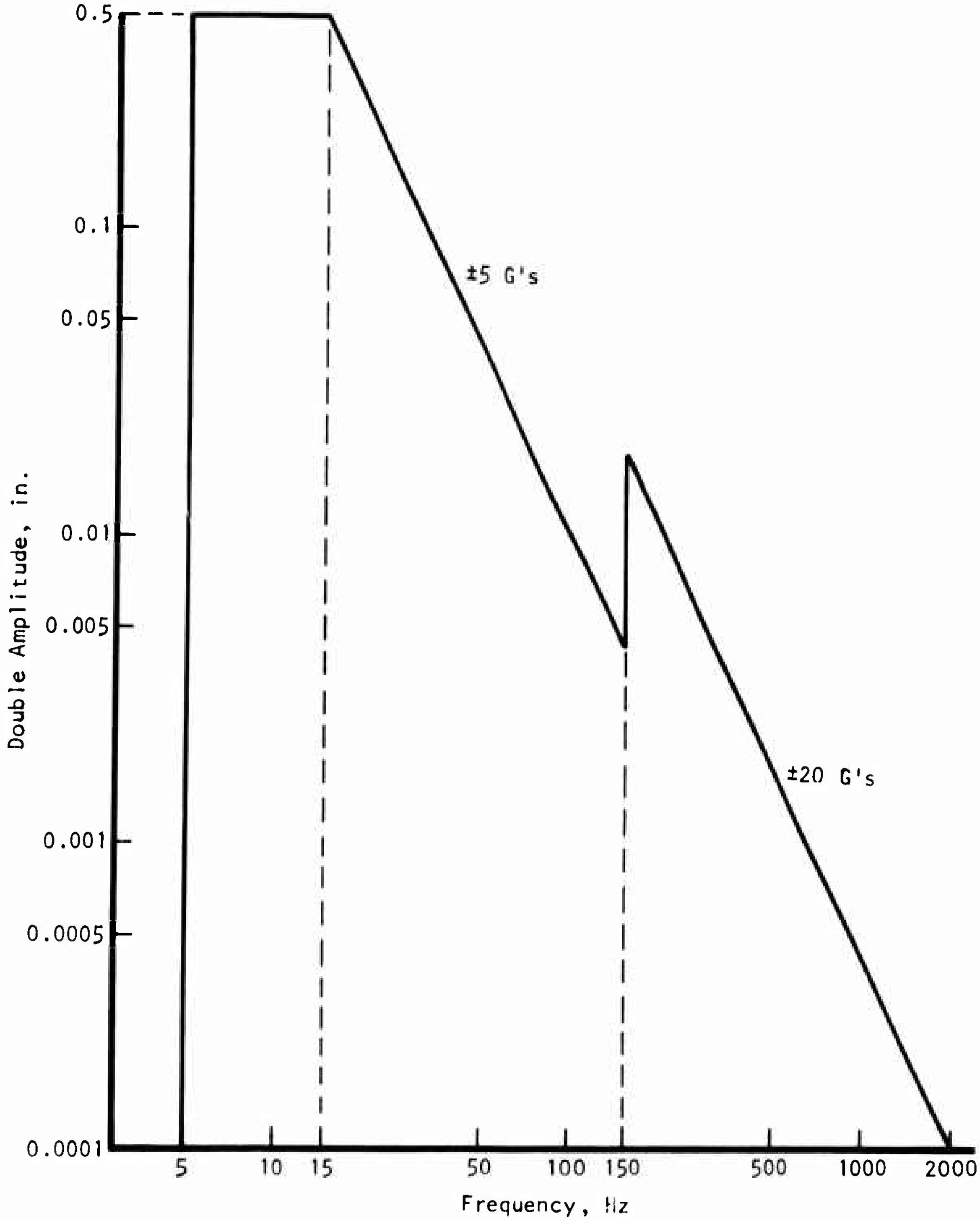

Figure 118. Vibration Envelope--Phase-Shift Torque System.

nominal reading provided a dissonance existed between the shaft speed and wobbling frequency. In the design approach selected, individual readings are obtained from a randomly selected pole piece. Therefore, a dissonance is created even though it may not mechanically exist. Results of the wobbling test should indicate that a spread of data occurs as the wobbling increases, but that the nominal (centered) value should not necessarily be affected. Since the nominal value is the output of the torque measurement system, the effect of wobbling on accuracy should be negligible.

Figure 119 presents the results of two tests. The nominal (centered) values do not change appreciably, but spread of data is indeed proportional to the amount of wobbling. Test results have good agreement with the theory.

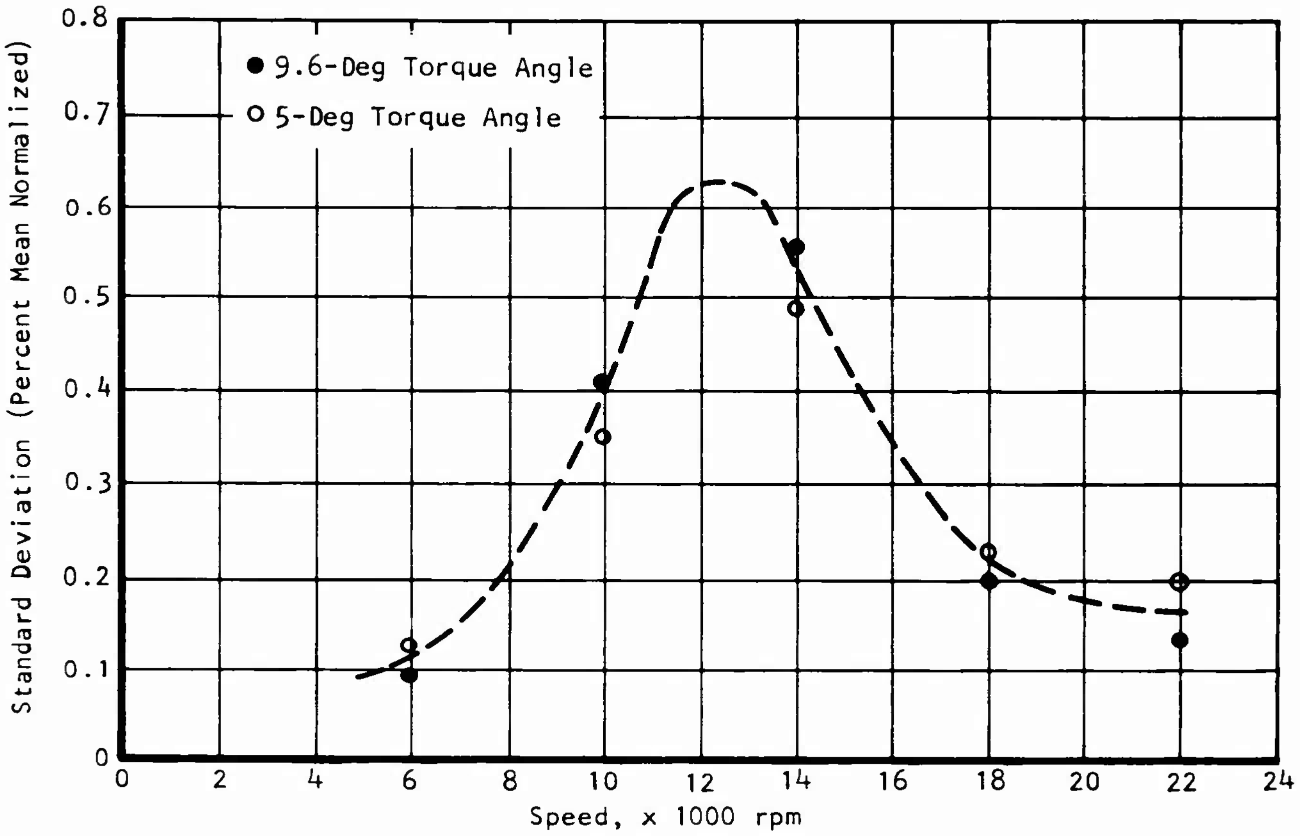

Figure 119. Data Spread Due to Wobble.

# CONCLUSIONS

The following conclusions can be drawn from the program results:

1. The digital coincidence interpolation technique for precise measurement of a twist angle is hardware implementable and economically feasible.

2. The performance of the hardware equipment that implements this technique is well within the ±1 percent tolerance band over the specified speed and the equivalent torque ranges. Degradation of system performance was observed over the 10,000-rpm to 14,000-rpm range due to the shaft resonant frequency of the test unit. Since none of the applications will be in that speed range and none of the operating shafts will be rotated at such a resonant frequency, the impact of the performance degradation due to shaft resonance on operating helicopters should be inconsequential.

3. Time needed to perform the measurement function depends upon the shaft rotational speed because of the coincidence checking operation. In general, it takes less than 3 shaft revolutions to achieve the measurement cycle. Consequently, the typical time needed for measurement is from 0.007 sec at 26,000 rpm to 0.03 sec at 6000 rpm. The time needed to complete the computations after the measurement is about 0.2 sec.

4. The accuracy of the system without temperature compensation is estimated to be about 2.38 percent, assuming a ±100°F temperature variation about the calibration point.

5. The weight of an aircraft-mounted sensing unit depends upon the location of the unit on the aircraft because of the difference in sensing unit housing design. For internal torsion shaft torque measurement applications, a total sensing unit weight of 5.5 lb appears to be accomplishable. For external drive shaft torque measurement applications, a total sensing unit weight of 10.5 lb is estimated, of which 7.5 lb is due to the housing structure and the supporting bearings. The size of the sensing unit for both application categories is estimated around 200 cu in. (e.g., a cylindrical volume of 6 in. in diameter and 7 in. in length).

6. The weight and size of an aircraft-mounted electronic processing unit are estimated to be 5 lb and 130 cu in., respectively (e.g., 5 in. x 7.5 in. x 3.5 in.). If the computation needed to calculate the value of torque from the measured coincidence counts and shaft temperature can be performed by an existing processor (such as a central diagnostic processor), the weight and size of the electronic processing unit can be reduced by 1/3 of the present estimate.

7. The weight and size of an aircraft-mounted digital display unit are estimated to be 0.5 lb and 14 cu in., respectively (e.g., 3 in. diameter x 2 in. long). This display unit can be eliminated if an integrated diagnostic display means is available on board the aircraft.

8. Test results indicated that the phase-measuring monopole pickups selected would survive and function properly over the specified temperature range of $-35^{\circ}$F to $+500^{\circ}$F.

9. Results from oil contamination tests indicated that there is no noticeable performance or structural deterioration caused by the contaminants.

10. Based on the existing in-house vibration test data on monopole pickups and eddy-current probes, it can be concluded that the sensing pickups and probes selected should also survive and function properly over the specified vibration environment.

11. Test results also indicated that a cable length of 10 to 20 ft from the sensing unit to the electronic processing unit is allowable.

12. The reasonably small size of the sensing probes used, the high environmental tolerance capability, the high reliability of the system, and the wide speed range that a single system can handle promise versatility and economy for many applications. The same system can be used for external aircraft shafts or internal engine shafts. It can be applied to any size shaft as long as a minimum twist angle of $\simeq 1$ deg is developed by the torque, and enough room around the shaft is available for sensor installation.

13. The use of eddy-current probes for noncontacting shaft temperature measurement is feasible. However, sensor optimization efforts appear to be needed in order to achieve better accuracy, more shaft-adaptation capability, more stable operation, and fewer parts-count in hardware implementation.

## RECOMMENDATIONS

It is recommended that:

1. The digital coincidence-interpolation torque sensing developed during the program be further tested on an actual aircraft or engine-mounted shaft to determine its performance under the real operating conditions.

2. A separate investigation on sensor optimization of the eddy-current temperature probes be conducted concurrently with the aforementioned test program so that better information exchange can be maintained between these two activities. This effort should be separated from the test effort because of the difference in nature of these two types of activities. A separate eddy-current temperature probe optimization effort would also allow the investigation of the use of such sensors for noncontacting measurement of turbine blade metal temperature for turboshaft or turbojet type engines.

# APPENDIX
# TYPICAL DRIVE SHAFT ANGULAR DEFLECTION

## FORMULAS, CONSTANTS, AND ASSUMPTIONS

Hollow concentric shaft: $r_1$ = outer diameter, $r_0$ = inner diameter (= 0 for solid shaft)

$$\text{Angular twist (deg)} = \theta = 57.3\,\frac{TL}{JG} \tag{89}$$

where T = twisting moment or torque (in.-lb)

L = length of shaft (in.)

J = polar moment of inertia = $1.2\,\pi\,(r_1^4 - r_0^4)$ (in.$^4$)

G = modulus of rigidity ~ $12 \times 10^6$ lb/in.$^2$ for steel

$$\text{Maximum shear stress} = (S_s)_M = \frac{Tr_1}{J} = \frac{2Tr_1}{\pi(r_1^4 - r_0^4)} \quad (\text{lb/in.}^2) \tag{90}$$

## Two Drive Cases Considered

1. Rotational speed = 6600 rpm ≃ 691 rad/sec (= N)

   Maximum torque = 725 ft-lb = 8700 in.-lb (= $T_M$)

2. Rotational speed = 26,000 rpm ≃ 2720 rad/sec (= N)

   Maximum torque = 300 ft-lb = 3600 in.-lb (= $T_M$)

## Material Characteristics

Assume the use of a suitable material with a conservative shear yield strength:

AM355 precipitation-hardened stainless steel shear yield strength = 79,500 lb/in.$^2$

A typical factor of safety that would be used to calculate allowable maximum shear stress for full-load conditions is 2.5. Therefore,

$$(S_s)_M = \frac{79{,}500}{2.5} = 31{,}800 \text{ lb/in.}^2 \tag{91}$$

## DRIVE SHAFT SIZING

Three sizes of shafts for each of the test drive cases will be considered to determine a range of twist: one solid shaft and two hollow concentric shafts.

### Solid Shafts

Using Equation (91) and noting that $r_0 = 0$,

$$r_I = \left(\frac{2T}{\pi(S_s)_M}\right)^{1/3} \qquad (92)$$

Case 1: $T = 8700$ in.-lb, $r_1 = 0.558$ in.

Case 2: $T = 3600$ in.-lb, $r_1 = 0.416$ in.

### Hollow Concentric Shafts

Values of $r_1$ are stipulated, and corresponding values of $r_0$ are calculated using Equation (91).

$$r_0 = \left(r_I^{\,4} - \frac{2Tr_I}{\pi(S_s)_M}\right)^{1/4} \qquad (93)$$

1. $r_1 = 0.50$ in.

   Case 1: Not applicable

   Case 2: $T = 3600$ in.-lb, $r_0 = 0.403$

2. $r_1 = 0.75$ in.

   Case 1: $T = 8700$ in.-lb, $r_0 = 0.655$

   Case 2: $T = 3600$ in.-lb, $r_0 = 0.715$

3. $r_1 = 1.0$ in.

   Case 1: $T = 8700$ in.-lb, $r_0 = 0.954$

   Case 2: Not applicable

Table XVI presents a summary of the shaft calculations.

## TABLE XVI. SHAFT CALCULATIONS

| Shaft Size | | | | | | |
|---|---|---|---|---|---|---|
| $r_1$ (in.) | $r_0$ (in.) | $J$ (in.$^4$) | Torque (in.-lb) | Twist/ft $\theta = 687.6\ T/JG$ (deg/ft) | N (rpm) | $\Delta t$ for $L = 1$ ft $\Delta_t = \theta/N$ ($\mu$sec) |
| 0.558 | 0 | 0.153 | 8700 | 3.26 | 6,600 | 82.3 |
| 0.75 | 0.655 | 0.205 | 8700 | 2.43 | 6,600 | 61.4 |
| 1.00 | 0.954 | 0.2735 | 8700 | 1.82 | 6,600 | 46.0 |
| 0.416 | 0 | 0.0471 | 3600 | 4.38 | 26,000 | 28.1 |
| 0.50 | 0.403 | 0.0566 | 3600 | 3.64 | 26,000 | 23.3 |
| 0.75 | 0.715 | 0.0849 | 3600 | 2.43 | 26,000 | 15.6 |